

The Pennsylvania State University

The Graduate School

Department of Physics

MEASUREMENT OF H, He, C AND O COSMIC RAY

PRIMARIES:

PRELIMINARY RESULTS FROM THE CREAM II

EXPERIMENT

A Dissertation in

Physics

by

S. A. Isaac Mognet

© 2009 S. A. Isaac Mognet

Submitted in Partial Fulfillment
of the Requirements
for the Degree of

Doctor of Philosophy

December 2009

The dissertation of S. A. Isaac Mognet was reviewed and approved* by the following:

Stephane Coutu
Professor of Physics
Professor of Astronomy and Astrophysics
Dissertation Adviser
Chair of Committee

Paul Sommers
Professor of Physics
Professor of Astronomy and Astrophysics

Richard Robinett
Professor of Physics

John Nousek
Professor of Astronomy and Astrophysics

Jayanth Banavar
Professor of Physics
Head of the Department of Physics

*Signatures on file in the Graduate School.

Abstract

The direct measurement of the energy spectrum and composition of the incoming cosmic-ray flux at multi-TeV energies is of great interest. A feature located somewhere between 1000-10,000 TeV in the all-particle spectrum, referred to as the ‘knee’ characterized by a steepening of the power-law flux, has been observed by ground-based detectors for many years. It is believed to be related to an upper limit or change in efficiency of the Galactic accelerators of cosmic rays and/or properties of the propagation of cosmic rays in the Galaxy. Presented here is a preliminary analysis of the flux of primary H, He, C and O cosmic-ray species measured using the CREAM II instrument. This analysis is conducted using the Penn State-built Timing Charge Detector, distinct from other charge detectors used in alternative published CREAM II results.

The second Antarctic flight of the CREAM instrument had a ~ 28 day flight in the 2005-2006 Antarctic flight season. The instrument was launched on December 16th 2005 from Williams Field near McMurdo Station, Antarctica. The analysis presented here used events collected throughout the flight to calibrate the charge response of the Timing Charge Detector. High-energy events collected during the entire flight time (except for the first ~ 3.5 days which were used for high-voltage tuning) are also analyzed here.

Also presented in this thesis is a novel optical simulation of the Timing Charge Detector used in the various flights of the CREAM instrument. The model suggests fundamental limitations on the timing resolution of the detector arising purely from photon propagation physics in the scintillation and light-guide elements.

Table of Contents

List of Tables	vii
List of Figures	x
Acknowledgments	xx
Chapter 1. Cosmic Rays	1
1.1 Cosmic Rays	1
1.1.1 The All-Particle Spectrum	2
1.1.2 Cosmic-Ray Elemental Composition	5
1.2 Propagation of Cosmic Rays	5
1.2.1 The Diffusion-Loss Equation for Cosmic Rays	7
1.2.2 Using the Diffusion-Loss Equation	9
1.2.3 Solar Modulation	11
1.2.4 Geomagnetic Cutoff	11
1.2.5 Solar Activity	11
1.3 Acceleration of Cosmic Rays	11
1.3.1 First Order Fermi Shock Acceleration	11
1.3.2 Reacceleration	16
1.3.3 The Limit of Acceleration	16
1.4 Other Particles of Interest	18
1.5 Cosmic-Ray Detection	19
1.5.1 Balloon-Based Measurements	20
1.5.2 Space-Based Measurements	21
1.5.3 Ground-Based Measurements	23
1.5.4 Sub-surface Measurements	25
1.6 Current Measurements of Elemental Abundances of Cosmic Rays . .	26
Chapter 2. The Cosmic Ray Energetics and Mass Instruments	28
2.1 Goals	28
2.2 CREAM I Instrument Overview	28
2.2.1 Timing Charge Detector	30
2.2.2 Transition Radiation Detector	31
2.2.3 Cherenkov Detector	31
2.2.4 Silicon Charge Detector	33
2.2.5 Calorimeter	34
2.2.6 Ballooncraft	36
2.3 The CREAM Payloads and Flights	36

Chapter 3.	CREAM TCD Design and Construction	40
3.1	Detector Description	40
3.2	Design Considerations	40
3.3	TCD Scintillation Paddles Construction	42
3.4	S3 Detector Construction	44
3.5	TCD Mechanical Support	45
3.6	High-Voltage Potting	46
3.7	TCD-Electronics Mounting	48
3.8	Testing and Validation	49
Chapter 4.	TCD Electronics	52
4.1	TCD Low-Voltage Power Systems	52
4.2	TCD HV System	53
4.2.1	CREAM I	53
4.2.2	CREAM II and Beyond	54
4.3	Photomultiplier Tubes and Electronics	54
4.3.1	Photomultiplier Tubes	54
4.3.2	Phototube-Base Electronics	55
4.4	Readout Electronics	57
4.4.1	Time to Digital Converters (TDCs)	60
4.4.2	Peak Detectors	62
4.5	High-Voltage and TDC Threshold Setting	63
4.6	Trigger Formation and Logic	66
4.6.1	TCD Trigger System	66
4.6.2	CREAM Instrument Trigger	66
4.7	TCD Concentrator System	68
4.8	Commanding and Data Readout	68
4.9	TCD Housekeeping	69
4.10	CD Readout (CREAM II and later)	70
Chapter 5.	CREAM TCD Timing and Tracking	71
5.1	Internal TCD Timing	71
5.2	Analysis Tools	74
5.3	CREAM II Data Overview	75
5.4	CREAM II Time-of-Flight	76
5.5	CREAM II End-to-End Paddle Timing	83
5.6	TCD Tracking Calibration using CREAM I	90
Chapter 6.	CREAM II Charge Calibration and Performance	98
6.1	Scintillator Response	98
6.2	ROOT File Processing	99
6.3	SCD Charge Calibration	100
6.4	TCD ADC Charge Calibration	101
6.5	ADC Range Stitching	102
6.6	ADC Charge Resolution	107

6.7	TDC Timing-Charge Dependence	108
Chapter 7.	CREAM Timing Charge Detector Optical Model	112
7.1	GEANT4 Coding Overview	112
7.2	Detector Definition	112
7.3	Sensitive Detectors and Hit Collections	114
7.4	Physics Models	114
7.5	Signal Digitization	115
7.6	Timing Resolution of the TCD Scintillator Paddles and Electronics	117
7.7	Light Attenuation	117
7.8	Simulated ADC Signals	119
7.9	Simulated TDC Signals	120
7.10	Reflective vs. Nonreflective Paddle-Wrapping Comparison	121
Chapter 8.	CREAM II Spectra	130
8.1	Calorimeter Energy Reconstruction	130
8.1.1	Bin Energy Value	131
8.2	Tracking	134
8.3	TCD Charge Measurement With Both Layers	136
8.4	TCD Charge With Energy	144
8.5	Measured Spectra	149
8.6	Note on Absolute Fluxes	153
8.7	Comparison with Previous Measurements	153
Chapter 9.	Conclusions	159
9.1	TCD Performance	159
9.2	Elemental Spectra	159
9.3	The Author's Contributions to the CREAM Project	160
9.4	The Way Forward for CREAM	161
Appendix A.	Particle Interactions in Matter Relevant for Detection	162
A.1	The Bethe-Bloch Equation	162
A.2	Scintillators	164
A.3	Silicon	165
A.4	Cherenkov Radiation	165
A.5	Transition Radiation	166
Bibliography	167

List of Tables

1.1	Approximate energy densities of particles arriving at Earth and various extensive fields in space relevant for cosmic-ray propagation.	2
2.1	The flights of the CREAM experiment to-date.	36
4.1	Vicor modules used in the CREAM TCD power-converter box.	53
4.2	Assignment of PMT signal taps to readout electronics.	58
4.3	CREAM I Master Trigger Modes. High-Z collects relativistic species with $Z \geq 3$ which produced a sufficient signal in the TCD and CD. EHI are for events which showered in the Calorimeter. CALIB is an external calibration trigger.	68
4.4	CREAM II Master Trigger Modes, with different selectable options shown. ELO is intended to collect events within the Calorimeter geometry that did not produce a trigger from the Calorimeter for whatever reason, but still triggered S3HI. ZCLB collects relativistic species with $Z \geq 3$ for calibration of the TCD and CD. EHI collects events which showered in the Calorimeter. CALIB is a calibration trigger for Calorimeter and SCD events, EXT is an external calibration trigger (ground only).	69
5.1	All trigger flags recorded in the CREAM II flight (See Section 4.6.1 for an explanation of the triggers). TRG is a count of the total number of individual event triggers (all events, but only counting events with multiple trigger types once).	76
5.2	Uncorrected and corrected TOF measurements for the CREAM II flight and associated distribution widths. The quoted uncertainty is the ROOT fitting uncertainty for the parameters from applying Gaussian fits to the peaks. The peak-position quoted here is that of the right-most peak corresponding to downward-going particles.	80
5.3	Corrected peak-positions and widths of the albedo distributions (left-most peaks in Figure 5.7), where the quoted uncertainty is the ROOT fitting uncertainty from applying Gaussian fits to the peaks. Also shown are the separation (in channels) between the albedo peak distribution and the downward-going distribution. Arithmetic means are calculated for the separations as well for the inner paddles (Paddles 1,2,5,6), outer paddles (Paddles 0,3,4,7) and for all paddles.	83

5.4	Uncorrected and corrected end-to-end measurements for the CREAM II TCD, with both the paddle mean-offsets and individual tile (pair of crossed paddles) distribution widths. The quoted offsets are the mean of the positions of the four tile distributions (given equal weight). The quoted uncertainty is the quadrature sum of the ROOT-output fitting uncertainty for the parameters (from applying Gaussian fits). Note that Paddle 5 is intentionally skewed so that the larger part of a bimodal distribution was correctly offset-subtracted (discussed in this section). .	86
5.5	Uncorrected and corrected end-to-end measurements for the stable subset of the CREAM I TCD (day 19 to day 26). Error estimations and measurements are made following the same procedure as for Table 5.4. For reasons discussed in this section, Paddles 0,5 and 6 omitted.	91
5.6	Results of constrained linear fits to the distributions in Figure 5.17. These measured parameters can be used with Equation 5.11 to find the particle hit position in a TCD paddle.	94
5.7	Average CREAM I end-to-end timing accuracy measured against TRD position, as taken from Figure 5.18. The errors on the mean values are the quadrature sum of the relevant uncertainties.	97
6.1	Charge resolution (for helium and carbon) for the SCD, TCD Paddle 1, and average of the two. Both TCD paddle tubes are required to agree to within one charge unit, and the TCD and SCD are required to agree within one charge unit for the average shown. Other Paddles were consistent with these values, and the charge-resolution for the TCD as a whole will be presented in Section 8.3	109
7.1	Most-probable-values and widths (σ) from Landau fits performed on the distributions in Figure 7.11. Results are in number of photons arriving at the single simulated PMT.	127
7.2	Mean ADC response and Gaussian distribution widths for the histograms in Figure 7.12.	127
8.1	Definitions of the energy bins used in the analysis presented in this chapter.	131
8.2	Charge resolutions of the TCD and SCD from this analysis for listed species. This is done here for all events with a calorimeter signal present and with the respective charge detector producing a proper charge reconstruction. The above resolutions were derived from fits performed on Figure 8.8 (for the TCD) and Figure 8.6b (for the SCD). Helium, carbon and oxygen quoted resolutions are the σ parameter from Gaussian fits, while the quoted quantity for hydrogen for the SCD is σ from a Landau distribution fit. The hydrogen in the TCD was fitted with a convolved Gaussian and Landau distribution function, and the quoted resolution here is the quadrature sum of the Gaussian and Landau σ parameters. .	143

8.3	The energy reported for each energy-bin, estimated number of hydrogen events and flux (in arbitrary units). The reported uncertainty on the number of events is the quadrature-sum of the Poisson uncertainty (\sqrt{N}) and the uncertainty of the numerical integral. The energy values are the result of looping Equation 8.2 with a starting guess of the spectral index of $\gamma = -2.5$ and requiring agreement to 0.0001 between loops. Values were found to be convergent after only the second execution of the loop. The fluxes quoted here are the number of events divided by the energy bin-width.	146
8.4	Energy bin values, number of events and fluxes (in arbitrary units) for helium events. Same error estimation as in Table 8.3.	148
8.5	Energy bin values, number of events and fluxes (in arbitrary units) for carbon events. Same error estimation as in Table 8.3.	148
8.6	Energy bin values, number of events and fluxes (in arbitrary units) for oxygen events. Same error estimation as in Table 8.3.	148
8.7	The peak positions for the species-fits performed in Figure 8.10. These are also plotted in Figure 8.11. Measurements marked with an “X” represent fits that were unsuccessful.	150
8.8	Widths of the species-fits performed in Figure 8.10. These are plotted in Figure 8.12. Measurements marked with an “X” represent fits that were unsuccessful.	151
8.9	The spectral indices measured for the indicated species as shown in Figure 8.13. The fits were performed excluding the two lowest-energy data points for each species.	152
8.10	The spectral indices measured for the four studied species in this analysis, after excluding the first 3 lower-energy data points shown in Figure 8.13. Only the power-law fit values are quoted here since the linear-fit method discussed above was again found to be consistent. The quoted uncertainties are those from the power-law fit performed on the data-points. Since this analysis does not include important instrumental and atmospheric corrections, the quoted spectral indices are not within errors of an alternative CREAM analysis presented in [1].	158
A.1	Quantities appearing in the Bethe-Bloch equation.	162

List of Figures

1.1	The all-particle spectrum of cosmic rays[2].	3
1.2	The all-particle spectrum of cosmic rays showing the possible second ‘knee’ as well as the ‘ankle’ and possible GZK cutoff feature above 10^{19} eV (From the Particle Data Group [3]).	4
1.3	Relative abundances of cosmic rays compared to solar system abundances. Prominent secondary species are circled. Fluxes are scaled to arbitrary units with Silicon set to 100 (modified from [4]).	6
1.4	Fluxes ϕ of particles through the surfaces of a box in energy-space parameter space. The fluxes ϕ_x and ϕ_{x+dx} are the number of particles flowing through the energy surfaces located at x and $x+dx$, respectively. The fluxes ϕ_E and ϕ_{E+dE} are analogous. The total number of enclosed particles is $N(E, x, t)dEdx$	7
1.5	Boron-to-carbon ratio as measured by the CREAM I experiment. The energy here is measured with a Transition Radiation Detector (TRD), with charge measurements by a Timing Charge Detector (TCD) and a Silicon Charge Detector (SCD) which are discussed in more detail in Chapter 2 of this thesis. The gray bars are systematic uncertainty in the measurements, while the solid vertical lines are statistical uncertainties. Horizontal error bars are estimates of the systematic uncertainty of the energy assignments. Also shown are several theoretical predictions for different values of δ	10
1.6	Views of a strong shock in various reference frames.(a) Seen from a frame at rest with respect to the surrounding undisturbed interstellar medium, the shock front is advancing with velocity U . (b) In the frame with the shock stationary, the ISM appears to be approaching the shock at velocity $v_1 = U $, and the downstream gas behind the shock appears to be receding at velocity $v_2 = \frac{1}{4}U$. (c) Again in the frame with stationary ISM, the gas behind the shock appears to be approaching at velocity $\frac{3}{4}U$ and (d) in the frame co-moving with the shocked gas, the ISM also appears to be approaching at velocity $\frac{3}{4}U$	13
1.7	The all-particle spectrum of ultra-high energy cosmic rays. This represents the highest part of Figure 1.2, with the flux rescaled by E^3 . The presence of the GZK cutoff feature above $10^{19}eV$ seems reasonable if Auger and HiRes energy reconstructions are accurate (from the Particle Data Group [3]).	24
1.8	Chemical composition estimations from the KASCADE ground array experiment. Results for the QGSJet hadronic interaction model and the FLUKA and GHEISHA Monte Carlo packages are also shown. The shaded region is the estimated systematic uncertainty for the QGSJet/-GHEISHA solutions. (From the KASCADE Collaboration [5]).	25

1.9	Proton and helium fluxes from CREAM-I and several other direct measurements by high-altitude payloads. The CREAM-I measurements here involve energy determination from an electromagnetic calorimeter, and charge determination from a silicon charge detector, both discussed in following chapters. (From the CREAM Collaboration [6]).	27
2.1	Exploded schematic representation of the CREAM I instrument (science detectors) [7]. The TCD, CD, TRD, SCD, S3 and CAL module are all discussed in this chapter. W1-20 are tungsten plates making up the absorber layers of the calorimeter module. SCN1-20 are scintillating-fiber readouts between each absorber. Target 1 and 2 are graphite blocks to initiate hadronic showers. S0/S1, S2 and S3 are scintillating-fiber hodoscopes for redundant charge measurement, tracking, time-of-flight and trigger uses.	29
2.2	TRD response (in arbitrary units) as a function of particle $\log \gamma$. The blue line is the GEANT4 simulated response of the proportional tubes only. The red line is the simulated response with transition radiation from the Ethafoam radiator included. Symbols are from CERN beam testing of prototype hardware both with and without TR. [8].	32
2.3	CREAM I SCD with cover removed.	33
2.4	CREAM II calorimeter stack during integration. The bottom structure is the calorimeter with fiber-optic readout visible. Above the CAL are the two carbon targets, with supporting metal pedestals at the corners.	34
2.5	CREAM calorimeter tungsten plates stacked for a fit check, before mounting of scintillating fibers and light tightening.	35
2.6	Installation of calorimeter scintillating fiber layer.	35
2.7	The CREAM II payload during flight readiness preparations in Antarctica (December 2005). The spherical antenna on top of the payload is the TDRSS antenna housing. The CDM is the reflective box in the lower-middle portion of the payload.	37
2.8	CREAM I ~ 42 day flight trajectory, originally from Columbia Scientific Balloon Facility (CSBF) tracking (currently at [9]). Different colors are for successive polar orbits (red first, green second, blue third).	38
3.1	CREAM TCD scintillation paddle light guide made of BC-802 acrylic plastic (from [10]). Each light guide is made from 10 pieces.	41
3.2	Two CREAM TCD scintillation paddles after gluing but before wrapping for light tightness.	42
3.3	Two CREAM TCD XP2020 PMTs being prepared for installation. The tube on the right has been mounted to the PMT active base circuit boards (Chapter 4). The tube on the left has also been potted and grounded to prevent HV breakown, had a Lucite extender and aluminum mounting ring attached (for coupling to the light guide) and wrapped for light-tightness. Not visible here under the light-tightening are two layers of μ -metal for shielding from the magnetic field of the earth.	43

3.4	The S3 scintillating fiber detector shown under test. Part of the clamping system is visible which allows for pressure to be applied to press the PMT into the optical coupling cookie (from NASA and University of Maryland Cosmic Ray Physics Laboratory [11]).	44
3.5	The CREAM I instrument (science only) before integration with balloon-craft components. The TCD support scheme is visible here, including outrigger arms for mounting of TCD electronics boxes and PMT/lightguide support brackets (marked with the green arrow). (From NASA and University of Maryland Cosmic Ray Physics Laboratory [11]).	45
3.6	The coordinate system used for the top of the TCD. The X and Y directions are defined for the entire instrument. PMTs are labeled from 0-15. Concentrators control and monitor two PMTs each.	47
3.7	Instrument Pallet-mounted TCD components. The scintillation paddle S3 is shown in green. Also shown is the TCD Power-Converter Box and the TCD Concentrator for S3.	47
3.8	A refurbished Ultravolt high-voltage power supply assembly for CREAM. The actual supply is not visible here, but is potted with Stycast in the larger box. The smaller box is present to split the voltage to power two PMTs (a small circuit board is also present for mounting of series-matching resistors if needed).	48
3.9	CREAM TCD electronics box (Concentrator). The boards (from bottom to top) are: power board, two peak detector ADC boards, a local trigger board, two TDC boards and the on-board computer board. The computer [12] actually resides in a small daughter-board at the very top of the stack.	49
3.10	CREAM electronics box refurbished and fully assembled. Visible on the top are gold-plated SMA headers from anode and dynode PMT signals. Each box takes input from two adjacent PMTs in the TCD. Also present on the top and side are connections for Ethernet, serial, trigger, event number input, and power input.	49
3.11	PVC vacuum chamber for PMT/HV testing at Penn State. The chamber consists of a center section of PVC sewer pipe, with end-caps. The center section has been light-tightened with a layer of Tedlar and electrical tape. One end-cap contains piping for the vacuum pump and venting, the other contains BNC electrical feed-throughs (neither end-cap shown).	50
3.12	Blue LED in a fixture for consistent mounting on CREAM TCD PMTs. This allowed for performance gain matching between PMTs so they could be grouped into pairs needing similar HV supply. This fixture contains a circuit board with a resistor for current limitation, blue LED, and BNC input for attachment to a fast-pulse generator. The fixture uses the standard PMT-mounting ring used in CREAM II and subsequent flights.	51
4.1	Schematic of one TCD power-converter circuit (6 Total). The fuse is a resettable surface-mount type. Table 4.1 lists the modules used for the different supplies.	52

4.2	Full schematic of the CREAM TCD PMT-base circuit. All transistors are Zetex FMMT458 NPN type, D1-12 are DL4148 diodes and D13-24 are 2.3V zener diodes. Signal taps are shown by circles. The XP-2020 PMT anode, dynodes (DY1-12), grids, and cathode are shown as well. High-voltage input is at the left-hand side. [10]	56
4.3	Simplified schematic of one stage of the PMT-base circuit. R1 and R2 are a voltage-divider to provide some wanted division of V_{cc} . Q1 acts as a follower and presents a voltage set by R1 and R2, but sinks current through its collector, thus not loading the voltage-divider chain.	57
4.4	Sketch of a PMT pulse showing the TDC and ADC readout. v_0 and v_1 are threshold voltages for the TDCs to begin timing, and t_0 and t_1 are two different common stop times. The TDC readout is the length of time from threshold crossing until the common stop, the ADC readout is the voltage stored in the peak detector at the time of the common stop. Note the discharge of the Peak Detector circuit is important if common stop times are substantially different.	58
4.5	Overview of the readout for one PMT.	59
4.6	Schematic of one TDC circuit	61
4.7	Schematic of one Peak Detector circuit. The DYNODE input comes from the PMT-base circuit and the PEAK level goes to the ADC section. RESET IN is to clear the peak-detector circuit of its currently stored value.	63
4.8	Charge histogram of stitched ADC0 and ADC2 readout (two crossed paddles) for a $158\text{GeV}/n$ indium fragment CERN beam-test from 2003. [10]	64
4.9	Atmospheric muon ground data taken on December 3 rd 2005 by the CREAM II TCD. Shown here are the ADC0 readouts for only the PMTs on the +X side of the instrument (Tubes 0-3). Calibration of the muon signal to 1000 channels was largely successful, but some other tubes (not shown) could not be brought to 1000 channels without exceeding their HV operating limit. Additionally, some pairs were not performance-matched sufficiently closely, and a compromise gain setting had to be chosen.	65
4.10	The TCD trigger system	67
4.11	Diagram of the TCD software readout and commanding scheme. eServer and cServer are server applications that reside in each TCD Concentrator box. eServer handles data, cServer handles command reception and execution. Not shown here are Ethernet switches which connect all 9 (or 10 for CREAM II and above) Concentrators to the SFC.)	70
5.1	Threshold crossing times and particle arrival times for a TCD paddle and the S3 detector. This is representative of the conditions for a TCD LoZ trigger type. The particle arrives at the TCD at time t_A and the S3 paddle at time t_B . The signals cross threshold in PMT 0-3 at times $t_0 - t_3$.	72

5.2	Representation of the TDC readouts for an event involving S3 (TCD LoZ type trigger). Note the PMTs which receive light first will have larger TDC readout signals than the ones hit subsequently.	72
5.3	Propagation distances in a TCD paddle of length L_{tcd} for a particle hit at location p measured with respect to the center of the paddle.	73
5.4	Number of hit X-direction TCD paddles per event for a) all events and b) events with a calorimeter track present (tubes at both ends required to cross threshold). Y-going paddles have qualitatively identical distributions, so are omitted here.	77
5.5	Uncorrected TCD-to-S3 time-of-flight measurements for all 8 TCD paddles in the CREAM II flight. The only cuts implemented here are to require that TDC <i>threshold</i> 0 be on scale for the two TCD paddle tubes and the two S3 tubes ($0 < tcd.fTDC[tube][0] < 4095$).	78
5.6	Uncorrected TCD-to-S3 time-of-flight measurements (channels) as a function of flight-time (in days) for all 8 TCD paddles in the CREAM II flight. Same on-scale cuts applied as in Figure 5.5.	79
5.7	Corrected TCD-to-S3 time-of-flight measurements for all 8 TCD paddles in the CREAM II flight. Again, the cuts implemented here are to require the two TCD paddle and the two S3 TDC <i>threshold</i> 0 readouts to be on scale ($0 < tcd.fTDC[tube][0] < 4095$).	81
5.8	Corrected TCD-to-S3 time-of-flight measurements as a function of flight-time for all 8 TCD paddles in the CREAM II flight. The same on-scale cuts are implemented as in the previous figures for the TDCs.	82
5.9	Raw end-to-end timing for the CREAM II TCD as a function of flight-time, for the entire flight. Only the first TDC threshold values are shown here, as higher thresholds are consistent with the distributions shown here.	85
5.10	Raw end-to-end timing for Paddle 1 in the CREAM II TCD, for a time-slice from $10 < t < 10.1$ days. The black distribution represents signals in any (but only one) crossed paddle. The colored distributions are for different crossed paddles (red for Paddle 4, blue for Paddle 5, green for Paddle 6 and yellow for Paddle 7).	86
5.11	Corrected end-to-end timing for the CREAM II TCD (stump analysis code variable <code>tcq.fETE[paddle][threshold]</code>) as a function of flight-time, for the entire flight. Here only entries for <i>threshold</i> 0 are shown, but higher threshold behavior was consistent with the trend shown here.	87
5.12	Corrected end-to-end timing for Paddle 1 for the CREAM II TCD (<code>tcq.fETE[1][0]</code>), for the entire flight.	88
5.13	Effect of the end-to-end TCD paddle timing corrections for one tile (defined here by requiring that both Paddle 1 and 6 have all four tubes cross <i>threshold</i> 0 and no other paddles with hits). This is representative of other paddles and thresholds.	88

5.14	End-to-end timing distribution for Paddle 5 (bottom), showing the smaller bimodal distributions to the right. The equivalent distribution for Paddle 4 (top) is shown for reference. The uncorrected plots shown are for a 0.1 day slice of the flight, so that the ~ 1 day variations did not wash out the distributions. The corrected plots are for the entire flight period.	89
5.15	Uncorrected end-to-end TCD time difference (in units of TDC channels), shown as a function of flight-time (in days), for the 5 CREAM-I paddles selected.	92
5.16	Time-corrected end-to-end TCD time difference (in units of TDC channels), shown as a function of flight-time (in days).	93
5.17	Time-corrected end-to-end TCD time differences for CREAM I paddles as a function of TRD-derived position.	95
5.18	Time-corrected end-to-end TCD measured position for CREAM I paddles compared to the TRD-derived position. The solid curves are Gaussian fits to the distributions.	96
6.1	SCD charge measurement (top and bottom layers averaged) for calibration-events requiring only TCD Paddle 1 hit in the X-direction and any (but only one) Y-direction paddle. The PLC correction is determined from TCD and SCD hit-locations. Peaks for H, He, Be, B, C and O are clear.	101
6.2	Hydrogen (top) and helium (bottom) calibration-events (selected by the SCD) for ADC 0, Tube 0, TCD paddle 1 (presented as a representative example). Each histogram is a 15 cm slice along the length of the paddle. For the hydrogen, Landau fits were done to find the most probable value, while Gaussian fits were done for helium. Gaussian fits were done for all higher species in ADC 1 as well (not shown).	103
6.3	SCD-selected hydrogen (top) and helium (bottom) calibration-events in TCD Paddle 1, for ADC 0 in both PMTs. The ADC signal here is that given by Equation 6.3, so path-length and pedestal corrections have already been included. Overlaid on the 2D histograms are the peak-locations found from fitting to the histograms shown in Figure 6.2 (the markers) and the 3 rd -order polynomial fits performed on those points.	104
6.4	ADC 1 calibration-events for both tubes in Paddle 1 (SCD-selected species). From top to bottom are helium, beryllium, boron, carbon and oxygen, respectively. The same ADC corrections and fit overlays as done in Figure 6.3 are present.	105
6.5	Example fits for extrapolation for ADC 1, tube 0, Paddle 1, for representative 15cm slices down the paddle-length. The points here are the calculated values from the position-fit functions, the fits performed are reciprocals of 3rd order polynomials.	106
6.6	Tube 0, Paddle 1, ADC 0 as a function of ADC 1. These ADCs are in units of channels and have no corrections applied. For reference, helium is typically located around 2500 channels and above in ADC0, while CNO are typically of order 2700 channels in ADC 1. The double-valued behavior is clear here.	107

6.7	(a)TCD charge measure for Paddle 1, including both PMTs, and a charge-agreement requirement for both tubes to agree within one charge unit. (b)Average of the TCD (from (a)) charge measure and the SCD charge measure, requiring agreement between the two detectors of within one charge unit.	108
6.8	Threshold 0-1 time difference (Tube 0, Paddle 1) measuring the leading-edge timing for CREAM II flight data. Events selected as hydrogen by the charge-calibrated ADCs are colored blue, while green are helium. The black distribution is the sum of the two, and shows no separation between the two species. The X-axis here is in TDC channels, which are 50 ps/channel in width, and contains an arbitrary offset.	110
6.9	Threshold 3-2 time difference measuring the leading-edge timing for CREAM II flight data (again for the same representative paddle and tube as used in Figure 6.8). Events selected as hydrogen and helium by the charge-calibrated ADCs are colored blue, while red are BCNO. The black distribution is again the sum of the two. The X-axis has the same units as in Figure 6.8. and the same cuts are applied.	111
7.1	GEANT4 model of a CREAM TCD scintillation paddle. Note that some parts are missing from this picture due to a known rendering issue with GEANT4, however all components are actually present in the code for physics interactions.	113
7.2	Average of 1024 single PE size events from an XP2020 photomultiplier tube. The voltage units here are arbitrary, and the polarity has been switched to make the pulse positive going.	115
7.3	The average PMT response for muons - simulated and measured.	116
7.4	Position measurement accuracy from the optical GEANT4 model of a TCD paddle.	118
7.5	Simulated TCD ADC (peak detector) response for a PMT at the +X end of the paddle. The simulated test beam consists of 10 GeV protons incident isotropically across the surface of the paddle, with all values normalized to the center of the paddle. Also shown is the response of a typical CREAM I paddle displaying qualitatively similar behavior (there was variation from paddle to paddle due to scintillator thickness and electronics response [13]).	119
7.6	ADC-based charge measurement for simulated 10 GeV hydrogen, helium, beryllium, and carbon.	120
7.7	Comparison of TDC threshold 1-0 time difference as a charge measurement technique. Simulated times with no electronics resolution convolved in are shown in (a) and (c), and in (b) and (d) the equivalent distributions are shown, broadened by additional electronics resolution folded in. These plots include 1000 simulated 10 GeV protons and 2000 simulated 10 GeV helium nuclei.	122

7.8	TDC Threshold 1-0 (Tube 0) time difference as a function of the ADC-based charge measurement for simulated 10 GeV hydrogen, helium, beryllium, and carbon (average of both tubes). The times shown on the Y-axis are negative here because TDC 0 will have a larger measured signal than TDC 1, since they both measure elapsed time since their respective thresholds have been crossed. This ordering of the subtraction was chosen so higher-charged species would be more positive in TDC timing difference.	123
7.9	Comparison of TDC threshold 1-0 time difference as a function of PLC. These plots include 1000 simulated 10 GeV protons and 2000 simulated 10 GeV helium nuclei. The color scale here is bin-counts in the 2-D histogram, and no color-coding of the individual species is present. . . .	123
7.10	Comparison of TDC threshold 1-0 time difference for charge measurement, with and without electronics resolution effects folded in. A position restriction of $x = \pm 20$ cm and $PLC < 1.5$ has been applied. These plots include 1000 simulated 10 GeV protons and 2000 simulated 10 GeV helium nuclei. In each case the top black line shows the total population.	124
7.11	Comparison of photon arrival numbers for H and He with both reflective and non-reflective paddle wrappings. These plots include 1000 simulated 10 GeV protons and 2000 simulated 10 GeV helium nuclei. Fit-parameters from the Landau-distribution fits shown are summarized in Table 7.1.	125
7.12	Comparison of ADC response (one tube) for H and He with both reflective and non-reflective paddle wrappings. These plots include 1000 simulated 10 GeV protons and 2000 simulated 10 GeV helium nuclei. The distributions have been path-length and square-root corrected consistent with Equation 6.3, but no attenuation corrections have been applied. Results of the fits are summarized in Table 7.2.	126
7.13	ADC-based charge measurement for simulated 10 GeV H and He with a non-reflective paddle wrapping.	127
7.14	Position measurement accuracy from GEANT4 model with non-reflective paddle wrapping.	129
8.1	The total energy deposit in the CREAM II calorimeter for all events with calorimeter signals present. The blue distribution represents events for which the tracking described in Section 8.2 was successful.	132
8.2	Estimated incident energy for all CREAM II events as measured by the calorimeter (and requiring successful tracking).	133
8.3	The number of hit TCD paddles per event (TDC threshold 0 crossed for the PMTs at both ends) for the CREAM II flight for events with Calorimeter data present. It is clear that there is a large amount of albedo present for any events having a CAL signal. (a) is for the X-going paddles while (b) is for the Y-going.	135

8.4	Time-of-Flight measures for progressively higher energy bins (energy from Calorimeter) as measured from the TCD paddles to the S3 detector. The time is shown in TDC channels here with an arbitrary (but consistent between paddles) offset. The rightmost distributions are for downward-going events, while the leftmost are for albedo.	137
8.5	(a)The predicted X hit locations in the CREAM II SCD (top layer only) from the TCD timing and CAL CM-based tracking shown on the Y axis as a function of the stored location of the maximum hit pixel in the SCD as recorded independently of tracking. There are a large number of hits which do agree with the tracking, but also significant outliers due to false hits caused by albedo particles (primarily for hydrogen and helium primary events). (b)The same plot but with the maximum-SCD pixel selected only from within 5 cm of the tracking. The Y direction and the bottom SCD layer display similar behavior as the X layer shown here. .	138
8.6	(a)The charge measurement for the SCD using the maximum-pixel selection method for the entire SCD (no tracking used for hit-location selection). The charge is reconstructed as outlined in Section 6.3, and the tracking available is used for path-length correction ($\sec \theta$) correction. Both layers are averaged together here. (b)The reconstructed SCD charge using the maximum pixel within 5 cm of the tracking. Additionally, the charge measures from both layers are required to agree to within one charge unit. Even with this additional cut, far more hydrogen and helium hits are correctly identified.	139
8.7	TCD measured charge for events having a calorimeter signal (shower present), for the two TCD layers. The long tails from hydrogen and helium are clearly visible, arising both from energy-deposit fluctuations and from albedo contamination.	141
8.8	TCD-measured charge for events having a calorimeter signal, using the minimum measured charge in the two layers. This procedure reduces the effect of the long tails from hydrogen and helium. A total of 14423 events are measured for the CREAM II flight in the TCD (after cuts).	142
8.9	TCD-measured charge as a function of the SCD-assigned charge, for events with both of these present (and with a calorimeter signal). Very few (perhaps no) charge-changing events appear to be present.	145
8.10	TCD-measured charge for events having a calorimeter signal. Each histogram is for one energy bin in Table 8.1 and starts with 1 TeV. Fits were done for H, He, C and O, as described in the text. Several C and O fits fail for low-statistics histograms, and species populations are instead estimated by counting histogram contents as described in this section. .	147

8.11	(a)The peak-positions for the species fits performed on the first 7 energy-bin histograms shown in Figure 8.10. The hydrogen peak value is the peak of a convolved Gaussian and Landau distribution while the helium value is derived from another Gaussian which was convolved with the hydrogen function to deal with the mixing between the populations. (b)The peak-positions for carbon and oxygen also from Figure 8.10. The Gaussian fits were unsuccessful for bins 5 and 6 for carbon and 0, 1 and 6 for oxygen.	149
8.12	The distribution-widths for the individual species fits shown in Figure 8.10. The hydrogen width is the quadrature-sum of the widths of the convolved Gaussian and Landau distributions used to fit this species. The other species widths are all the Gaussian σ parameters from the fits.	150
8.13	The spectra for hydrogen, helium, carbon and oxygen with charges identified by the TCD and energies reported by the calorimeter. The individual data points are summarized in Tables 8.3, 8.4, 8.5 and 8.6. The measured spectral indices are reported in Table 8.9	152
8.14	The elemental abundances of cosmic-ray hydrogen (top) and helium (bottom) nuclei as found in the analysis presented in this thesis. Results from several recent experiments are also presented for comparison (RUNJOB [14], JACEE [15], ATIC II [16] and CREAM I preliminary results presented in [6]). The CREAM II results from this thesis have also been scaled by an arbitrary factor of $10^{-8.6}$ to make the arbitrary units compatible with previous measurements of the absolute flux for hydrogen. All the helium fluxes have further been scaled by additional factor of 0.01 to better separate the species.	154
8.15	The same results as presented in Figure 8.14, except that the fluxes are scaled by $E^{2.5}$ to flatten the spectra and make visual comparison of the spectral indices easier. Also, the two lowest-energy data points have been removed since their fluxes are clearly suppressed due to instrumental inefficiencies at the lower end of the energy scale. The helium fluxes have not been scaled by the additional factor of 0.01 that was applied in Figure 8.14.	155
8.16	Carbon and Oxygen spectra as measured by the CREAM II experiment. The results found in this thesis have been scaled in flux by an arbitrary factor of $10^{-7.2}$ to make them consistent with the absolute-flux corrected points from the analysis by P. Maestro [1]. Energy-dependent efficiencies in the calorimeter response are probably largely responsible for the suppressed flux at lower energy. Also shown are results from the space-based HEAO-3-C2 [17] experiment and the TRACER [18] and ATIC II [16] balloon-borne experiments.	157
A.1	Results of the Bethe-Bloch equation for several types of typical absorber materials. Scales showing momentum for several different types of incident-particles are shown as well. This figure is from the Particle Data Group [3]	163

Acknowledgments

- I would like to thank my wife Sunita for her understanding, patience and support throughout the process of preparing this thesis: without your help, I could not have finished this.
- To my adviser Stephane Coutu I also extend warm thanks for his steadfast support, mentoring and patience of both my progress and my questions, large and small. He also deserves special thanks for his extensive help editing and proof-reading this thesis with great patience and diligence.
- To my thesis committee members: Paul Sommers, Richard Robinett and John Nousek. Thank you for your careful consideration of my work presented here and your insightful questions and comments.
- I would like to thank James Beatty for introducing me to this fascinating field of research and for offering me support as a graduate student by being my first adviser.
- Much of what I know about the construction and simulation of particle detectors I have learned from Scott Nutter and his collaboration and mentoring over many years has been greatly appreciated.
- Special thanks to Nick Conklin, whose close collaboration and friendship (and excellent computer programing) throughout all of my research was essential to the completion of my thesis work.
- I would like to thank professors Robert Coakley, Charles Armentrout, Jerry LaSala and Paul Nakroshis of the University of Southern Maine who provided me with a fabulous undergraduate education and understanding of fundamental experimental principles.
- My fellow graduate student and friend Nathan Urban provided me with amazing insights into physics throughout our first few years of graduate school and helped me with the concepts of many of my graduate courses. Thank you Nathan.
- To Ted Rodgers, thank you for your friendship and discussions of physics.
- Finally I would like to thank my parents Robert and Judith Mognet for raising me and for allowing me time to indulge my interests, whatever they were.

Chapter 1

Cosmic Rays

1.1 Cosmic Rays

A multitude of different particle types arrive at Earth from space: photons, neutrinos, electrons, anti-particles and fully-ionized atomic nuclei. The sources of these particles are varied. Photon emission can be from various sources including: thermal sources such as star light, synchrotron radiation from charged particles in magnetic fields, bremsstrahlung radiation from other particle interactions with matter and fields, and γ -ray production from the decay of particles. Once emitted, the photons are susceptible to alteration by absorption, gravitational lensing, polarization by passage through magnetic fields and processes such as inverse Compton scattering. Other neutral species, namely neutrinos can propagate with very little attenuation indeed, because of their very small interaction cross-sections.

Charged-particle species generally have a much different propagation history. Their trajectories are altered by propagation through the magnetic fields in space. Additionally, processes where the propagating particle interacts with a particle in the interstellar or intergalactic medium can also alter their energy and their identity. The fully-ionized atomic nuclei are the subject of this thesis. Generally, fully-ionized atomic nuclei are referred to as Cosmic Rays and that is the convention I will use here.

Since cosmic rays, photons, and the interstellar/intergalactic medium are all coupled electromagnetically and/or through nuclear forces, it is useful to see the approximate relative densities of these species and fields in space. This is shown in Table 1.1. Of particular note is the similar energy densities of the Galactic magnetic field and the cosmic rays. This is likely some sort of mutually regulating relationship (see pp. 321-322 of Longair [19]).

The study of cosmic rays involves deconvolution of two different classes of processes that contribute to the observed spectrum: the nature of the acceleration process(es) and the alteration of the source spectrum due to propagation. Before we begin discussing the acceleration and propagation of cosmic rays, we should review briefly what is known about the cosmic rays arriving at earth. After this, the development of some theoretical models for possible source acceleration and propagation will be useful. Once this theoretical framework is introduced, some quantities of interest accessible experimentally will be apparent, and a more detailed survey of the current best data on cosmic rays will be presented.

<i>Particles Arriving at Earth and Fields in Space</i>		
<i>Particle Type</i>	<i>Source(s)</i>	<i>Energy Density (eV/m³)</i>
Solar Wind (protons)	Sun	$\sim 2.5 \times 10^9$ [20] ^a
Solar Wind (magnetic field)	Sun	$\sim 6.2 \times 10^7$ [20] ^a
Star Light	Galactic	$\sim 6 \times 10^5$ [19]
Cosmic Rays	Galactic and Beyond	$\sim 10^6$ [19]
Interstellar Medium (local)	Galactic	$(\sim 10^5 - 10^6 \text{ protons/m}^3)$ [19] ^b
Galactic Magnetic Field	Galactic (local)	$\sim 2 \times 10^5 (\sim 3 \mu\text{G})$ [19]
Cosmic Microwave Background	Early Universe	$\sim 2.6 \times 10^5$ [19]

Table 1.1 Approximate energy densities of particles arriving at Earth and various extensive fields in space relevant for cosmic-ray propagation.

^aAverage value for a quiet sun.

^bOutside of molecular and diffuse clouds.

1.1.1 The All-Particle Spectrum

The all-particle spectrum of observed cosmic rays at earth is a remarkably smooth power-law of the form $dN/dE \propto E^{-\gamma}$ with γ between ~ 2.6 and ~ 3 from an energy of 10^9 eV $\lesssim E \lesssim 10^{20}$ eV. Several breaks in the spectral index are observed, however. The first occurs when the all-particle spectral index changes from ~ 2.6 to ~ 3 somewhere between 10^{15} eV $\leq E \leq 10^{16}$ eV and is known as the ‘knee’ (Figure 1.1). A possible second ‘knee’ is observed around 10^{17} eV (Figure 1.2). Finally a feature known as the ‘ankle’ is present above 10^{18} eV where the spectral index becomes less steep briefly. Beyond this is possibly a dramatic steepening of the spectrum corresponding to the Greisen-Zatsepin-Kuz’min [21] [22] (GZK) cutoff of extragalactic cosmic rays.

The acceleration of cosmic rays to such high energy is an outstanding question (actually a set of questions) in physics. Acceleration of particles up to the ‘knee’ region is plausibly explained by Fermi shock acceleration in supernova remnants (SNRs) in the Galaxy as shown in Section 1.3.1. The model of shock acceleration presented reproduces a source spectrum very consistent with that expected from observation (if propagation effects are included). The model also suggests an energy limitation (Section 1.3.3) of the SNR accelerators roughly consistent with the observed energy scale of the ‘knee’. The origin of the ‘knee’ feature has been a long-standing question of cosmic-ray physics, and it is exciting to consider the possibility that at least part of the origin is due to a limitation in SNR acceleration.

Beyond the ‘knee’ region some of the cosmic-ray population is believed to still be primarily of Galactic origin. Eventually a transition to extra-galactic sources is probably occurring. The origin of the possible second ‘knee’ feature mentioned above may represent such a transition [3]. The ‘ankle’ feature could represent another such transition to a different type of source, or could represent a pile-up of cosmic rays formerly of higher energy which have lost energy because of the GZK limit.

The GZK limit arises because in the frame of a 5×10^{19} eV particle, the cosmic microwave background (CMB) photons are blue-shifted to sufficient energy for photo-pion

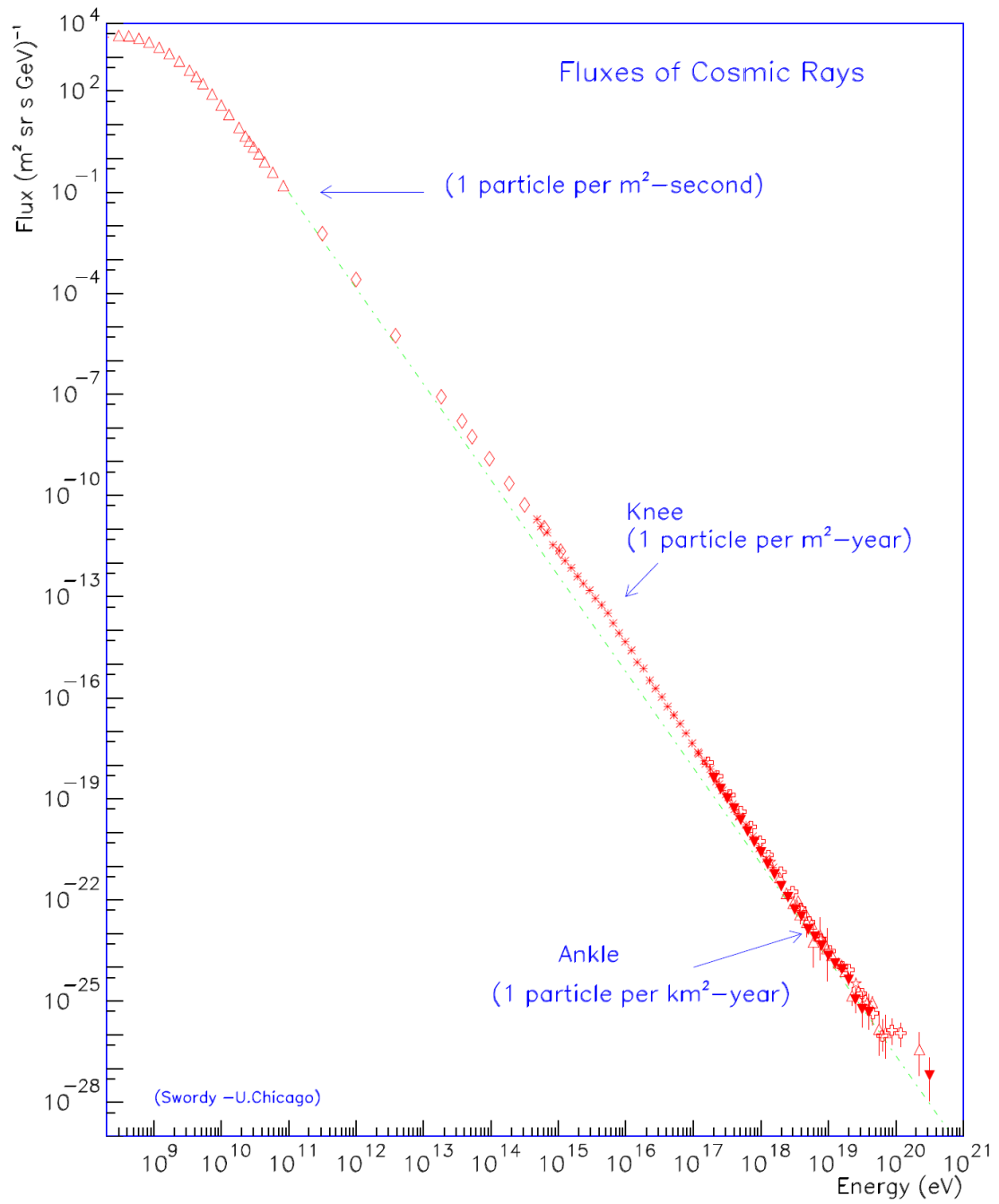


Fig. 1.1 The all-particle spectrum of cosmic rays[2].

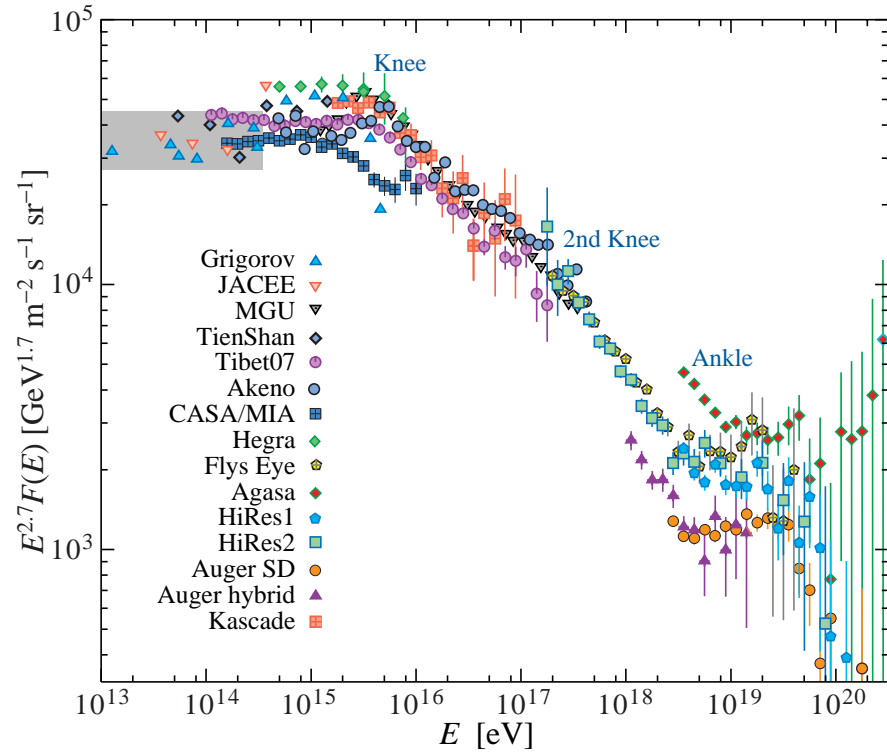


Fig. 1.2 The all-particle spectrum of cosmic rays showing the possible second ‘knee’ as well as the ‘ankle’ and possible GZK cutoff feature above 10^{19} eV (From the Particle Data Group [3]).

production to take place via a Δ^+ resonance [23]. This introduces an energy-loss mechanism to the propagation of ultra-high-energy cosmic rays. The maximum propagation length for a cosmic-ray proton in this energy range is ~ 50 Mpc. This suggests that the sources for any cosmic rays above the GZK cutoff would either need to be reasonably local, or some process such as the breaking of Lorentz invariance is allowing their passage through cosmological distances. The presence of particles beyond the GZK cutoff is therefore another question of interest. Some early analysis from AUGER (Section 1.5.3) suggested nearby active-galactic nuclei as possible point sources, but the issue is not yet settled.

1.1.2 Cosmic-Ray Elemental Composition

Cosmic rays contain fully-ionized elemental nuclear species from protons to iron and beyond. Cosmic rays appear to contain a mixture of species consisting of both primary nuclei which have propagated unaltered from their sources, as well as secondary nuclei which are spallation products of heavier species interacting with the interstellar medium (ISM).

Compared to solar system abundances (which are assumed to be consistent with the abundances of the material the cosmic rays are drawn from), two differences are apparent. One is an underabundance of species having first ionization energies higher than 10 eV and thus being somewhat harder to introduce into the cosmic-ray acceleration process [19].

The second difference is the large enhancement of some species over solar system abundances. Specifically, species such as Li, Be, B, F and some of the sub-iron elements (Figure 1.3) are present in a greatly increased proportion in the cosmic-ray flux. These species are believed to be the products of spallation of heavier species in the ISM. This feature, that the cosmic rays are a mixture of primary and secondary particles, provides some very important information about the typical path length of material which they have traversed since acceleration. If the cosmic rays were very old, the abundances of primary species such as C, O, Ne, Mg, Si and Fe would be suppressed far below that observed. If they were very young, the enhancement in the secondary species would be much less than that observed.

1.2 Propagation of Cosmic Rays

As discussed above, the spectrum of cosmic rays is essentially shaped by a combination of two phenomena: the source spectrum and abundances of the cosmic rays on the one hand, and the propagation of the cosmic rays from the sources to earth on the other. The mathematical expression for the spectrum can, in principle, be split into components arising from the source spectrum and the propagation, $dN/dE \propto E^{-\gamma}$ with $\gamma = \alpha + \delta$. Here α is the component of the spectral index arising from the sources, and δ is the component from propagation. The probable origin of δ will be discussed in this section, while α will be discussed in Section 1.3 below, discussing the acceleration of cosmic rays.

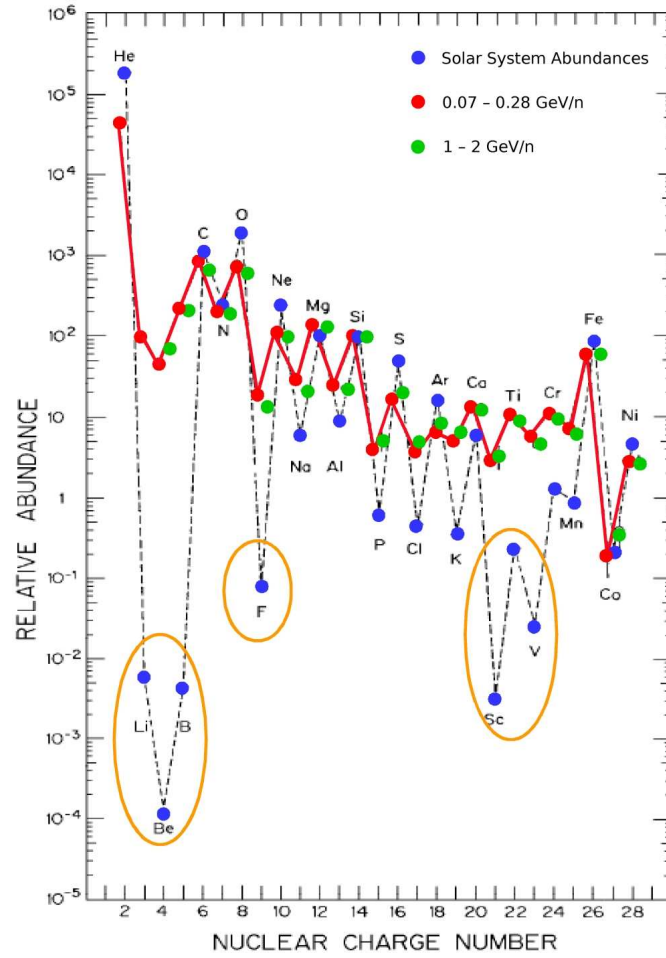


Fig. 1.3 Relative abundances of cosmic rays compared to solar system abundances. Prominent secondary species are circled. Fluxes are scaled to arbitrary units with Silicon set to 100 (modified from [4]).

Also present at lower energies are effects local to the solar system and at even smaller scale the local magnetic field of the earth. These effects are not relevant to the energy range explored in this thesis, so their discussion is limited.

1.2.1 The Diffusion-Loss Equation for Cosmic Rays

The general propagation of cosmic rays in the Galaxy is given by the diffusion-loss equation. What follows is a physical motivation for the diffusion-loss equation relevant for cosmic rays which is very similar to that of Longair [19]. Let $N(E, \mathbf{r}, t)$ be the particle density (with units $\frac{\text{particles}}{(\text{unit energy})(\text{unit volume})}$) which is the number of particles of energy E , at position \mathbf{r} in the Galaxy, and at time t . If we limit ourselves to one spatial dimension, Figure 1.4 shows graphically the box containing N particles to be $N(E, x, t)dEdx$.

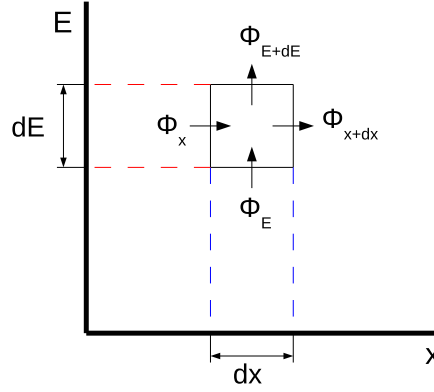


Fig. 1.4 Fluxes ϕ of particles through the surfaces of a box in energy-space parameter space. The fluxes ϕ_x and ϕ_{x+dx} are the number of particles flowing through the energy surfaces located at x and $x+dx$, respectively. The fluxes ϕ_E and ϕ_{E+dE} are analogous. The total number of enclosed particles is $N(E, x, t)dEdx$.

If we allow for the presence of sources of particles Q in our volume, the time rate of change for particle density is:

$$\begin{aligned} \frac{d}{dt}N(E, x, t)dEdx &= (\phi_x - \phi_{x+dx})dE + (\phi_E - \phi_{E+dE})dx + QdEdx \\ &= -d\phi_x dE - d\phi_E dx + QdEdx . \end{aligned}$$

So,

$$\frac{dN}{dt} = -\frac{\partial \phi_x}{\partial x} - \frac{\partial \phi_E}{\partial E} + Q . \quad (1.1)$$

Fick's first law [24] states that matter will flow down a concentration gradient from high to low:

$$\phi_x = -D \frac{\partial N}{\partial x}$$

with D called the diffusion coefficient. For the net flux through the energy surfaces, if the loss rate of particles of energy E is $b(E)$ we have

$$\phi_E = N(E) \frac{\partial E}{\partial t} = -b(E)N(E)$$

thus, the one-dimensional diffusion loss equation becomes:

$$\frac{dN}{dt} = D \frac{\partial^2 N}{\partial x^2} + \frac{\partial}{\partial E} [b(E)N(E)] + Q.$$

Generalizing to 3 dimensions, we get:

$$\frac{dN}{dt} = D \nabla^2 N + \frac{\partial}{\partial E} [b(E)N(E)] + Q. \quad (1.2)$$

If the diffusion coefficient is not constant throughout space, the derivation must be modified slightly and the first term becomes $\nabla \cdot (D \nabla N)$. So far in equation 1.2 the processes present are diffusion, energy loss/gain and source terms. If there is a flow of particles of velocity \mathbf{v} , the process of convection must be included. In one dimension, the time rate of change of particle density from convection is $\frac{dN}{dt} = -v \frac{dN}{dx}$, or generalized to three dimensions:

$$\left(\frac{dN}{dt} \right)_{convection} = -\nabla \cdot \mathbf{v} N(E). \quad (1.3)$$

Since in general we are concerned with a collection of different species in the flux of cosmic rays, we will label the density of species i as N_i . While propagating through space, the process of spallation will cause the population of all species j to occasionally be transformed into species i for species $j > i$.

$$\frac{dN_i}{dt} = -\frac{N_i}{\tau_i} + \sum_{j>i} \frac{P_{ij}}{\tau_j} N_j \quad (1.4)$$

where the first term is the rate at which species i is removed due to spallation to lighter species, and the second term is the rate at which it is added from the spallation of heavier species. τ_i and τ_j are spallation lifetimes of the species, and P_{ij} is the probability for the production of species i from species j in an inelastic collision producing spallation.

If the produced nucleus is radioactive, we can include the decay by a term of the same form as the first in Equation 1.4. If a species is the product of a radioactive decay, a term of the same form as the second term in Equation 1.4 can be included.

The generalized diffusion-loss equation in a form useful for cosmic rays (neglecting radioactivity) is thus:

$$\frac{dN_i}{dt} = D\nabla^2 N_i + \frac{\partial}{\partial E}[b(E)N_i(E)] + Q_i - \nabla \cdot \mathbf{v}N(E) - \frac{N_i}{\tau_i} + \sum_{j>i} \frac{P_{ij}}{\tau_j} N_j. \quad (1.5)$$

1.2.2 Using the Diffusion-Loss Equation

In principle the diffusion-loss equation above (with suitable additions for other processes) provides a method of understanding the propagation of cosmic rays in the Galaxy. In practice, however, much of the information required to set proper boundary conditions and correct values for the various free parameters complicates its usage.

One current, very widely used method of constructing realistic models with the diffusion-loss equation is the computer package GALPROP [25]. The package solves the diffusion-loss equation numerically using the best available current information about the Galactic magnetic fields, interstellar gas distributions, experimental constraints on the diffusion coefficient, etc. The user is able to input a source spectrum as desired. Iterative execution is used for calculating all secondary species and isotopes, γ -rays, electrons and positrons, and other emissions.

A widely used, very simple model for Galactic propagation of cosmic rays is the so-called *leaky box model*. The simplest form of the model consists of particles free to propagate in a confined space (the Galaxy), but with reflection off the boundaries and finite probability of escape from the volume (with characteristic time τ_e). We will also include a delta function source term. In this case the diffusion-loss equation becomes [26]:

$$\frac{\partial N}{\partial t} + \frac{N}{\tau_e} - N_0(E)\delta(t) = 0$$

with solution:

$$N(E, t) = N_0(E)e^{-t/\tau_e}. \quad (1.6)$$

The escape time can be related to the mean amount of matter (path length) which the cosmic rays have traversed since leaving their sources, $\lambda_e = \rho\beta c\tau_e$ (here ρ is the density of matter in space the particles traverse and $\beta = v/c$). Conveniently, spallation provides an excellent probe of the amount of matter cosmic rays have passed through during propagation. Longair [19] shows, using the ratio of the abundances of light (Li, Be, B) to medium elements (C, N, O), the typical path length for the medium elements to be $\sim 50 \text{ kg/m}^2$.

Exploration of the evolution of secondary-to-primary abundance ratios as a function of energy also allows for detecting any energy dependence in λ_e . Energy dependence (or more specifically rigidity dependence $R = \frac{pc}{Ze}$ with $p = \gamma mv$ the relativistic momentum and Z the integer charge) is not surprising since for higher energy (rigidity) the ability of magnetic fields in the Galaxy to contain cosmic rays should decrease. Empirically, this can either be treated in terms of the path length with $\lambda_e \propto R^{-\delta}$ [26], or for models using the diffusion coefficient as $D = D_0\beta R^\delta$ [27]. This means δ here is the modification to the overall particle spectrum caused by propagation as discussed in the introduction to this section.

The boron-to-carbon ratio (B/C) is a classic probe used to find δ . Extension of this measurement to higher energy was in fact one of the main goals of the first Cosmic Ray Energetics and Mass (CREAM) flight [28]. Previous measurements such as those of HEAO-3-C2 (Section 1.5.2) have suggested a value of $\delta \simeq 0.6$ and the CREAM measurement is largely consistent with this (Figure 1.5).

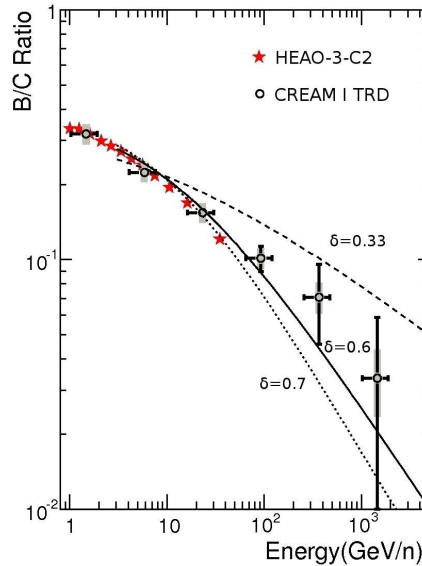


Fig. 1.5 Boron-to-carbon ratio as measured by the CREAM I experiment. The energy here is measured with a Transition Radiation Detector (TRD), with charge measurements by a Timing Charge Detector (TCD) and a Silicon Charge Detector (SCD) which are discussed in more detail in Chapter 2 of this thesis. The gray bars are systematic uncertainty in the measurements, while the solid vertical lines are statistical uncertainties. Horizontal error bars are estimates of the systematic uncertainty of the energy assignments. Also shown are several theoretical predictions for different values of δ .

Since the overall spectral index for the all-particle spectrum is $\gamma \simeq 2.6 - 2.7$ at earth, the value of $\delta \simeq 0.6$ implies a source spectrum of $\alpha \simeq 2.0 - 2.1$. As we shall see in the next section, acceleration from strong shocks very naturally predicts a source spectral index of $\alpha = 2$, lending weight to the idea that this process is the primary source of cosmic rays up to the ‘knee’.

Another probe of the cosmic-ray propagation history, which spallation also provides, is through the production of radioactive isotopes. The β decay of ^{10}Be to ^{10}B is perhaps the best studied example. To do this, the terms dealing with radioactivity discussed in the derivation of the Diffusion-Loss equation above must be included, and the ratio of radioactive to total Be ($[^{10}\text{Be}]/[^7\text{Be} + ^9\text{Be} + ^{10}\text{Be}]$) must be experimentally measured[19]. This yields an escape time $\sim 10^7$ years. When combined with the path

length (matter the cosmic rays have passed through) of $\sim 50 \text{ kg/m}^2$ the mean density of the ISM the cosmic rays have propagated through is found to be $\sim 3 \times 10^5 \text{ protons/m}^3$.

1.2.3 Solar Modulation

The heliosphere acts to exclude lower energy cosmic rays from the solar system. During periods of solar-maximum activity, the flux of sub-GeV cosmic rays can be suppressed by an order of magnitude over solar-minimum periods [26]. At higher energies solar modulation becomes negligible. It is not relevant for energies discussed here.

1.2.4 Geomagnetic Cutoff

The magnetic field of the earth also affects the flux of lower-energy cosmic rays. It introduces a rigidity-dependent cutoff, also dependent on latitude. At the poles the cutoff is less than 1 GeV for protons, and ranges up to $\sim 15 \text{ GeV}$ near the equator. This is of practical consideration for any balloon payload flying in a polar environment such as CREAM, since the flux of low-energy cosmic rays can be much higher (and hence the triggers for events not of interest is much higher).

1.2.5 Solar Activity

During the first flight of CREAM in the 2004-2005 Antarctic flight season, a very intense solar flare event occurred and flooded the near-earth environment with a very high flux of solar cosmic rays. The performance of some instruments was affected due to increased dead-time which was initially interpreted as detector component failures. After several days, the storm subsided and detector trigger rates returned to near normal [7].

1.3 Acceleration of Cosmic Rays

The origin of cosmic rays is arguably the most interesting question to ask about them. If the cosmic-ray population is in an equilibrium state, and has a reasonably homogeneous distribution throughout the Galaxy, the total energy required to maintain the population is $\sim 5 \times 10^{40} \frac{\text{ergs}}{\text{sec}}$ [26]. This suggests supernovae may be a source, since they are the most energetic potential sources known and are distributed throughout the Galaxy. The total power output of supernovae in the Galaxy is of order $\sim 3 \times 10^{42} \frac{\text{ergs}}{\text{sec}}$, so an acceleration efficiency of a few percent could account for the observed Galactic cosmic-ray flux. As seen below, strong shocks from supernova remnants have the other very attractive feature of having a predicted spectral index very close to that needed to fit the observed index (if propagation effects are included).

1.3.1 First Order Fermi Shock Acceleration

Strong astrophysical shocks are currently one of the most promising theoretical mechanisms for the acceleration of charged cosmic rays to high energies. As we shall see below, they are both physically plausible situations and can efficiently (and in a

reasonable amount of time) raise cosmic rays to high energies. The following derivation of first order Fermi shock acceleration follows closely from Longair [19].

Consider a strong shock propagating out into a pre-existing undisturbed medium. The shock is propagating faster than the speed of sound in the undisturbed medium, but is traveling at non-relativistic velocity. Also, the shock front is assumed to be flat, on the order of the dimension of the typical propagation region of relativistic particles being accelerated.

The basic mechanism for the particles to be accelerated consists of numerous repeated scatterings across the shock front, with a certain probability of escape from the accelerating region with each crossing. The actual shock is largely invisible to the relativistic particles passing through; however, the media upstream and downstream of the shock can scatter the particles. For the downstream medium (behind the expanding shock), turbulent flow would provide a ready source for non-uniformity in material density and possibly magnetic fields for changing the directions of the relativistic particles in a random way. For the upstream situation, the medium is unperturbed from the shock since the shock is supersonic in that medium. However, discontinuities may already be present in the medium, or the relativistic particles themselves may disturb the medium ahead of the shock front.

Regardless of the exact mechanism, we expect the density of the trapped accelerating particles to fall off exponentially with the distance from the shock. Additionally, since the expected scattering distance in each medium is different, we expect different rates of decay in the particle density for given distances from the shock.

Let P be the probability of the particle remaining in the accelerating region after one collision and $E = \beta E_0$ be the energy of the particle after the collision. With k collisions, there are then $N = N_0 P^k$ particles still in the region with energy $E = E_0 \beta^k$. Eliminating k , we get,

$$\frac{\ln \frac{N}{N_0}}{\ln P} = \frac{\ln \frac{E}{E_0}}{\ln \beta}$$

thus,

$$\frac{N}{N_0} = \left(\frac{E}{E_0} \right)^{\frac{\ln P}{\ln \beta}}. \quad (1.7)$$

However, in this case, N is the number of particles with energy greater than or equal to energy E :

$$N = N(\geq E) = \int_E^\infty N(E) dE$$

so,

$$N(E) = \frac{d}{dE}(N(\geq E)) = \frac{\ln P}{\ln \beta} \left(\frac{E}{E_0} \right)^{\frac{\ln P}{\ln \beta} - 1} \quad (1.8)$$

thus,

$$N(E) dE = \text{const} \times \left(\frac{E}{E_0} \right)^{\frac{\ln P}{\ln \beta} - 1} dE. \quad (1.9)$$

As we can see, a power law is obtained. It remains now to determine the power, by finding an expression for $\frac{\ln P}{\ln \beta}$.

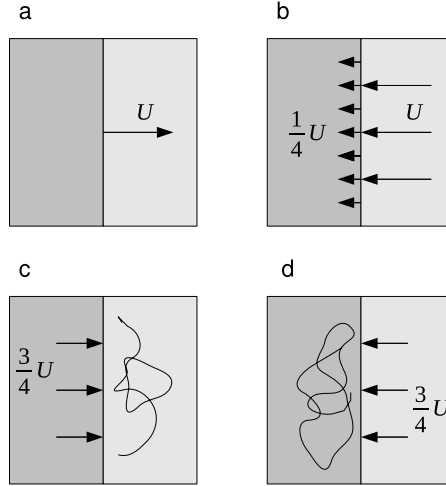


Fig. 1.6 Views of a strong shock in various reference frames. (a) Seen from a frame at rest with respect to the surrounding undisturbed interstellar medium, the shock front is advancing with velocity U . (b) In the frame with the shock stationary, the ISM appears to be approaching the shock at velocity $v_1 = |U|$, and the downstream gas behind the shock appears to be receding at velocity $v_2 = \frac{1}{4}U$. (c) Again in the frame with stationary ISM, the gas behind the shock appears to be approaching at velocity $\frac{3}{4}U$ and (d) in the frame co-moving with the shocked gas, the ISM also appears to be approaching at velocity $\frac{3}{4}U$.

The next step is to more carefully consider the properties and assumptions of the shock and the media on either side of it. Let U be the supersonic velocity of the shock in the undisturbed interstellar medium (Figure 1.6a). Then in the moving frame where the shock is stationary, we have the interstellar gas approaching the shock at velocity $v_1 = |U|$ and receding from the shock at some velocity v_2 (Figure 1.6b).

Since mass flow is conserved across the shock we get the continuity equation, $\rho_1 v_1 = \rho_2 v_2$. For a very strong shock (Mach number $\gg 1$), the density ratio is $\rho_2/\rho_1 = (\gamma + 1)/(\gamma - 1)$ [20]. For a monatomic gas (or fully-ionized plasma in this case), the ratio of specific heats is $\gamma = \frac{5}{3}$. Thus, the ratio of velocities for the two media is $v_1/v_2 = 4$, which gives $v_2 = \frac{1}{4}U$ for the velocity of the upstream flow.

In the rest frame of the upstream gas (the ISM), the downstream gas has a velocity pointing toward the shock and has velocity $V = \frac{3}{4}U$. Likewise, in the frame of the downstream gas behind the shock, the ISM *also* appears to be approaching the shock at velocity $\frac{3}{4}U$ (Figure 1.6c and d)! It is clear that if we picture the particle entering each medium, then scattering off some scattering centers embedded in the medium and

eventually transferring back to the other medium, then with each crossing, the particle will gain some energy.

Consider a particle crossing from the unshocked region into the shocked region (or vice-versa) behind the shock. The energy transformation for the particle can be found by application of the correct Lorentz transformations [29]:

$$E' = \gamma_V(E + p_x V) \quad (1.10)$$

with p_x the particle momentum in the direction perpendicular to the shock front and V is defined above. Since the shock and gas flow velocity are all non-relativistic, $\gamma_V \simeq 1$ and the energy transformation reduces to,

$$E' = E + p_x V$$

thus the apparent energy gain from the transformation is,

$$\Delta E = p_x V = pV \cos \theta \quad (1.11)$$

and the proportional change in energy is

$$\frac{\Delta E}{E} = \frac{pV \cos \theta}{pc} = \frac{V}{c} \cos \theta . \quad (1.12)$$

For an isotropic distribution of relativistic particles, the rate of particles approaching the shock is $rate \propto c \cos \theta$ since the relativistic particles have velocity $|\vec{v}| \approx c$. Also, the number of particles approaching the shock between θ and $d\theta$ is proportional to the solid angle element $d\Omega = \sin \theta d\phi d\theta$ with θ the zenith angle and ϕ the azimuthal. Thus, the number of incident particles per unit time is $N \propto \sin \theta d\theta$ between θ and $d\theta$. Therefore the total probability of a particle crossing the shock is $p(\theta) \propto \sin \theta \cos \theta d\theta$, normalizing we get,

$$p(\theta) = 2 \sin \theta \cos \theta d\theta . \quad (1.13)$$

The average fractional energy gain per crossing is then found by solving the following integral (using integration by parts):

$$\left\langle \frac{\Delta E}{E} \right\rangle = \int_0^{\frac{\pi}{2}} p(\theta) \frac{\Delta E}{E} = \frac{2V}{c} \int_0^{\frac{\pi}{2}} \cos^2 \theta \sin \theta d\theta = \frac{2}{3} \frac{V}{c} . \quad (1.14)$$

For each shock crossing and subsequent scattering, the particle receives an average fractional energy boost of $\frac{2}{3} \frac{V}{c}$, thus, for each round-trip, the particle gains $\frac{4}{3} \frac{V}{c}$. Therefore we now find:

$$\beta = \frac{E}{E_0} = \frac{E_0 + \Delta E}{E_0} = 1 + \frac{4V}{3c} = 1 + \frac{U}{c} . \quad (1.15)$$

Now it remains to find an expression for the escape probability P of the particle per each round trip (one collision) across the shock. Let us define the number density of the relativistic particles to be $N = \frac{\#ofparticles}{unitvolume}$. From kinetic theory (See Atkins,

p. 725 [24]) the number of particles crossing per unit area per unit time is given by $Z_W = \frac{1}{4}Nc$ since the particles are relativistic and $|\vec{v}| \approx c$. In the downstream region behind the shock, the flow of material is away from the shock with velocity $v_2 = \frac{1}{4}U$ (Fig. 1.6b). However, after the collision, the particles are isotropic in this flow. Some will cross back over the shock, but some fraction will escape the region of the shock. The number leaving the shock region per unit area per unit time will be the number density times the flow velocity of the material, $L = \frac{1}{4}Nv_2 = \frac{1}{4}NU$. The fraction lost per collision (round trip) is then,

$$\frac{L}{Z_W} = \frac{\frac{\#lost}{area \times time}}{\frac{\#crossing}{area \times time}} = \frac{\#lost}{\#crossing} = \frac{\frac{1}{4}NU}{\frac{1}{4}Nc} = \frac{U}{c}. \quad (1.16)$$

Since $U \ll c$, the fraction of lost particles per collision is small. The probability of escape per crossing is then,

$$P = 1 - \frac{U}{c}. \quad (1.17)$$

We are now in a position to calculate the exponent in the power law in Equation 1.9. Taking the series expansions to first order since $\frac{U}{c} \ll 1$ we have,

$$\frac{\ln P}{\ln \beta} = \frac{\ln 1 - \frac{U}{c}}{\ln 1 + \frac{U}{c}} = \frac{-\frac{U}{c}}{\frac{U}{c}} = -1 \quad (1.18)$$

thus predicting a power law of the following form,

$$N(E)dE = constant \times E^{-2}dE. \quad (1.19)$$

Our simple model has predicted a power law with exponent -2 , all from very simple physical assumptions about the accelerating region and the particles. Of course the observed power law at Earth is closer to -2.6 , but this is consistent with the rigidity-dependent propagation effects discussed earlier.

Another great advantage of this picture over the original formulation of Fermi acceleration is that the fractional energy change per crossing is of first order in $\frac{V}{c}$ (Equation 1.14), hence the name First Order Fermi acceleration. The original formulation of Fermi acceleration considered particles trapped in the Galaxy repeatedly scattering off moving gas clouds in the Galaxy [19]. However, since some of the scatterings resulted in loss of energy, the energy gain turned out to be of second order in $\frac{V}{c}$. All crossings in the first order process result in energy gain, and the acceleration takes place in a much more confined space.

Another interesting feature of the process as outlined here is that the particles escape the acceleration region (the shock) by being convected *into* the SNR. While the shock is still strong, the particles are effectively trapped in the SNR, and acceleration can recommence if the particle again crosses the shock. Once the shock becomes weak (~ 1000 years), the particles are able to propagate into the Galaxy.

1.3.2 Reacceleration

The original model of shock acceleration presented by Fermi was a very different physical process [19]. The original picture had cosmic rays reflecting off of randomly moving magnetic mirrors in the Galaxy. Alternately we can describe the cosmic rays interacting with randomly moving magnetohydrodynamical waves in space. This process is referred to as Second Order Fermi acceleration because the energy gain per interaction is $\propto (V/c)^2$ while from First Order Fermi shock acceleration the average energy gain per interaction is $\propto V/c$ (Equation 1.14).

This process is not sufficient to accelerate particles to energies beyond ~ 1 GeV/n however[25]. It suffers from two major limitations. The first is the very long time between interactions. The second is the 2^{nd} order nature of the energy gain. This 2^{nd} order behavior is a direct result of the fact that not all reflections produce an energy gain. A reflection off a receding wave will produce an energy loss in fact. On average, over many reflections, there is a net energy gain; however it is a very slow process.

This process is generally treated as a propagation process and not a source of cosmic rays. It is generally referred as reacceleration in this context and can be treated as part of the Diffusion-Loss equation (Equation 1.5). It can either be treated as part of the energy loss/gain term or the Diffusion-Loss equation can be reformulated to include a diffusion term in momentum space[25].

1.3.3 The Limit of Acceleration

Since the lifetime of a SNR strong shock is limited, the maximum energy to which First Order Fermi shock acceleration, as described in Section 1.3.1, can accelerate a particle is also limited [26]. The acceleration rate per particle (rate of change of energy increase) is:

$$\frac{dE}{dt} = \frac{\xi E}{T_{cycle}} . \quad (1.20)$$

Here $\xi = 2 \langle \frac{\Delta E}{E} \rangle = \frac{4}{3} \frac{V}{c}$ (from Equation 1.14) is the fractional energy gain per round trip of the particle across the shock and T_{cycle} is the average time for each round trip. An upper limit for SNR strong shock acceleration can be found by integrating Equation 1.20 but to do so an expression for T_{cycle} must be found.

The current of particles through the shock surface is once again given by Fick's first law [24], $\mathbf{J} = -D_1 \nabla N$. We must however include convection because of the flow (in the shock frame) of ISM material into the shock at velocity $\mathbf{v}_1 = -|U|\hat{k}$ (Figure 1.6):

$$\mathbf{J} = -D_1 \nabla N + \mathbf{v}_1 N$$

with the z-axis defined to be normal to the shock surface. Upstream (in the ISM), \mathbf{v}_1 is negative, and the net flux across the shock is 0 (equal number of particles crossing each way). Treating the situation one-dimensionally then (since \mathbf{v}_1 is perpendicular to the shock surface), we get:

$$\frac{dN}{dz} = -\frac{v_1}{D_1} N .$$

The solution of this equation is thus,

$$N(z) = \rho_{CR} e^{-\frac{v_1}{D_1} z}$$

with ρ_{CR} the density of cosmic rays at the shock. The total number of particles upstream of the shock (in the ISM) per unit area is thus:

$$\sigma = \int_0^\infty N(z) dz = \int_0^\infty \rho_{CR} e^{-\frac{v_1}{D_1} z} dz = \frac{\rho_{CR} D_1}{v_1} .$$

Atkins shows ([24], pp. 724-725) that the number of particles crossing a surface per unit time (or colliding with a wall) is $\frac{1}{4} \rho_{CR} c$ since in our case the particles are relativistic. The total upstream time the particles spend per cycle is thus:

$$T_U = \frac{\sigma}{\frac{1}{4} \rho_{CR} c} = \frac{4 D_1}{c v_1} .$$

The downstream (inside the shock region) calculation is somewhat different but ends up having the same solution, thus the time for each cycle is:

$$T_{cycle} = \frac{4}{c} \left(\frac{D_1}{v_1} + \frac{D_2}{v_2} \right) . \quad (1.21)$$

To arrive at an upper limit for the acceleration energy from integrating Equation 1.20, a lower limit for T_{cycle} needs to be estimated. To do this, we must determine reasonably minimum estimates for D_1 and D_2 . For a perfect gas, Atkins ([24], p.728) shows that the diffusion coefficient is related to the particle speed and mean free path by:

$$D = \frac{1}{3} \lambda_D c . \quad (1.22)$$

A lower limit for λ_D would be some lower limit for the distance needed to fully randomize the velocity direction of the particle. If the scattering is due to irregular regions of magnetic field, the lower limit on λ_D would be the Larmor radius for the particles:

$$r_g = \frac{p}{ZeB}$$

Here p is the particle momentum $p \sim E/c$, Ze is the particle charge, and B the magnetic field. A minimum estimate for both D_1 and D_2 is thus:

$$D_{min} \simeq \frac{1}{3} \frac{E}{ZeB} .$$

Thus an estimate for the lower limit for T_{cycle} is:

$$T_{cycle} \simeq \frac{20}{3} \frac{E}{ZeBv_1c}$$

where we have taken Equation 1.21 and remembering that $v_2 = \frac{1}{4}v_1$. Integrating Equation 1.20 we get:

$$E_{max} \simeq \frac{3}{20} Z e B \xi v_1 c \int dt = \frac{3}{20} Z e B v_1^2 T_A . \quad (1.23)$$

Where we have used the proper value for ξ and T_A is the lifetime over which the shock is still strong (supersonic). To arrive at an actual estimate for the upper limit for acceleration, some estimates for T_A , B and v_1 will need to be made. However, one very important prediction is already apparent, which is that we expect the maximum energy to scale linearly with particle charge Z . If physically reasonable estimates for the still unknown parameters yield an energy scale compatible with the ‘knee’ feature in the all-particle spectrum, this will be a very suggestive result.

According to Gaisser [26] (p.159) it is reasonable to assume that a SNR shock will remain strong until the shock has swept up approximately its own mass in the ISM.

$$\frac{4}{3} \pi r_{SNR}^3 \rho_{ISM} = M_{ejecta} \quad (1.24)$$

with,

$$r_{SNR} \simeq v_1 T_A .$$

Reasonable estimates for a $10M_\odot$ SNR are $v_1 = 5 \times 10^6$ m/s. Using reasonable estimates for the density of the ISM of $\rho_{ISM} \sim 1$ proton/cm³ and the magnetic field strength of $B \simeq 3\mu G$ we find $T_A \sim 1000$ years. Thus we can estimate the maximum energy to which a typical SNR can accelerate a cosmic ray to be $E \leq Z \times 30$ TeV. The energy scale is suggestive of the ‘knee’ feature discussed in Section 1.1.1, but is of course very dependent on the accuracy of our guesses for the parameters.

The scaling with Z does however allow us to make qualitative predictions about what we might observe in the all-particle spectrum if we probe for species charge. If this is accurate and the ‘knee’ represents a limitation of SNRs as Galactic accelerators, then as we move into the knee region we expect an enrichment of heavier species in the spectrum. Results from KASCADE (Section 1.5.3) and other similar ground detectors suggest just such a trend toward heavier species into the ‘knee’ region.

1.4 Other Particles of Interest

Information about possible cosmic-ray sources and propagation can come from many other types of particles, besides just observation of the cosmic rays themselves. Of course the study of these particles goes beyond providing information directly related to the hadronic cosmic rays themselves, and this brief discussion is not meant to be exhaustive in any way.

Electrons should properly be included in a discussion of cosmic rays, but have been neglected from this discussion since they are not detected by the CREAM experiment. Some component of the electron spectrum observed at earth is likely primary in origin and is probably accelerated in the same sorts of sources as Galactic cosmic rays, such as SNRs. Some component is also secondary in origin, arising from the end products of

particle interactions and decays in the ISM. There is also a positron component present, but it is unclear at present if any component of this is of primary origin. Possible excesses in the positron spectrum have been searched for by such experiments as HEAT [30], PAMELA [31] and others, though the presence of an excess inconsistent with a purely secondary origin is still an unresolved question. The presence of such an excess is of great interest because some models of dark matter weakly-interacting massive particle (WIMP) annihilation predict antimatter production [30]. The presence of a primary positron component possibly from pulsars or other astronomical objects in the Galaxy would also be very interesting.

There also exists an antiproton flux in the cosmic rays, with a ratio to protons of the order of $\bar{p}/p \simeq 2 \times 10^{-4}$ in the energy range 10 – 20 GeV [3]. There is no evidence to-date of any primary component to the flux of antiprotons. No detections of antihelium or antideuterons have been made so far in the cosmic-ray spectrum, though using antideuterons as a novel probe for neutralino dark matter annihilation is under investigation [32].

X-ray and γ -ray astronomy also offer amazing insights relevant to the study of cosmic rays. Emission from SNRs consistent with both synchrotron losses from high-energy electrons or from pion production from high-energy nuclei impacting material in the SNR has been observed for example (see [33] among many others). Also, diffuse γ -ray emission consistent with π^0 decay from cosmic-ray interactions with the ISM have been observed (p. 307 of [19]).

Finally, the observation of neutrinos is also fundamental to the study of high-energy processes in the cosmos. Solar neutrinos provide a probe of the fusion reactions taking place in the sun, as well as providing the puzzle which eventually led to the discovery of neutrino oscillations and the existence of neutrino mass. Neutrinos of higher energy originating from cosmological sources are of great interest as well.

1.5 Cosmic-Ray Detection

Figures 1.1 and 1.2, for energies > 100 TeV, are primarily derived from air-shower experiments conducted on the surface of the earth (Section 1.5.3). Since the fluxes are so low, direct detection of particles in the ‘knee’ region and above is an experimental impossibility currently. However, since the particles deposit their energy in the atmosphere (as a particle shower), measurement of the air shower can be used to access this region.

For lower-energy cosmic rays (and hence higher fluxes), direct detection is practical, either from spacecraft (Section 1.5.2) or from high-altitude balloons (Section 1.5.1). Practical limitations on detector size and exposure time restrict how far into the low-flux region these measurements have been made however. One of the goals of the Cosmic Ray Energetics And Mass (CREAM) experiment is to extend the single species energy spectra up to as high an energy as possible, by maximizing flight time on a high-altitude balloon to ~ 1 year.

1.5.1 Balloon-Based Measurements

The history of cosmic rays in fact begins with scientific ballooning. In 1912 Victor Hess and others began to fly electroscope devices in manned balloon flights of between 5 and 9 km in altitude. The electroscopes operated by measuring the discharge of a piece of metal foil in a sealed dry atmosphere. What they discovered was that above ~ 1.5 km in altitude the ionization rate (rate of discharge of the electroscopes) increased. This led to the interpretation that this was a very penetrating radiation coming from space. This inference was partially correct. This radiation was due to particles coming in from space, but we now know it to be secondary particles (mainly muons) produced in showers of cosmic rays in the upper atmosphere. In fact, at altitudes higher than shower maximum (the altitude where there are the most numerous charged particle secondaries in the shower), the ionization rate will fall off.

Today balloons offer a compromise between ground and space-based observations. This is only partially true, as a more correct statement would be that they offer a much more economical direct measurement opportunity for observation of cosmic rays (and other radiation which is blocked by the atmosphere). They offer several great advantages over space missions: an order of magnitude or more less costly, much quicker mission timetables are possible, more generous payload size and mass constraints. Scientific ballooning is not limited to cosmic-ray research either, as telescopes operating at other wavebands have been flown as well.

However, balloons are not 100% equivalent to spacecraft either, as long exposure usually requires multiple flights, and atmospheric interactions above the instrument are still present. Traditionally, flights in the continental US were limited to a few hours to several days at most due to overflight limitations for the payloads over populated areas. Longer flights are possible in the Arctic, Antarctic and Russia however. For the last several years, flight durations on the order of a month have become more common in Antarctica with the Long Duration Balloon vehicle. The record for flight duration for a Long Duration Balloon was in fact set by the first CREAM flight in the 2004-2005 Antarctic flight season (a duration of ~ 42 days). A goal for the future of scientific ballooning is the development of super-pressure balloons such as the Ultra-Long Duration Balloon [34] and some means of limited propulsion for trajectory modification which will allow for missions of ~ 100 days.

Two missions predating CREAM that are of interest here are JACEE [35] and RUNJOB [36]. Both projects consisted of multiple flights of passive emulsion calorimeters. JACEE had 15 flights in total, with a total exposure of 1436 m²hours, and RUNJOB had 575 m²hours in 11 flights. Both payloads were concerned with measuring the elemental fluxes of cosmic rays in the energy range $\sim 1 - 1000$ TeV, to both measure secondary/primary ratios and to look for any break in the spectrum of protons which would be a signature of a limit in cosmic-ray accelerators, as already discussed in this chapter. The payloads were successful in gathering a large number of TeV-scale events and those results will be presented later in the discussion of the current knowledge of cosmic-ray spectra approaching the ‘knee’ (Section 1.6).

ATIC [16] is a more recent contemporary experiment to CREAM consisting of a BGO-based calorimeter and silicon-based charge detector. It has had 4 flights to-date

(flight 3 was unsuccessful due to balloon failure). It is designed for individual species resolution from protons to iron, but with a somewhat lower energy range (tens of TeV) than CREAM. It is also sensitive to electrons [37] and reported along with PAMELA [38] an anomalous excess in the electron spectrum, though this is still an unsettled topic (in fact, very recent results by the Fermi-LAT satellite instrument seem to contradict the ATIC electron result [39]).

The HEAT [30] experiment was mentioned above in the electron section. This experiment had four successful flights, with different configurations, either for antiproton/proton measurements or for positron/electron measurements. The instrument used a cryogenic superconducting magnetic spectrometer to distinguish between positively and negatively charged species.

Other cosmic-ray balloon projects of note include TRACER [18] which is focused on secondary/primary ratios and absolute fluxes of species from boron to iron, and TIGER [40] which probed the abundances of ultra-heavy species beyond iron.

Another current balloon experiment relevant to particle astrophysics is CREST [41] which will search for high-energy electrons (> 2 TeV) as evidence of nearby Galactic sources. It utilizes a novel configuration of X-ray sensitive BGO crystals surrounded in a box of scintillator paddles to veto charged cosmic rays. The detector is thus sensitive to X-ray synchrotron radiation from the high-energy electrons interacting in the terrestrial magnetic field.

The ANITA [42] experiment is another Antarctic balloon payload with two flights to-date searching for high-energy neutrinos. Such neutrinos are expected to exist as secondary products of super-GZK cosmic rays interacting either with the cosmic microwave background radiation, or else possibly within their acceleration region. Since the neutrinos travel unattenuated and undeflected from their emission, they should provide valuable information about the sources of the ultra-high energy cosmic rays.

The CREAM project will be discussed in much greater detail in the remainder of this document, but I will briefly restate its purposes here. It is sensitive to cosmic-ray nuclear species from protons and up. For the first flight the instrument had a sensitivity to $Z \geq 3$ particles above \sim GeV energies, with an acceptance of $2.2 \text{ m}^2\text{sr}$ for measurements of secondary/primary ratios of cosmic rays, as already discussed. This measurement was done with a Transition Radiation Detector (discussed in the next chapter) with redundant charge detectors. In all 4 flights to-date, the payload has also had a sensitivity to higher-energy cosmic rays using an electromagnetic sampling calorimeter (also discussed in the next chapter), of approximate acceptance $\sim 0.3 \text{ m}^2\text{sr}$ and minimum energy threshold ~ 1 TeV. There are two main goals for CREAM: measure secondary/primary ratios at higher energy than previously (to constrain propagation models), and to extend individual species spectra to energies approaching the ‘knee’ feature and look for a break in the proton spectra consistent with a limit of astrophysical cosmic-ray sources.

1.5.2 Space-Based Measurements

Characterizing the radiation environment in space was one of the first concerns of the first generation of Soviet and American satellites. The first American satellite in

space, Explorer 1, in fact carried a Geiger-Müller tube for cosmic-ray detection. This instrument (actually saturation of this instrument) was responsible for the discovery of the Van Allen radiation belts.

Huge discoveries in X-ray and γ -ray astronomy have been made largely because of the ability to put detectors on spacecraft. Notable spacecraft dedicated to X-ray and γ astronomy include Uhuru, HEAO 1-3, the Compton Gamma Ray Observatory, XMM-Newton, the Chandra X-ray Observatory, Swift and the recently launched Fermi/GLAST γ -ray Observatory.

The HEAO 3 satellite contained two dedicated cosmic-ray experiments (in addition to a γ -ray experiment) [19]. The C-2 (Cosmic Ray Isotope Experiment) detector was sensitive to nuclei from beryllium to iron and energies from ~ 0.5 GeV/n to ~ 25 GeV/n. This experiment provided the highest statistics for B/C ratio measurements in this energy range at the time. Also, isotopic measurements were done using the Earth's magnetic field as a mass spectrometer. The C-3 (Heavy Nuclei Experiment) detector was concerned with cosmic rays with $Z \geq 30$. The HEAO 3 satellite was in orbit for about 2 years, from 1979-1981.

The Voyager [43] spacecraft both carry instruments relevant for cosmic-ray physics, and are unique as the only (currently active) space probes leaving the solar system. Relevant instruments include magnetometers and particle detectors including plasma detectors for measuring solar wind, a cosmic-ray detector and an electron detector. The cosmic-ray detectors are still active on both spacecraft, and are sensitive to species from protons to iron and an energy range of $1 - 500$ MeV/n. In situ measurements of cosmic rays (solar and Galactic) and solar wind and magnetosphere are underway. Both spacecraft appear to have crossed the Termination Shock and are continuing to probe the heliosheath region, before eventually passing into interstellar space while still possibly operational (on-board power expected to be sufficient until ~ 2025). Voyager 1 is currently ~ 110 AU (as of mid 2009) radial distance away from the Sun, while Voyager 2 is at ~ 89 AU.

PAMELA [31] is a current space mission launched in 2006 and is attached to the Russian Resurs-DK1 Earth observation satellite. Its primary mission is characterization of the electron and positron, proton and antiproton, light nuclei of the cosmic-ray flux, and searches for light anti-nuclei. It has the following energy sensitivities: 50 MeV-400 GeV for electrons, 50 MeV-270 GeV for positrons, up to 2 TeV for $e^- + e^+$, 80 MeV-700 GeV for protons, 80 MeV-190 GeV for antiprotons and up to 200 GeV/n for light nuclei.

The AMS-02 [44] payload is a cosmic-ray detector meant to attach to the International Space Station. Its launch needs to be done with the Space Shuttle, and it is currently manifested to fly on STS-134 in mid 2010. Its primary objectives are characterizing the antimatter spectrum (positrons and antiprotons and searches for any other antinuclei), the cosmic-ray spectra in general, searches for exotic particles such as strange matter and some sensitivity to \sim TeV γ -rays. A test version of the payload (AMS-01) [45] flew on STS-91 in 1998, and established an upper limit fraction for antihelium of 1.1×10^{-6} .

1.5.3 Ground-Based Measurements

When a cosmic ray of sufficient energy enters the atmosphere of the earth, it will produce an extensive air shower of secondary particles. This was first noticed in the late 1930's by Auger and others when they observed that counters separated by up to several hundred meters horizontally on the surface would have coincident detections at a rate much higher than expected if the incoming particles were of random origin. The charged particles in the shower effectively arrive in several slightly curved sheets, whose surface is perpendicular to the original track of the primary particle.

Up until the early 1950's, observations of cosmic-ray shower particles arriving at the surface of the earth was the main technique available for experimental particle physics at high energy (\sim GeV) [20]. At that time, accelerator technology progressed to the point where more controlled and higher-luminosity beams could be produced in the laboratory.

Two main techniques are currently available for detecting these extensive air showers from the surface: air fluorescence and surface detectors. The air fluorescence technique involves watching the sky for optical light from fluorescence from air molecules excited by particles in the shower. Additionally, optical Cherenkov light from the high-energy charged particles in the shower (and in some cases the primary particle as well) also contribute to the signal. The surface-detector method samples the shower components that reach the surface, either with a single large detector, or with an array of smaller detectors spread over an area.

These techniques have several experimental difficulties. One is that they are very dependent on extrapolations of cross-section values from known energy ranges into energy ranges as yet inaccessible by accelerators. Beyond the limitation of the knowledge of the first interaction, the observations are also limited by the accuracy of the shower development and propagation models. Reconstructions are also dependent on very good measurements and models of the atmosphere properties at the time of the shower. Atmospheric conditions can change rapidly, and the range of meteorological measurements available can be limited by practical considerations. Detectors which sample the shower at the surface can generally operate 24 hours a day; however, fluorescence detectors are generally limited to mainly moonless nights in isolated locations with clear skies, which imposes duty cycle limitations on them. The development of air-shower ground arrays progressed in the 1960's and 70's, and by the 1970's it had been observed that the all-particle cosmic-ray spectrum extended to very high energies ($\sim 10^{20}$ eV) and generally obeyed a power-law spectrum as discussed previously in this chapter. To collect significant statistics at 10^{20} eV (where the flux is of order one particle/km²century), detectors with larger and larger acceptances have been necessary. Throughout the 1980's and 90's, detectors such as Fly's Eye and its follow-up project HiRes [23] (both fluorescence type) and the surface array AGASA [46] took data to investigate the highest-energy region. A follow-up project called Auger [47] has been constructed this decade and has already collected significant statistics (Figure 1.7). Auger uses both an array of surface detectors (water Cherenkov tanks) for detection of shower muons and electrons, and a collection of air fluorescence telescopes to view the extensive air shower in the air. This allows events collected with both detectors to have in principle better energy assignments than with

either technique separately, and allows for cross-calibration of the two techniques. This technique was actually pioneered at the HiRes site, where the CASA-MIA [48] ground array was deployed.

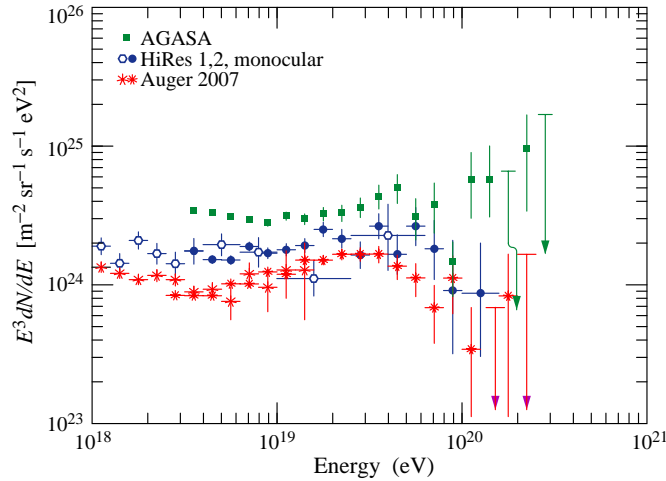


Fig. 1.7 The all-particle spectrum of ultra-high energy cosmic rays. This represents the highest part of Figure 1.2, with the flux rescaled by E^3 . The presence of the GZK cutoff feature above 10^{19} eV seems reasonable if Auger and HiRes energy reconstructions are accurate (from the Particle Data Group [3]).

A related technique to the air fluorescence method above is relevant for detecting GeV and TeV scale γ -rays. This is atmospheric Cherenkov imaging using ground-based telescopes to image the Cherenkov light from electromagnetic showers initiated in the atmosphere by incoming high-energy γ -rays. At these energies, the fluxes of γ -rays are too low to allow for direct measurements from spacecraft or balloons with meaningful statistics. Two telescope arrays with similar capabilities are VERITAS [49] in the northern hemisphere and HESS [50] in the southern. A large number of results have been forthcoming from these projects about many astrophysical objects. Cosmic-ray showers produce a large background for these detectors, but since the cosmic rays are charged, it is possible to see the initial Cherenkov signal from the cosmic ray propagating in the atmosphere before shower production, if good time resolution is available. Thus, cleaner γ -ray signals are obtainable and cosmic-ray physics can be done as well. Even cosmic-ray electron spectra have been measured to TeV energies [51]

At comparatively lower energies in the region around the ‘knee’ feature (above 1000TeV), ground detection is still the only current means of probing the cosmic rays, since the flux is too low for direct measurements with today’s detectors and flight times. As mentioned earlier, to understand the nature of the ‘knee’ feature and whether it is related to limitations of Galactic accelerators, composition information is necessary.

Some information about the chemical composition of the primary particle initiating the extensive air shower is recoverable in principle from information about the relative abundances of electrons and muons in the shower (this is a complicated, simulation-dependent process beyond the scope of this document). The KASCADE [5] array in Germany has produced results (Figure 1.8) suggesting a steepening of the proton spectrum relative to helium and CNO. Measurements have also been made by the TIBET [52] collaboration and others, though at this point the full picture is not clear.

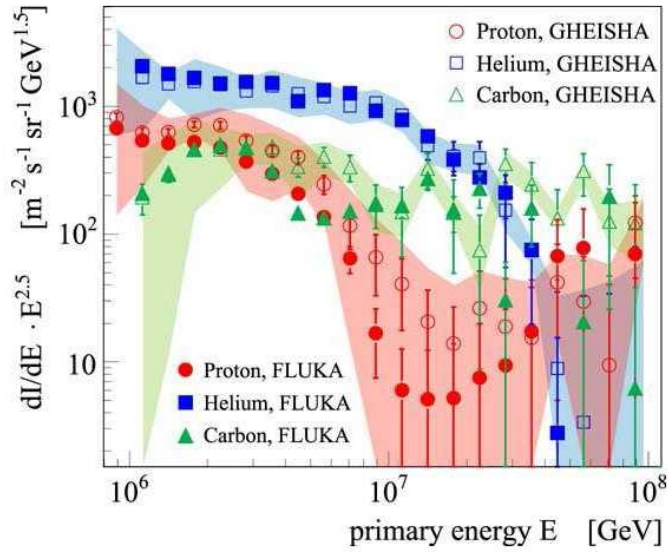


Fig. 1.8 Chemical composition estimations from the KASCADE ground array experiment. Results for the QGSJet hadronic interaction model and the FLUKA and GHEISHA Monte Carlo packages are also shown. The shaded region is the estimated systematic uncertainty for the QGSJet/GHEISHA solutions. (From the KASCADE Collaboration [5]).

1.5.4 Sub-surface Measurements

Since neutrinos are uncharged and have such small interaction cross-sections, they can propagate more or less freely since production. In fact, neutrinos from SN1987A are still the only (non-photon) particles arriving at earth which have been correlated with a specific astronomical source outside of the solar system.

Their very small interaction cross-sections also make their detection very challenging. Generally subterranean detectors [26] of very large sizes are required. Atmospheric muons from cosmic-ray air showers are very penetrating, and thus several km of depth underground are required to attenuate them. Still present as a background contribution are radioactive decay products from the detector itself, and from the surrounding

earth. Current subterranean neutrino detectors include water Cherenkov detectors such as Super-Kamiokande [53], as well as a variety of other detectors based on other techniques including measuring elemental transitions from charged current interactions, in liquid scintillators, heavy water (deuterium being sensitive to interactions with neutrinos), as well as other techniques.

The AMANDA and the follow-up IceCube [54] neutrino detectors take a somewhat different approach. The detectors are located at the south pole in Antarctica and consist of photon sensors embedded in the deep clear ice starting 1450 m under the surface and extending below. The IceCube detector when fully deployed will have an instrumented volume of 1 km^3 . Other neutrino detector techniques such as deep-ocean environments have also been studied.

Another class of detection experiment which is necessary to conduct underground for background suppression is direct dark matter searches. These searches often utilize cryogenic liquids and look for effects from nuclear recoil from interactions by dark matter particles.

1.6 Current Measurements of Elemental Abundances of Cosmic Rays

The KASCADE results presented above suggest a steepening of the proton spectral index somewhere above 1000 TeV in energy. If so, this would suggest that direct measurements have little hope of acquiring adequate statistics to measure individual species when this steepening begins. The uncertainties associated with this are still quite large, however, and the unfolding is a non-trivial task and is still model-dependent. Additionally, better direct measurements in the energy region directly below 1000 TeV will help to calibrate these ground-array measurements at the low end, even if they end up not directly accessing the energy region of interest.

As can be seen in Figure 1.9, the picture from direct measurements at energies above a TeV is still far from clear. There are still systematic uncertainties which lead to disagreements between the different measurements. The agreement for protons is reasonable, but is not as good for helium. There is much better agreement between the CREAM I results shown here and the ATIC2 results than between for example the CREAM and older RUNJOB results. While there is probably a difference in spectral index between protons and helium nuclei here, there is no clear signature for a kink in the proton index which would be a signature for a SNR shock acceleration limit. Of course, as mentioned above, if the KASCADE results are true, we do not expect to see such a feature in this energy range anyway.

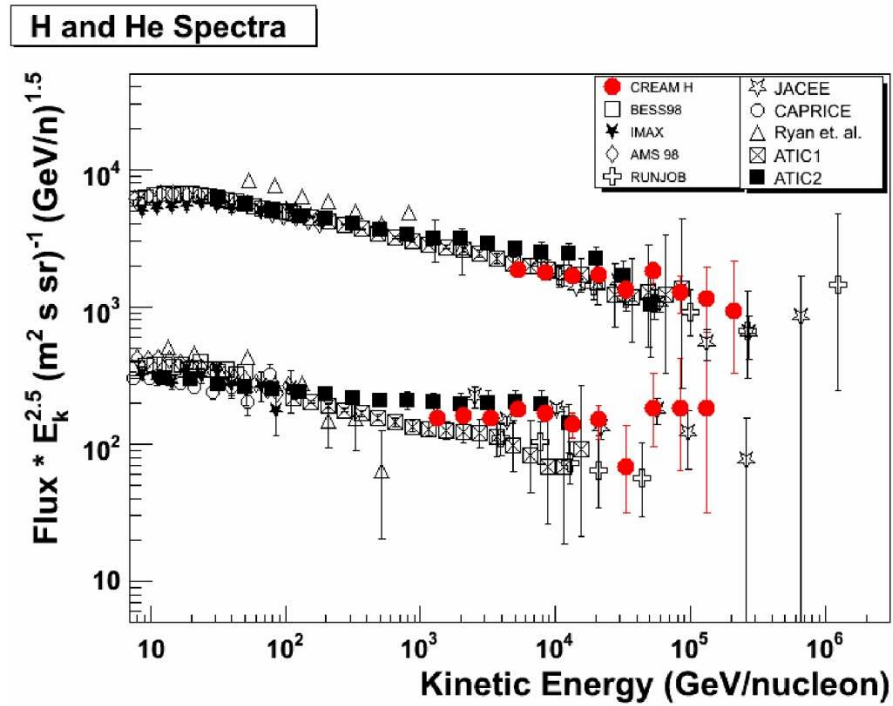


Fig. 1.9 Proton and helium fluxes from CREAM-I and several other direct measurements by high-altitude payloads. The CREAM-I measurements here involve energy determination from an electromagnetic calorimeter, and charge determination from a silicon charge detector, both discussed in following chapters. (From the CREAM Collaboration [6]).

Chapter 2

The Cosmic Ray Energetics and Mass Instruments

2.1 Goals

The two main goals of the CREAM program are to characterize the primary high-energy cosmic-ray spectrum above ~ 1 TeV and to measure secondary-to-primary ratios for species such as boron/carbon, nitrogen/oxygen and sub-iron/iron to higher energy than in the past. Redundant charge measurements allow for improved resolution, cross-calibration and exclusion of particles fragmenting in the instrument. Redundant energy measurements allow for cross-calibration of detector types with different systematic uncertainties (e.g., a transition radiation detector (TRD) and a sampling hadronic calorimeter (CAL), both used to measure incident particle energy in CREAM) and greater sensitivity in coverage in both particle type and energy.

To meet the science goals of CREAM, especially for the elemental abundances at high energy, sufficient exposure is necessary. The geometric acceptance for TRD measured events is $2.2 \text{ m}^2\text{sr}$ [55]. For protons in the CAL, the geometric acceptance (also taking into account a $\sim 50\%$ efficiency of carbon target blocks above the CAL in initiating a hadronic shower) is $\sim 0.3 \text{ m}^2\text{sr}$. The efficiency of shower generation does rise for higher species, up to $\sim 60\%$ for iron [8]. To gather significant statistics for species beyond ~ 100 TeV in energy, an exposure ~ 1 year is necessary.

Originally CREAM was intended to utilize the Ultra-Long Duration Balloon (ULDB) [34] vehicle which has been under development by NASA since the 1990's. The ULDB is a super-pressure balloon designed for long ~ 100 day operation. Existing Long Duration Balloon (LDB) vehicles have demonstrated typical flight duration of order a week or so, with a maximum (the first flight of CREAM) of almost 42 days.

2.2 CREAM I Instrument Overview

The primary energy detectors of the CREAM I instrument are an imaging calorimeter (CAL) and a Transition Radiation Detector (TRD), as already mentioned above. The primary charge-sensitive detectors are a scintillator based Timing Charge Detector (TCD) and a Silicon Charge Detector (SCD). Since CREAM operates in Antarctica, the geomagnetic cutoff of low-energy cosmic rays is suppressed, so a Cherenkov Detector (CD) is present to exclude these particles from overwhelming our trigger. This combination of detectors provides multiple redundant charge measurements (TCD and SCD), as well as complementary (with some redundancy for cross-calibration as well) energy measurements (Figure 2.1). The physics principles of the detector subsystems is discussed in Appendix A.

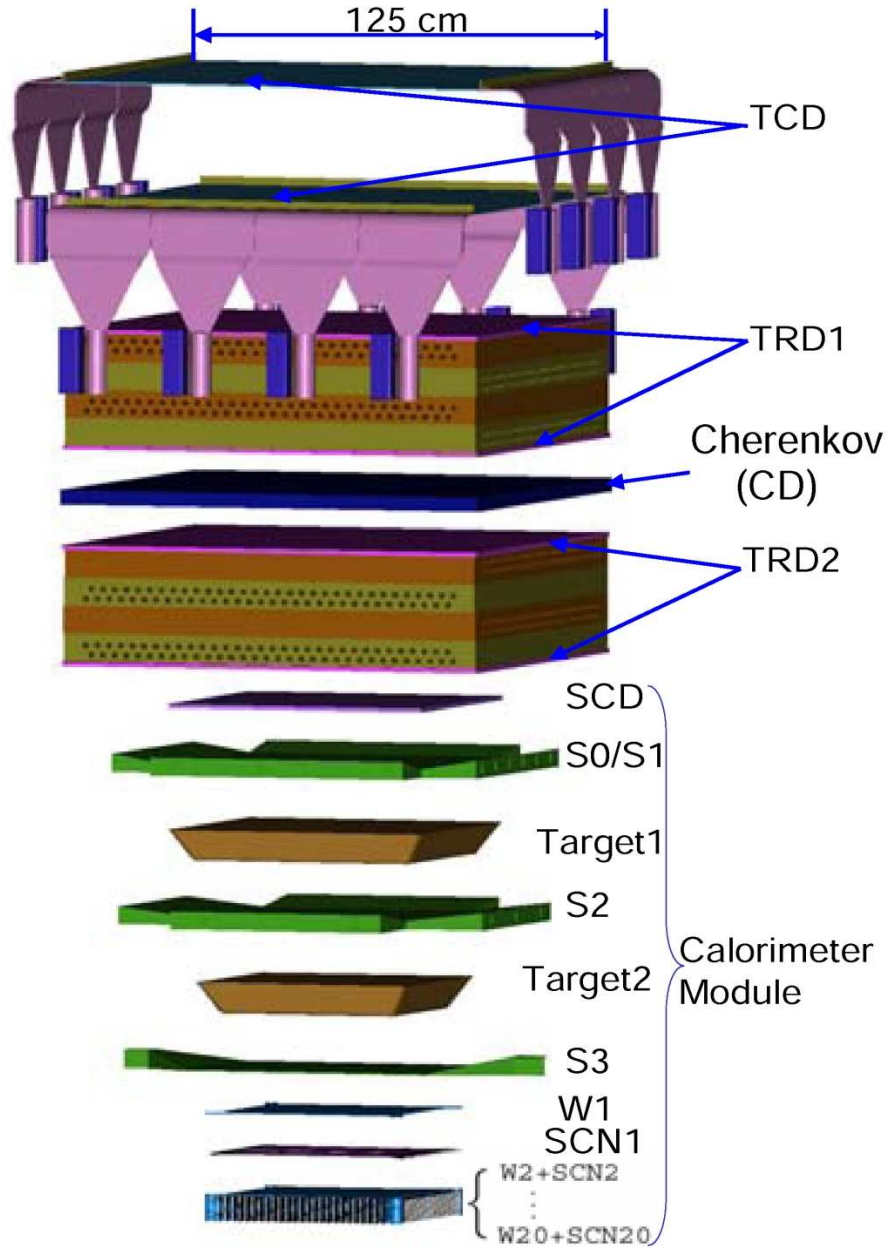


Fig. 2.1 Exploded schematic representation of the CREAM I instrument (science detectors) [7]. The TCD, CD, TRD, SCD, S3 and CAL module are all discussed in this chapter. W1-20 are tungsten plates making up the absorber layers of the calorimeter module. SCN1-20 are scintillating-fiber readouts between each absorber. Target 1 and 2 are graphite blocks to initiate hadronic showers. S0/S1, S2 and S3 are scintillating-fiber hodoscopes for redundant charge measurement, tracking, time-of-flight and trigger uses.

2.2.1 Timing Charge Detector

The TCD for CREAM is one of two main charge-measurement detectors in the payload (the other being the Silicon Charge Detector). It is positioned at the very top of the stack of detectors. It utilizes eight plastic scintillation paddles arranged in two crossed layers instrumented with fast photomultiplier tubes (PMTs), coupled to fast readout electronics. The TCD both measures the charge of the primary incident particle, and also contributes to the overall instrument trigger.

In addition to the TCD paddles located at the top of the instrument, there is a scintillation detector located directly above the calorimeter (S3), which is part of the TCD system. The S3 detector is of different construction than the TCD paddles (scintillating fiber layers vs. solid scintillator slabs), but is read out with the same type PMTs and electronics as the TCD. This detector allows for Time-of-Flight (TOF) measurements to discriminate between downward- and upward-going particles, as well as restricting one TCD trigger mode to only particles in the CAL acceptance.

Since CREAM operates in a polar region, the geomagnetic cutoff is suppressed and the flux of lower-energy cosmic rays is not nearly as attenuated as at more equatorial latitudes (Section 1.2.4). In order to limit the trigger rate to ≤ 30 Hz for the TCD system, two basic trigger modes are used. The first requires that PMT signals cross thresholds consistent with above-noise signals on at least 3 of the 4 sides of the TCD and that the logical OR of the S3 PMTs also cross a sufficient threshold. This trigger scheme permits triggering on $Z \geq 1$ primaries only in the geometrical acceptance of the calorimeter, and is referred to as the Zlo trigger mode in the TCD. Otherwise, as discussed above, the trigger would be flooded with lower-energy protons and α -particles.

The second trigger mode of operation of the CREAM TCD is called the Zhi mode. This mode again requires a minimum 3-fold coincidence between TCD sides, but at a higher PMT signal threshold. The Cherenkov Detector discussed below is also required to cross a minimum threshold usually set to be consistent with $Z \geq 3$ species. This is again to limit events to roughly the geometric acceptance of another detector, in this case the TRD. After CREAM I, despite the lack of a TRD this trigger mode was still used, so that sufficient events above protons and α -particles could be collected for proper calibration of the TCD. The TCD trigger is discussed in more detail in Chapter 4.

The TCD system has flown in all flights of CREAM to-date in a very similar configuration, with some small changes in hardware. Most scintillator slabs were not reused from flight to flight since most of them were not recovered intact after each flight. Those pieces that were returned intact often had extensive crazing and surface abrasions from rubbing of the foil wrapping on the scintillator. Most of the twisted-strip adiabatic light guides used to read out the TCD scintillator slabs were recovered in a useable state however, which was fortunate since they are more expensive than the scintillator material, being hand-crafted items. For the first CREAM flight, the PMTs were glued directly to the light-guide ends, but for later flights they were made removable with a metal-collar mounting system and optical grease coupling. Electronics boxes were identical, except for occasional replacement of failed boards.

The construction and design of the TCD and S3 detectors and readout electronics are described in much greater detail in Chapters 3 and 4.

2.2.2 Transition Radiation Detector

The Transition Radiation Detector [8] in CREAM is an energy-measurement and tracking detector filling most of the middle portion of the payload. The TRD consists of an upper and a lower block, each containing Dow Ethafoam 220 [8] radiator blocks with embedded thin-walled proportional tubes. The Ethafoam serves as both mechanical support for the proportional tubes and for the generation of transition radiation (TR is discussed in Appendix A). Each TRD block contains 256 tubes, arranged in four layers each alternating in direction. Each TRD block is $120 \times 120 \times 35 \text{ cm}^3$. In flight the TRD was operated with a gain appropriate to measure species of charge 3 and above. For ground operation the gain was also adjusted high enough to track atmospheric muons.

The proportional tubes are filled with a 95% xenon, 5% methane gas mixture. Xenon has one of the largest relativistic rises of any gases before the onset of saturation [28]. The TRD proportional tubes were constructed to be as gas-tight as possible, and maintained excellent pressure throughout the flight. The controllable gas-manifold system was used several times to equalize pressure throughout the TRD system, but no resupply of gas from the on-board reserve was necessary.

Particle tracking in the TRD is accomplished by measuring primary-particle hits through multiple proportional tubes. Because the individual-tube response is a function of primary charge and path length of the particle track through the tube, very good tracking can be produced with a multiple-pass track-fitting routine. Tracking position resolution for the CREAM I TRD (with a 3-level iterative track fitting) is on the order of $\sim 1 \text{ mm}$.

The TRD measures primary particle γ (Lorentz factor) by two different physical processes (Figure 2.2). The first is ionization losses when the primary particle goes through a proportional tube. Eventually this effect saturates at high particle γ . To extend the upper range of γ response of the detector, transition radiation (TR) X-rays can be used. TR photons are emitted when the electric field of a moving charged particle transitions between vacuum and a dielectric medium. The X-ray photons are emitted with very small angle with respect to the primary particle and thus produce extra ionization in the same proportional tubes hit by the primary.

Each proportional tube is read out by a dual-gain application-specific integrated circuit (ASIC) readout scheme. This provides for a dynamic range of ~ 4000 , enabling readout for species from lithium with $\gamma \simeq 10^3$ to nickel with $\gamma \simeq 10^5$. From Figure 2.2 at low γ the ionization losses in the proportional tubes increase, which introduces a degeneracy in the TRD response. To deal with this situation, a Cherenkov detector as outlined in the next section is utilized. Also, since the TRD response is proportional to Z^2 , very good charge resolution is necessary for correct energy determination. The redundant charge measurements provided by the TCD and SCD are helpful for this.

2.2.3 Cherenkov Detector

The Cherenkov Detector is positioned between the two TRD blocks in CREAM I. The CD radiator is a plastic acrylic material with a refractive index of $\simeq 1.5$, and so is sensitive to particles with $v/c = \beta \simeq 0.67$ [28] and above for incoming charged particles, and can therefore be used to select only high-velocity particles for the trigger. Since the

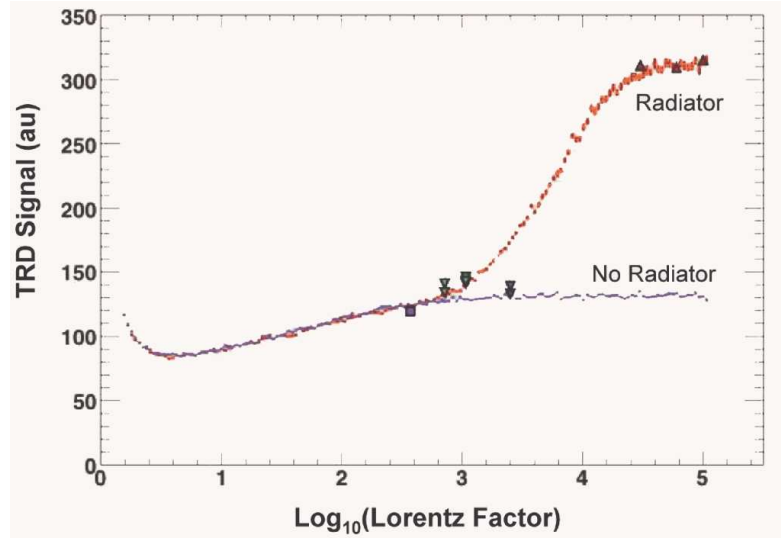


Fig. 2.2 TRD response (in arbitrary units) as a function of particle $\log \gamma$. The blue line is the GEANT4 simulated response of the proportional tubes only. The red line is the simulated response with transition radiation from the Ethafoam radiator included. Symbols are from CERN beam testing of prototype hardware both with and without TR. [8].

signal is also proportional to Z^2 (Equation A.6) the trigger threshold can also be set high enough to exclude H and He from the trigger mode of interest for TRD measurement. The CD actually provides a quiescent veto signal to the TCD internal trigger system, and only stops vetoing when a high β event occurs.

By combining the charge measurement from the TCD and SCD with the Cherenkov signal in the CD, it is possible to measure β of lower-energy primary particles, before saturation sets in. In this way, the CD is also an energy measurement instrument, and covers a range sufficient to deal with the TRD-response degeneracy discussed above. As β approaches 1 however, the CD saturates, and energy measurements must be done by the TRD or the CAL.

The CD consists of a radiator slab of dimensions $120 \times 120 \text{ cm}^2$. Wavelength-shifting plastic bars are positioned on each outer edge of the radiator and held in place with springs (this permits a small gap of air or vacuum to be present between the bar and the radiator, necessary for efficient photon piping down the wavelength-shifting bar). The end of each bar is read out with with 0.5" XP1910 PMTs. The outer corners of the radiator are machined out to physically accommodate the PMTs. There are a total of 8 PMTs in the CD. Dynamic range is extended by having the PMTs gain-matched into two sets: a low-gain set and a high-gain set. A low-gain and a high-gain tube read out each wavelength-shifter bar (each side of the detector).

For the CREAM I flight, the CD readout was handled by the TRD subsystem using a 12-bit peak-sensing analog-to-digital converter (ADC) readout scheme. For later

flights the TRD was not present however, and instead the CD readout was done by a modified TCD electronics box, with an external front-end pulse-shaper board. The pulse-shaper board modified the CD PMT signals to place them on scale for the TCD electronics, and also generated the veto signal for the internal TCD trigger system.

2.2.4 Silicon Charge Detector

The SCD is the other major charge-measurement detector in the CREAM instrument (Figure 2.3). In CREAM I the SCD consisted of one layer of silicon pixels, but for subsequent flights, a second layer was added. The CREAM I SCD has an active area of $78 \times 79 \text{ cm}^2$ and contains 2912 pixels [8]. Each pixel is $1.55 \times 1.37 \text{ cm}^2$ and the pixels overlap slightly to eliminate any dead region from gaps. The SCD is positioned directly above the upper CAL carbon target and directly below the TRD.

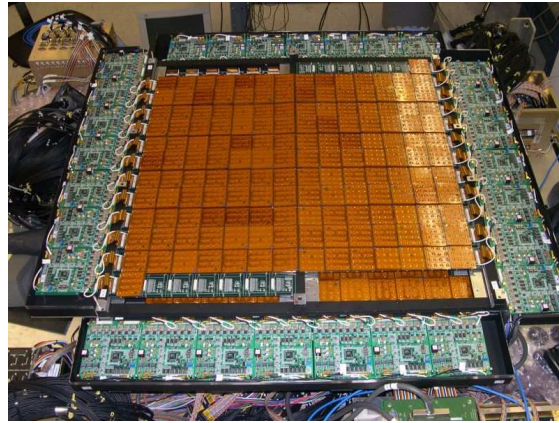


Fig. 2.3 CREAM I SCD with cover removed.

The SCD is tested before each flight during a calibration of the calorimeter module at the European Organization for Nuclear Research (CERN), as described below. The detector is moved in an accelerator particle beam so that each pixel can be exposed. This helps to measure relative pixel gains, and also identifies dead or damaged pixels.

Because the SCD is located close to the calorimeter, albedo particles coming back up through the instrument present a significant background signal, especially for low-charge species. The SCD is highly segmented however, so if there is reasonable tracking for the primary particle, most albedo signal can be excluded by doing a position cut. For nuclear species heavier than H and He, selection of the pixel with the largest signal is sufficient, since signal size is proportional to Z^2 , and the albedo particles are singly-charged and thus will produce much smaller signals.

2.2.5 Calorimeter

The CREAM calorimeter [8] is an imaging sampling calorimeter positioned at the bottom of the instrument science stack. Above the calorimeter are two graphite carbon targets to help initiate electromagnetic particle showers. The carbon targets together total approximately half an interaction length for incoming cosmic-ray protons (slightly more for heavier species). Also present (in CREAM I only) are two scintillating fiber hodoscopes, for improved tracking and redundant charge measurement, labeled S0/S1 and S2, respectively, on Figure 2.1. These were not deemed necessary for subsequent flights.



Fig. 2.4 CREAM II calorimeter stack during integration. The bottom structure is the calorimeter with fiber-optic readout visible. Above the CAL are the two carbon targets, with supporting metal pedestals at the corners.

The calorimeter consists of 20 layers of $50.1 \times 50.1 \times 0.35 \text{ cm}^3$ tungsten plates (with support tabs in the corners) (as shown in Figure 2.5). Between each layer of tungsten is a layer of 0.5 mm clad scintillating fibers. The fibers are glued into ribbons of 19 fibers each (for a total width of 1 cm each) before being glued down into a layer (Figure 2.6). Each layer of fibers alternates in direction. Light from each ribbon is collected by a small ‘fish-tail’ light guide to couple it to an optical fiber bundle for readout.

Each optical fiber bundle from a ribbon is split at the readout end into 3 smaller bundles (of 37+5+1 fibers). All 25 fiber bundles from a side of each layer from the calorimeter (25 ribbons total) are collected into an optical cookie. The first and second sub-bundles from each large fiber bundle are read out individually pixel-by-pixel in a Hybrid Photo-Diode (HPD) device. The last sub-bundles, however, (the one with 1 fiber from each) is collected into 5 total groupings for readout by HPD pixels. A total 25+25+5 pixels are thus used for signal readout. Additionally, 3 are used for LED calibration, and 6 are read out electrically but with no optical input to measure coherent electrical behavior. Thus, 64 of 73 available pixels are instrumented in each HPD. The

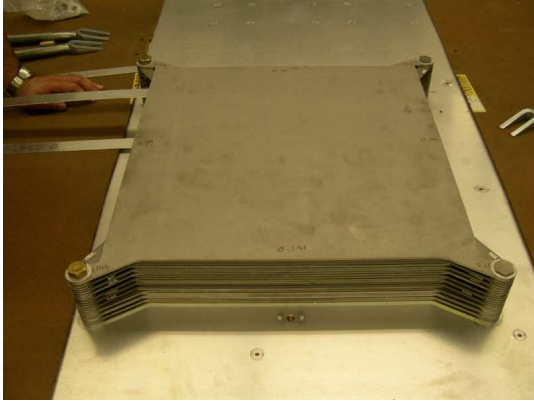


Fig. 2.5 CREAM calorimeter tungsten plates stacked for a fit check, before mounting of scintillating fibers and light tightening.

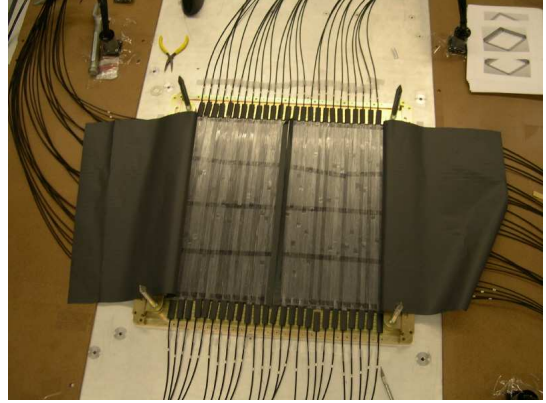


Fig. 2.6 Installation of calorimeter scintillating fiber layer.

splitting of the ribbon fibers into 3 groups allows for readout of 3 different gain ranges using ~ 11 bit ASIC devices.

The CREAM calorimeter requires calibration with a high-energy charged-particle beam every time it is rebuilt. Ideally this would be done with test beams of protons and heavy nuclei, with energies 10^{12} eV to 10^{15} eV. Unfortunately, these beams are unavailable in terrestrial accelerators, so lower-energy beams of electrons, pions, protons and heavy nuclei must be used to calibrate the lower-energy response on a ribbon-by-ribbon basis. Additionally, simulations are used for extension to higher energies, as well as gain-stitching between low-, medium- and high-signal readouts using flight data. Simulations suggest that the calorimeter response should be very linear with energy [7], and the resolution should be nearly constant with energy. Thus the energy of the primary can be measured by summing the total energy deposit in the calorimeter, and using the transformation measured from the particle beam calibration and predicted from simulations. The typical fraction of primary energy deposited in the calorimeter is 0.15%. The overall energy resolution is $\sim 50\%$.

Tracking of the shower core is possible by finding the center of distribution of hit ribbons in each layer, and fitting over multiple layers. This is useful for projecting back to the SCD for selection of the primary hit area (to exclude albedo hits). Also, in CREAM I there were two dedicated tracking hodoscopes located above the calorimeter (S0/S1 and S2). The S0/S1 hodoscope consisted of 4 crossed layers of scintillating fiber, while S2 had two crossed layers. S0/S1 was located above the upper carbon target, below the SCD. It provided redundant charge measurement, and tracking. S2 was located between the targets and provided tracking and a measurement of whether the primary had interacted in the top target. Both S0/S1 and S2 were read out with the same type HPD devices used for the calorimeter readout. The S3 paddle was positioned between the bottom target and the top of the CAL, and was also used for shower sensing. As discussed above

in the TCD section it was instrumented into the TCD system, and also served a TOF function.

2.2.6 Ballooncraft

The CREAM ballooncraft contains various subsystems that support the science portion of the payload (Figure 2.7). The science portion of the payload is surrounded by insulation for thermal control, and many sub-systems of the payload are equipped with temperature sensors and heaters that are controlled by the ballooncraft systems. A radiator system is also installed to dump excess heat. Housekeeping of the entire vehicle, commanding and science data return are all performed by the Command Data Module (CDM) which is mounted on the underside of the CREAM payload. Various antennas for receiving and transmitting are also mounted on the detector, including a NASA Tracking and Data Relay Satellite System (TDRSS) link. The CREAM payload is also oriented with a rotator which is positioned between the payload and the balloon to maintain proper pointing of the solar panels and radiators.

2.3 The CREAM Payloads and Flights

CREAM has had four flights (Table 2.1), all launched from Williams Field located near McMurdo Station in Antarctica. The CREAM I payload flew during the 2004-2005 Antarctic summer campaign, and had a flight duration of just under 42 days and 3 circumnavigations of the South Pole (Figure 2.8). As of this writing this is still the record for longest NASA LDB science flight. A longer ULDB engineering flight was conducted in the 2008-2009 season.

<i>Payload</i>	<i>Antarctic Season</i>	<i>Flight Duration (Days)</i>	<i>Instrumentation</i>
CREAM I	2004-2005	~ 42	TCD+TRD+CD+SCD+CAL
CREAM II	2005-2006	~ 28	TCD+CD+SCD+CAL
CREAM III	2007-2008	~ 28	TCD+CD+CherCam+SCD+CAL
CREAM IV	2008-2009	~ 19	TCD+CD+CherCam+SCD+CAL

Table 2.1 The flights of the CREAM experiment to-date.

The CREAM I payload consisted of all detectors shown above. Later flights differed somewhat, however. The TRD was only flown on the first flight. A second layer of SCD was added for the second and all later flights. In the third and fourth flight, a proximity-focused Cherenkov imager (CherCam) [56] was also flown, but will not be discussed here. The calorimeter, TCD, CD, SCD and S3 detectors were all largely similar over the flights, with refurbishment and some design refinements.

The calorimeter in the CREAM II payload was very similar to the CREAM I calorimeter and was built to be a functional copy. The CREAM II payload flew in the

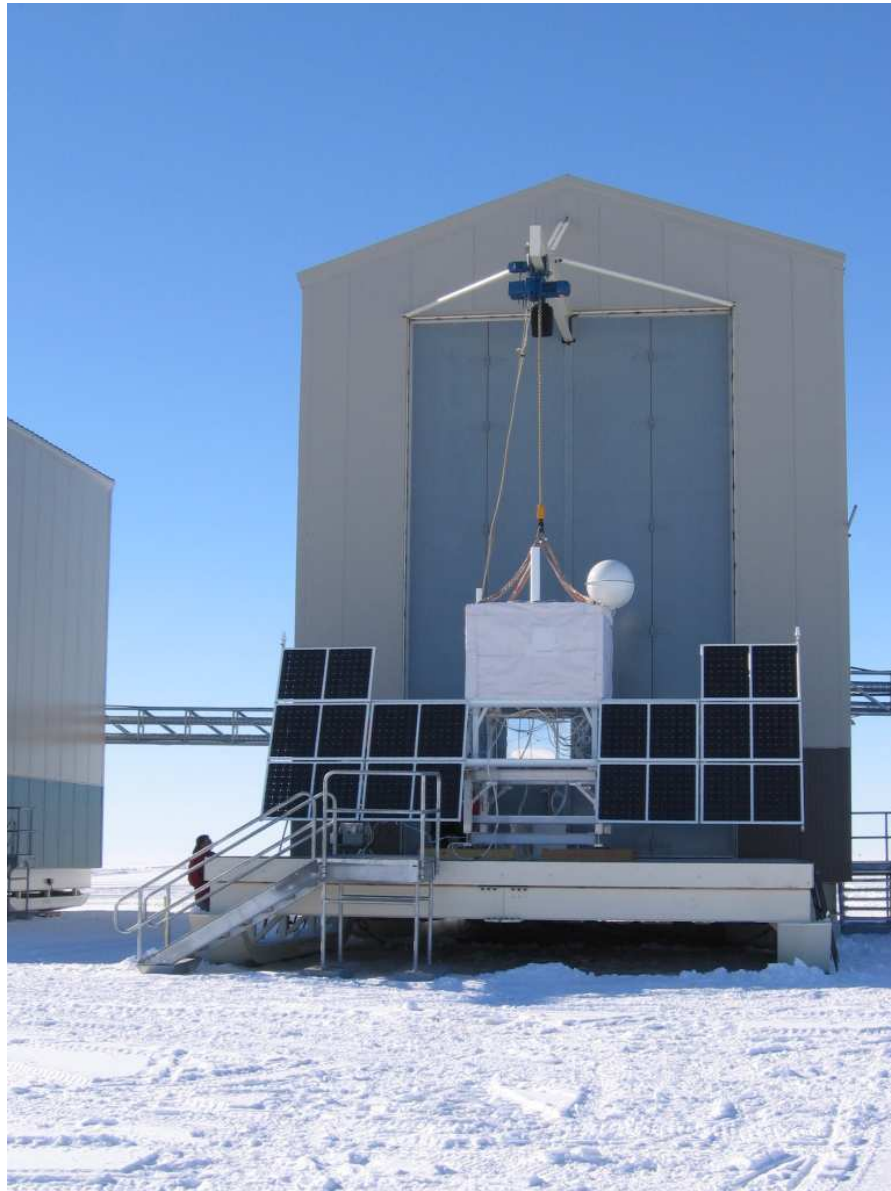


Fig. 2.7 The CREAM II payload during flight readiness preparations in Antarctica (December 2005). The spherical antenna on top of the payload is the TDRSS antenna housing. The CDM is the reflective box in the lower-middle portion of the payload.

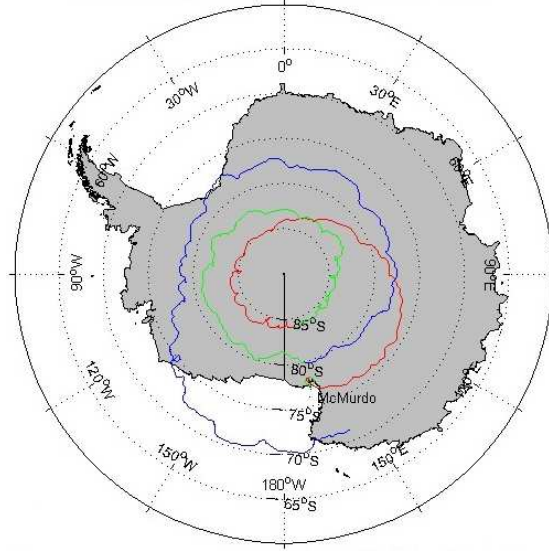


Fig. 2.8 CREAM I ~ 42 day flight trajectory, originally from Columbia Scientific Balloon Facility (CSBF) tracking (currently at [9]). Different colors are for successive polar orbits (red first, green second, blue third).

2005-2006 Antarctic summer campaign season, and had an approximately 28 day flight with 2 orbits around the continent.

The third flight of CREAM took place in the 2007-2008 Antarctic flight season, with a duration also of 28 days. In this flight the calorimeter, SCD and CherCam all functioned properly, but the TCD and CD both failed early in the flight. As mentioned in Section 2.2.1, the TCD has two basic trigger modes: TCD+S3 for events in the CAL geometry and TCD+CD for high Z events. Unfortunately high-voltage breakdown occurred for components in the S3 PMT power system (PMTs, HV cabling and potted power supplies), and in one of the two HV systems (4 of 8 PMTs affected). Additionally, the CD pulse-shaping board which couples the PMT signals into the modified TCD readout box and generates a \overline{VETO} logic for the TCD trigger to exclude low-energy cosmic rays also suffered a failure. All systems were checked out immediately before flight and manifested themselves as soon as the instrument was powered up at float altitude. The consensus after a failure review was that the HV Reynolds cable [57] used to carry the high-voltage current to PMTs in both subsystems probably had been damaged before launch and suffered outgassing once at float altitude. When the CREAM III payload was shipped from the University of Maryland to NASA-Wallops Flight Facility for payload integration, an accident occurred when the instrument became unsecured in the back of the semi trailer transporting it, and suffered damage from slamming into the inside of the trailer when the truck had to make a hard stop to avoid another vehicle. There is a high likelihood that this accident caused damage to these wires, that was not detected by later visual inspections. For later flights two design changes were made: separate HV

power supplies were introduced for the S3 PMTs to add redundancy, as well as protection diodes to prevent blowing of the CD pulse-shaper board.

CREAM IV flew in the 2008-2009 season, and all subdetectors operated satisfactorily. The S3 PMT power-supply design change implemented after the CREAM III flight did prove very valuable however, since part way throughout the flight one of the S3 PMT systems showed signs of HV breakdown. Since the trigger involves a logical OR of the PMT signals however, the TCD trigger was not affected.

Chapter 3

CREAM TCD Design and Construction

3.1 Detector Description

The TCD is positioned at the very top of the CREAM instrument, sitting directly above the top TRD block (in CREAM I). It completely covers the top of the instrument, and so has a large geometric acceptance. Also, because it is the first detector encountered and is instrumented with a fast readout scheme, it contributes to the overall instrument trigger. To facilitate time-of-flight measurements and limit triggers to events in the geometry of the CREAM Calorimeter, another scintillation detector (S3) was positioned directly above the top plate in the Calorimeter. This also provides a geometrical constraint on the particle trajectories (requires the primary to have hit the calorimeter).

3.2 Design Considerations

The design goal of the TCD is to measure charges of cosmic rays in the CREAM payload, from protons to beyond iron. Single-species charge resolution was desired, as well as good timing characteristics. A major design challenge for the TCD was the presence of albedo particles backscattering from high-energy showers in the calorimeter. The worst case time between arrival of an initial PMT pulse from the primary and the signal from an albedo particle has been shown to be of order 3 ns [10].

There are two main ways to deal with this sort of albedo problem: use very fast electronics to catch the initial PMT pulse and then ignore the albedo signal, or use a very segmented detector with good tracking to pick out only the primary track. The first scheme requires fast electronics, but allows the physical detector to be much simpler than in the second case. This is the scheme which was selected for the CREAM TCD.

Plastic scintillator paddles are a very common charge-detector design. The BC-408 [58] plastic scintillator material was chosen for the CREAM TCD. It has a very pronounced light output at a wavelength around 430 nm (well-suited to PMTs), fast time characteristics suitable for TOF measurements and high light output (64% anthracene or about 10000 photons per MeV deposited energy) (see [58] and p.167 of Leo [59]). The Bethe-Bloch equation (Equation A.1) gives a general expression for the energy-loss rate in matter (dE/dx). For singly-charged species such as protons above minimum-ionizing energy, $dE/dx \simeq 2 \text{ MeV}(\text{g}/\text{cm}^2)^{-1}$. Here we are using mass thickness (density times thickness) instead of conventional thickness. For BC-408, the material density is $\rho = 1.032 \text{ g}/\text{cm}^3$, and for CREAM we chose to use 0.5 cm-thick scintillator, so that normally incident protons above minimum-ionizing ($\sim 1 \text{ GeV}$) produce ~ 10000 photons.

Of course not all photons generated in the scintillator will reach the end of the paddle to be counted by a PMT. Only photons which are incident on the inside surface of the scintillator with an incident angle less than the critical angle will propagate with total internal reflection. One technique used to increase the light propagation efficiency is to wrap the scintillator and light guides in some sort of specular reflective material to attempt to reflect photons which escape the scintillator back in with a randomized angle. Some percentage of these photons will then be totally internally reflected in the scintillator and eventually reach an end. A simulation was implemented to test the effectiveness of this approach (Chapter 7). While probably only producing a marginal increase in signal size because of the readout scheme implemented in CREAM, the increase in total photon collection efficiency is significant with the specular reflective wrapping.

Also affecting the photon-collection efficiency is the choice of how to couple the scintillator material to the PMTs. If using solid sheets of scintillator (as for the CREAM TCD), generally a light guide is used. One fundamental principle of light guides is that they cannot concentrate the light and at best can only transmit it by total internal reflection down a shape of constant cross-sectional area [59]. The design chosen for the CREAM light guides is a twisted-strip adiabatic design, which also introduces a gradual 90° bend (Figure 3.1). This design is more effective at coupling the light than a simpler ‘fish tail’ design, but is more expensive due to labor costs. The CREAM light guides are made from BC-802 [60] acrylic plastic. This acrylic is UV-absorbing so that Cherenkov light (either produced in the paddle from the passage of the primary particle or from other particles passing through the light guides themselves) is attenuated before reaching the PMTs.

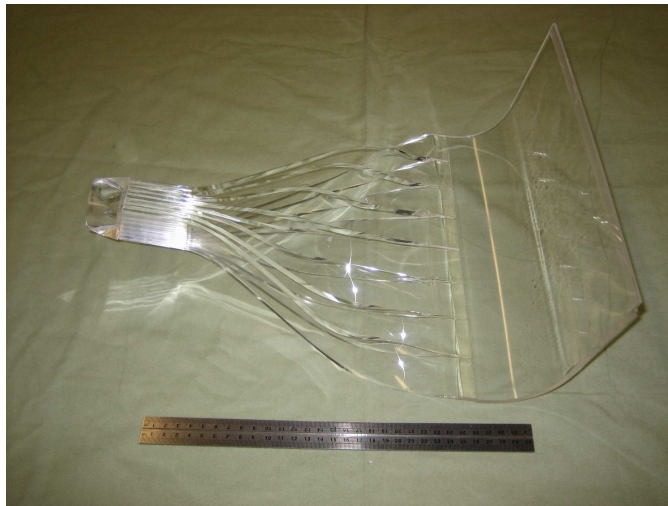


Fig. 3.1 CREAM TCD scintillation paddle light guide made of BC-802 acrylic plastic (from [10]). Each light guide is made from 10 pieces.

The area covered by the TCD is $120 \times 120 \text{ cm}^2$, so scintillators of area $120 \times 30 \text{ cm}^2$ (and 0.5 cm thickness) were chosen to make up the detector. Two layers of paddles at the top of the instrument were made as well, to allow for timing-based tracking in both directions in the plane of the detector, and to improve charge resolution. The cross-sectional area of each end of the scintillators was 15 cm^2 , which matched very well the area of the photocathode of the XP2020 PMT ($\pi(2.2 \text{ cm})^2 = 15.2 \text{ cm}^2$) which was chosen for the TCD. As mentioned above, the light guides in the TCD maintained this cross-sectional area while coupling the scintillator to the PMTs.

3.3 TCD Scintillation Paddles Construction

Each TCD paddle consists of a solid piece of BC-408 plastic scintillator and two twisted-strip adiabatic light guides (Figure 3.2). The end of each paddle and light guide form a simple lap-joint about 1 cm wide down the entire length of the paddle end (30 cm). They are glued together with BC-600 optical cement. The extension of the light guides from the end of the scintillators is $\approx 20 \text{ cm}$, and the light guides overall length below the scintillator is $\approx 35 \text{ cm}$.



Fig. 3.2 Two CREAM TCD scintillation paddles after gluing but before wrapping for light tightness.

Each paddle and light guides are wrapped in crinkled aluminum foil to act as a specular reflector. This way some light that exits the paddle because of too large an angle for total internal reflection is returned to the paddle at a randomized angle. Some fraction of the reflected light will have a new angle consistent with total internal reflection.

After the foil wrapping the paddles are then wrapped in black DuPont Tedlar sheeting for light-tightening. One layer of Tedlar is sufficient to completely light-tighten a detector, however, several layers are wrapped around each paddle in case of accidental nicking and other damage. Adhesive transfer tape (3M brand Y966) and aluminized kapton tape are used for sealing the Tedlar wrapping to the paddles. The transfer tape was used to attach two surfaces of Tedlar to each other.

The light guides couple the scintillators to XP2020 PMTs (one at each end) for fast readout of the light signals. In CREAM I the PMTs were directly glued to the light guide ends with optical RTV (GE RTV615A). This makes removal of the PMTs difficult, so the scheme was modified for later flights. Instead of directly gluing the tubes to the light guides, the tubes were instead glued (again using GE RTV615A) to 2" diameter Lucite cylinders, each 1" in height. Aluminum rings (visible in Figure 3.3 attached to a PMT) were machined such that one could be mounted to the outside of this Lucite cylinder (with set screws) while another was mounted to the light guide. The rings could then be joined with screws. Optical grease was applied between the light guide and the cylinder, and the joint was worked so that no visible air bubbles were present.



Fig. 3.3 Two CREAM TCD XP2020 PMTs being prepared for installation. The tube on the right has been mounted to the PMT active base circuit boards (Chapter 4). The tube on the left has also been potted and grounded to prevent HV breakdown, had a Lucite extender and aluminum mounting ring attached (for coupling to the light guide) and wrapped for light-tightness. Not visible here under the light-tightening are two layers of μ -metal for shielding from the magnetic field of the earth.

The PMTs are potted to prevent HV breakdown (discussed in much more detail later in this chapter) and also wrapped for light-tightness. Light-tightening is again done with the same Tedlar material used for paddle light-tightening. Additionally, two layers

of 0.004 in-thick μ -metal shielding are installed beneath the light-tightening Tedlar to shield the PMTs from the magnetic field of the earth. This is to prevent the PMT performance from being degraded by the magnetic field.

3.4 S3 Detector Construction

The S3 detector (Figure 3.4) consists of $2 \times 2 \text{ mm}^2$ square scintillator fibers (Saint-Gobain BCF-12MC) in a single layer collected into a detector of dimensions $115 \times 52 \text{ cm}^2$. The fibers are collected at each end and attached to a 2 in-diameter Lucite cylinder. The PMTs (the same XP2020 type used in the TCD) are then coupled to the cylinders with a silicone optical cookie in CREAM I. For later flights the same system as used for the TCD PMTs was implemented for mounting, but with the optical cookies still present.

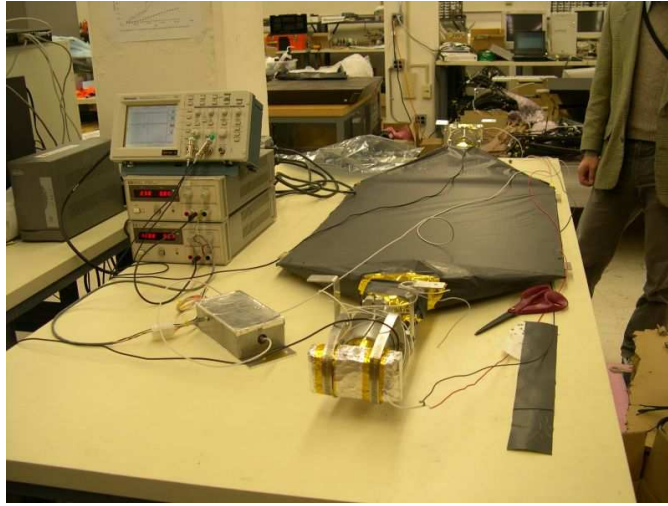


Fig. 3.4 The S3 scintillating fiber detector shown under test. Part of the clamping system is visible which allows for pressure to be applied to press the PMT into the optical coupling cookie (from NASA and University of Maryland Cosmic Ray Physics Laboratory [11]).

The S3 detector is constructed in an aluminum box for structural support and partial light-tightening. It is also wrapped in Tedlar for full light-tightness. The PMTs are secured into position using mounts attached to the aluminum structure. Further PMT support is provided by supports attached to the main instrument pallet. The mounts attached to the S3 structure allow inward pressure to be applied to the PMTs to ensure good optical contact with the coupling cookies.

3.5 TCD Mechanical Support

For the CREAM I instrument, the TCD scintillators were supported directly by the TRD. A 1/8" sheet of Neoprene rubber was positioned over the TRD, and the paddles were placed over this. Four sections of u-channel aluminum were also used to secure the paddles to the top as well, by acting as a clamp to hold the paddles into the rubber. The u-channel sections were run along each side of the TCD, with each overlapping the end of four paddles, over part of the light guide near the scintillator joint.

Four outrigger arms were mounted from the CREAM frame to support the TCD electronics boxes, and also for securing the paddle PMTs and light guides (Figure 3.5). The PMTs were secured around their diameter with a machined plastic support and Teflon cable tie. The bottom of each PMT base was supported with an aluminum sheet metal bracket with a 90° bend. The plastic support was mounted to the aluminum support bracket with screws going through slots for adjustment. There was a piece of open cell foam inserted between the plastic support and the bracket, so the distance could be adjusted for individual fit.

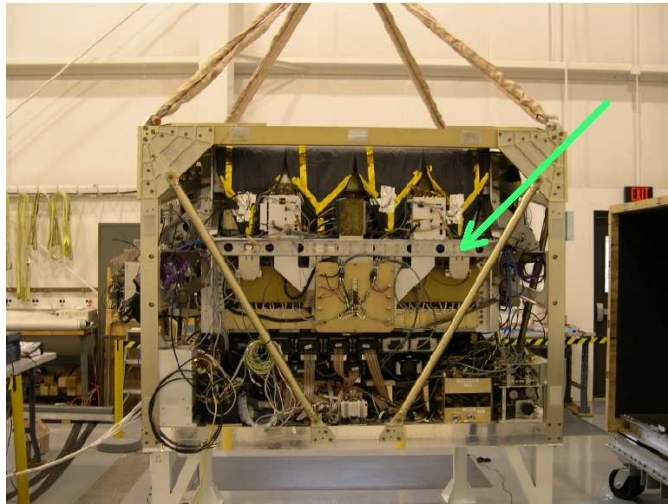


Fig. 3.5 The CREAM I instrument (science only) before integration with ballooncraft components. The TCD support scheme is visible here, including outrigger arms for mounting of TCD electronics boxes and PMT/lightguide support brackets (marked with the green arrow). (From NASA and University of Maryland Cosmic Ray Physics Laboratory [11]).

The lengthwise sections of the outrigger assemblies contain two rows of 1.5" spaced mounting through-holes. All TCD-electronics mounting hardware was designed to have screw spacing in multiples of 1.5", to facilitate flexible electronics attachment.

For CREAM II, no TRD was present, and no other detector was placed directly under the TCD, so an alternate support structure was produced. This support consisted of an aluminum box for the paddles to sit on, which mounts inside the main CREAM frame. The box also provided mounting for the CD, since no TRD was present for mounting that detector either. The same outrigger hardware was used in CREAM II as had been used in CREAM I for mounting electronics boxes.

The naming convention used in the CREAM TCD for PMTs is to count 0-15 for the TCD PMTs, beginning on the left of the +X side of the instrument, and count up counter-clockwise (Figure 3.6). The electronics boxes (also called Concentrators) are labeled in an abbreviated fashion such as Positive X Left = PXL. The TCD-related components mounted on the instrument pallet are shown in Figure 3.7. The PMTs attached to the S3 detector are numbered 16 and 17.

3.6 High-Voltage Potting

All high-voltage circuits in the TCD and S3 systems are potted in Emerson and Cuming Stycast 4640 White [61] potting compound. The potting material was mixed with Catalysis 50, and then degassed by placing the mix under a bell jar and holding at vacuum until the most vigorous outgassing had ceased (on the order of 15 minutes). After the Stycast had been poured into whichever component was being potted, it was again degassed in the same procedure. Typically, potted components were allowed to air cure at room temperature, but the process could also be sped up by placing the items in an oven set to a curing temperature of 50°C . All surfaces were primed before potting with S-11 Clear primer. All high-voltage interconnections between the PMT bases and the Ultravolt [62] high-voltage supplies were done with Type L Reynolds high-voltage coaxial cable.

The Ultravolt supplies were mounted in an aluminum project box and a length of Reynolds cable and a multi-conductor low-voltage cable was soldered to all power and control lines (Figure 3.8). Rubber panel grommets were used to safely feed the wires through the box, then the inside of the box was primed and potted full. Junction boxes were mounted on top of each power-supply box to fan out the high voltages to all tubes (4 tubes in CREAM I, 2 tubes in later flights). Inside each junction box is a circuit board for installation of series gain-matching resistors (if needed) as well as attachment of Reynolds cables for the input and output to all PMTs. Once the wires and matching resistors were installed, the inside of the box was primed and the box was potted.

The PMT-base electronics and PMT leads were potted in a multistage process. The Reynolds cable was soldered to one circuit board, and mechanically secured with Insulcast I-CAST 116 FR epoxy. The other circuit board was soldered to the flying leads of the XP2020 PMTs. All surfaces were primed, and then a layer of stycast was applied to both faces of each circuit board. A cylindrical mold was used to pot around the flying leads of the PMTs. The two circuit boards were mated with GE RTV 162 Silicone rubber sealant for mechanically securing both headers. Finally, the whole assembly was cast in a block of Stycast.

All potted high-voltage units also required having the outer surfaces of the potting to be grounded (Figure 3.3). This was required because while the potting material

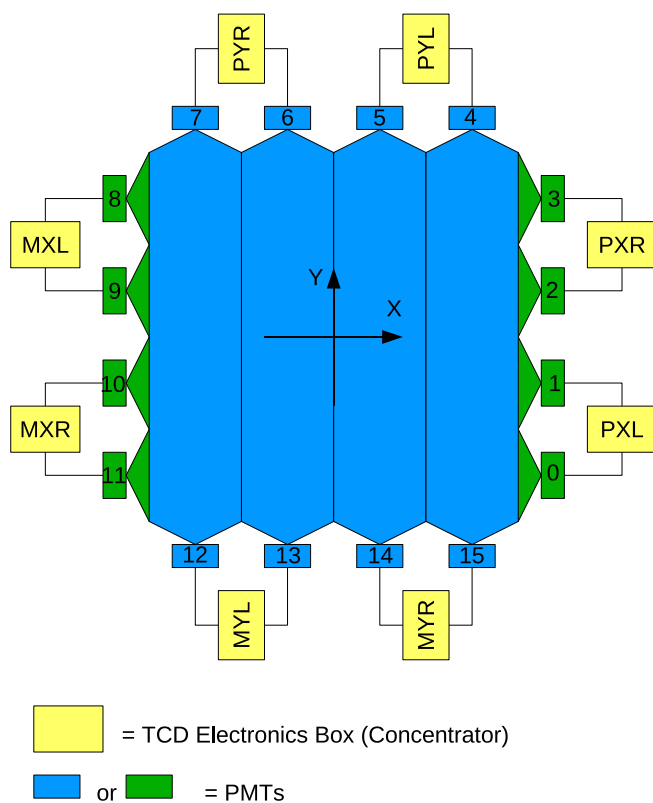


Fig. 3.6 The coordinate system used for the top of the TCD. The X and Y directions are defined for the entire instrument. PMTs are labeled from 0-15. Concentrators control and monitor two PMTs each.

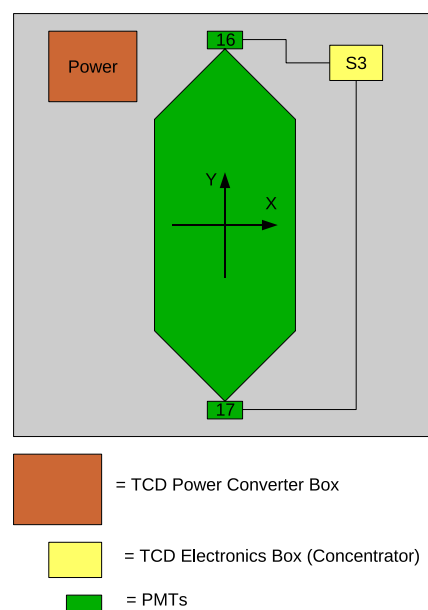


Fig. 3.7 Instrument Pallet-mounted TCD components. The scintillation paddle S3 is shown in green. Also shown is the TCD Power-Converter Box and the TCD Concentrator for S3.

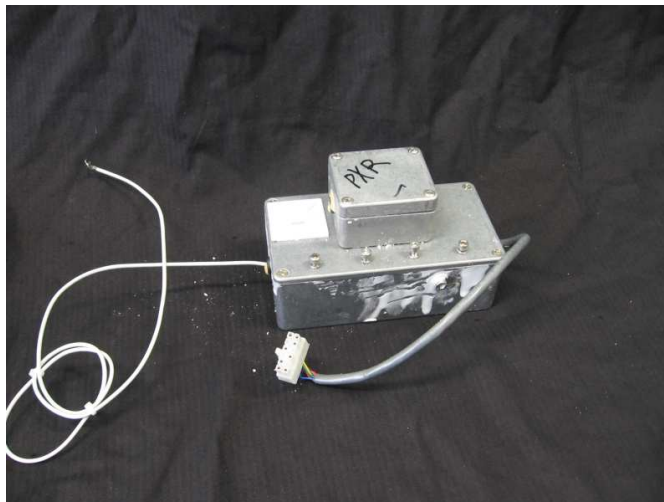


Fig. 3.8 A refurbished Ultravolt high-voltage power supply assembly for CREAM. The actual supply is not visible here, but is potted with Stycast in the larger box. The smaller box is present to split the voltage to power two PMTs (a small circuit board is also present for mounting of series-matching resistors if needed).

prevents dielectric breakdown around whatever was potted, strong electric fields are still present outside of the potting material. This should be obvious from a simple application of Coulomb's law. In fact, when a potted PMT base was tested under a vacuum bell jar, it was readily observed to spark.

The high-voltage supplies and junction boxes were grounded by virtue of being potted into aluminum boxes. The PMT bases were grounded by wrapping the outside of the potting material in Aluminum tape with a conducting adhesive.

3.7 TCD-Electronics Mounting

The TCD-electronics boxes contain 7 circuit boards (with the TCD-Master Trigger box containing two additional boards). The boxes are assembled starting with an aluminum bracket, with threaded taps for hex standoffs to be attached (Figure 3.9). The circuit boards are secured to the standoffs, and each successive board is secured with more standoffs, forming a stack of standoffs, with boards in between.

After all boards have been mounted, another aluminum bracket is mounted to the other end of the stack. Finally, sheet metal covers are mounted to all stack surfaces (Figure 3.10).

Thermal abatement is provided for most components by simple heat conduction through their pins to the ground planes in the multi-layer circuit boards used. The heat then was conducted to the aluminum standoffs used for mounting, to the mounting brackets of the electronics boxes and finally to the outrigger support structure. The outriggers were attached to the instrument frame, which was thermally regulated by



Fig. 3.9 CREAM TCD electronics box (Concentrator). The boards (from bottom to top) are: power board, two peak detector ADC boards, a local trigger board, two TDC boards and the on-board computer board. The computer [12] actually resides in a small daughter-board at the very top of the stack.



Fig. 3.10 CREAM electronics box refurbished and fully assembled. Visible on the top are gold-plated SMA headers from anode and dynode PMT signals. Each box takes input from two adjacent PMTs in the TCD. Also present on the top and side are connections for Ethernet, serial, trigger, event number input, and power input.

the ballooncraft systems. Heat sinking was however required for the on-board computer CPU present in each TCD-electronics box. This was done with a small square of copper plate, with two pieces of 14AWG stranded core wire attached, with both wires then attached to the end bracket. The ends of these wires are visible in the top of Figure 3.9.

3.8 Testing and Validation

Extensive performance and environmental testing was conducted on CREAM before the first flight (and subsequent flights). Performance testing consisted of LED and laser testing of optical readout systems, observation of atmospheric muons and testing of detector components in particle test beams. Some of the particle beam testing was already discussed in Chapter 2. Environmental testing involved several subdetector-level vacuum and thermal-vac tests. Before the first flight, a full-instrument thermal-vac test was undertaken as well, of several days duration. Subsequent vacuum testing of just subdetector components has been deemed appropriate.

TCD environmental testing began with vacuum testing of PMT bases in a bell-jar. This allowed for quick testing of base potting and surface ground techniques. Eventually, a thermal-vac test was conducted at CSBF in Palestine, TX [63] of the TCD paddles with attached PMTs. Unfortunately, the test was of insufficient duration (~ 5 hours) to discover a flaw related to slow outgassing in the high-voltage supplies used in the PMT bases. A detailed discussion of this flaw, and the remedy implemented appear in

Chapter 4. This flaw was eventually discovered during a full-instrument thermal-vacuum test conducted at NASA/Goddard [64] in 2004.



Fig. 3.11 PVC vacuum chamber for PMT/HV testing at Penn State. The chamber consists of a center section of PVC sewer pipe, with end-caps. The center section has been light-tightened with a layer of Tedlar and electrical tape. One end-cap contains piping for the vacuum pump and venting, the other contains BNC electrical feed-throughs (neither end-cap shown).

After the experiences from the first flight, it became apparent that longer-term vacuum testing of the TCD PMTs and high-voltage supplies was necessary, at least of order a week. To facilitate this, an in-house vacuum chamber was constructed using PVC components (Figure 3.11). One endplate of this chamber has BNC connector feed-throughs for monitoring signals for PMTs under test, and also for feeding in the low-voltage supply and control signals for the Ultravolt high-voltage supplies. The other endplate contains valves and piping attachments for a vacuum pump, venting of the chamber and attachment of a vacuum gauge. This vacuum chamber with its endcaps properly tightened can maintain a vacuum with a leakage rate of order ~ 1 torr/hour. This is completely sufficient for our operating needs since the instrument operates in flight at an atmospheric pressure of between 4 – 10 torr. Occasional pump-downs are necessary, either manually or by placing the vacuum pump on a 24 hour timer.

The thermal design of the TCD electronics was evaluated by operating the circuit boards (with thermocouples attached to various high-dissipation components) under a bell jar. All components except the uCdim CPU were found to be sufficiently heat-sunk by their pins conducting heat to the internal ground plane inside their circuit boards. The uCdim CPU has power dissipation of order a few watts, and is not sufficiently connected to a ground plane, and so did require heat sinking as discussed above.

TCD-performance evaluation consisted of both using light sources (LEDs and lasers) for testing of PMTs and paddles, as well as testing with particle beams and atmospheric cosmic-ray muons. Testing with LEDs and a fast UV nitrogen-pulsed laser permitted evaluation of PMTs both stand-alone and integrated into paddles. This was necessary since muons would only produce signals on scale for the anode and first two dynodes of the PMTs. In order to verify the operation and gain relationships between all PMT taps, larger light signals were needed from the LEDs or laser. The LEDs (driven with a fast pulse generator) were useful for direct illumination of the PMTs, while the UV laser was necessary for exciting the wavelength-shifter dye in the scintillation paddles and producing large light signals to mimic heavier-charged species. To facilitate rough gain matching between PMTs, a mountable LED fixture was produced (Figure 3.12). The performance of the TCD sub-system was also evaluated in a particle beam in 2003 at CERN [10] using prototype components, and is discussed further in Chapter 4.

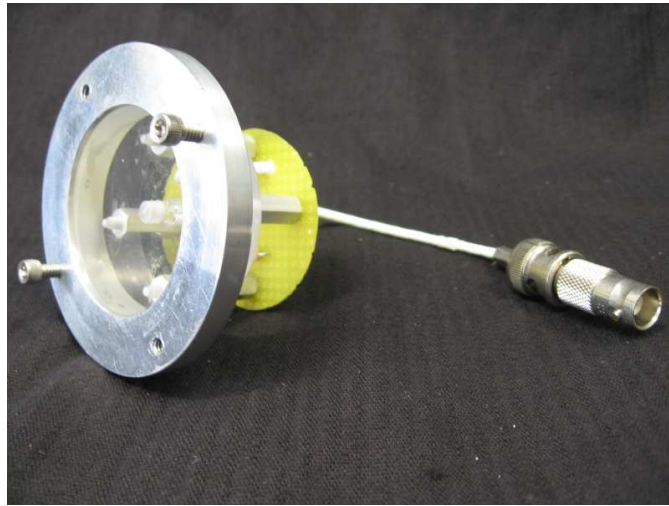


Fig. 3.12 Blue LED in a fixture for consistent mounting on CREAM TCD PMTs. This allowed for performance gain matching between PMTs so they could be grouped into pairs needing similar HV supply. This fixture contains a circuit board with a resistor for current limitation, blue LED, and BNC input for attachment to a fast-pulse generator. The fixture uses the standard PMT-mounting ring used in CREAM II and subsequent flights.

Chapter 4

TCD Electronics

4.1 TCD Low-Voltage Power Systems

Low voltage for the TCD system is supplied from the TCD power-converter box mounted on the instrument pallet. Each voltage is provided by a circuit board consisting of an industrial grade Vicor [65] DC-DC converter module and a Vicor ripple-attenuation module (Figure 4.1). The input to each board also contains a resettable fuse and an LC filter. Six supplies are present in the power-converter box to provide the following voltages for the TCD electronics: 12V, +5V(Analog), +5V(Digital), -5V, +3.3V and -2V.

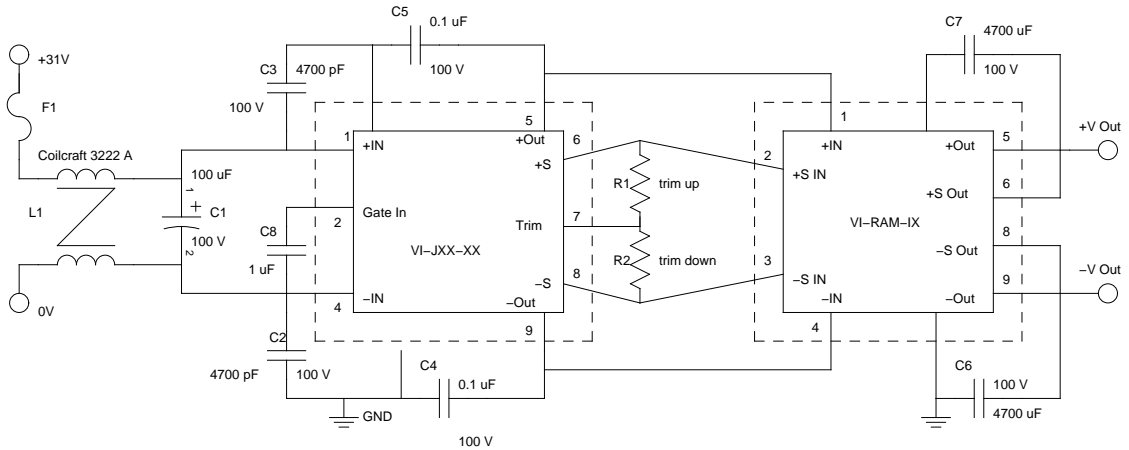


Fig. 4.1 Schematic of one TCD power-converter circuit (6 Total). The fuse is a resettable surface-mount type. Table 4.1 lists the modules used for the different supplies.

Input to the TCD power-converter box comes from the Command Data Module and is nominally 31V. It is supplied via two circuits due to current limitations of individual supply lines. Molex Mini-Fit Sr connectors and 12 AWG wire are used for all input and output to the power-converter box due to high-current requirements for some of the low-voltage lines. Two power fan-out boards are located on upper-instrument outrigger arms in between TCD electronics boxes on the + and - Y sides (see Figure 3.6 for coordinate system explanation). The fan-out boards are each supplied with power directly from the power-converter box. Each fan-out board has a total of six 12 pin

<i>Voltage (V)</i>	<i>Vicor DC-DC Converter Module</i>	<i>Ripple Attenuation Module (RAM)</i>
+12	VI-JW1-IY	VI-RAM-I1
+5 analog	VI-JW0-IY	VI-RAM-I1
+5 digital	VI-JW0-IZ	VI-RAM-I1
-5	VI-JW0-IY	VI-RAM-I2
+3.3	VI-JWY-IZ	none
-2	VI-JWZ-IY	none

Table 4.1 Vicor modules used in the CREAM TCD power-converter box.

Molex Mini-Fit Jr headers present to supply power to the individual TCD electronics boxes. Additionally, +5 volts is provided on a dedicated two-conductor wire for two Ethernet switches used in TCD networking.

In the CREAM I instrument, 8 TCD electronics boxes plus one box for the S3 detector were powered, with the unused Mini-Fit Jr plug used for sending TCD voltages to the science housekeeping system. In later flights a modified TCD electronics box was added to read out the Cherenkov Detector previously read out by the TRD electronics. For CREAM II and III, one of the cables supplying one of the TCD electronics boxes was modified to add power taps to send to the housekeeping system. For CREAM IV, a box was added next to one of the TCD electronics boxes which acted as a pass-through for the power for the adjacent box, as well as providing an interface for other TCD housekeeping functions such as temperature and HV monitoring.

4.2 TCD HV System

4.2.1 CREAM I

The original scheme for PMT high voltage in CREAM I involved a totally on-board design. Small EMCO C40 [66] potted switching power supplies were mounted in each PMT base assembly on the outer-most circuit board. This seemed to be an ideal solution for this application, since no routing of high voltage was necessary on cables, and all high voltage was contained in each potted PMT base. Initial vacuum testing (~ 1 hour) showed no issues, both under a bell-jar and in a TCD paddle thermal-vacuum test (~ 5 hours) conducted at the CSBF facility in Palestine, TX.

After instrument integration and prior to shipment to Antarctica a full thermal-vacuum test was conducted at NASA Goddard of the science component of the payload. After ~ 12 hours there was a TCD PMT failure involving a short-circuit condition in the 12V supply whenever the failed tube HV was dialed up. The decision was made to continue the test after the installation of resettable fuses in the 12V line of each TCD PMT. More PMT failures occurred, and by the end of the several day test, more than half the TCD PMTs had become inoperable in vacuum.

Oddly some of the PMTs would become operable again after some time at atmospheric pressure. After some testing it was determined that the EMCO potted power

supplies where failing at low pressure. Insufficient time was available to try to determine a fix involving the EMCO supplies, and instead a method was implemented using Ultravolt supplies of a type already used in the TRD systems.

In the high-voltage scheme used in CREAM I the four TCD PMTs on each side of the instrument are controlled by a single Ultravolt potted power supply (model 4A12-P4-F)[62]. The same type power supply is used for the two S3 PMTs. The TCD PMTs were deployed in such a way that all four on each side of the instrument are roughly gain-matched. Further gain-matching is accomplished with series resistors.

The Ultravolt supplies are a switching type supply with a DC supply voltage of 12V, with the output high-voltage set by a low-voltage control level. The rated output of this model is 4000V at 4W, with the control voltage ranging from 0-5V. The 12 V power was obtained from the local power distribution board located in each concentrator electronics stack. The control voltage was set in a Digital-to-Analog Converter (DAC) located on the TDC boards in each concentrator stack.

Each Ultravolt supply is potted in an aluminum box, with the board containing the matching series resistors potted in a separate box. The boxes and PMT voltage dividers are all potted with Emerson and Cuming Stycast 4640 White [61] material. Extensive vacuum testing was performed for each circuit prior to flight, resulting in no failures due to operation in a near vacuum at float altitudes. High-voltage vacuum-safe Reynolds [57] coaxial cable (Type L) is used for all interconnections.

4.2.2 CREAM II and Beyond

For CREAM II and subsequent flights, two HV supplies were installed per side of the instrument, instead of one as in CREAM I. This increased the fault tolerance because a HV power module failure would just bring down two PMTs, instead of 4. Also, gain-matching sets of tubes was simplified to matching 2, instead of 4.

The same boxes were used for the Ultravolt supplies, but a slightly smaller box was used to contain the series matching resistors, because just 2 tubes were being used per supply instead of 4. The same potting material was used, as was the same type high-voltage cable.

After the failure on the CREAM III flight of the high-voltage system for S3, a second Ultravolt supply was added for the CREAM IV flight. In this scheme, each S3 PMT has a dedicated Ultravolt supply, thus removing a single-point failure from one of the two possible TCD trigger modes. This proved to be advantageous, because on the CREAM IV flight one of the S3 PMT high-voltage systems did develop a breakdown problem part way through the flight.

4.3 Photomultiplier Tubes and Electronics

4.3.1 Photomultiplier Tubes

The Photonis XP-2020 [67] is a 12 stage 2 inch diameter fast-response phototube. The tubes exhibit desirable gain and linearity properties which make them well-suited to this application [67]. Typical operating voltages for the XP-2020/URFL (ultra-fast, flying lead) range between 2.2 and 3.2kV, with gains of between 1.2×10^5 to 1×10^7 .

For CREAM I, XP-2020/URFL phototubes were used which are special down-selects of the normal XP2020 production. They have a higher gain (because of a higher maximum voltage rating) than the normal production XP-2020. S3 also used XP-2020/URFL tubes in CREAM I.

For CREAM II normal XP-2020 tubes were used because the preliminary look at the CREAM I performance suggested the normal model tubes were sufficient. Also, procurement times for the UR tubes proved prohibitive given the tight production schedule. This choice proved largely satisfactory but not entirely. A few of the tubes used had to be run at maximum rated voltage to position the charge-one peak (muons at the ground) nicely on scale above pedestal.

4.3.2 Phototube-Base Electronics

The base electronics that powers and reads out the CREAM phototubes is unusual in both its method of supplying voltage and in the readout scheme. The driving considerations were a very low-power base circuit, but one with very good stability and many dynode taps for extended dynamic range.

Most typical photomultiplier-tube base-circuit designs utilize a relatively stiff voltage-divider chain of resistors to provide the stepped high voltage to the phototube dynodes. So called ‘bucket capacitors’ are also present at most dynode taps to provide a charge reservoir, so the voltage remains stable when there is a signal in the phototube. This circuit is very simple and is a good solution if sufficient power is available. The voltage divider requires a large quiescent current to remain stable however, so if low-power consumption is a consideration, this topology is less than ideal.

Simply raising the values of the resistors in the voltage divider will not work because, as the value of the current required to recharge each stage gets close to the quiescent current in the divider, the voltage at each stage becomes much less stable. The linearity of the tube response is then severely compromised.

An alternate photomultiplier-tube base design that was utilized in CREAM is the active-base design (Figure 4.2). The voltage divider is still present but has a much lower quiescent current. The main difference is that the divider is now only a voltage reference and does not supply the charge to each stage. This allows for significant power savings from a conventional-base design (without sacrificing stability). The voltage stepping of the divider chain was a compromise between maximum tube gain, linearity, timing and dynamic range. Stepping which maximized anode gain proved to be unstable in the deeper dynodes for example.

Current for each stage of the phototube is supplied through transistors operated as followers (NPN transistor Q1 in Figure 4.3). In this scheme the large quiescent current needed in a conventional PMT base is not an issue, because the current for supplying charge to the PMT does not come through the voltage-divider chain. The series diodes between the base and emitter of each transistor are present to keep the base from becoming more than $\approx 3V$ higher than the emitter. Such a condition will cause a large inrush current and damage the transistors.

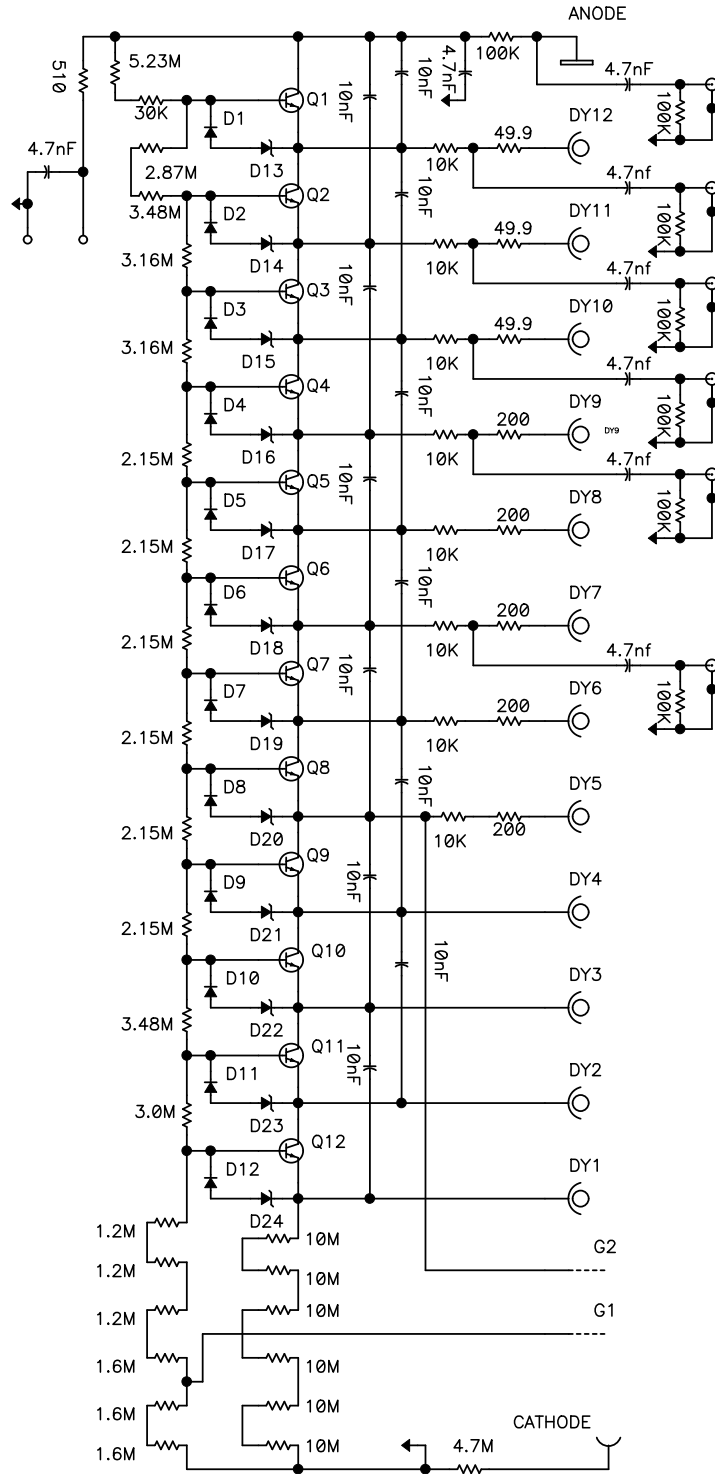


Fig. 4.2 Full schematic of the CREAM TCD PMT-base circuit. All transistors are Zetex FMMT458 NPN type, D1-12 are DL4148 diodes and D13-24 are 2.3V zener diodes. Signal taps are shown by circles. The XP-2020 PMT anode, dynodes (DY1-12), grids, and cathode are shown as well. High-voltage input is at the left-hand side. [10]

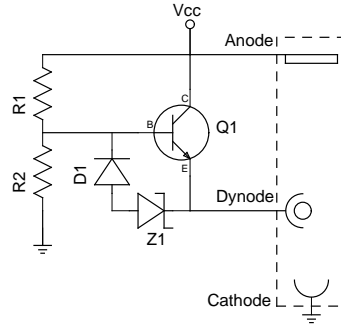


Fig. 4.3 Simplified schematic of one stage of the PMT-base circuit. R1 and R2 are a voltage-divider to provide some wanted division of V_{cc} . Q1 acts as a follower and presents a voltage set by R1 and R2, but sinks current through its collector, thus not loading the voltage-divider chain.

The other very unusual feature of the CREAM active base is the large number of signal taps (six total, the PMT anode and 5 dynodes). There are this many taps present to extend the dynamic range of the signals which can be read out.

Photomultiplier-tube dynamic range is typically limited by saturation. Saturation is simply the limit of the tube to amplify the signal further because of the finite charge available. The tube-output signal stops increasing for larger input-light signals. There is, however, a way out of this limitation. The important thing to remember is that the anode of the phototube is the first to saturate. Next is the dynode closest to the anode, and so on. If one can tap signals out of deeper dynodes (without disrupting the circuit) the dynamic range can be greatly increased. A detailed discussion of the relative gains between taps and the species on scale for each will appear in the next section.

4.4 Readout Electronics

The CREAM TCD readout electronics consists of Time-to-Digital Converters (TDCs) for triggering, time-of-flight (TOF) and leading-edge pulse slope measurement as well as Peak Detector type Analog-to-Digital Converters (ADCs) for pulse-height measurement (Figure 4.4). By instrumenting the anode and 5 dynodes, a very wide dynamic range is achieved. In the CREAM TCD, the anode and second-highest gain dynode are instrumented with two TDCs each (for a total of 4), and each remaining dynode is instrumented with one ADC each (Table 4.2).

The overall readout scheme for one PMT is shown in Figure 4.5. Each TCD electronics-readout box (concentrator) is instrumented to read two tubes, with the two readouts sharing a local trigger board and a local computer board (concentrator). The function of each board is discussed in the following sections.

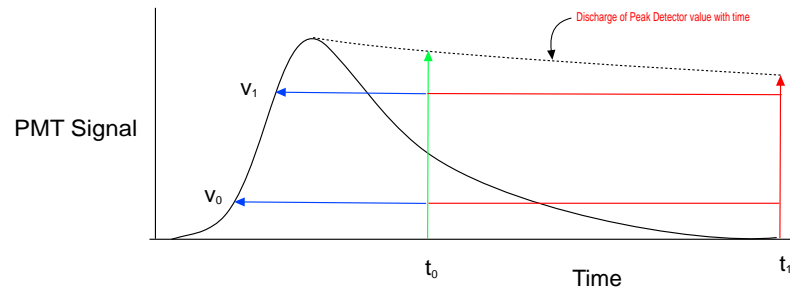


Fig. 4.4 Sketch of a PMT pulse showing the TDC and ADC readout. v_0 and v_1 are threshold voltages for the TDCs to begin timing, and t_0 and t_1 are two different common stop times. The TDC readout is the length of time from threshold crossing until the common stop, the ADC readout is the voltage stored in the peak detector at the time of the common stop. Note the discharge of the Peak Detector circuit is important if common stop times are substantially different.

<i>CREAM PMT Readout Electronics</i>			
<i>PMT Signal</i>	<i>Readout</i>	<i>Gain Relative to Anode</i>	<i>Typical species on scale</i>
Anode	TDC 0 and 1	1	H and He
D12	ADC 0	~ 0.67	H and He
D11	TDC 2 and 3	~ 0.21	He and above
D10	ADC 1	~ 0.14	above He, CNO
D9	ADC 2	~ 0.028	Ne, Mg, Si
D7	ADC 3	~ 0.015	Si and beyond

Table 4.2 Assignment of PMT signal taps to readout electronics.

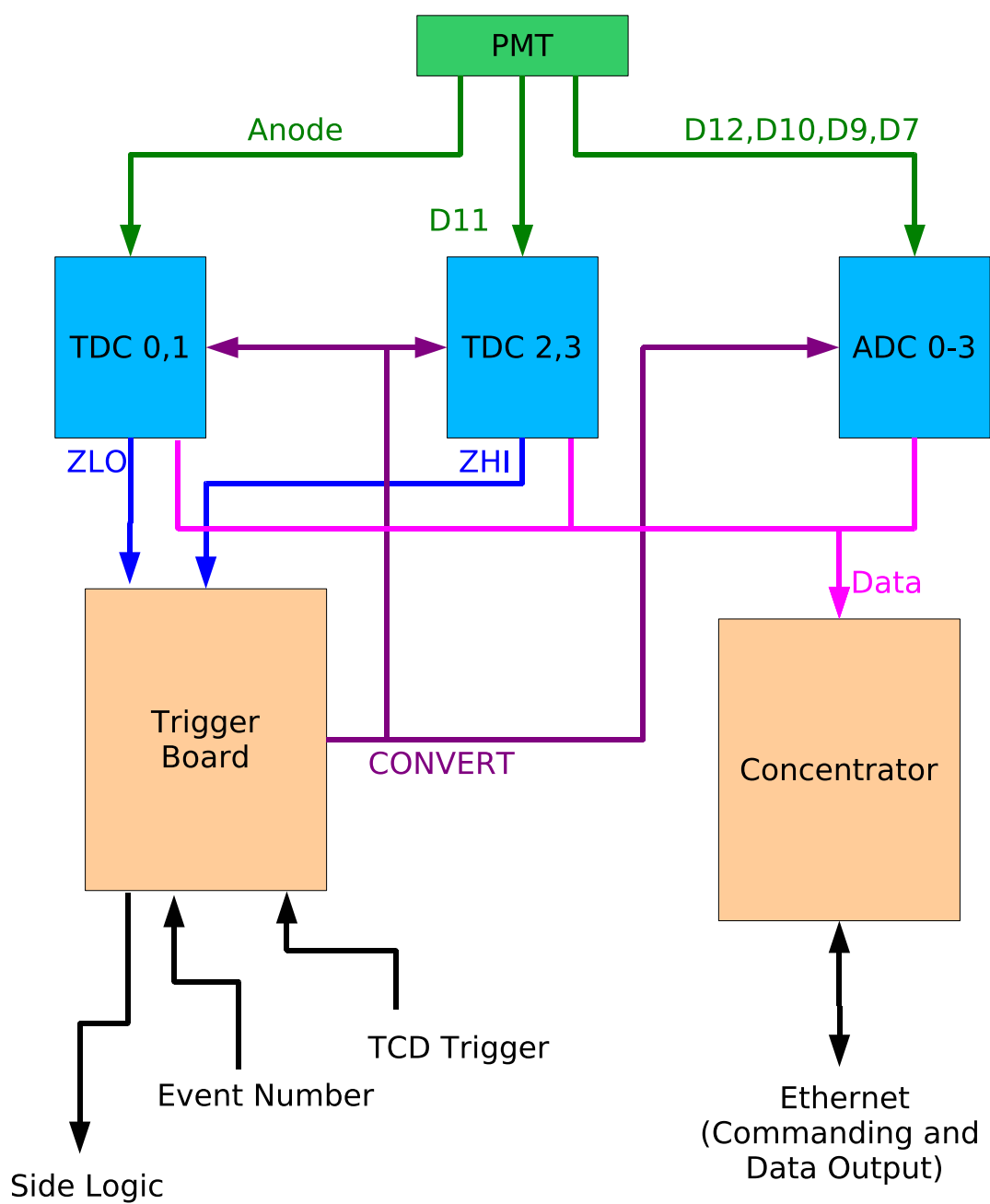


Fig. 4.5 Overview of the readout for one PMT.

4.4.1 Time to Digital Converters (TDCs)

The anode and second-highest gain dynode (D11) are each instrumented with two fast time-to-digital converters (TDCs), for a total of 4 TDC channels per tube. Each TDC measures the time that elapses between the PMT signal crossing a preset voltage threshold and a common stop signal sent to all TCD electronics with a precision of 50 ps. The TDCs have several important functions in the TCD: contributing to the instrument trigger, time-of-flight measurement between the TCD and S3 scintillators, paddle end-to-end timing for position measurement, and potentially leading-edge slope measurement.

When the PMT signal crosses a preset voltage threshold, a fast comparator (U1, Figure 4.6) turns on and clocks in a fast emitter-coupled logic type flip-flop (U2, Figure 4.6). This sets off the charging of a capacitor (C1, Figure 4.6), which continues to charge until either the common stop is received, or a timeout condition is reached and the TDC auto-clears. Capacitors Q2 and Q3 provide a temperature-compensated current source for C1. The common stop is received from the TCD master trigger if the desired trigger conditions are met. In this case the TIME value is held until it is digitized by an AD7854L ADC chip, and the value is sent across the local concentrator bus to the local concentrator processor.

An auto-clear signal will be generated in the TCD circuit itself if the capacitor charge reaches a certain value (LEVEL) and causes a comparator to initiate the auto-clear process. It is also possible for the concentrator electronics to reset the TDC.

By subtracting the average TDC values for both S3 PMTs from the average of both TDC values (all for one threshold) in one paddle in the TCD, we can get a rough measure of the time-of-flight for particles in the instrument (Section 5.4). This is sufficient for rough discrimination between downward-going particles (cosmic rays) and upward-going albedo particles.

By subtracting the TDC values (of the same threshold) for tubes at either end of a hit paddle, the hit location of the particle can be measured. This end-to-end timing is related in a very linear way to hit position (Section 5.6). The TCD position measurement can be calibrated off of the very high accuracy TRD-derived position measurement, and then used as tracking for events which did not produce a good TRD track (such as low-charge events).

By comparing a GEANT4-based optical simulation (Chapter 7) of a CREAM paddle to the measured residual of the end-to-end timing position and TRD position, an estimate of the TDC time resolution is possible. From the residual measure, a combined resolution of $\sigma = 410$ ps (Section 5.6) is estimated. From the optical simulation (Section 7.6), the resolution purely due to photon propagation is estimated to be $\sigma_{paddle} = 280$ ps. Since Gaussian distributions add in quadrature, we estimate the TDC electronics resolution to be $\sigma_{TDC} = 300$ ps for both tubes combined, or $\sigma_{tube} = 210$ ps for a single TDC on a single tube.

The crossing of TDC thresholds also contributes to trigger formation. A ZLO level is generated whenever TDC *threshold* 0 is crossed and a ZHI is generated whenever *threshold* 2 is crossed (Figure 4.5). Appropriate adjustment of *thresholds* 0 and 2 allows for a rough trigger selection of different species.

Fig. 4.6 Schematic of one TDC circuit

Another function which the TDCs were intended to fill was discrimination between H and higher-charge species. This technique was to use the timing difference between different threshold TDCs on one tube to measure the slew rate of the PMT pulse. The slew rate of the PMT pulse is steeper for larger pulses, and thus should be useable as a charge measure [68]. Performance of the CREAM TDCs was mixed at best and is discussed in Sections 6.7 and 7.9.

4.4.2 Peak Detectors

Four different dynode taps of each PMT are instrumented with fast analog peak-detector type ADCs. The peak-detector circuit's function is to simply measure the peak value that a PMT signal reaches in a given time frame. The circuit holds the highest signal level reached at its input since the last time it was reset. Readout is initiated when the trigger system sends a CONVERT signal, and is typically ~ 75 ns after the initial TDC threshold is crossed. The decay time of the peak-detector voltage holding is $\sim 50 \mu\text{s}$, which is much larger than the trigger + readout time of $\sim 1 \mu\text{s}$.

The peak-detector readout is not faster than the arrival time for albedo particles. However, since the albedo particles are all singly-charged, this is not a huge concern, as long as timing can be used for correct differentiation between cosmic-ray and albedo hits. The presence of an albedo background will contribute to some broadening of the Hydrogen distribution and some misidentification as Helium events (see Chapter 6), but the distribution for Hydrogen is rather wide anyway because of the large Landau fluctuations in the scintillator.

The peak detector circuit (Figure 4.7) operates by providing a charging path for a capacitor (C1) whenever the input voltage is higher than the stored voltage already on the capacitor. The dual diode (D1) allows the capacitor to charge, but does not allow it to discharge. A dual transistor package (Q1) provides two matched N-Channel JFET devices to prevent leakage current from inputs of the op-amp (U1-B) from charging the capacitor. The circuit is reset by an ADG417 switch, after either a readout, or a self-clear in the TCD electronics. The ADG417 has extremely low charge injection ($\sim 10pC$) so the capacitor is reset to typically 10 mV or less.

A DC pedestal is applied to all ADC channels, producing a pedestal of approximately 425 channels in the readout. This is to ensure that all pedestals from component and temperature variations are positive, and thus on scale for the digitization section. Readout of the peak value is done by AD7854L ADC chips (the same type used in the TDC readout).

Again, the approximate gain ranges for the different ADC ranges are shown in Table 4.2. Prototype TCD paddles and electronics were tested at CERN before the first flight and the ADCs displayed excellent readout characteristics (Figure 4.8) [10]. This figure is constructed from the averaged ADC0 and ADC2 readouts from 3 PMTs operated on two crossed TCD paddles (the fourth PMT was non-functional). The test beam used here was a fragment beam from 158 GeV/n indium nuclei. The 'No Data' gap is present because ADC1 was not used in the stitching of ADC gain ranges. The ADCs have a combined dynamic range extending from $Z=1$ to well past iron, with charge resolution $\simeq 0.2e$ for oxygen and $\simeq 0.35e$ for iron.

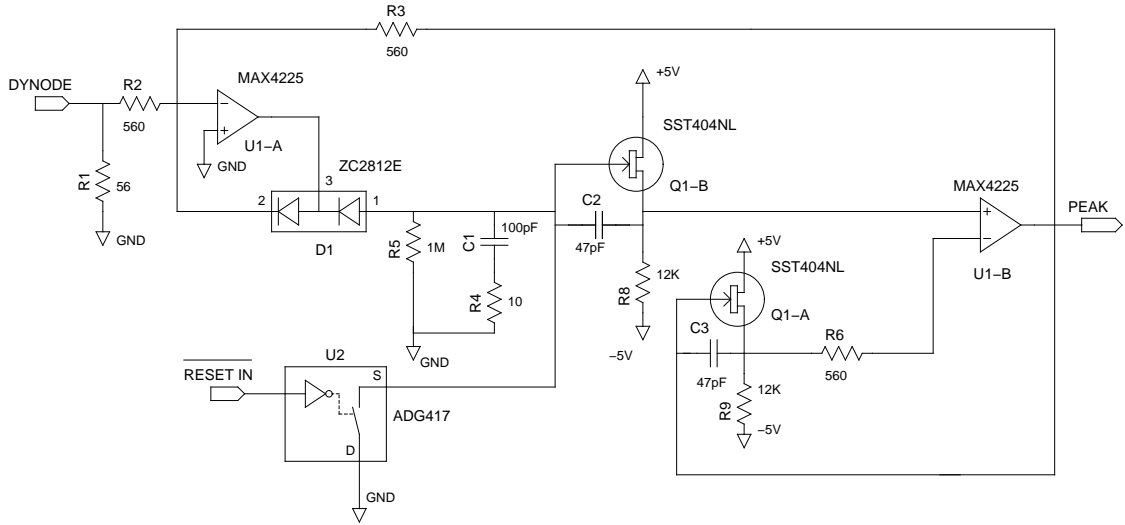


Fig. 4.7 Schematic of one Peak Detector circuit. The DYNODE input comes from the PMT-base circuit and the PEAK level goes to the ADC section. RESET IN is to clear the peak-detector circuit of its currently stored value.

4.5 High-Voltage and TDC Threshold Setting

The PMT high voltage is set by commanding to each TCD readout box. The outputs from two digital-to-analog converters (DACs) on each TDC board are available at a socket on each TCD readout box. One of these outputs is used to control the Ultravolt high-voltage supply connected to the two PMTs attached to that box. The 12V supply for each high-voltage supply is also provided by the power-fanout board contained in each readout box.

The HV settings in the TCD are adjusted on the ground prior to launch so that the muon peak is located as close to 1000 channels in ADC0 as possible (Figure 4.9). Because the tubes are grouped in pairs for CREAM II and later (grouped into groups of 4 for CREAM I), exact positioning of the peak is not always possible. The installation of series resistors is done for some PMTs and does assist in gain matching. Further HV adjustments are possible after launch by updating configuration scripts.

The pedestal for each ADC is ~ 425 channels, and each channel corresponds to ~ 1 mV. Therefore, if the PMT high voltage has been set so the ADC0 muon signal distribution peak is at 1000 channels in the ADC, the muon pulse is about 575 channels above pedestal. Each channel corresponds to 1mV of tube signal. The approximate gains relative to the anode for the dynode taps are shown in Table 4.2.

Assuming these ratios, it is possible to estimate desired initial threshold settings. For example, if the peak in ADC0 from atmospheric muons is positioned at 1000 channels (and assuming that the muons are minimum-ionizing particles or MIPs), then the 1 MIP signal in the anode and D11 are as follows:

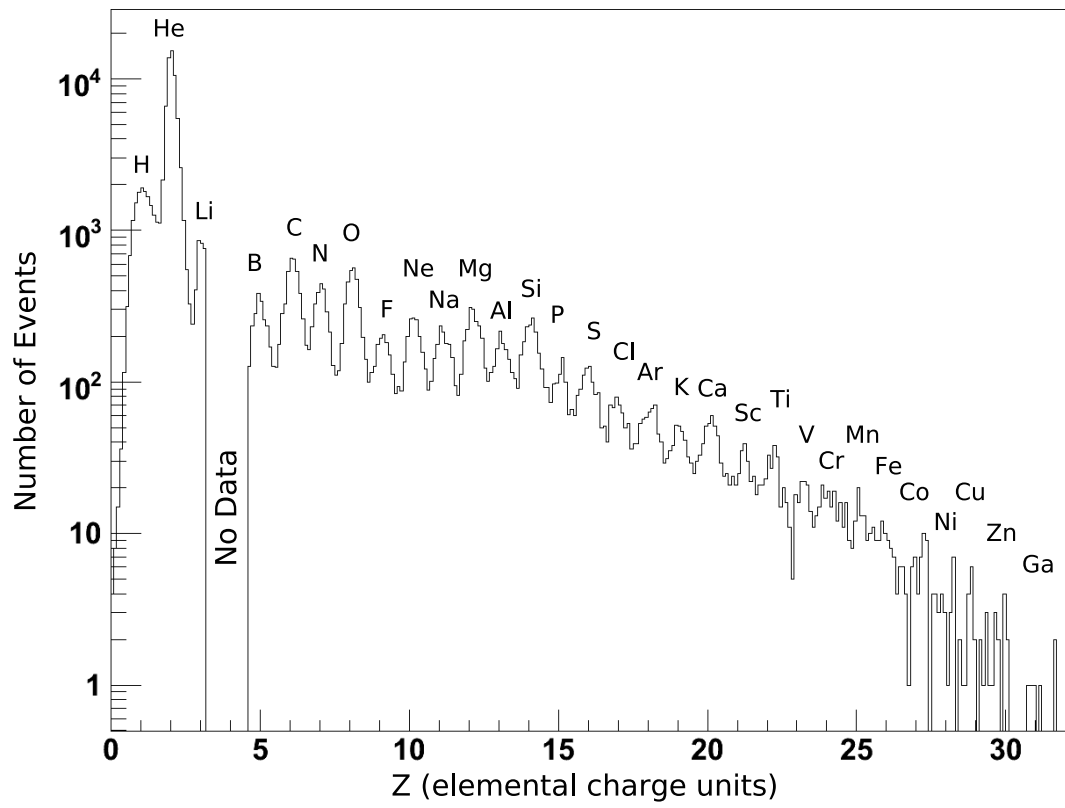


Fig. 4.8 Charge histogram of stitched ADC0 and ADC2 readout (two crossed paddles) for a $158\text{GeV}/n$ indium fragment CERN beam-test from 2003. [10]

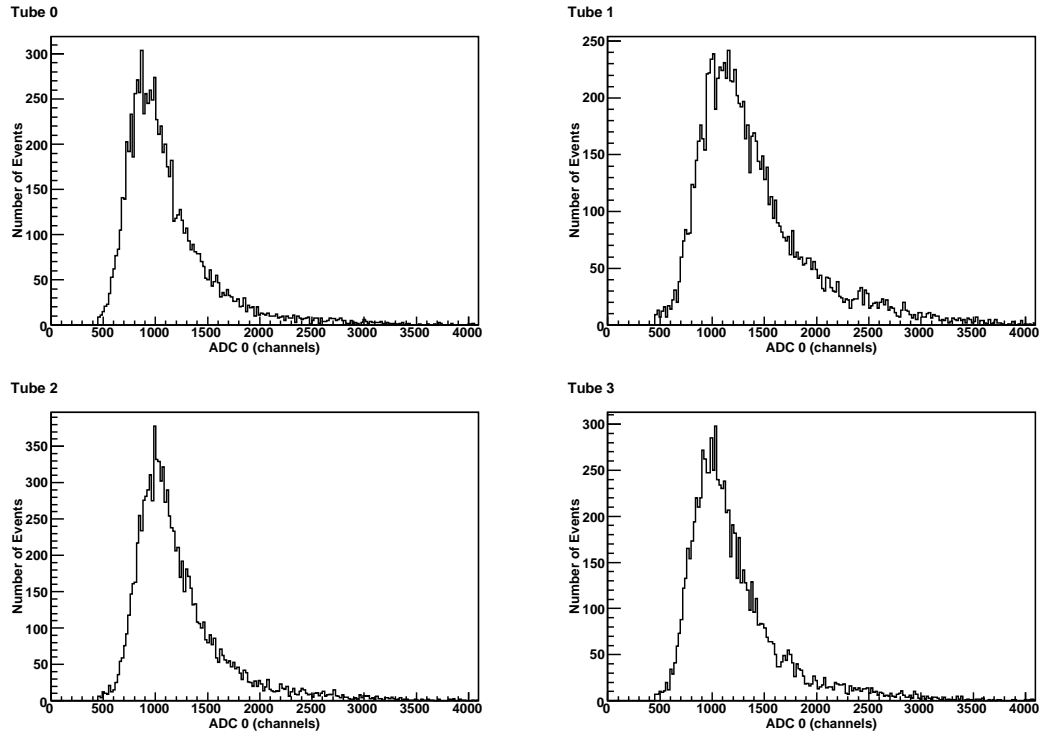


Fig. 4.9 Atmospheric muon ground data taken on December 3rd 2005 by the CREAM II TCD. Shown here are the ADC0 readouts for only the PMTs on the +X side of the instrument (Tubes 0-3). Calibration of the muon signal to 1000 channels was largely successful, but some other tubes (not shown) could not be brought to 1000 channels without exceeding their HV operating limit. Additionally, some pairs were not performance-matched sufficiently closely, and a compromise gain setting had to be chosen.

$$S_{anode} = \frac{V_{anode}}{V_{D12}} S_{D12} = \frac{4.0V}{2.7V} 575mV = 851mV \quad (4.1)$$

$$S_{D11} = \frac{V_{D11}}{V_{D12}} S_{D12} = \frac{0.83V}{2.7V} 575mV = 177mV \quad (4.2)$$

Thresholds can then be set in TDC 0-3 to provide triggering on specific sized pulses as a % of a 1 MIP signal. Typically, threshold 0 is set to 100 channels (~ 100 mV) to be small but above noise, threshold 1 is set to ~ 1 MIP, threshold 3 to between H and He and threshold 2 set highest of all, generally above He, to provide triggering optimized for BCNO measurements.

4.6 Trigger Formation and Logic

4.6.1 TCD Trigger System

Each TDC board provides 4 trigger flags to the local trigger system, one for each of the TDCs instrumented on each tube. All trigger levels sent from the TCD local trigger boards use LVDS (low-voltage differential signaling). Each local trigger board combines the triggers for both tubes instrumented by the corresponding electronics stack, and broadcasts the result to the TCD trigger system. All four thresholds are broadcast to the TCD trigger system, though only *threshold* 0 and 2 contribute to the LoZ and HiZ TCD triggers, respectively (Figure 4.10).

The LoZ trigger from the TCD is generated and sent to the instrument master trigger. The rules for the formation are that *threshold* 0 is crossed on at least 3 sides (3-fold coincidence) and that S3 crosses *threshold* 0 (an OR of the two S3 tubes). The requirement for S3 is meant to require the calorimeter is hit.

The HiZ trigger from the TCD requires a 3-fold coincidence in *threshold* 2 being crossed and for the CD to see a signal above some pre-set threshold. The CD requirement provides for selection of relativistic particles.

4.6.2 CREAM Instrument Trigger

The two main trigger modes of interest in flight are $Z \geq 3$ events within the geometry of the TRD and TCD and events which produce a shower in the Calorimeter module (Table 4.3). The High-Z trigger mode in CREAM I was generated whenever the TCD trigger system returned the HiZ signal. The EHI (high-energy) trigger was for events showering in the Calorimeter.

The HiZ TCD trigger generation is essentially the same in CREAM II as in CREAM I except that the CD readout and veto generation is now done by modified PSU concentrator electronics instead of University of Chicago TRD electronics. The LoZ generation is the same as CREAM I.

There is also the addition of two more trigger signals sent to the science instrument master trigger from the TCD system: S3LO and S3HI. S3LO is given by the OR of *threshold* 1 from the two S3 tubes. S3HI is given by the OR of *threshold* 3 from the two

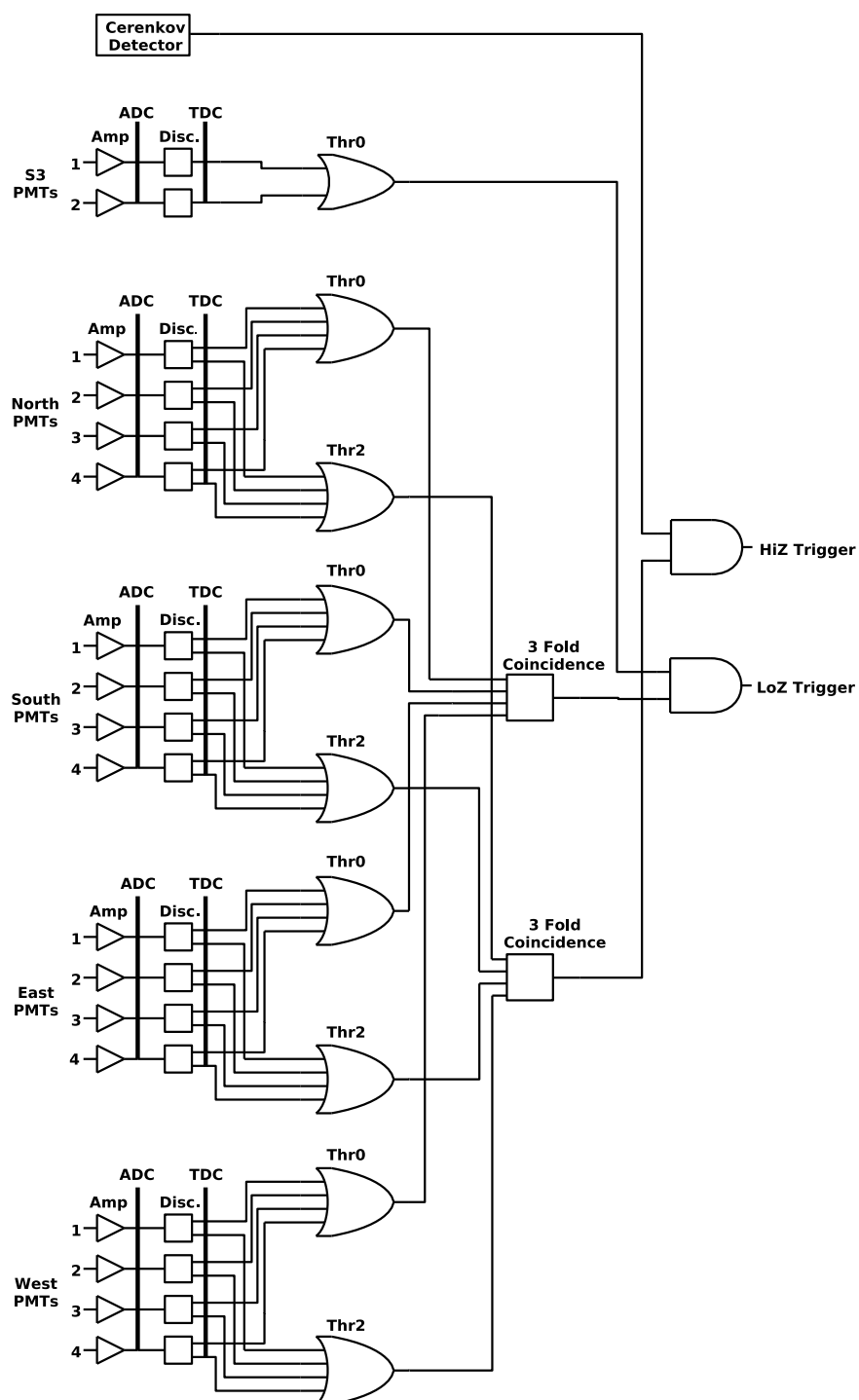


Fig. 4.10 The TCD trigger system

S3 tubes. NOTE: these signals were not long enough to set the S3LO and S3HI bits in the master trigger (they would have needed to be about twice as long in time), but they were actually sufficient to trigger correctly. As long as the configuration is known, no information is lost due to this, but the trigger flags were not written to the data files as intended. This was fixed for subsequent flights by altering the master trigger.

<i>CREAM I Trigger</i>	
<i>Master Trigger Type</i>	<i>Source</i>
High-Z	HiZ from TCD
Low-Z	LoZ from TCD
CAL	CAL
CALIB	external

Table 4.3 CREAM I Master Trigger Modes. High-Z collects relativistic species with $Z \geq 3$ which produced a sufficient signal in the TCD and CD. EHI are for events which showered in the Calorimeter. CALIB is an external calibration trigger.

4.7 TCD Concentrator System

The TCD Concentrator system is a small computer system for control of various readout-electronics settings, and for readout and packaging of event data. The computer board is an Arcturus Networks uCdim ColdFire 5272 [12] running the uClinux operating system. The computer board has the same form factor as 144-pin soDIMM laptop computer memory, so is very compact and useful for embedded systems. It contains a Motorola MCF5272 microcontroller, and provides two USB 1.1, two serial, and two 10/100 Ethernet ports.

4.8 Commanding and Data Readout

All commanding and data readout for the CREAM TCD takes place over an Ethernet system using the TCP/IP protocol. Each TCD concentrator board has two Ethernet ports present (only one is currently utilized). Each electronics box is connected to one of three extended temperature switches (Parvus 5-port fast ethernet switch) using standard CAT-5 cable. Two Ethernet switches are located at the top of the instrument, and are attached to the outside of two TCD electronics boxes. The output from each switch then goes to the switch attached to the S3 electronics box located on the instrument pallet. Finally the output from the S3 mounted switch goes to the Science Flight Computer (SFC), also located on the instrument pallet.

Each TCD Concentrator contains two server applications [10] which communicate with a single client running on the Science Flight Computer (Figure 4.11). The server concerned with data packing and transmission is called eServer. When the trigger system indicates that an event has occurred, the SFC requests the event from all TCD boxes by sending a request to eServer; the event data is then sent, and a correctly formatted

<i>CREAM II Trigger</i>	
<i>Master Trigger Type</i>	<i>Source and Modes</i>
ELO	LoZ + S3HI
ZCLB	HiZ + S3LO
	HiZ
EHI	CAL
	CAL+S3HI
	S3HI
CALIB	
EXT	

Table 4.4 CREAM II Master Trigger Modes, with different selectable options shown. ELO is intended to collect events within the Calorimeter geometry that did not produce a trigger from the Calorimeter for whatever reason, but still triggered S3HI. ZCLB collects relativistic species with $Z \geq 3$ for calibration of the TCD and CD. EHI collects events which showered in the Calorimeter. CALIB is a calibration trigger for Calorimeter and SCD events, EXT is an external calibration trigger (ground only).

event is then constructed in the client running on the SFC. This is then incorporated into the event record for all detectors and archived on the on-board SFC hard disks. A sparsified data stream is also downlinked to the ground containing high-value science events. The cServer server also resides on each Concentrator and receives commands from the SFC client and implements them. It also returns configuration information about the Concentrator (thresholds, HV settings, etc.) when requested as part of the housekeeping system. Both eServer and cServer are designed to accept connections from more than one client if one is present. This permits attaching another computer to the TCD network for debugging purposes without disconnecting the SFC. Dedicated user-interactive client programs were written for this purpose.

4.9 TCD Housekeeping

There are two independent housekeeping systems in CREAM, one implemented through the CDM (Section 2.2.6) and one through the science flight computer. The CDM-based system is present to monitor overall payload health and science-voltage supply. The science-flight computer-based system monitors the science systems more closely. For the CREAM I TCD, 5 representative temperatures were monitored as well as all DC voltage levels supplied by the TCD power-converter system. The TCD components monitored for temperature are: S3 Concentrator Box, S3 Ethernet switch, TCD Power Converter Box, MYL Concentrator, and one of the PMTs attached to MYL. This was maintained for later flights, and for CREAM III and beyond, HV sense lines from the TCD HV supplies were also instrumented into the science monitored housekeeping. The sense lines are features of the Ultravolt supplies, and are just the HV output sensed with a resistor voltage-divider circuit.

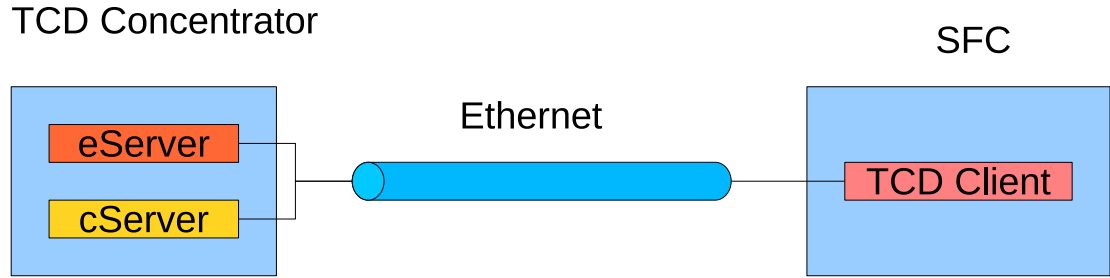


Fig. 4.11 Diagram of the TCD software readout and commanding scheme. eServer and cServer are server applications that reside in each TCD Concentrator box. eServer handles data, cServer handles command reception and execution. Not shown here are Ethernet switches which connect all 9 (or 10 for CREAM II and above) Concentrators to the SFC.)

4.10 CD Readout (CREAM II and later)

For CREAM II and later the Cherenkov detector readout is done by modified TCD electronics. A TCD electronics box is used but no TDC boards are present, and the box is prompted to readout by the TCD trigger fanout. An external pulse-shaping and summing board couples the 8 anode signals from the CD PMTs to the 8 dynode polarity inputs of the TCD-electronics ADC inputs. The external board also provides a veto signal for the TCD-trigger system and a currently unused PMT sum output.

A software bug in the CREAM II event packing partially corrupted the CD data from the flight. While no TDC boards are present in the CD stack, the concentrator system still sent levels for some of the TDC lines because of the chatter on the VALID signal. Some recovery of the ADC signals was possible however. This was corrected for subsequent flights.

Chapter 5

CREAM TCD Timing and Tracking

5.1 Internal TCD Timing

The TCD detector (including the S3 paddle) is all read out with fast readout electronics, as described in previous chapters. This readout includes fast Time-to-Digital Converters (TDCs) from which we can derive both X and Y hit-positions in the TCD and a time-of-flight (TOF) measurement to distinguish primary cosmic-ray hits from upward-going albedo particles.

The TDCs are described in Section 4.4.1 in more detail, but their basic operation is easy to understand. Whenever a PMT pulse crosses its pre-set threshold, a counter is started and a trigger signal is sent to the TCD trigger system. If the trigger system determines that the correct set of conditions has been met (as described in Section 4.6.1), the TCD is informed that an event of interest has occurred and to commence readout. A common-stop is generated and broadcast to the entire TCD, and any TDCs and ADCs with valid data preset are read out. This includes channels which did and did not contribute to the trigger conditions being met. Since a common-stop is used, relative timings between TDCs on different tubes are meaningful.

In reality there are offsets present between channels, some due to light propagation through detector components and some due to varying cable lengths and individual electrical component variation. Some of these offsets display a time dependence, and this topic will be the subject of much of the rest of this chapter. First, however, let us discuss what quantities derived from the relative TCD timings are of interest.

Figure 5.1 shows the various arrival times for PMT signals from particle hits in the TCD and S3 paddles. Once the TCD trigger system determines that conditions are satisfied, a common-stop is generated sent at time t_{stop} . The value recorded by the TCD for the TDCs is the time (in channels) that elapses between the threshold crossing $t_0 - t_3$ and t_{stop} (Figure 5.2). In the TCD each TDC channel is 50 ps. In this introduction we will neglect timing offsets between channels, but they will be dealt with in later sections.

Since the earliest time in an event occurs at t_A (for downward-going events), it makes sense to set $t_A = 0$. The times recorded by the TDCs (in time units here, not channels) are thus:

$$tdc_0 = t_{stop} - t_0 \tag{5.1}$$

$$tdc_1 = t_{stop} - t_1 . \tag{5.2}$$

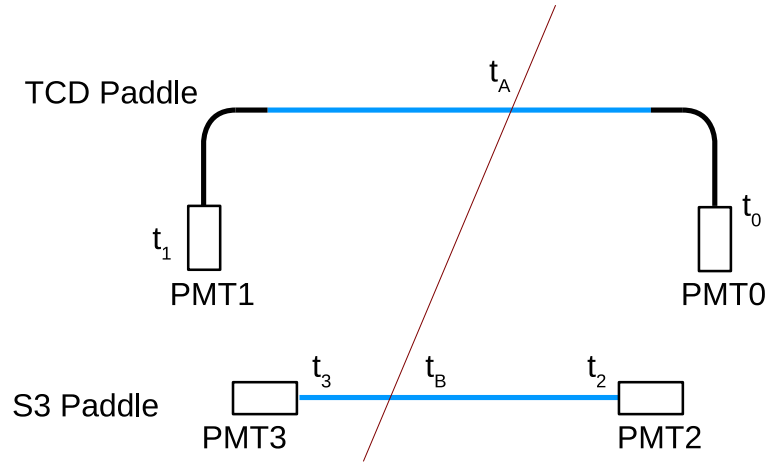


Fig. 5.1 Threshold crossing times and particle arrival times for a TCD paddle and the S3 detector. This is representative of the conditions for a TCD LoZ trigger type. The particle arrives at the TCD at time t_A and the S3 paddle at time t_B . The signals cross threshold in PMT 0-3 at times $t_0 - t_3$.

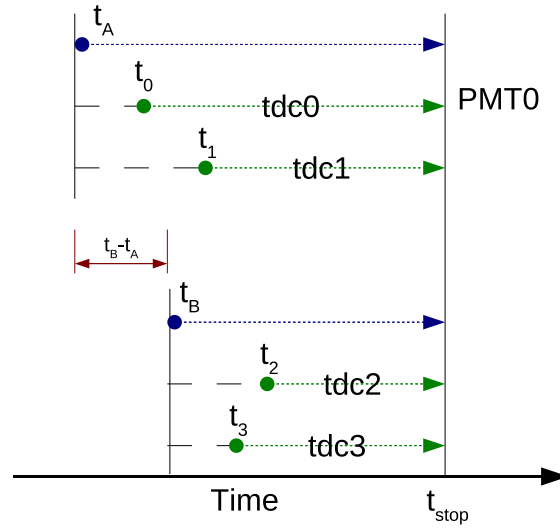


Fig. 5.2 Representation of the TDC readouts for an event involving S3 (TCD LoZ type trigger). Note the PMTs which receive light first will have larger TDC readout signals than the ones hit subsequently.

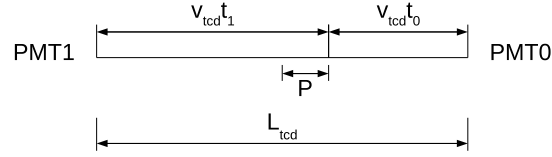


Fig. 5.3 Propagation distances in a TCD paddle of length L_{tcd} for a particle hit at location p measured with respect to the center of the paddle.

If the particle hits a TCD paddle of length L_{tcd} at position p and the light signals propagate at velocity v_{tcd} (assuming constant velocity in the scintillator and the light-guides), (Figure 5.3), then $\frac{L_{tcd}}{2} - p = v_{tcd}t_0$ and $\frac{L_{tcd}}{2} + p = v_{tcd}t_1$, which yields:

$$p = \frac{v_{tcd}(t_1 - t_0)}{2}.$$

Using equations 5.1 and 5.2 and noting the elimination of the unknown t_{stop} , we arrive at:

$$p = \frac{v_{tcd}}{2}[tdc_0 - tdc_1]. \quad (5.3)$$

Thus, the hit position in the paddle is expected to be linearly related to the end-to-end TDC timing difference in the paddle. In fact we note that the proportionality constant is $v_{tcd}/2$. The TCD can therefore provide a layer of particle tracking (if properly calibrated) at the top of the instrument in both the X and Y directions since there is a layer of paddles aligned with each direction. There is an important caveat to this however, as all particle hits in the TCD will generate position values, including albedo hits. Some means of distinguishing between downward-going and upward-going tracks is important (and will be developed now). We also expect that there are also offsets present, some time-dependent and some not. It will be a task of later sections to remove these through analysis of the flight data.

To distinguish downward-going from upward-going hits in the TCD, we can use the TDC timing from the S3 scintillator. The timings are shown in Figures 5.1 and 5.2. However, we must note that the signals in S3 are not in general just from the passage of the primary particle through the scintillator. S3 is located under the calorimeter carbon targets, so S3 is actually recording a much broader shower-hit (for primaries interacting in the targets which all events of science interest will) mixed with any albedo signals. The end-to-end timing in S3 would therefore be a poor position measure in general. It also means that the reference time provided by S3 will have some extra spread in it, compared to a non-shower and non-albedo case.

Again setting $t_A = 0$, the time-of-flight from a TCD paddle to S3 is just $TOF = t_B$. If we again take the relations $\frac{L_{tcd}}{2} - p = v_{tcd}t_0$, $\frac{L_{tcd}}{2} + p = v_{tcd}t_1$ and Equations 5.1 and 5.2 but now we eliminate p instead of $L_{tcd}/2$, we get the following relation for t_{stop} :

$$t_{stop} = \frac{tdc_0 + tdc_1}{2} + \frac{L_{tcd}}{2v_{tcd}} \quad (5.4)$$

where we have noted that the propagation velocity in the TCD paddles (v_{tcd}) will be somewhat different than in S3, because of the different paddle geometry and construction (scintillator slabs vs fibers, slightly different scintillator material). A relation of similar form as above can be derived for S3. We again start with the following relations:

$$tdc_2 = t_{stop} - t_2 \quad (5.5)$$

$$tdc_3 = t_{stop} - t_3 \quad (5.6)$$

and,

$$\frac{L_{S3}}{2} - p = v_{S3}t_2 \quad (5.7)$$

$$\frac{L_{S3}}{2} + p = v_{S3}t_3 . \quad (5.8)$$

Combining equations 5.5 and 5.6 to eliminate the hit-position again, and substituting in 5.7 and 5.8, we again arrive at an expression for t_{stop} :

$$t_{stop} = \frac{tdc_2 + tdc_3}{2} + \frac{L_{S3}}{2v_{S3}} + t_B . \quad (5.9)$$

Eliminating t_{stop} by combining the above expressions, we arrive at an expression for the time-of-flight:

$$TOF = t_B = \frac{tdc_0 + tdc_1}{2} - \frac{tdc_2 + tdc_3}{2} + \frac{L_{tcd}}{2v_{tcd}} - \frac{L_{S3}}{2v_{S3}} . \quad (5.10)$$

Thus the TOF can be measured by taking the difference of the average of the TCD and S3 TDC timings (plus some constant term offset, which will get absorbed into the experimentally determined offsets). Now we will set about producing both corrected end-to-end timing and time-of-flight timing for the CREAM II detector. To calibrate the tracking in distance units, we will also examine some CREAM I data where the excellent TRD tracking was available.

5.2 Analysis Tools

The CREAM data are packaged during flight by the science-flight computer into a custom binary format. Some subset of the flight data is sparsified and sent to the ground in real-time (TDRSS connection permitting, see Section 2.2.6), while some is archived on-board on solid-state hard-drives. The data downlinked have the *.dat extension, while the archived files have *.arc. Pedestal runs are also conducted throughout the flight for some of the detectors such as the CAL and SCD, and these files are also recorded.

The internal format of the *.dat and *.arc files are the same, so the same analysis tools can be used on them. Interacting with the data and pedestal files is done by

the `crmfile` collection of classes, all written in C++. These classes allow the files to be unpacked and make available all instrument channels recorded by the science-flight computer. The `crmfile` classes were written by the CREAM collaboration to provide a common interface between the raw data files and the analysis, diagnostic, and ground-based monitoring software used during instrument ground and flight operations.

To perform actual data analysis, the event information made available by `crmfile` must be loaded into some sort of format usable by data analysis packages. The package ROOT [69] was used for most CREAM data analysis (and all data analysis at Penn State), and separate programs were created to facilitate analysis. ROOT is a very powerful object-oriented histogramming and analysis package written, maintained and made freely available by the CERN laboratory and has wide usage in the high-energy, nuclear and astro-particle communities, among others. It is C++ based, and can be used to make either interpreted or compiled routines for analyzing very large data sets.

The University of Chicago produced an analysis program called `canal`, primarily for analysis of secondary/primary species (events measured by the TRD). Penn State (primarily Nick Conklin) produced another program called `stump` which was extended to access flights beyond CREAM II. The `stump` program was used extensively in the CREAM II analysis presented in this thesis. Both of these programs take the events depackaged by `crmfile` and put the events into ROOT TTree [70] structures stored in *.root files.

TCD readout channels are stored as individual leaves in the `tcd` branch of the TTree structures produced by `stump`. The peak detector ADC channels are labeled as `tcd.fADC[tube][dynode]` with the *tube* index running from 0-17 (as shown in Figures 3.6 and 3.7) and the *dynode* index running from 0-3 (discussed in Table 4.2). The TDC readouts are labeled as `tcd.fTDC[tube][threshold]` with the *threshold* index being the TDC threshold. After the initial leaves are filled with the basic detector readout channels for each event, more leaves can be filled with quantities of interest derived from functions combining those values (along with any other depackaged quantities made available by `crmfile`) such as time-corrected quantities, time-of-flight measurements as presented shortly, pedestal-subtracted quantities, tracking parameters and others.

5.3 CREAM II Data Overview

The CREAM II instrument recorded over 15.5 million triggers during its flight (Table 5.1). The TCD generated over 11 million trigger flags as well, so a high percentage of events have TCD data present. The total triggers presented here contain both science events and a much larger set of various calibration-type events (pedestal runs, etc.). The actual number of events producing showers in the calorimeter (and a charge measurement in the TCD or SCD) is much smaller, on the order of 15-20 thousands.

The TCD trigger scheme that actually produces the flags in Table 5.1 was described in Section 4.6.1. Briefly, the trigger conditions are that 3 sides of the TCD record hits above the TDC threshold of interest. No requirement is made on 3 tubes agreeing on a specific set of crossed paddles being hit for the trigger flag to be produced. This condition can be imposed during analysis however, and that is the procedure employed in the rest of this thesis, when required. The 3-side requirement was included so that a

<i>Trigger Type</i>	<i>Count (Entire Flight)</i>
LoZ	11167181
HiZ	6424900
CALIB	28689
CAL	3537851
TRG	15505030
S3HI	186
S3LO	445
ZCLB	6456389
ELO	6222604
EHI	3562970

Table 5.1 All trigger flags recorded in the CREAM II flight (See Section 4.6.1 for an explanation of the triggers). TRG is a count of the total number of individual event triggers (all events, but only counting events with multiple trigger types once).

limited number of tube failures would not blind the end of paddles opposite the failed tube.

Since CREAM II had a full set of operating TCD and S3 PMTs for its flight, we can impose a more stringent set of requirements in the analysis for what constitutes a valid hit. From here on, a paddle will only be considered hit if *threshold 0* was crossed for both PMTs on the paddle. Also, since all events of science interest will be in the geometric acceptance of the calorimeter, we will also require both S3 tubes to have crossed *threshold 0* as well.

As already mentioned, an important consideration in CREAM is dealing with the problem of albedo particles from the calorimeter introducing spurious signals in the charge detectors in the instrument (the TCD and S3). A valid question to ask initially is how bad this problem of albedo contamination is? Figure 5.4 (b) shows that for events with a CAL track present and with a TCD signal (many of the events with no TCD data here are CAL calibration events) the most probable configuration is in fact to have all TCD paddles hit (4 of them). This suggests that albedo is in fact going to be a large background to be suppressed by further analysis. The TOF measurement in the next section is one such measure which can be implemented to tackle this issue.

5.4 CREAM II Time-of-Flight

TOF measurements for each of the CREAM II TCD paddles can be produced by using Equation 5.10 and the TDC channels as described above. The later constant terms in this equation will just be folded into a constant term to be found empirically. In this analysis only *threshold 0* signals were used, since they are the first thresholds crossed by PMT signals and all species are on scale. Higher threshold timings were examined, but offered no improvement in resolution. The paddle numbering scheme used for the remainder of this text is to label the Paddles 0-7, with the numbering matching the first 8 PMTs shown in Figure 3.6.

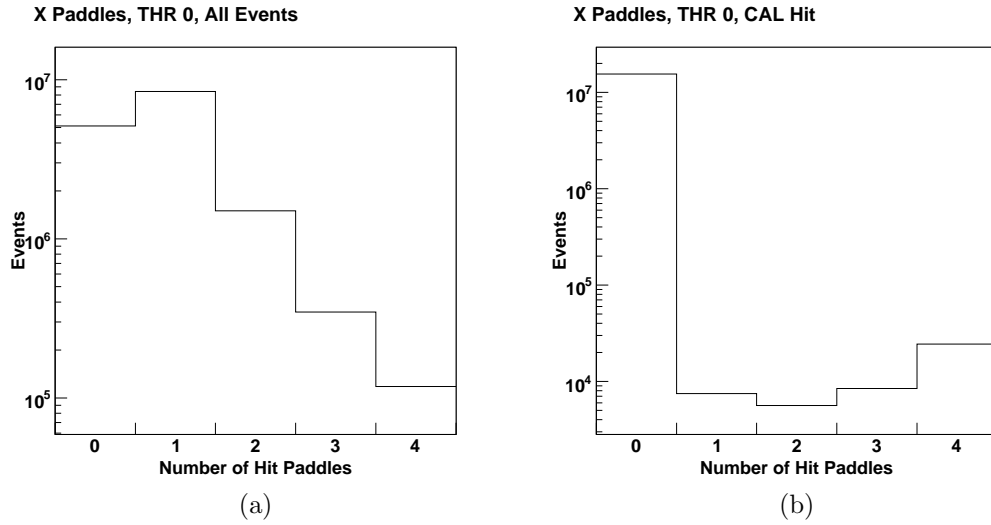


Fig. 5.4 Number of hit X-direction TCD paddles per event for a) all events and b) events with a calorimeter track present (tubes at both ends required to cross threshold). Y-going paddles have qualitatively identical distributions, so are omitted here.

Uncorrected TOF measurements (consisting of just the first two terms in Equation 5.10) are shown in Figures 5.5 and 5.6. The right-most peak represents downward-going particles (cosmic rays) while the left-most peak includes albedo particles coming back up through the instrument. There are several types of variation evident in the time dependence of the TOF measurements. First, there are sudden jumps in the DC offset due to restarts and resets in the electronics. Second, there are also sinusoidal variations with ~ 1 day period due to temperature variations with the rising and lowering sun-angle. And third, we have to account for longer-term trends which are also probably temperature dependent but caused by the change in average solar energy hitting the instrument as the Antarctic seasons change.

To correct the time-of-flight measurements for time variations, the flight was divided up into 0.1 day slices. This was shorter than the ~ 1 day variations and so would allow to correct for this plus the large jump-discontinuity variations. Next, for each 0.1 day section of the flight, a histogram was generated of the same form as those in Figure 5.5, with the same TDCs on-scale requirement cuts.

A Gaussian fit was then done to each time slice histogram (to the right-most peak which corresponds to downward-going particles), and the channel position of the peak was recorded. This Gaussian position was then recorded in an ASCII file to be used as a correction term for the TOF measurements. By subtracting the stored correction term from the original value of the TOF, corrected TOF measurements were made (Figures 5.7 and 5.8). This both removed time-dependent variations in the TOF measurements and normalized away all the DC offsets present both from the last two terms of Equation 5.10 and from paddle-to-paddle offsets introduced by electronics and cable-length differences. The peak of the downward-going distributions was thus positioned at ~ 0 channels for all paddles. This represents an arbitrary (but consistent between paddles) offset in

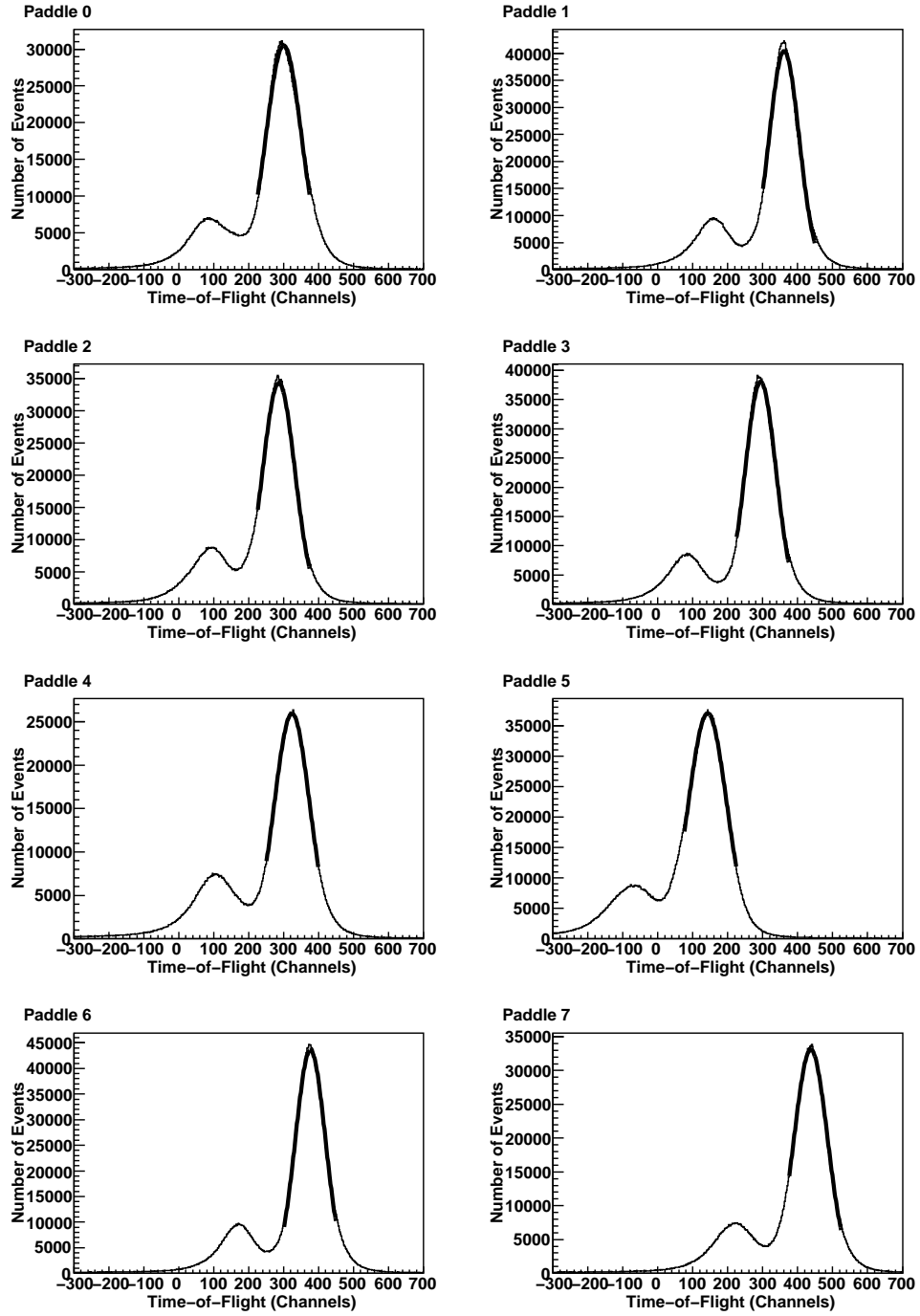


Fig. 5.5 Uncorrected TCD-to-S3 time-of-flight measurements for all 8 TCD paddles in the CREAM II flight. The only cuts implemented here are to require that TDC *threshold* 0 be on scale for the two TCD paddle tubes and the two S3 tubes ($0 < tcd.ftDC[tube][0] < 4095$).

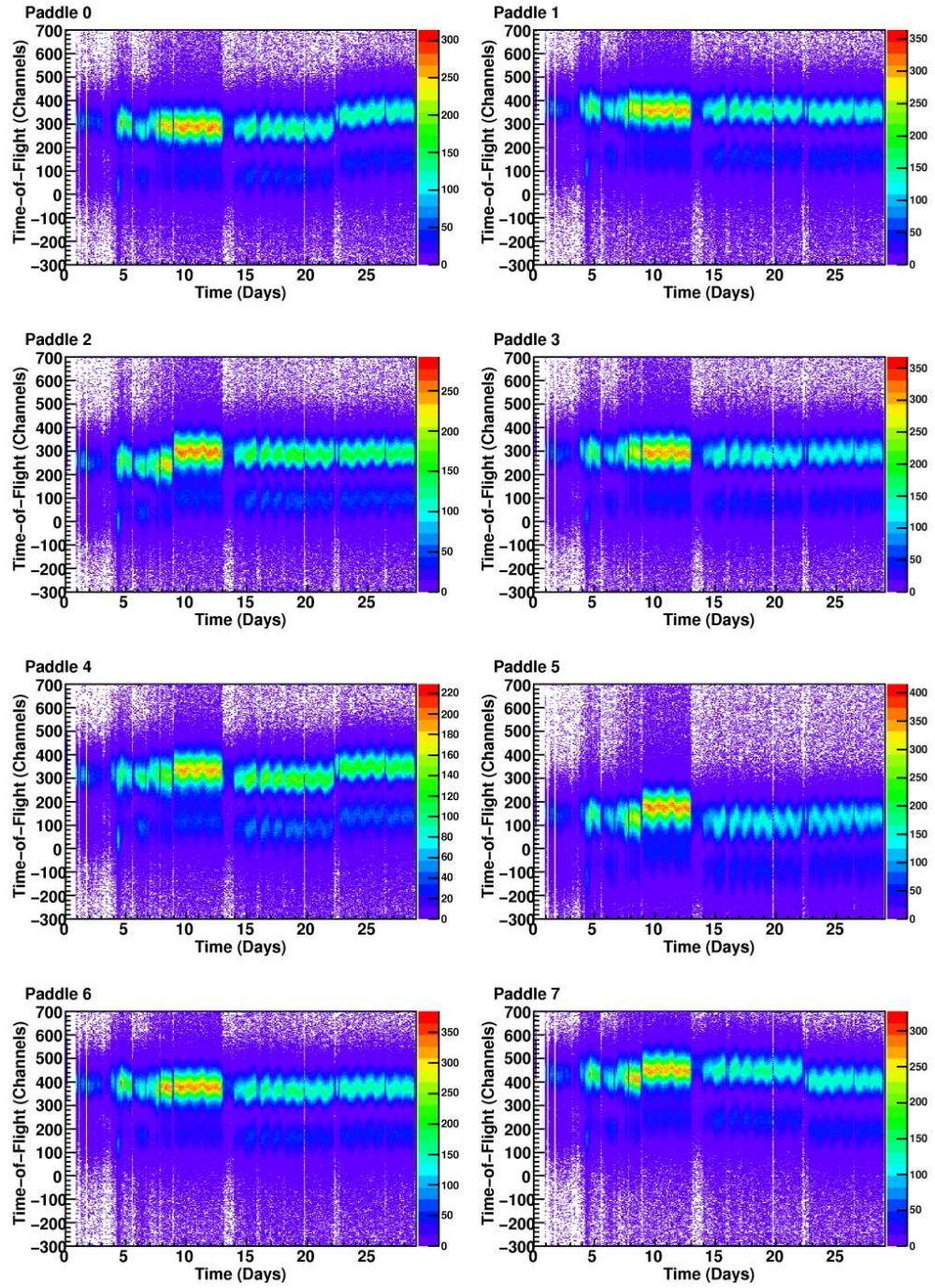


Fig. 5.6 Uncorrected TCD-to-S3 time-of-flight measurements (channels) as a function of flight-time (in days) for all 8 TCD paddles in the CREAM II flight. Same on-scale cuts applied as in Figure 5.5.

time. The quoted uncertainties here are the uncertainty on the Gaussian fit mean. The peaks are not located exactly at zero because individual 0.1 day histograms had lower statistics than the histograms for the entire flight. Additionally, the fitting algorithm for each 0.1 day histogram worked by selecting a region within 75 channels of the local-maximum bin value, which taken together would introduce some uncertainty in peak location measurements.

As can be seen from these plots and the values listed in Table 5.2, the corrections did improve the separation between the peaks somewhat, though there is still mixing present between the upward (albedo) population on the left and downward-going (cosmic-ray) population on the right. The time-corrected and offset-normalized top-to-bottom timing was added to the stump analysis code under the name of the `tcq.fTOF[paddle]` variable, with the *paddle* index running from 0-7.

<i>Paddle</i>	<i>Uncorrected</i>		<i>Corrected</i>	
	<i>TOF Peak (Channels)</i>	<i>Peak Width (σ) (Channels)</i>	<i>TOF peak (Channels)</i>	<i>Peak Width (σ) of (Channels)</i>
0	300.052 ± 0.052	50.191 ± 0.066	-2.712 ± 0.049	38.968 ± 0.073
1	361.174 ± 0.040	42.879 ± 0.043	-1.412 ± 0.044	38.316 ± 0.065
2	285.942 ± 0.048	46.142 ± 0.053	-1.845 ± 0.049	39.569 ± 0.074
3	293.868 ± 0.039	43.987 ± 0.043	-3.509 ± 0.052	41.153 ± 0.081
4	323.742 ± 0.057	50.002 ± 0.072	-1.926 ± 0.056	39.967 ± 0.086
5	142.149 ± 0.056	54.393 ± 0.073	2.210 ± 0.057	44.678 ± 0.067
6	376.408 ± 0.036	42.713 ± 0.040	-0.744 ± 0.044	39.013 ± 0.066
7	437.467 ± 0.051	47.879 ± 0.058	-0.915 ± 0.050	39.622 ± 0.075

Table 5.2 Uncorrected and corrected TOF measurements for the CREAM II flight and associated distribution widths. The quoted uncertainty is the ROOT fitting uncertainty for the parameters from applying Gaussian fits to the peaks. The peak-position quoted here is that of the right-most peak corresponding to downward-going particles.

At this point the timing is left in terms of channels, though it can be converted to time units by the conversion factor of 50 ps/channel. Table 5.3 summarizes the positions of the albedo peaks, as well as the separations of the albedo peaks from the downward-going peaks. The TCD paddles can be broken into two groups, an inner group and an outer group. Paddles (1,2,5,6) are all located in the center of the TCD and should have largely equal geometric acceptance (the ends of S3 are still active scintillator fibers, so some non-symmetrical behavior can be expected). Likewise for the four outer paddles (0,3,4,7), with the two groups having a somewhat different expected mean TOF. As can be seen in Table 5.3 this is the behavior observed. The inner paddles have a somewhat smaller separation between the upward and downward-going peaks, which is consistent with the closer to vertical requirement on particle trajectories. For the inner paddles (1,2,5,6), we estimate a separation between the peaks of 9.909 ± 0.015 ns and a separation of 10.388 ± 0.017 ns for the outside paddles, on average.

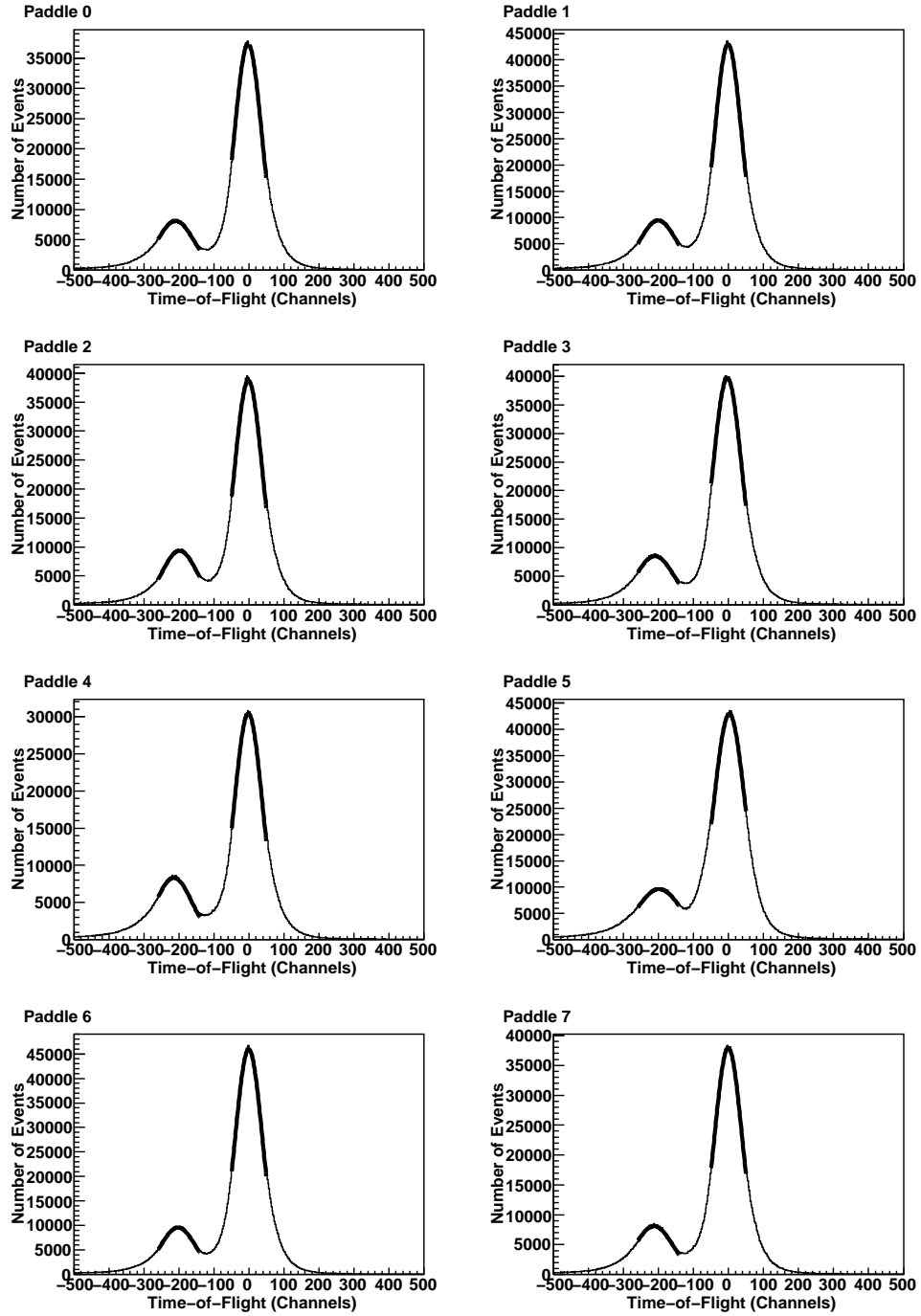


Fig. 5.7 Corrected TCD-to-S3 time-of-flight measurements for all 8 TCD paddles in the CREAM II flight. Again, the cuts implemented here are to require the two TCD paddle and the two S3 TDC *threshold* 0 readouts to be on scale ($0 < tcd.ftDC[tube][0] < 4095$).

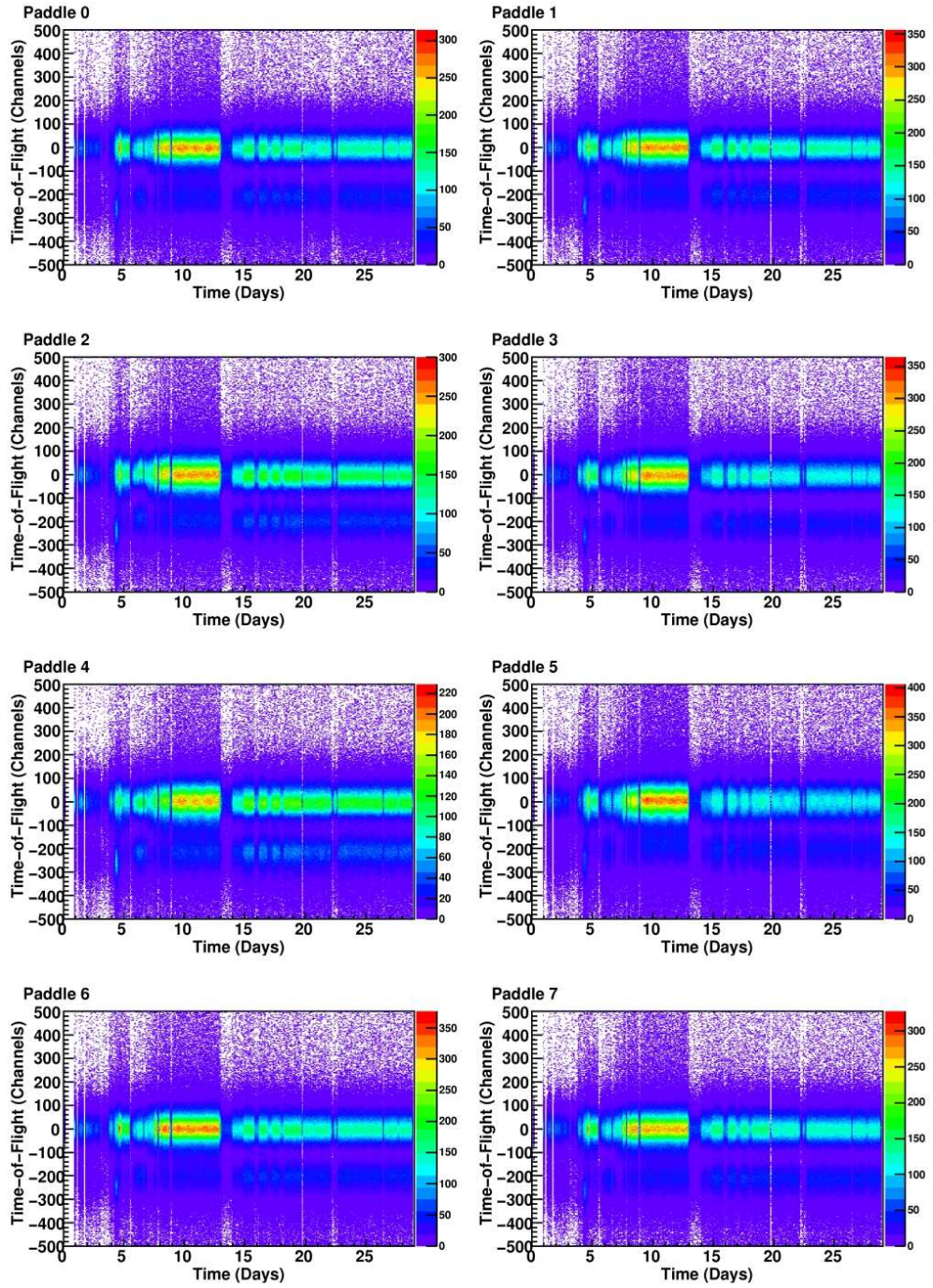


Fig. 5.8 Corrected TCD-to-S3 time-of-flight measurements as a function of flight-time for all 8 TCD paddles in the CREAM II flight. The same on-scale cuts are implemented as in the previous figures for the TDCs.

<i>Paddle</i>	<i>Albedo Peak (Channels)</i>	<i>Peak Width (σ) (Channels)</i>	<i>Peak Separation (Channels)</i>
0	-209.76 ± 0.15	51.72 ± 0.23	207.05 ± 0.16
1	-201.33 ± 0.12	51.43 ± 0.20	199.92 ± 0.13
2	-198.47 ± 0.12	49.85 ± 0.19	196.63 ± 0.13
3	-210.51 ± 0.16	53.71 ± 0.24	207.00 ± 0.17
4	-214.84 ± 0.17	51.83 ± 0.23	212.91 ± 0.18
5	-198.58 ± 0.18	63.70 ± 0.36	200.79 ± 0.19
6	-202.79 ± 0.12	50.20 ± 0.19	195.35 ± 0.13
7	-213.18 ± 0.17	53.72 ± 0.25	204.03 ± 0.18
Mean (Inner Paddles)			198.17 ± 0.29
Mean (Outer Paddles)			207.75 ± 0.34
Mean (All Paddles)			202.96 ± 0.45

Table 5.3 Corrected peak-positions and widths of the albedo distributions (left-most peaks in Figure 5.7), where the quoted uncertainty is the ROOT fitting uncertainty from applying Gaussian fits to the peaks. Also shown are the separation (in channels) between the albedo peak distribution and the downward-going distribution. Arithmetic means are calculated for the separations as well for the inner paddles (Paddles 1,2,5,6), outer paddles (Paddles 0,3,4,7) and for all paddles.

This is not the TOF for top-to-bottom timing, but rather the separation between the population of downward-going and upward-going particles. The approximate TOF would be measured to the midpoint between the two peaks. The rough value of about 5 ns for the estimated typical time-of-flight time is consistent with rough speed-of-light calculation for a downward-moving particle ($1.1m/3 \times 10^8 \text{ m/s} = 3.7 \text{ ns}$). The fact that the distributions are mixed, with some particles consequently measured to have infinite velocity effectively, limits this TOF measure for any sort of particle β measure. It is however quite useful for applying a simple, consistent cut to remove much of the albedo particles. It can also be used as a parameter to help choose which paddle was the most likely to have been hit by a cosmic ray in an event, by choosing the paddle with the most positive value of this parameter (as mentioned in the previous section, since most science events have multiple hit paddles). The width (and consequent mixing) of these distributions arises from a combination of instrumental uncertainty, particle-track dependence (this is a mean for all particles within each paddle's acceptance) and particle velocity distributions.

5.5 CREAM II End-to-End Paddle Timing

Equation 5.3 relates how the TDC timing readouts at either end of a TCD paddle can be used to measure hit position down the length of the paddle. In principle this can be done for all four TDC thresholds available in the CREAM TCD, though in practice the first is the most desirable (though all have been calibrated in the course of this analysis). The first threshold has the advantage of being the lowest, and so is

on scale for all species. To utilize the end-to-end timing for tracking, two things must be done: removal of any time-dependent offsets, and translation from channel units to position units. Additionally, the TOF (or tracking from another detector) must be used to differentiate the TCD paddles hit by the primary particle (if any) from any hit by albedo particles.

Similar time dependencies were observed in the end-to-end timing as was observed in the TOF (Figure 5.9), so a similar scheme was used for correction. The same 0.1 day time slicing was used, but because of the differences in paddle efficiencies and electronics gain, the whole-paddle distributions were rather non-uniform and asymmetric (Figure 5.10). What was done instead was to divide the paddle into four sections (or tiles), each defined by one of the 4 perpendicular paddles crossing the paddle under study. To provide for unambiguous calibration events, only the subset of events with exactly one X-going and one Y-going paddle hit (meaning both tubes in each of the paddles) were considered for generating these corrections. Again, this was only for finding the time-dependent offset corrections, not as a permanent cut on subsequent analysis. Events of these types are shown in Figures 5.9 and 5.10.

Four individual histograms (Figure 5.10 is an example) were created for each 0.1 day time-slice in the data. Gaussian fits were performed on each histogram to find the center of the distribution for that tile. Finally, the 4 positions from the fits were averaged together for each time slice to find a correction term. Thus, equal weight was given to each tile distribution, regardless of the number of entries. Thus the asymmetric form of the whole-paddle distributions did not skew the corrections the same way that taking a simple mean and subtracting would have. This scheme was applied to all four TDC thresholds (*thresholds* 0,1,2 and 3) and for all 8 paddles.

The correction term found above was simply subtracted from the raw end-to-end timing to produce a corrected variable for each paddle and threshold in the stump analysis code. The variable is entered as `tcq.fETE[paddle][threshold]`, with *paddle* running from 0-7 and *threshold* running from 0-3. Figure 5.11 shows the corrected end-to-end timing values for all paddles in CREAM II. Figure 5.12 shows the individual tile slices for Paddle 1 for the entire flight, and Figure 5.13 shows the effectiveness for an individual tile with time. The paddle offsets (and individual tile distribution widths) are shown in Table 5.4 (for *threshold* 0 only) both before and after corrections. Higher thresholds were consistent, but ended up not being utilized in the rest of the analysis.

The above correction scheme worked well for all paddles except Paddle 5, which showed a strong bimodal distribution in the end-to-end timings (Figure 5.14 and the figures above). Paddle 4 had a similar but much less pronounced effect, which only produced a slight broadening of the timing distribution. The effect showed a rough time dependence where the second distribution was more prominent at certain times (Figure 5.9), but no other dependencies were found and its origin is unknown. Oddly it is also present in the CREAM I data, which will be discussed in the next section. There was no correlation with which thresholds were crossed, it was not occurring at a much smaller timescale than 0.1 days (or if it was, the statistics were too small to tell), and it did not correlate with any specific triggers, or when other paddles were hit either. The most likely candidate problems are faulty TDC or local trigger circuits (some marginal circuit-board component(s) with some temperature dependence).

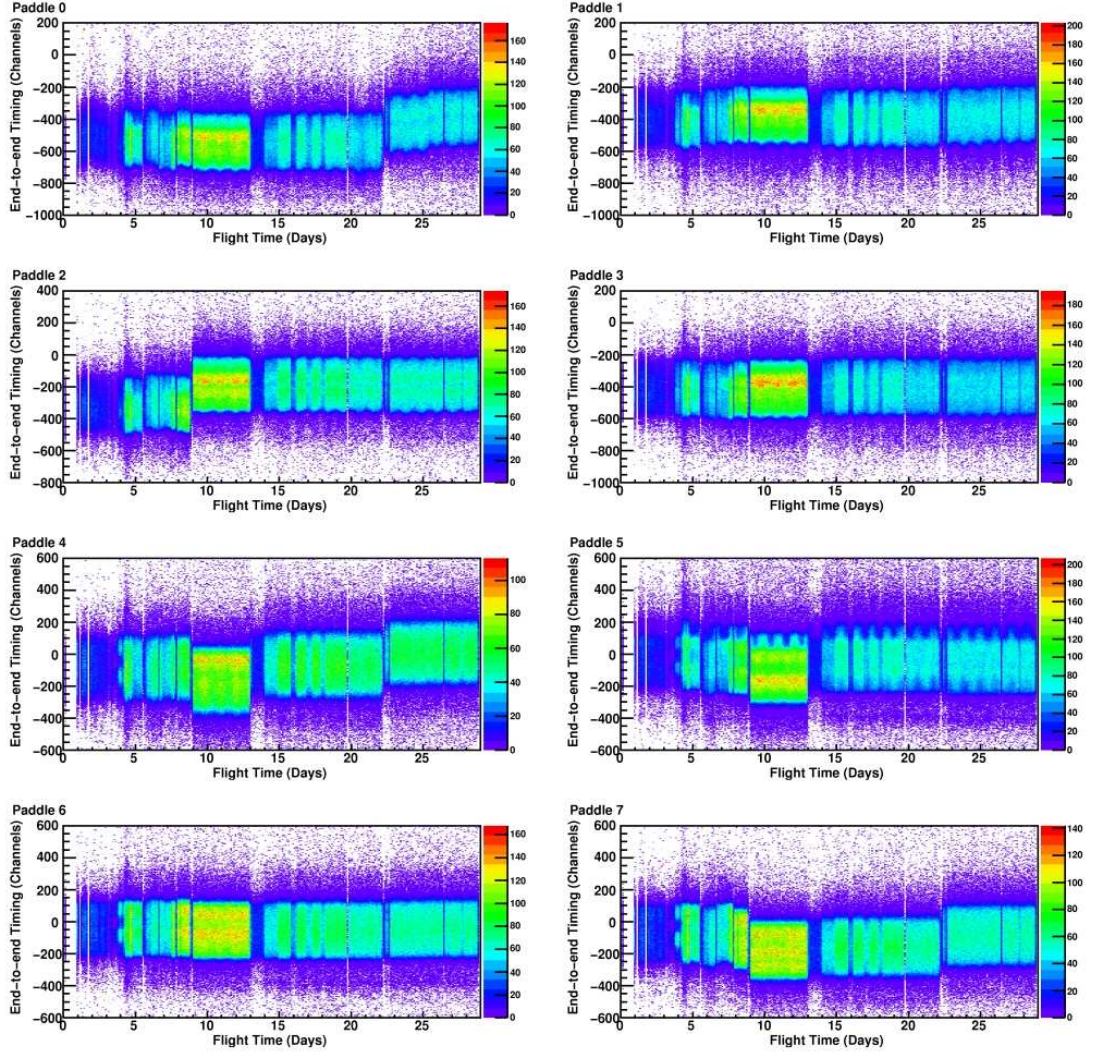


Fig. 5.9 Raw end-to-end timing for the CREAM II TCD as a function of flight-time, for the entire flight. Only the first TDC threshold values are shown here, as higher thresholds are consistent with the distributions shown here.

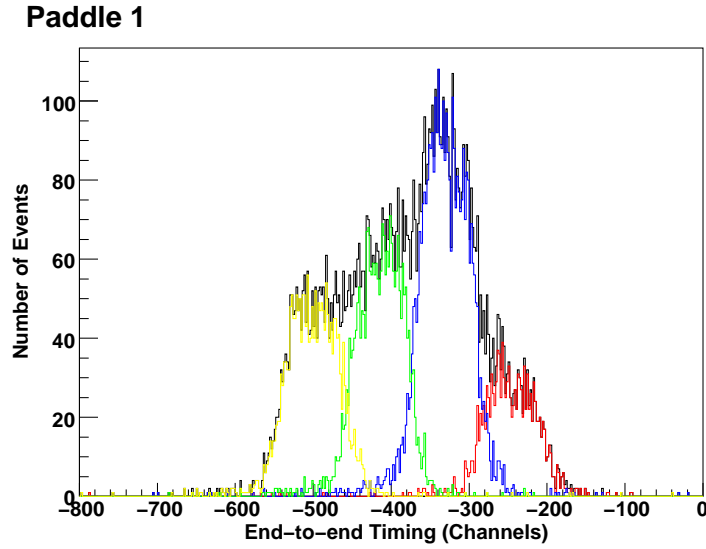


Fig. 5.10 Raw end-to-end timing for Paddle 1 in the CREAM II TCD, for a time-slice from $10 < t < 10.1$ days. The black distribution represents signals in any (but only one) crossed paddle. The colored distributions are for different crossed paddles (red for Paddle 4, blue for Paddle 5, green for Paddle 6 and yellow for Paddle 7).

<i>Paddle</i>	<i>Uncorrected</i>		<i>Corrected</i>	
	<i>Mean Offset (Channels)</i>	<i>Mean Tile Width (σ) (Channels)</i>	<i>Mean Offset (Channels)</i>	<i>Mean Tile Width (σ) (Channels)</i>
0	-516.80 ± 0.25	46.15 ± 0.17	0.85 ± 0.11	32.292 ± 0.078
1	-382.04 ± 0.11	34.754 ± 0.081	0.02 ± 0.10	31.784 ± 0.073
2	-188.73 ± 0.12	31.469 ± 0.098	-0.07 ± 0.10	28.714 ± 0.067
3	-405.70 ± 0.10	31.900 ± 0.069	0.56 ± 0.10	31.054 ± 0.067
4	-67.06 ± 0.26	70.66 ± 0.17	-0.62 ± 0.14	38.28 ± 0.10
5	-59.67 ± 0.19	60.03 ± 0.13	38.53 ± 0.17	45.56 ± 0.11
6	-47.17 ± 0.10	31.304 ± 0.065	-0.02 ± 0.10	30.713 ± 0.063
7	-123.41 ± 0.18	52.39 ± 0.10	0.18 ± 0.11	33.279 ± 0.077

Table 5.4 Uncorrected and corrected end-to-end measurements for the CREAM II TCD, with both the paddle mean-offsets and individual tile (pair of crossed paddles) distribution widths. The quoted offsets are the mean of the positions of the four tile distributions (given equal weight). The quoted uncertainty is the quadrature sum of the ROOT-output fitting uncertainty for the parameters (from applying Gaussian fits). Note that Paddle 5 is intentionally skewed so that the larger part of a bimodal distribution was correctly offset-subtracted (discussed in this section).

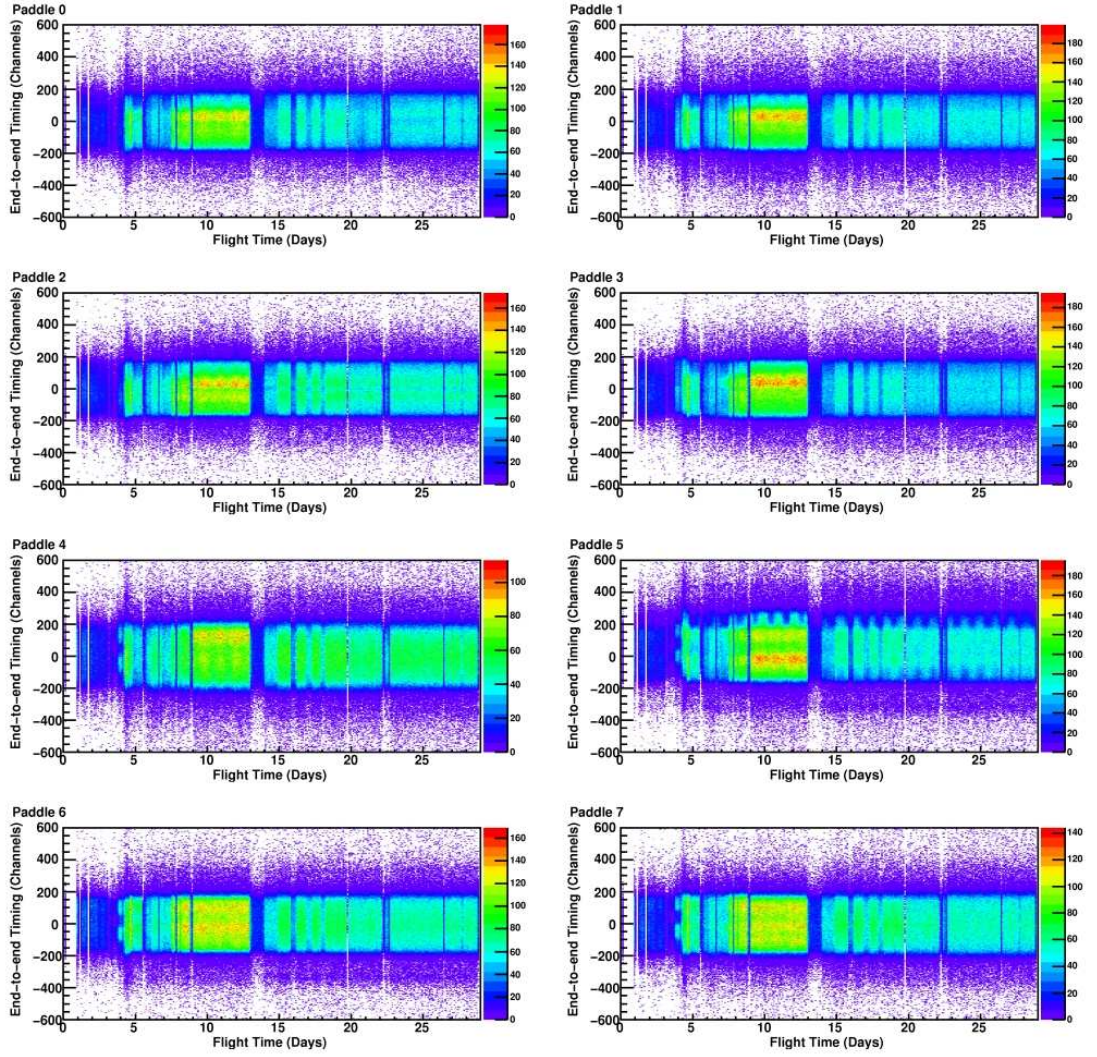


Fig. 5.11 Corrected end-to-end timing for the CREAM II TCD (stump analysis code variable `tcq.fETE[paddle][threshold]`) as a function of flight-time, for the entire flight. Here only entries for *threshold* 0 are shown, but higher threshold behavior was consistent with the trend shown here.

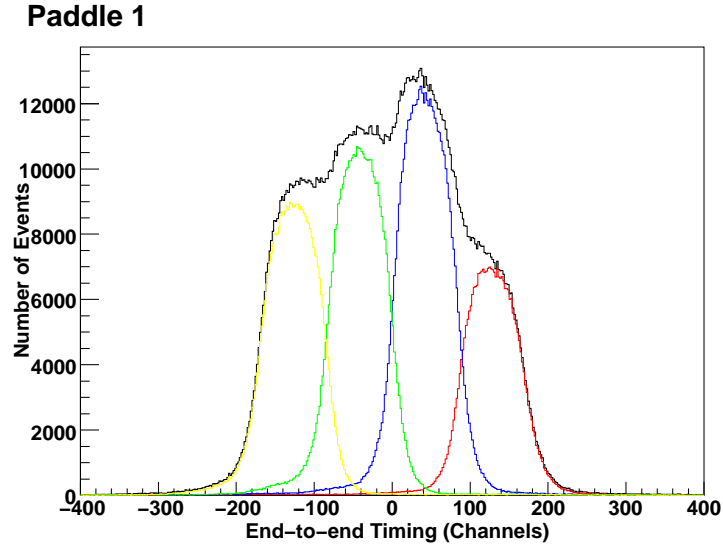


Fig. 5.12 Corrected end-to-end timing for Paddle 1 for the CREAM II TCD (`tcq.fETE[1][0]`), for the entire flight.

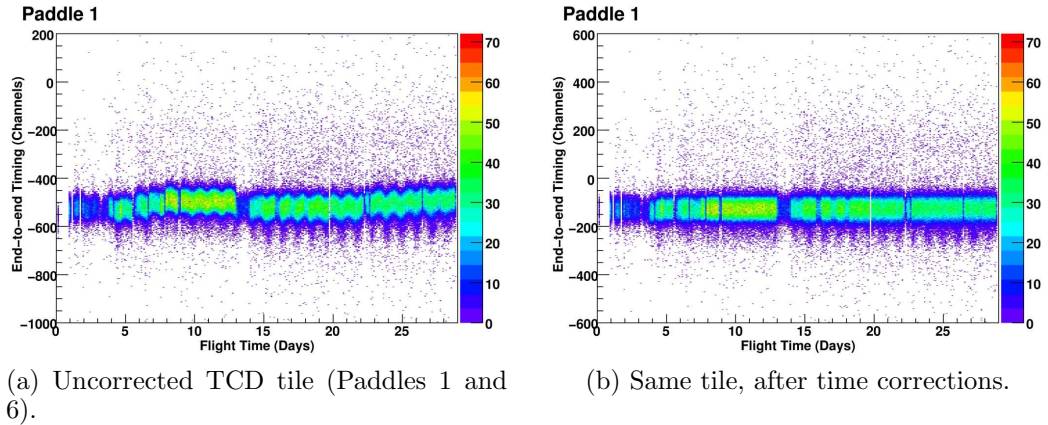


Fig. 5.13 Effect of the end-to-end TCD paddle timing corrections for one tile (defined here by requiring that both Paddle 1 and 6 have all four tubes cross *threshold* 0 and no other paddles with hits). This is representative of other paddles and thresholds.

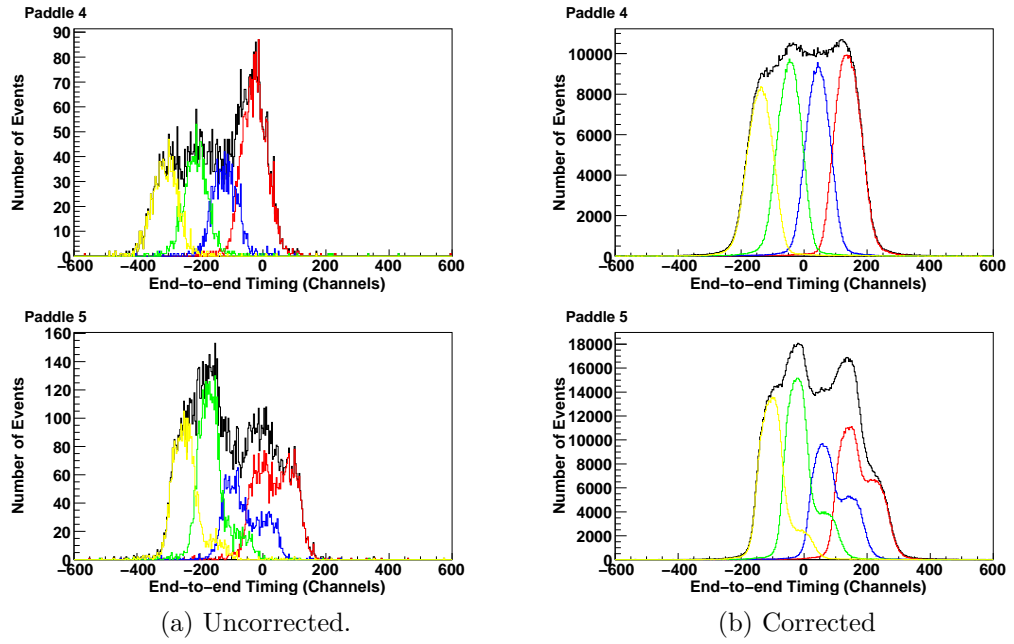


Fig. 5.14 End-to-end timing distribution for Paddle 5 (bottom), showing the smaller bimodal distributions to the right. The equivalent distribution for Paddle 4 (top) is shown for reference. The uncorrected plots shown are for a 0.1 day slice of the flight, so that the ~ 1 day variations did not wash out the distributions. The corrected plots are for the entire flight period.

To produce corrections for this paddle, a slightly different technique was needed. The basic approach taken was to try and produce corrections that ignored the right-most distribution as much as possible. Since the distributions were close in channels and there was mixing between the two (Figure 5.14a), a simple cut of the right-most part was not possible (if it were, it would have also been possible to splice them back together by applying an extra correction to the right-most peak events to move them back on top of the ‘correct’ population). For *threshold* 0, this situation was handled by using a Landau fit for each time slice instead of a Gaussian, because the bimodal component was (usually!) small. For the higher thresholds the bimodal nature was actually more prominent (in value, not in separation), so a more rigorous method was used. The flight was split into 7 time regions where the end-to-end timing had no jump-discontinuities (the edges of the regions were defined by the jumps in DC offset). For each region an upper and lower bound were found visually so that only the more prominent (left-most) of the bimodal contributions were loaded into the histograms for finding the corrections.

Utilizing Paddle 5 for tracking is somewhat problematic, though the situation can be improved somewhat by requiring that the reconstructed position be consistent with the physical pair of crossed paddles. This is in general a very sensible cut anyway and will typically be applied for all paddles, since there is some tail to the distributions even for the healthy paddles. Some extra ambiguity in the position information from Paddle 5 is clearly unavoidable however.

To actually utilize the end-to-end timings corrected in this section for tracking, we must transform from TDC channel-difference to position-units. One approach would be to use the four positions of the tile histograms, and assume 30 cm spacing between them. This would work, but would not be ideal, since we expect the individual tile distributions to be slightly asymmetric (more vertical tracks for the center tiles, more inclined for the outside tiles). An alternate approach is to calibrate off of another detector, which has tracking present at the TCD. In CREAM II, the only other tracking detector is the calorimeter, but its extrapolated tracks would not be expected to be very accurate at the TCD position because of the limited lever-arm (< 10 cm) available. In CREAM I, the TRD was present and provided excellent ~ 1 mm scale resolution extrapolated to the position of the TCD. This is the approach taken in the next section to figure out the proportionality constant to convert from channels to distance.

5.6 TCD Tracking Calibration using CREAM I

The TRD in the CREAM I payload provided excellent mm-scale resolution tracking for particles with charge greater than He. There was no TRD present in CREAM II, so the best tracking available at the z-position of the TCD is derived from TCD end-to-end timing. However, it is possible to use the CREAM I TRD position to provide a calibration for the TCD-derived position for CREAM II (and CREAM I as well).

To turn TCD timing into position, first the end-to-end TDC timing for each paddle is corrected for time-dependent variations as outlined in the CREAM II analysis in Section 5.5. Next, the time-corrected end-to-end is studied as a function of the TRD derived position[28] at the TCD. As will be shown shortly, the relationship between the TCD end-to-end timing and the paddle hit position is very linear.

For the CREAM I flight, the anode PMT readout on tube 11 was not functioning because of a preflight mechanical failure in the PMT base circuit board. All dynode taps performed normally however. Also, tube 6 failed partway through the flight. For this analysis then, Paddles 1,2,3,4,5 and 7 were potentially available. Tracking for Paddle 0 can be recovered for events on scale for TDC 3 and 2, but this was not done here.

Interestingly, the double-valued end-to-end timing behavior observed in Paddle 5 (Figure 5.14) in the CREAM II flight is also present in the CREAM I flight. Paddle 4 also has degraded timing resolution, when compared to other working paddles. Paddle 4 exhibits a different behavior from Paddle 5 because it does not show the multiple-valued behavior with time, but does show a wider timing distribution than the other functioning paddles (Figure 5.18). Some issue common to one of the electronics readout boxes present on one of the ends of these paddles is probably responsible for this. No diagnosis has yet been made, but possible causes are malfunctioning TDC or local-trigger boards. For this analysis then, Paddles 1,2,3,4 and 7 were examined, but the quoted results are presented both with and without Paddle 4 included.

A subset of the CREAM I flight from day 19 to day 26 (January 2nd to January 9th) was used for this position-calibration because it was a period of the flight with fairly stable TCD timing response, and good instrument stability. The following cuts were implemented for the TCD: require that both S3 PMTs pass the first TDC threshold and require that both tubes on a paddle pass the first TDC threshold as well. The uncorrected and corrected end-to-end timing in the CREAM I paddles are shown in Figures 5.15 and 5.16, respectively. Consistent with the procedure for CREAM II, the overall paddle timing offsets have been removed and the individual tile distributions slightly tightened. However, since this is for a stable subset of the flight data and not the entire flight, the changes in the individual tile-width distributions is much less pronounced. Table 5.5 summarizes the offset subtraction and tile width distributions in the same fashion as Table 5.4 did for CREAM II.

<i>Paddle</i>	<i>Uncorrected</i>		<i>Corrected</i>	
	<i>Mean Offset (Channels)</i>	<i>Mean Tile Width (σ) (Channels)</i>	<i>Mean Offset (Channels)</i>	<i>Mean Tile Width (σ)(Channels)</i>
1	-389.02 ± 0.57	27.20 ± 0.35	-0.14 ± 0.56	26.80 ± 0.34
2	-334.91 ± 0.68	29.80 ± 0.47	0.36 ± 0.62	27.17 ± 0.41
3	-304.69 ± 0.71	30.70 ± 0.45	-0.26 ± 0.60	25.77 ± 0.36
4	-62.00 ± 0.98	32.47 ± 0.70	-1.36 ± 0.98	32.40 ± 0.69
7	-32.27 ± 0.65	27.17 ± 0.40	-0.99 ± 0.63	26.26 ± 0.38

Table 5.5 Uncorrected and corrected end-to-end measurements for the stable subset of the CREAM I TCD (day 19 to day 26). Error estimations and measurements are made following the same procedure as for Table 5.4. For reasons discussed in this section, Paddles 0,5 and 6 omitted.

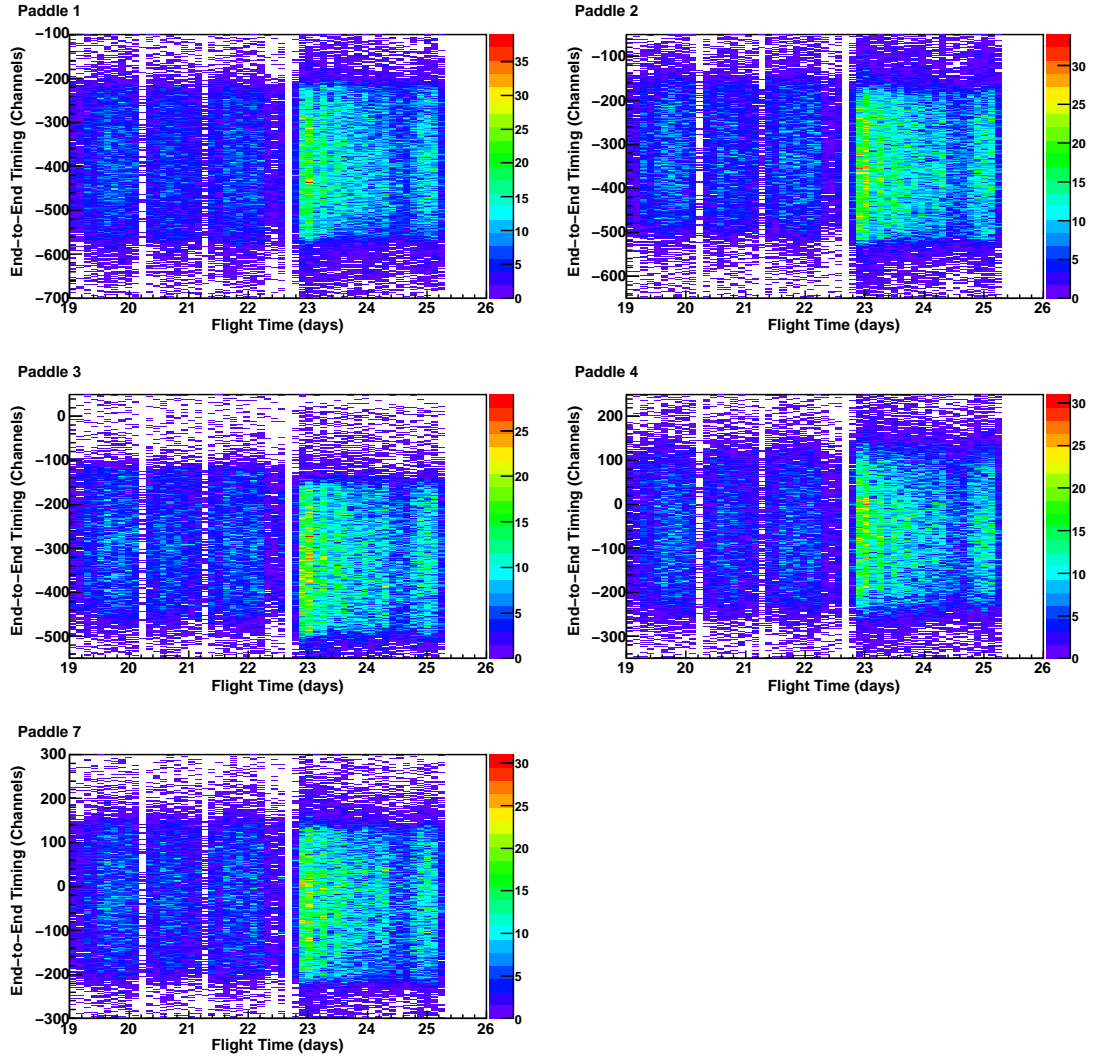


Fig. 5.15 Uncorrected end-to-end TCD time difference (in units of TDC channels), shown as a function of flight-time (in days), for the 5 CREAM-I paddles selected.

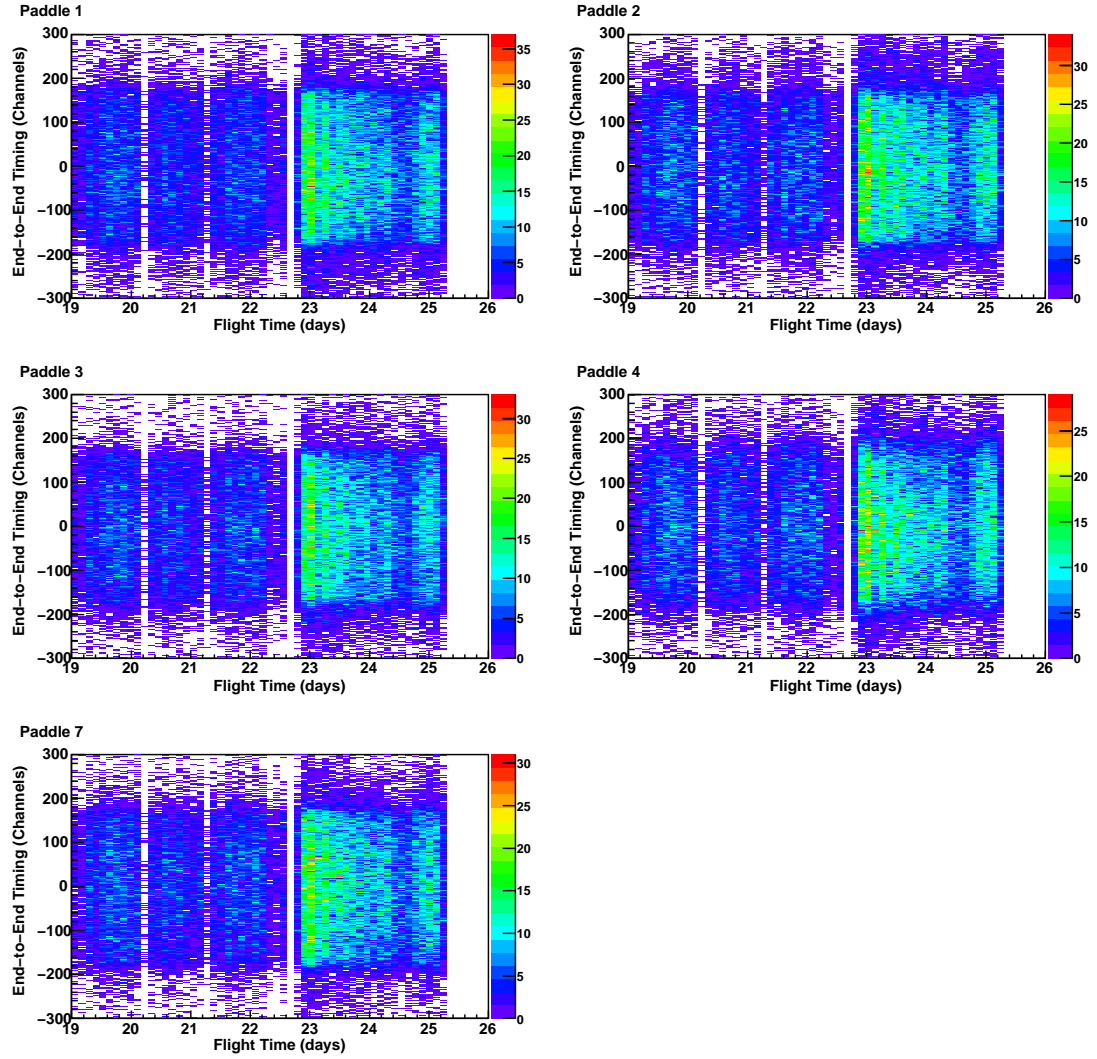


Fig. 5.16 Time-corrected end-to-end TCD time difference (in units of TDC channels), shown as a function of flight-time (in days).

The corrected timing distributions for Paddles 1,2,3 and 7 in CREAM I are quite consistent with each other, and we use them here to find our timing-to-tracking conversion (Figure 5.17). Paddle 4 shows degraded timing resolution, but can be included to try and find a more conservative worst case tracking accuracy. The corrected end-to-end timing is quite linear with TRD-derived position so we use a simple linear relationship to convert to distance units.

An unconstrained simple linear fit would be skewed by the background of uncorrelated points in these plots, so instead the following procedure is used: A linear fit is done to the histogram, then the histogram is regenerated with a cut removing all points that do not lie within 10 cm of the best-fit line. This procedure is iterated until the current slope and offset-values agree to within 1% of the previous best-fit values. Between 5-9 loops were necessary for the fits to converge. Table 5.6 summarizes the results of these fits.

<i>CREAM I End-to-End Timing-to-Position Conversion</i>		
<i>Paddle</i>	<i>Slope (Channels/cm)</i>	<i>Intercept (Channels)</i>
1	2.854 ± 0.028	0.2377 ± 0.0024
2	2.737 ± 0.027	-1.025 ± 0.010
3	2.768 ± 0.028	-0.998 ± 0.010
4	2.931 ± 0.029	-6.277 ± 0.063
7	2.796 ± 0.028	0.2139 ± 0.0021
Mean	2.817 ± 0.063	-1.567 ± 0.065
Mean (No Pad. 4)	2.789 ± 0.056	-0.393 ± 0.014

Table 5.6 Results of constrained linear fits to the distributions in Figure 5.17. These measured parameters can be used with Equation 5.11 to find the particle hit position in a TCD paddle.

To convert end-to-end timing to position we use:

$$x = \frac{\Delta t - b}{m} \quad (5.11)$$

where Δt is the corrected end-to-end timing. For tracking in the CREAM I instrument, the intercept values b can be included, but for CREAM II and beyond we do not know what the values of the intercepts are, so they will be assumed to be zero. Since they were all close to zero for the CREAM I data presented here (and *should* be very close to zero if the offset subtraction correction was successful), this is a reasonable step.

The residual plots (Figure 5.18) of the corrected TCD position-measurement and the TRD track extrapolated to the TCD z-position are shown for all of the five chosen paddles in CREAM I. This provides an excellent estimate of the intrinsic timing-accuracy of the TCD position measurement (since the TRD track can be assumed to provide a much more accurate position than that from the TCD). The individual standard deviations (extracted from the Gaussian fits in Figure 5.18) for the paddles used in this analysis are shown in table 5.7.

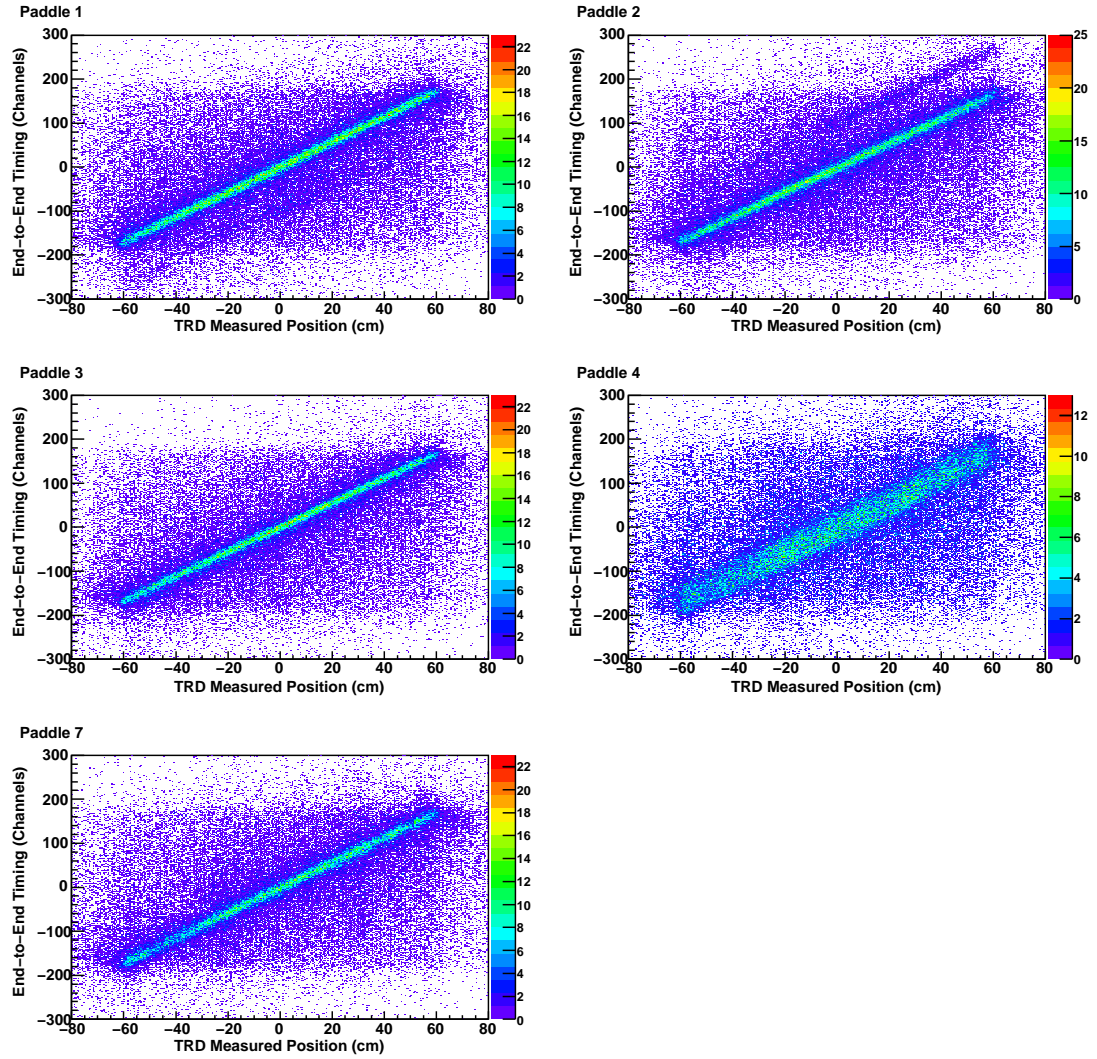


Fig. 5.17 Time-corrected end-to-end TCD time differences for CREAM I paddles as a function of TRD-derived position.

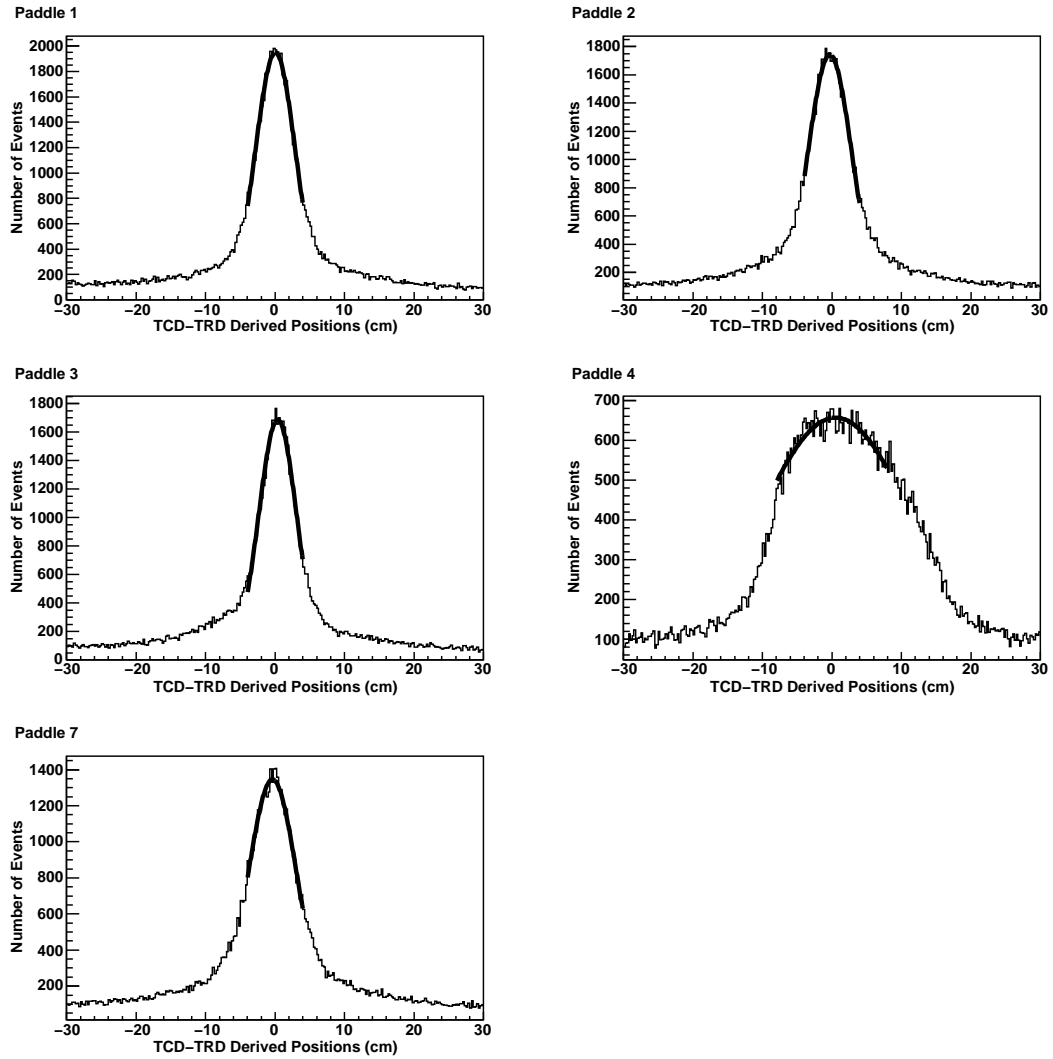


Fig. 5.18 Time-corrected end-to-end TCD measured position for CREAM I paddles compared to the TRD-derived position. The solid curves are Gaussian fits to the distributions.

<i>TCD Position Accuracy</i>	
<i>Paddle</i>	<i>Standard Deviation (cm)</i>
1	2.869 ± 0.026
2	3.137 ± 0.034
3	2.721 ± 0.025
4	11.35 ± 0.40
7	3.523 ± 0.053
Mean	4.72 ± 0.41
Mean (No pad.4)	3.063 ± 0.073

Table 5.7 Average CREAM I end-to-end timing accuracy measured against TRD position, as taken from Figure 5.18. The errors on the mean values are the quadrature sum of the relevant uncertainties.

Excluding Paddle 4, we measure the overall total resolution of the TCD tracking to be $\delta_{TCD} = 3.063 \pm 0.073$ cm. Equation 5.11 (using the conversion of 50 ps/channel) implies a combined TCD (including both tubes on a paddle) timing resolution of $\sigma_{TCD} = 0.427 \pm 0.011$ ns. The error here has been estimated by propagation of errors as shown on p. 102 of [59]. This value of the timing resolution is the quadrature sum of the resolution for the individual tube TDCs. Therefore, we estimate the timing resolution for an individual tube TDC to be:

$$\sigma_{tube} = \sqrt{\frac{1}{2}}\sigma_{TDC} = 0.3019 \pm 0.0080 \text{ ns} . \quad (5.12)$$

In Section 7.6 we will estimate the expected TCD timing resolution arising purely from photon propagation physics. Using this and the estimate above, we will deconvolve the total resolution found above into a resolution due to the physical-detector and that due to the readout-electronics/PMTs.

Chapter 6

CREAM II Charge Calibration and Performance

6.1 Scintillator Response

The response of scintillator material to ionizing radiation is discussed in Appendix A. Of particular note here is the Z^2 dependence of the scintillator response, which makes scintillators well suited as charge-sensitive detectors (among other reasons). The light output from a scintillator is also directly proportional to the path-length of the incident charged particle through the scintillator material and the light emission is also isotropic in the material. Attenuation due to propagation in the material is also an important effect to account for, as is non-linear scintillator response (for higher-charged ions) due to saturation in the scintillator material. All these effects convolved together require tracking and energy (or β) dependent corrections on the order of 50% to provide for maximum charge resolution from a scintillator-based detector [28]. Conklin [13] expresses the response of a scintillator as:

$$f_{PMT}(Z, \beta, x, y) = \alpha Z^2 f_{BB}(\beta) f_{sat}(Z, \beta) f_{map}(x, y) \sec \theta \quad (6.1)$$

with α a normalization constant, f_{BB} the Bethe-Bloch (Equation A.1) response (with the Z^2 response explicitly separated), f_{sat} is the scintillator-saturation response and f_{map} is the attenuation response (a function of the impact position, (x,y)) and θ the particle angle-of-incidence (measured relative to the vertical). In the CREAM I flight, excellent tracking was available from the TRD for species $Z \geq 3$. Additionally, β was available from the CD. This allowed for determination of the factors above using flight data, as presented by the thesis from Conklin [13].

For CREAM II the TRD was not present, so alternate tracking was needed. TCD-based tracking derived from time-of-flight and end-to-end paddle timing was instead used in the analysis presented in this thesis. Also, the CD readout in CREAM II did not function properly (discussed in Section 4.10) so β was not an available quantity for TCD calibration. Fortunately, the energy regime of interest for CREAM II ($> 1TeV$) is the $\beta \approx 1$ region, so β -dependent corrections are less important than for the CREAM I TRD-based analysis. The more limited tracking resolution is a factor which does reduce the ultimate TCD charge-resolution available however.

For our purposes, we can recast Equation 6.1 into a form more useful for the situation at hand. First, there is an electronics pedestal present from the ADCs which must be subtracted; it has the value of 425 ADC channels. The actual measured PMT ADC signal (f_{ADC}) is thus related to the signal above by $f_{PMT} = f_{ADC} - 425$. The path-length correction and Z^2 dependence can also be taken into account. We can also make the approximation that $f_{BB} = const.$ since $\beta \approx 1$. This also reduces the saturation

behavior to just a function of Z . Solving Equation 6.1 for Z (and collecting correction terms and only treating the attenuation in one dimension) thus yields:

$$Z = \frac{1}{\sqrt{\alpha f_{BB}(\beta) f_{sat}(Z, \beta) f_{map}(x, y)}} \sqrt{\frac{f_{ADC} - 425}{\sec \theta}} \simeq C(Z, x) \sqrt{\frac{f_{ADC} - 425}{\sec \theta}}. \quad (6.2)$$

We will need to empirically find the correction-coefficient function $C(Z, x)$ for each paddle. This procedure is detailed in the remainder of this chapter. There is also some small time-dependent variation in response, which was dealt with in CREAM I [13], but will be neglected here since the variation is of order a few percent. With the precision tracking and β measurement available for CREAM I this was possible to correct for, but it is not as relevant (or as possible to do) for CREAM II. Also folded into this correction coefficient function is a variation in light output due to thickness variations in the scintillator material. These were observed to be of order 10% – 20% during TCD construction so they will have an effect on paddle response. This is one reason why a single attenuation-response function is not found common to all TCD scintillator paddles.

A more useful form of Equation 6.2 can be found if instead of considering the correction-coefficient function to be a function of Z and x we approximate it as a function of the path-length, pedestal-corrected ADC signal (ADC_{pc} , as defined below) and x .

$$ADC_{pc} = \sqrt{\frac{ACDSignal - 425}{PLC}} \quad (6.3)$$

Thus the charge measure from the ADCs will be of the form:

$$Z = C(ADC_{pc}, x) ADC_{pc}. \quad (6.4)$$

6.2 ROOT File Processing

To speed up the development of analysis code, a technique was used to create ROOT files containing only specific subsets of the output from the stump analysis code. In general, with time-corrected TCD quantities, SCD hits and CAL hits all recorded, the ROOT file output from stump would generally consist of a TTree split across 3 different files (due to file-size limitations) with a total size of order 4.5GB.

To produce smaller ROOT files containing only events of interest, post-processing was performed with ROOT scripts that would create ROOT files subject to user-selectable cuts. This was accomplished using the following steps: create a TChain of the root files, define a series of cuts, create a new root TFile using the “recreate” option, use the TTree::CopyTree() function with the cuts applied to make the subset trees, finally, the new file with the new TTree was written to disk.

For the charge-calibration process, separate ROOT files were generated for each paddle being calibrated (8 total). The first cut required was for the `tcq.fTOF[paddle]` variable to be present for the paddle under study. This means that TDC *threshold* 0 was crossed (at a minimum) in both tubes in the paddle and in the two S3 tubes. Next, all other tubes on parallel paddles were required to have no *threshold* 0 crossed. This assured

a limited number of albedo events, and no ambiguity in the path-length correction value found. Finally, any one of the four crossed paddles was permitted to have a signal (both tubes in one paddle, no tubes in the others) for each event. This cut was only applied for the generation of correction coefficients and was not a cut required for analysis of flight data. The same general method was also used to generate a ROOT tree file that contained only events with CAL tracks present.

6.3 SCD Charge Calibration

The SCD analysis code in the stump program finds the pixels in the top and bottom SCD with the maximum signal size (after pedestal-subtraction, gain-corrections and dead/hot pixel masking). This is an effective method of hit-location selection for species above H and He and for events with little albedo present for all species. This method will get the correct hit-locations for charge 1 events without much albedo present. For the charge-calibration outlined here, this method is sufficient, though in general tracking from other detectors is necessary. A more rigorous method to select the proper SCD pixels is to use CAL tracking to find the general area in the SCD where the primary particle passed through, then take the largest SCD signals within a small distance of that location [71]. However, if no CAL track is available for the given event (as it is for most of the calibration events here), then the maximum-pixel method is the best that can be done for determining hit-location.

For tracking we first require that the top and bottom SCD hit-locations agree within 5 cm of each other. We then average them to find X, Y and Z hit-locations in the SCD. The hit-location in the TCD is found from the time-corrected paddle hit-locations found previously (stored in the `tcq.fTCDPos[paddle][threshold]` variables from the stump code). It is required that the measured locations agree with the physical locations of the two paddles in the event. The *threshold* 0 position measurements are used. Once the hit-locations are found in the SCD and the TCD, the particle track can be used to find the path-length correction ($\sec \theta$) for the event using Equation 6.5.

$$PLC = \sec \theta = \frac{\sqrt{(x_{TCD} - x_{SCD})^2 + (y_{TCD} - y_{SCD})^2 + (z_{TCD} - z_{SCD})^2}}{z_{TCD} - z_{SCD}}. \quad (6.5)$$

At this point, the top and bottom SCD signals can be roughly calibrated into charge-units. Empirically the SCD charge was found to be related to the SCD signal by the following functional form and constants (Equation 6.6). An example distribution is shown in Figure 6.1.

$$Z = \frac{\sqrt{\frac{SCDSignal}{PLC}} + 4.7}{6.82} \quad (6.6)$$

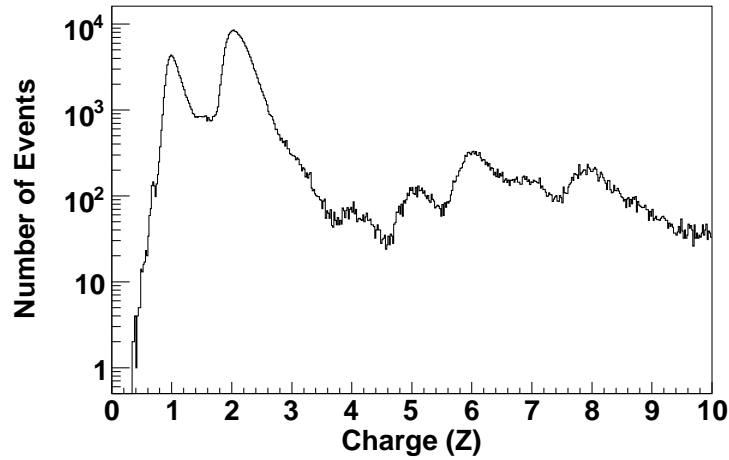


Fig. 6.1 SCD charge measurement (top and bottom layers averaged) for calibration-events requiring only TCD Paddle 1 hit in the X-direction and any (but only one) Y-direction paddle. The PLC correction is determined from TCD and SCD hit-locations. Peaks for H, He, Be, B, C and O are clear.

6.4 TCD ADC Charge Calibration

The goal of the TCD charge-calibration is to find the calibration functions to allow us to use Equation 6.4 to measure the charge of the primary cosmic-ray particles entering the detector. A first step in the correction procedure is to apply the electronics pedestal-subtraction and path-length corrections (Equation 6.3).

Next, the correction-coefficient functions $C(ADC_{pc}, x)$ must be found for each paddle so effects such as light-attenuation in the paddle, nonuniform scintillator response due to thickness-variation, scintillator saturation, etc. are corrected for. Since the results of all these effects are convolved together and each paddle has a unique response, an empirical method is presented here to generate corrections unique to each paddle.

The basic outline of the correction method used is to select specific charge-species events from the corrected SCD response, then examine the response of the TCD ADCs for those events. Charge peaks are evident for H, He, Be, B, C, and O in the SCD, and all those species are used here (Figure 6.1). For ADC 0 for all tubes, H and He are typically on-scale, with He off-scale for some tubes and positions. ADC 1 for all tubes typically has a dynamic range running from He to a bit past Oxygen.

Charge-calibration events were selected in the SCD by requiring that Z be within 0.1 to 0.5 charge-units (depending on species). This was an aggressive cut but was necessary to provide a pure enough selection of test-beam events. For each species, each paddle was sliced into 8 sections of 15 cm each. A histogram was generated for each slice, and a fit was performed to find the most probable ADC channel response for each charge (Figure 6.2). For hydrogen a Landau fit was done for each slice while Gaussian

fits were performed for all other species. For some ADC channels, He would be off-scale for part of the paddle response. If this happened for ADC0 channels, the response-curve was estimated by measuring the distance between the H and He peaks for the portion of the paddle where both were on scale. For the He positions where the He response was off-scale, a position was just generated by adding the measured separation above to the hydrogen value. A similar method was used when He went off-scale in some of the ADC 1 channels with the beryllium-to-helium separation used. For no tubes or ADC ranges was He found to be off-scale for all paddle hit locations or in both ADC gain-ranges simultaneously.

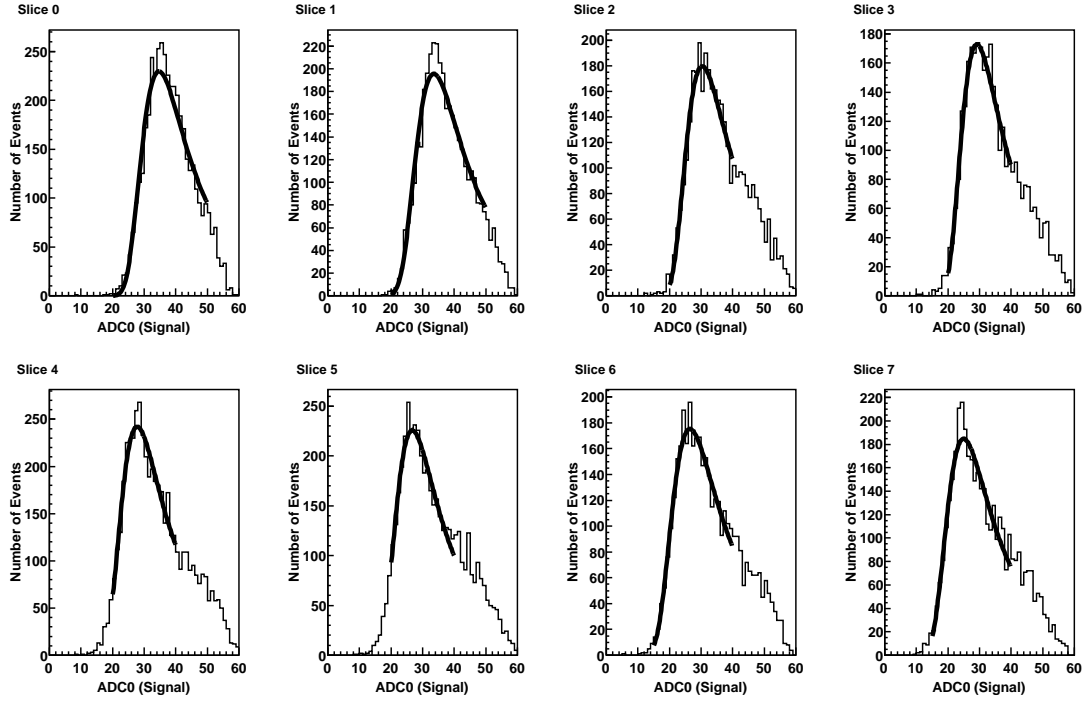
The peaks from all the slice-fits in Figure 6.2 were then plotted in a ROOT TGraph to find a functional relationship between position and ADC response for the species. Third-order polynomials were found to be appropriate for this, and are consistent with experience from the CREAM I TCD corrections (See [13]). Figure 6.3 shows the response-curves found for ADC 0, Paddle 1 and 6.4 shows higher species. The fit-parameters for these species, tube numbers and paddle numbers were stored in files to be read in by the stump analysis software or by stand-alone ROOT programs for extracting charge values from the raw ADC channels, as outlined below.

The individual species-fits in Figures 6.3 and 6.4 are effectively samples at constant Z of the inverse of the correction-coefficient function $C(ADC_{pc}, x)$ which we wish to find. What is needed here is some form of extrapolation between the individual species-curves shown in Figures 6.3 and 6.4. If saturation was not present (and other non-linear effects) we would expect these curves to all be equidistant from each other but clearly they are not. For ADC 0, we only have two data points (H and He) for extrapolation so a linear extrapolation-function is justified (also, saturation is expected to be less important for the lighter species). For ADC 1 however, we have many more points available, so a more sophisticated extrapolation can be done. It was found that the reciprocal of a 3^{rd} -order polynomial performed very well (Figure 6.5).

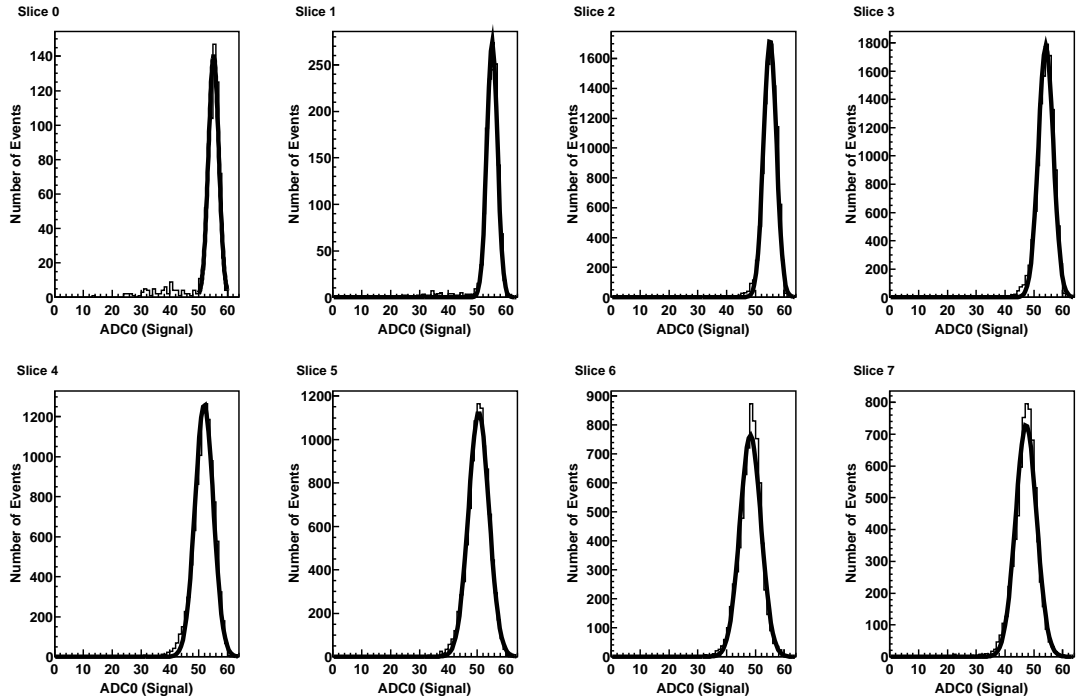
Note that the interpolation is done on a continuous basis: the path-length and pedestal-corrected ADC signal (ADC_{C1}) is calculated for both ADC ranges (if a proper signal is present), then the timing-derived paddle position (from the stump variable `tcq.ftCDPos[tube][threshold]`) is used with the stored species fit-parameters to calculate the extrapolation function necessary to finally generate the charge measured by that ADC (in charge-units). We do require that the raw ADC have a proper signal present as well (not -10 (no data) or 4096 (off-scale)).

6.5 ADC Range Stitching

For stitching the CREAM I ADC 1 and higher-range channels together, a standard approach was used elsewhere [13]. Two adjacent gain-range ADCs were plotted against each other (1 vs. 2 and 2 vs. 3), and a linear region was observed where both ADCs were on-scale. For two reasons this method was unacceptable for stitching ADC 0 and 1 in CREAM II. First, as can be seen in Figure 6.6, there is no linear region between the two ADC ranges. When ADC 0 is saturating, ADC 1 is still turning on. More importantly, ADC 0 displays a saturation behavior that leads to a double-valued behavior. For CNO-scale signals, ADC 0 reads a signal size consistent with a charge between H and He.



(a)



(b)

Fig. 6.2 Hydrogen (top) and helium (bottom) calibration-events (selected by the SCD) for ADC 0, Tube 0, TCD paddle 1 (presented as a representative example). Each histogram is a 15 cm slice along the length of the paddle. For the hydrogen, Landau fits were done to find the most probable value, while Gaussian fits were done for helium. Gaussian fits were done for all higher species in ADC 1 as well (not shown).

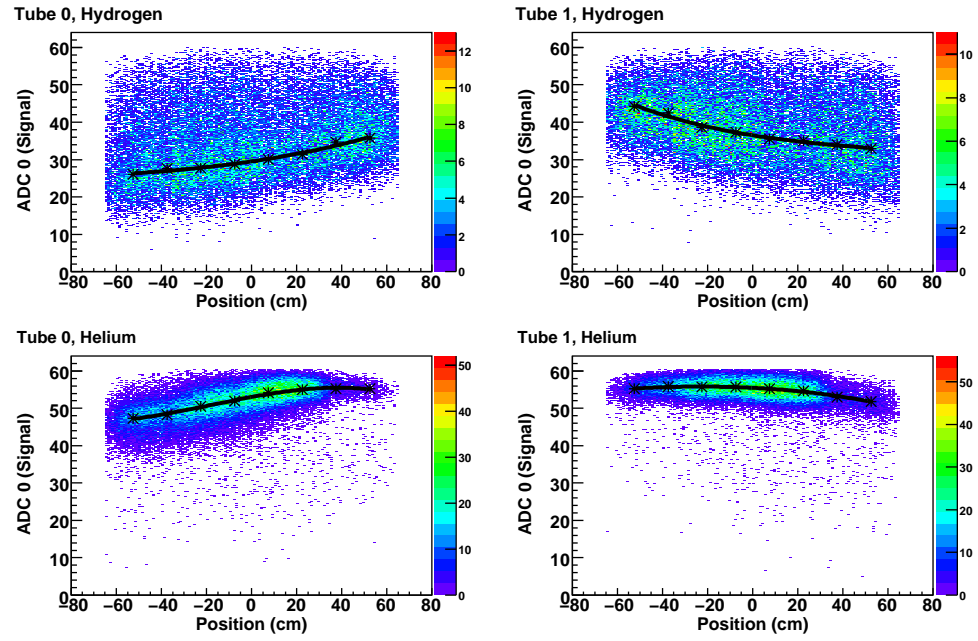


Fig. 6.3 SCD-selected hydrogen (top) and helium (bottom) calibration-events in TCD Paddle 1, for ADC 0 in both PMTs. The ADC signal here is that given by Equation 6.3, so path-length and pedestal corrections have already been included. Overlaid on the 2D histograms are the peak-locations found from fitting to the histograms shown in Figure 6.2 (the markers) and the 3^{rd} -order polynomial fits performed on those points.

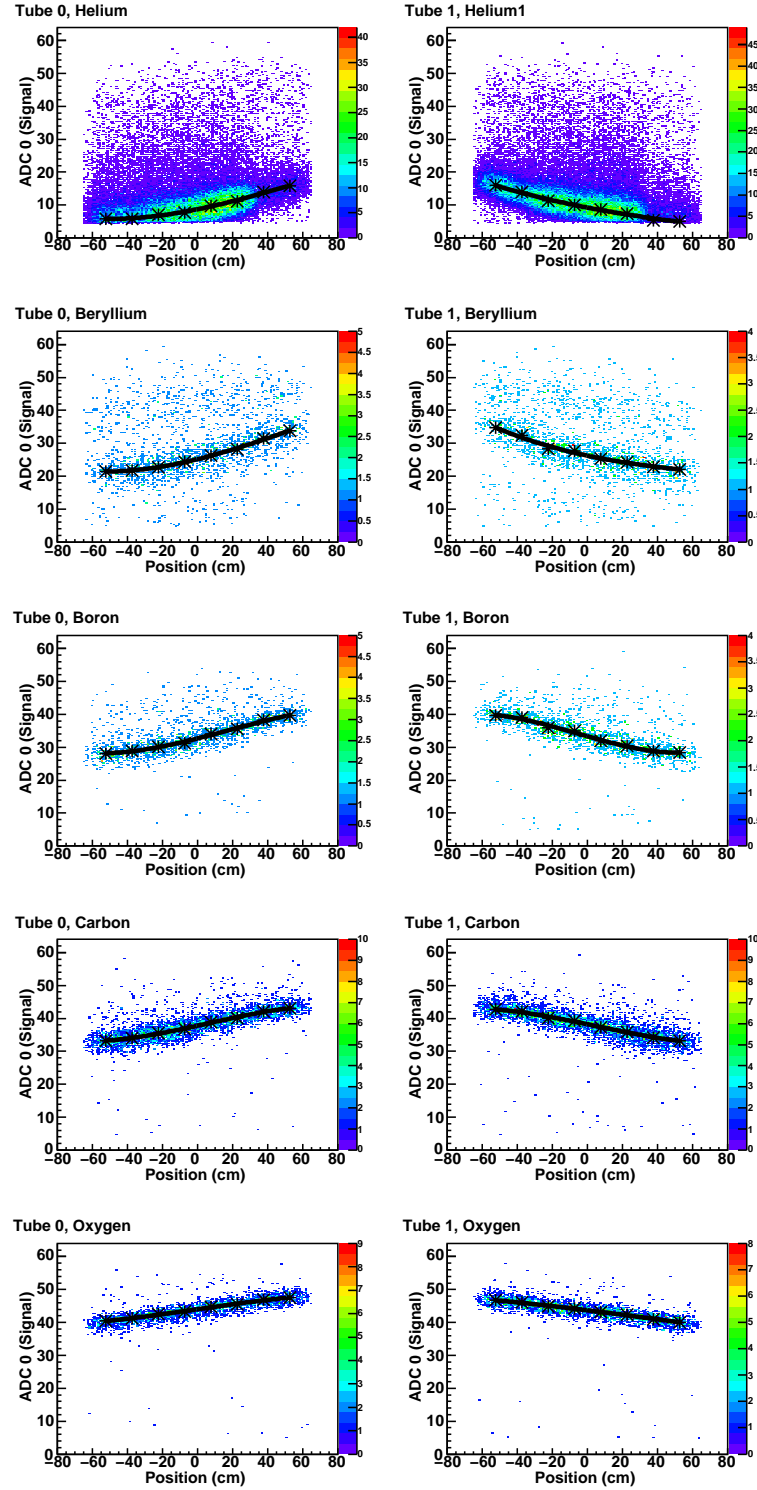


Fig. 6.4 ADC 1 calibration-events for both tubes in Paddle 1 (SCD-selected species). From top to bottom are helium, beryllium, boron, carbon and oxygen, respectively. The same ADC corrections and fit overlays as done in Figure 6.3 are present.

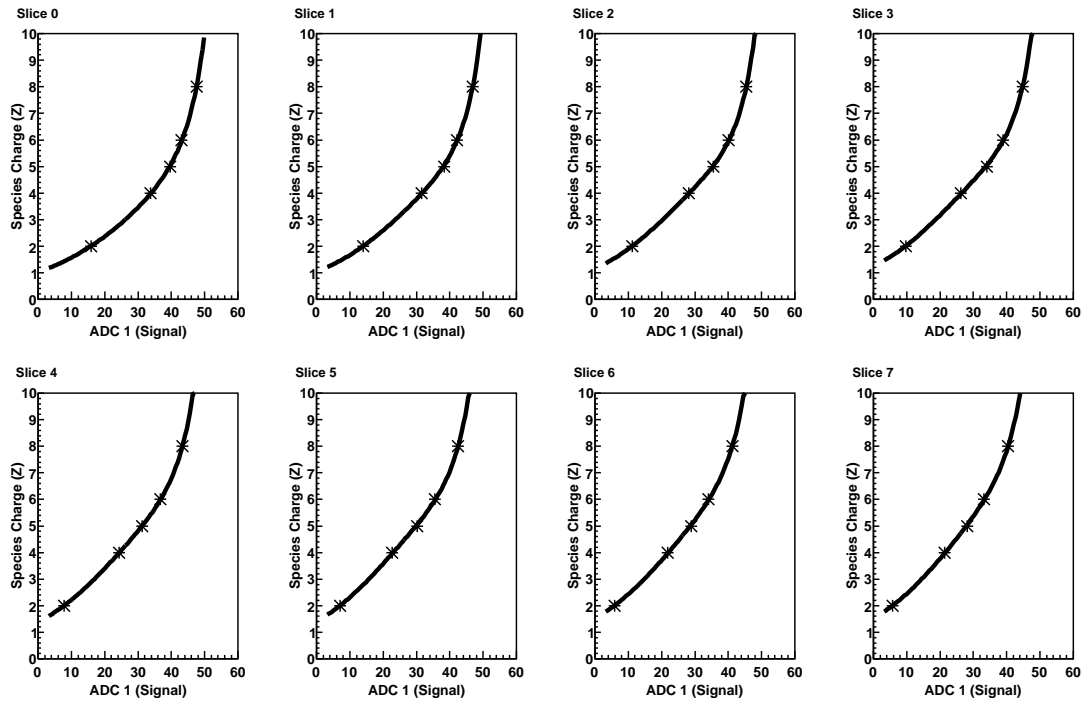


Fig. 6.5 Example fits for extrapolation for ADC 1, tube 0, Paddle 1, for representative 15cm slices down the paddle-length. The points here are the calculated values from the position-fit functions, the fits performed are reciprocals of 3rd order polynomials.

Therefore it is not acceptable to simply splice the ADCs together at an arbitrary value of ADC 0. This double-valued behavior is believed to be an effect in the PMT base-circuitry or in the PMTs themselves and not a readout-electronics issue, though the exact cause is not currently known.

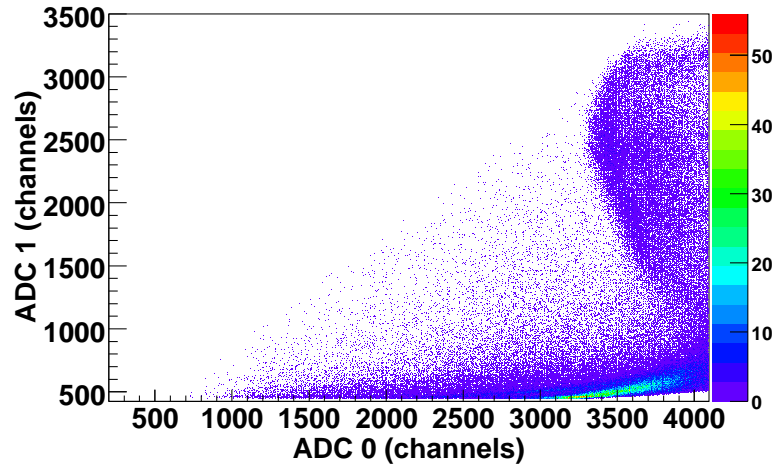


Fig. 6.6 Tube 0, Paddle 1, ADC 0 as a function of ADC 1. These ADCs are in units of channels and have no corrections applied. For reference, helium is typically located around 2500 channels and above in ADC0, while CNO are typically of order 2700 channels in ADC 1. The double-valued behavior is clear here.

A very simple solution to ADC gain-stitching was implemented which was insensitive to the double-valued behavior and not affected by the lack of a linear overlap region between the ADCs. The individual ADCs (0 and 1) were each separately corrected into charge units as outlined above, then the two were compared, and the one with the highest charge value was taken as the correct charge measure for that particular PMT. This is sensible since the double-valued behavior will manifest itself as ADC0 claiming to measure a smaller charge than is correct when ADC1 will be reporting the correct charge. Before ADC1 is on scale, ADC0 will not experience the double-valued behavior. Thus this simple method will correctly transition between the ADC gain ranges, and not be sensitive to false under-reporting of charges due to the double-valued response in ADC0.

6.6 ADC Charge Resolution

The ADC measured TCD charge for Paddle 1 is shown in Figure 6.7, along with the average charge of the SCD and the TCD together. There is an agreement-cut included here for the average plot, requiring that the two detectors agree to within one charge

unit. The widths (σ of the Gaussian fits) of the helium and carbon peaks are shown in Table 6.1.

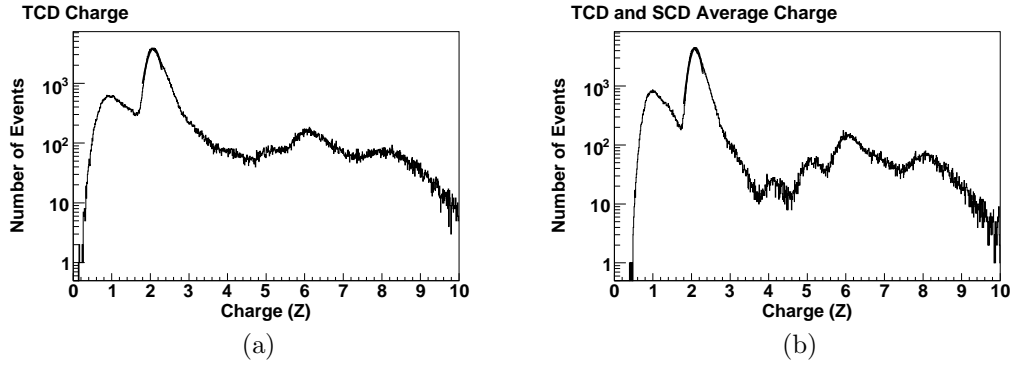


Fig. 6.7 (a)TCD charge measure for Paddle 1, including both PMTs, and a charge-agreement requirement for both tubes to agree within one charge unit. (b)Average of the TCD (from (a)) charge measure and the SCD charge measure, requiring agreement between the two detectors of within one charge unit.

The ADC-derived charge resolution found here for one paddle only is not as good as will be found in Chapter 8 when we include both TCD paddle layers, as well as introduce an implicit low-energy cut when we require calorimeter hits to be present. The distributions here contain large numbers of lower-energy events, presumably below minimum-ionizing energy in the Bethe-Bloch equation (Equation A.1). Thus we do expect some broadening of these distributions.

6.7 TDC Timing-Charge Dependence

An original goal of the CREAM TCD was to use the Time-to-Digital Converters to measure the slope of the leading-edge of the PMT pulses (slew-rate). This measure would be very good at excluding any contamination from albedo particles since the charge measurement would take place in the first few ns of the signal. Because the ADCs simply record the peak PMT pulse value that arrives in a window of several micro-seconds, they are susceptible to contamination if there is a large amount of albedo present. The minimum arrival-time for light from an albedo particle at a PMT in a TCD paddle is ~ 3.6 ns after the arrival of light from the primary as calculated by Conklin [13]. For species above helium and for energies with little albedo present, this should not present a problem, but for hydrogen and helium at energies sufficient to create large calorimeter showers, it is an issue. This will be discussed in more detail in the next chapter.

To evaluate the leading-edge timing method, a period of the flight with stable TDC response was chosen. As seen in Chapter 5, the uncorrected end-to-end and time-of-flight measures displayed time variations, including large jump-discontinuities occurring around instrument resets and power cycles. These arose because of jumps present in

<i>Detector</i>	<i>Species</i>	<i>Width (Sigma)</i>
SCD	He	0.16975 ± 0.00075
	C	0.2601 ± 0.0082
TCD	He	0.16888 ± 0.00080
	C	0.405 ± 0.028
Average of SCD and TCD	He	0.14633 ± 0.00049
	C	0.296 ± 0.012

Table 6.1 Charge resolution (for helium and carbon) for the SCD, TCD Paddle 1, and average of the two. Both TCD paddle tubes are required to agree to within one charge unit, and the TCD and SCD are required to agree within one charge unit for the average shown. Other Paddles were consistent with these values, and the charge-resolution for the TCD as a whole will be presented in Section 8.3

the raw TDCs, before subtraction and averaging. The flight period $14 < T < 22$ days in CREAM II had stable TDCs not displaying these sorts of jumps and was chosen for investigating the effectiveness of the edge-timing method.

As discussed in Section 4.4.1, there are four TDCs instrumented to every PMT in the CREAM TCD. In the stump analysis code, they are recorded as the variable `tcd.fTDC[tube][threshold]`. Thresholds 0 and 1 are instrumented on each PMT anode, and 2 and 3 are on dynode 11 (Table 4.2).

Threshold 0 is set low but above noise so it is sensitive to all species with full efficiency, while threshold 1 is set approximately at the peak of the hydrogen distribution. Specifically, it is calibrated on the ground using atmospheric muons which are all generally at or above minimum-ionizing. The difference in the TDCs for thresholds 0 and 1 should give a quantity for discriminating between hydrogen and helium. As we will see in Section 7.9 from the results of an optical simulation (with readout electronics resolution factored in), this measurement might not have sufficient resolution to discriminate between the species. Figure 7.7 (b) results from that simulation and shows simulated hydrogen and helium events in the TDC 0-1 difference with a large degree of mixing, and no clear separation between the distributions. For the time-limited sample for Paddle 1, Tube 0 examined here, Figure 6.8 shows the same plot for flight data, with species selection using the charge-calibrated ADCs instrumented on that paddle. Also present are cuts excluding species above helium and requiring only one crossed paddle (Paddle 7) to partially exclude position variation. As expected, the distributions appear mixed to a similar degree as in the simulated events. The same plots were tried for all other tubes and paddles with the same results. This behavior is not limited to this paddle or tube, thus we can conclude that the TDC difference measure is not helpful for discriminating between cosmic-ray hydrogen and helium.

Threshold 3 was set on-scale for helium, while threshold 2 was set to exclude most helium so it could contribute to the TCD ZHI trigger and limit the trigger rate so that efficiency would not be compromised for BCNO and higher events (primarily CREAM I related in this case). Figure 6.9 shows the difference in threshold 3-2 timing (again,

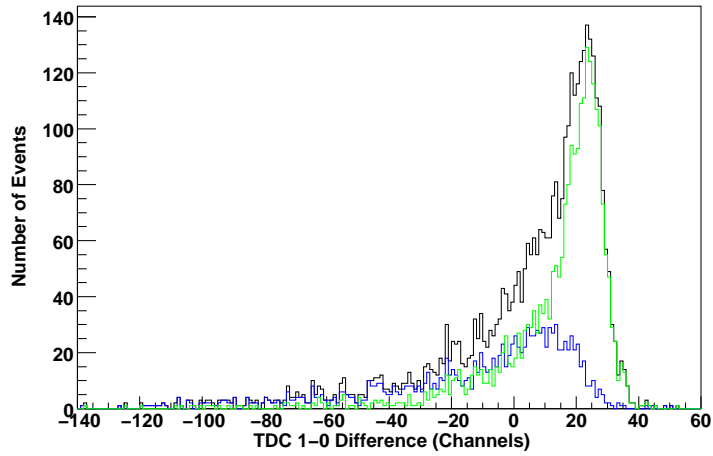


Fig. 6.8 Threshold 0-1 time difference (Tube 0, Paddle 1) measuring the leading-edge timing for CREAM II flight data. Events selected as hydrogen by the charge-calibrated ADCs are colored blue, while green are helium. The black distribution is the sum of the two, and shows no separation between the two species. The X-axis here is in TDC channels, which are 50 ps/channel in width, and contains an arbitrary offset.

threshold 2 is set higher than 3 here). In this case, the leading-edge slope measure does seem useful for at least discriminating between hydrogen and helium tail events and BCNO species. This measurement is not used in the analysis presented in this thesis, but it might prove useful for later work.

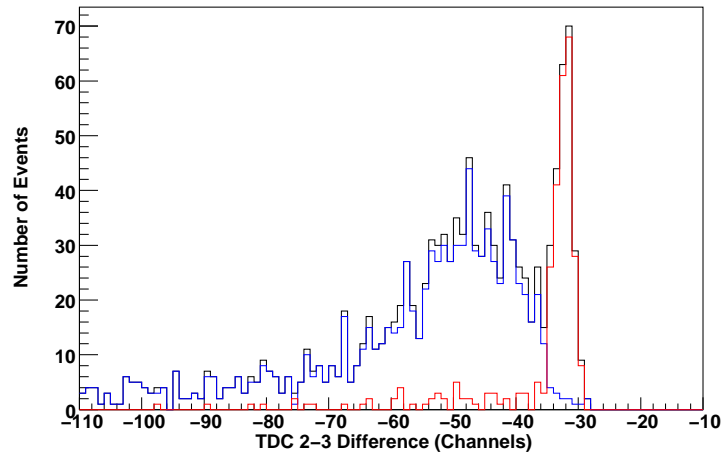


Fig. 6.9 Threshold 3-2 time difference measuring the leading-edge timing for CREAM II flight data (again for the same representative paddle and tube as used in Figure 6.8). Events selected as hydrogen and helium by the charge-calibrated ADCs are colored blue, while red are BCNO. The black distribution is again the sum of the two. The X-axis has the same units as in Figure 6.8. and the same cuts are applied.

Chapter 7

CREAM Timing Charge Detector Optical Model

A model of a CREAM TCD paddle was constructed using the GEANT4 [72] simulation package. The purpose of this model was to better understand the optical response of the paddles to both the primary cosmic rays, and to albedo particles from the calorimeter.

The complete simulation consists of a GEANT4-based model of one TCD paddle, plus optionally the tungsten calorimeter and associated carbon targets. Optical photon physics is included in a separate module which is then registered with any physics model being used. The output for each event is written to an ASCII file. The output file is read in by a stand-alone C++ program which models PMT and electronics response, and outputs a ROOT [69] tree for analysis.

7.1 GEANT4 Coding Overview

The GEANT4 simulation toolkit provides a large collection of C++ classes tailored to the simulation of nuclear and particle detectors. The simulation code is generally split into source code and header files dedicated to separate tasks.

The physical configuration and material properties of the various components (both sensitive and passive material) are usually contained in a Detector Definition. This definition contains an instance of the `G4VPhysicalVolume` which defines the physical world that objects will be placed into. Objects to be placed into the world volume are first created as so-called logical volume using the `G4LogicalVolume` class to create a definition for an object (shape, dimensions, composition, optical properties, etc). After the object is defined and its attributes are set, a physical copy (or arbitrary number) of the object can be placed into the world volume using `G4PVPlacement` class.

The selection and construction of a physics model follows a similar approach. Although included physics models are available pre-packaged with GEANT4, it is also possible to construct custom physics models by selectively adding only the particles and interactions of interest. Classes are available for many other functions as well including messaging (for implementing commands that change the detector or physics properties at run-time), defining types of sensitive detectors, tracking, output and user-defined cuts.

7.2 Detector Definition

The TCD paddle model consists of a block of plastic scintillator of dimensions $120\text{ cm} \times 30\text{ cm} \times 0.5\text{ cm}$, twisted adiabatic light guides, aluminum foil wrapping, a glass face for the PMTs, and small aluminum disks to approximate the PMT photocathodes. Figure 7.1 illustrates the paddle elements modeled.

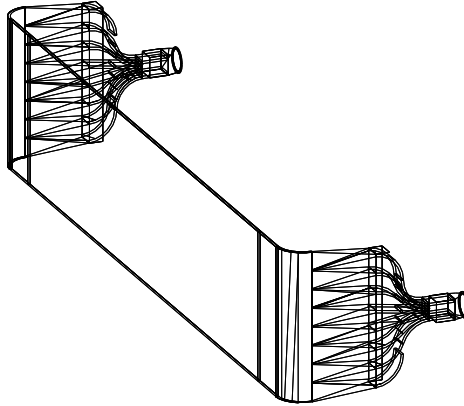


Fig. 7.1 GEANT4 model of a CREAM TCD scintillation paddle. Note that some parts are missing from this picture due to a known rendering issue with GEANT4, however all components are actually present in the code for physics interactions.

The light guide models each consists of 28 individual pieces of BC802 acrylic. The light guide parts are assembled into a `G4LogicalVolume` using repeated iterations of `G4AdditionSolid`, `G4UnionSolid` and `G4SubtractionSolid` classes. These classes allow simple shapes predefined by classes such as `G4Box`, etc., to be combined into one logical volume to make an object of arbitrary complexity. The foil wrapping is constructed in a similar way.

Once all the individual parts for the paddle are assembled into logical volumes, physical instances of all the parts are placed into a `G4AssemblyVolume` (this is necessary to make a collection of logical volumes into one logical volume). Then one copy of the paddle logical-volume is placed where desired in the world volume. Using the `G4AssemblyVolume`, we could extend this model to include placing more than one paddle if desired, though this has not been done.

The calorimeter consists of 20 tungsten plates, plus two carbon targets. By default the calorimeter is not placed in the detector, but it can be inserted with a simple command.

The bulk material properties of BC408 (scintillator), BC802 (acrylic light-guide material), glass, aluminum, tungsten, and graphite were defined manually. The optical properties (both bulk and surface) were also defined for all materials present in the paddle using instances of the `G4MaterialPropertiesTable` class. The optical surface properties of each part were also set by creating a `G4OpticalSurface` class for each, and attaching a `G4MaterialPropertiesTable` to it.

One important optical property of the BC408 scintillator is the scintillation yield. This was made adjustable for debugging and prototyping reasons via a `G4UI messenger` class. The yield for BC408 is approximately 10,000 photons/MeV deposited energy ([58] and p.167 of [59]), however the simulation runs were typically done at a value of 3000. The reasons for this were twofold: to approximate the quantum efficiency of the PMTs,

and to dramatically increase the speed of the code because there were 2/3 fewer optical tracks to calculate.

7.3 Sensitive Detectors and Hit Collections

Two different types of sensitive detectors were implemented in the model. One detector was used to find the energy deposited in the TCD scintillator paddle, the other to find photon arrival times at each PMT.

In the first implementation of the detector, the scintillator logical volume itself was set as a sensitive detector. The scintillator sensitive detector then yielded the total energy deposited in the scintillator, and the average position of the hit. The sensitive detector then recorded those values into an instance of the G4VHit hits collection class.

The PMT sensitive detector is a bit more involved because GEANT4 does not implement a PMT type detector. To work around this limitation, the G4UserSteppingAction class is implemented. The boundary status of each track is examined such that those optical photons which reach one of the photocathodes defined in the detector definition each count as a hit. The PMT sensitive detector is called by the stepping action when this occurs, and then the desired quantities are stored in the PMT hits collection.

For each photon which arrives at a PMT we store the following: the PMT struck (PMT ID), the arrival time, the time it entered one of the light guides (to study dispersion), the number of reflections it underwent, and the total distance it traveled from generation.

The detection efficiency of the PMT photocathodes is parametrized in the detector definition. For a realistic PMT this would be the quantum efficiency of the PMT, and would also be dependent on the wavelength of the incident photons. Since our PMT wavelength response and the output of our scintillator were well matched we did not include any energy dependence in our PMT response. Furthermore, the efficiency of photon detection for our PMTs was set to 100%, because this was compensated for by setting the scintillation yield to 30% as discussed above.

7.4 Physics Models

This simulation can utilize any of the built-in GEANT4 physics models to handle electromagnetic and hadronic interactions, such as QGSP (Quark-Gluon String Precompound), QGSC (Quark-Gluon String CHIPS), LHEP (Low and High Energy Parametrized) and others. Optical physics is added separately by creating an instance of the G4VPhysicsConstructor class to which we add all the relevant physics for the G4OpticalPhoton class. We then register this module with any particular physics model that is being used. The GEANT4 optical processes included were the following: scintillation, Cherenkov radiation, optical absorption, optical Rayleigh scattering and optical boundary processes.

7.5 Signal Digitization

An output for each event is generated in the `G4UserEventAction` class. At the end of each event, the contents of the two hits collections, plus some additional information about the event, are formatted and appended to an ASCII file for later processing. Information stored includes arrival time of photons at each PMT and light guide, energy deposit in the scintillator, position of the primary hit, incidence angle of the primary track, number of reflections for each photon, number of photons absorbed (and in what volume), charge of the primary and an event number.

The PMT output from the GEANT4 simulation is a list of photon arrival times. To produce realistic PMT-like pulses, each photon needs to be convolved with the PMT single-photoelectron (PE) response. The average single-PE response was measured with an actual flight XP2020 PMT, read out with a fast digital oscilloscope. The PMT was placed in a dark box, with a blue LED driven by an HP 33120A fast waveform generator. The PMT anode was read out by an HP Infinium digital oscilloscope.

To measure single-PE pulses, the LED driving voltage and pulse width was adjusted down until the PMT output became small and intermittent. Once in this intermittent state, the average pulse size stopped decreasing, and the intermittent nature was a manifestation of the statistical nature of the PMT response to single photons (the quantum efficiency). The oscilloscope was set to trigger off the PMT output so that LED pulses which did not produce a PMT signal were excluded from the average. This also prevented time-jitter in the light output of the LED-pulsar system from smearing the average PMT pulse. The waveform was output from the oscilloscope at a sampling of 1 ns .

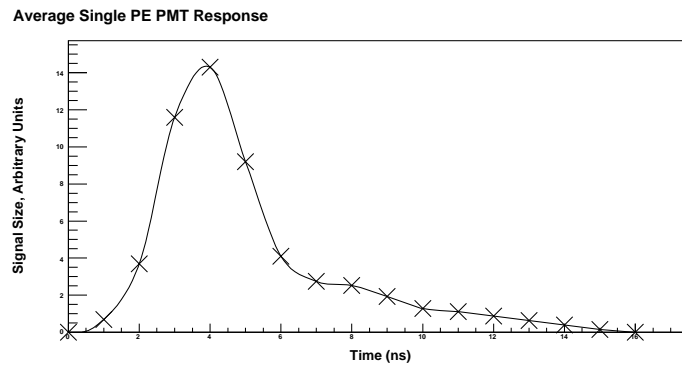


Fig. 7.2 Average of 1024 single PE size events from an XP2020 photomultiplier tube. The voltage units here are arbitrary, and the polarity has been switched to make the pulse positive going.

In several different stand-alone C++ programs written for analysis of the GEANT4 output, a total simulated waveform for each PMT was generated by convolving the average individual PE response with the arrival times of all photons incident on the photocathode. The single PE response was stored in a 17-element array, with each entry being the signal height (in arbitrary units)(Fig. 7.2), and each sampling separated by 1 ns. Since the expected resolution of the readout electronics is of order 50 ps, the generated PMT pulse needs higher resolution than the sampling of the single PM pulse. To compensate for this, a version of the single PE pulse is created in a new array with 320 elements (50 ps spacing), and is filled by extrapolation between the elements of the initial 17-element array.

To store each generated PMT pulse, a large 5000-element (250 ns) array is created for each PMT. To generate the total pulse for each PMT per event, the single PE response arrays are time-shifted by the arrival time of each photon, then summed in the storage array for that PMT. One version of the digitization software simply outputs the PMT waveform for comparison with actual PMT waveforms measured in the lab. The output is in the form of a ROOT tree.

In general it is desirable to experimentally measure the average waveform for a large number of PMT pulses to determine an average response. This is possible in this version of the digitization software as well. If more than one event is present in the file being processed, all generated waveforms are averaged but with a time offset introduced to ensure a consistent trigger threshold for the start time, consistent with how an oscilloscope triggers at a specific signal level. The convolution of the simulated photon arrival times with the measured single-PE response yields a realistic PMT response. This is illustrated in Fig. 7.3, which shows the average of 256 experimentally measured atmospheric muon pulses, with the average of 1000 simulated muon pulses. An overall 90% scale factor was applied to the time of the simulated PMT pulse to decrease the width of the pulse. This was introduced to adjust for any systematic bias introduced from slew rate and sampling limitations of the single PE pulse measurement.

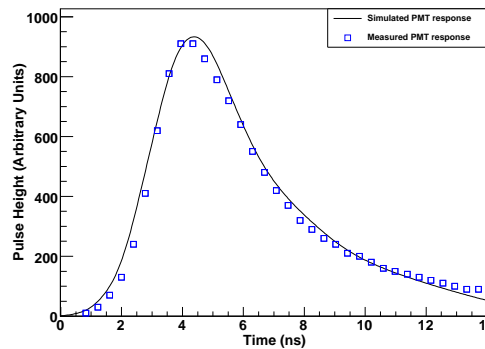


Fig. 7.3 The average PMT response for muons - simulated and measured.

A version of the digitization software which output simulated event information in a form consistent with the flight readout electronics was also produced. TDC (Section 4.4.1) readout was simulated by finding the time over which the constructed PMT pulse for each event crossed a preset threshold (4 total per tube, just as in the flight electronics). The determination of a calibration conversion to threshold values similar to the ones in flight was possible by utilizing a procedure similar to that described in Section 4.5 using simulated muon information. An ADC (Section 4.4.2) readout was created simply by measuring the peak value of the constructed PMT pulses for each event.

All TDC and ADC simulated readouts were output into a ROOT tree. Additionally, primary charge, energy deposit in scintillator, tracking information such as hit location and path length correction ($\sec\theta$, PLC), as well as number of photons generated and number which reached a photocathode for exploration of efficiency were also stored in the tree. Using the CREAM I TRD tracking-based measurement described below, an estimate of the TCD electronics resolution was possible. TDC values with the appropriate Gaussian smearing were added to the tree as well.

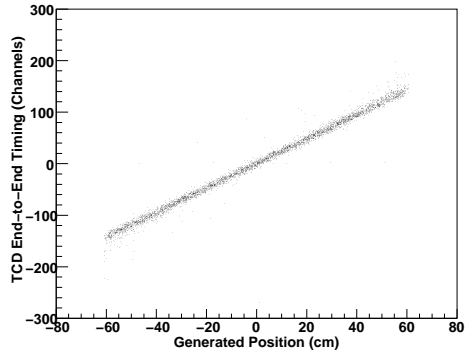
7.6 Timing Resolution of the TCD Scintillator Paddles and Electronics

By comparing the measured tracking accuracy from Section 5.6 with the predicted tracking accuracy from the GEANT 4 model, the timing resolution of the actual CREAM flight electronics can be estimated. Recall the overall TCD tracking accuracy to be $\sigma_{TCD} = 0.427 \pm 0.011$ ns and $\sigma_{TDC} = 0.3019 \pm 0.0080$ ns for each tube on a paddle. We expect the overall timing resolution of the TDCs to be a quadrature sum of the timing resolution of the TCDs, based on photon propagation physics, and the resolution of the electronics.

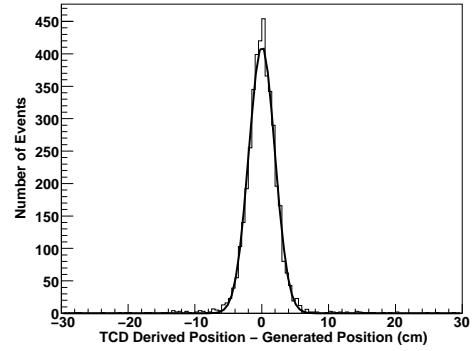
Figure 7.4a and b illustrate the limitation in position resolution arising purely from photon propagation physics in the TCD paddle. From Figure 7.4b, we estimate the resolution due to photon propagation physics to be 1.948 ± 0.025 cm = 0.272 ± 0.020 ns for a whole paddle (both tubes). Using this result from the simulation and the previous measurement of the overall (readout electronics+photon propagation) resolution quoted in the above paragraph, it is possible to separate out the component expected to come purely from noise in the readout electronics. Because we expect the overall resolution to be a quadrature sum of the physics-based and electronics-based noise, we estimate the overall electronics resolution (both tubes) to be 0.329 ± 0.028 ns, or 0.233 ± 0.020 ns for one tube. In TDC channels this represents a stability of ~ 4 channels. Figure 7.4c and d show the simulated events again, but with this estimated electronics-noise convolved in. Figure 7.4d has a measured resolution of 3.198 ± 0.040 cm = 0.446 ± 0.026 ns, which compares favorably with the measured paddle resolution (within estimated errors).

7.7 Light Attenuation

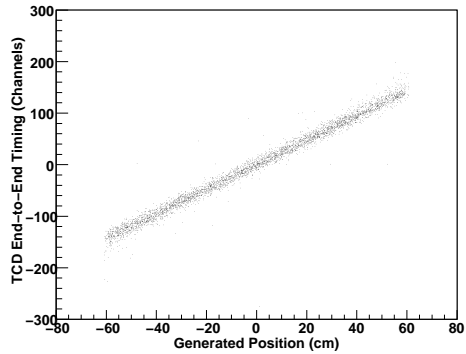
Figure 7.5 shows the average simulated ADC (peak detector) response of a PMT at the +X end of the TCD paddle as a function of the hit-position along the paddle. The simulated test-beam consists of 10 GeV protons isotropically incident (and with arrival



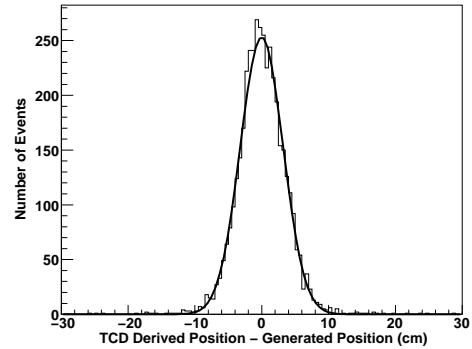
(a) End-to-end paddle time difference as a function of paddle hit position.



(b) Residual distribution of the timing-derived position compared to the recorded hit position. The solid curve is a Gaussian fit.



(c) End-to-end paddle time difference (Gaussian convolved) as a function of paddle hit position.



(d) Residual distribution of the timing-derived position (Gaussian convolved) compared to the recorded hit position. The solid curve is a Gaussian fit.

Fig. 7.4 Position measurement accuracy from the optical GEANT4 model of a TCD paddle.

angle weighted by $\cos \theta$, but with a path-length correction applied such as in Section 6.1). This is compared with an experimentally measured typical attenuation curve also shown in Figure 7.5, derived from a PMT in the CREAM I flight data. This is presented as a qualitative consistency check of the response of the model, compared with actual flight hardware and electronics. The actual flight paddles displayed variation in the position-response arising from scintillator thickness variations (and hence light yield) across the length of the paddles as well as PMT non-linear response [13].

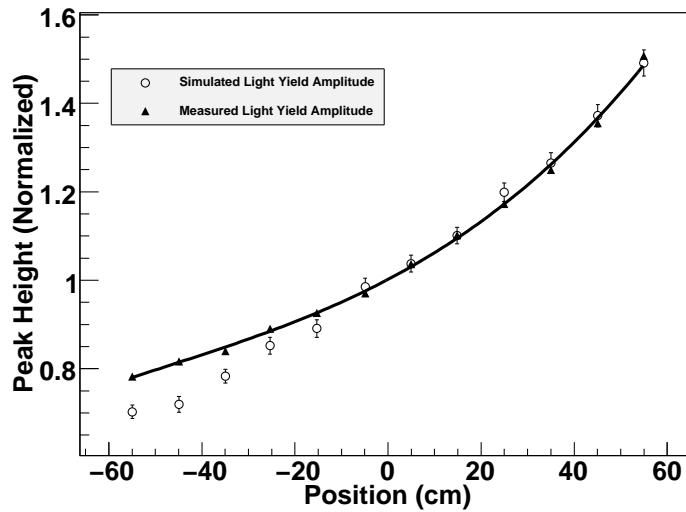


Fig. 7.5 Simulated TCD ADC (peak detector) response for a PMT at the +X end of the paddle. The simulated test beam consists of 10 GeV protons incident isotropically across the surface of the paddle, with all values normalized to the center of the paddle. Also shown is the response of a typical CREAM I paddle displaying qualitatively similar behavior (there was variation from paddle to paddle due to scintillator thickness and electronics response [13]).

7.8 Simulated ADC Signals

A correction scheme similar to that implemented in Section 6.4 was carried out for a set of simulated events. The events presented here contain simulated 10 GeV H, He, Be and a limited number of carbon events. The species and energy used here were not chosen to reflect cosmic-ray abundances or elemental spectra in any way, but to simply provide an event set to test charge-reconstruction schemes (primarily involving the TDCs).

Consistent with Equation 6.3, path-length ($\sec \theta$) and square-root corrections were first applied to the simulated events, then attenuation functions were found (third-order

polynomials) for each species. The individual-species attenuation functions were later used to generate the position-dependent corrections to the simulated ADC signals. The corrected charge measurement for the ADCs (both tubes corrected into charge units, then averaged) is shown in Figure 7.6. One important difference between the charge-correction scheme used for the simulated events here and the real events in Section 6.4 is that only one ADC range is implemented here and all species are on the same scale (it does not have any included non-linearity arising from PMT saturation, readout-electronics pedestals or other effects).

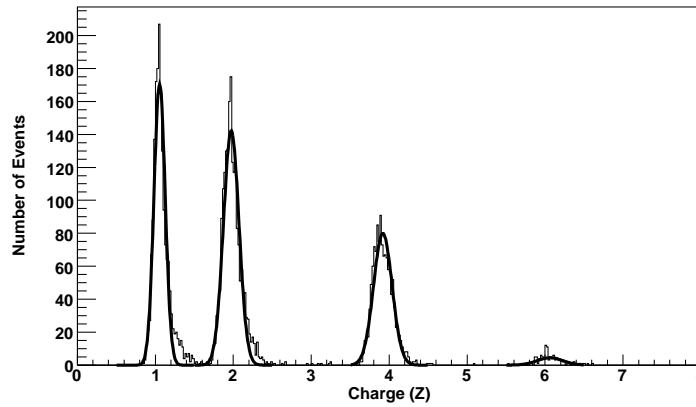


Fig. 7.6 ADC-based charge measurement for simulated 10 GeV hydrogen, helium, beryllium, and carbon.

As can be seen, the idealized charge resolution found here is better than the experimental response presented in Section 6.6. This is hardly surprising since these simulated events are mono-energetic and lack limitations of real detectors such as scintillator saturation, physical variations in materials and realistic electronics limitations. The resolutions found here are $0.0720 \pm 0.0017 e$ for hydrogen, $0.0996 \pm 0.0022e$ for helium, $0.1185 \pm 0.0028e$ for beryllium and $0.165 \pm 0.028e$ for carbon. This compares to experimental resolutions found for CREAM II flight data of $0.16888 \pm 0.00080e$ for helium and $0.405 \pm 0.028e$ for carbon (Table 6.1). From the CREAM I analysis using superior TRD-based tracking for attenuation and PLC corrections, the resolution for oxygen (similar for B,C,N and O) was $0.2e$ [10].

7.9 Simulated TDC Signals

The TDC values from the model can be convolved with a Gaussian of width 0.233 ns to include the resolution of the readout-electronics and PMTs (Fig. 7.4c and 7.4d) as discussed previously. In this way, TDC readouts with realistic timing resolution and charge response can be simulated for the testing of analysis strategies.

As described in Section 6.7, the slope of the PMT pulse leading edge (slew rate) is steeper for higher-charge species. Thus, in principle a comparison of TDC timing at two different thresholds can be used as a charge measurement. However, in Section 6.7 the slew-rate measurement method appeared to have insufficient resolution to discriminate between hydrogen and helium (though some discrimination between helium and higher species was demonstrated). The TDC simulated signals presented here can be used to further evaluate the effectiveness of this method and to determine why it does not appear to work. Figure 7.7a shows that even for the idealized unconvolved TDC values, the difference method shows poor charge separation for H and He. The distributions with the electronics resolution folded in show a very high level of smearing. The TDC difference (for one tube) compared with the ADC-based charge measurement is shown in Figure 7.8.

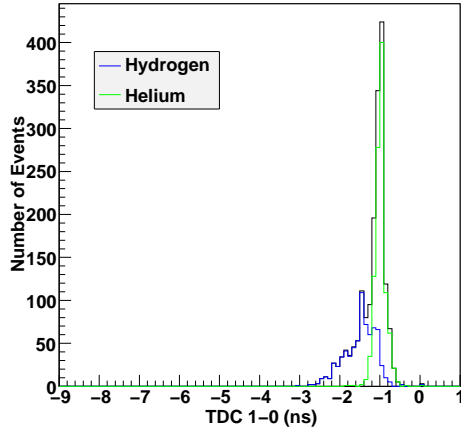
Even in the case of ‘perfect’ readout electronics (the simulated TDCs with no electronics noise included) the TDCs show only very limited ability to discriminate between charge-species for reasons arising purely from photon-propagation physics in the scintillator and light-guide materials. Once realistic timing resolution is included (which is actually comparable in magnitude to the photon-propagation resolution) for the electronics, the ability to discriminate between species is fully washed out (for hydrogen and helium at least).

Some dependence on PLC and signal attenuation is certainly expected for the TDC difference slope measurement. Figure 7.7c does show some position dependence, however for the convolved values in Figure 7.7d, which includes electronics noise, a high level of smearing is evident. The TDC threshold difference variation with PLC is shown in 7.9. Some variation with PLC is evident in Figure 7.9a, however, from Figures 7.9b and 7.7d it appears that with the electronics noise included, applying PLC and position corrections will still not result in useful charge discrimination. In Figure 7.10 the TDC threshold 1-0 time difference is shown with cuts requiring a position of $-20 < x < 20$ cm and $PLC < 1.5$. This is a quick test to see if a position correction (approximated here by just requiring events within a small region) and a path-length correction (similarly tested here by selecting a small range of PLC) might improve resolution.

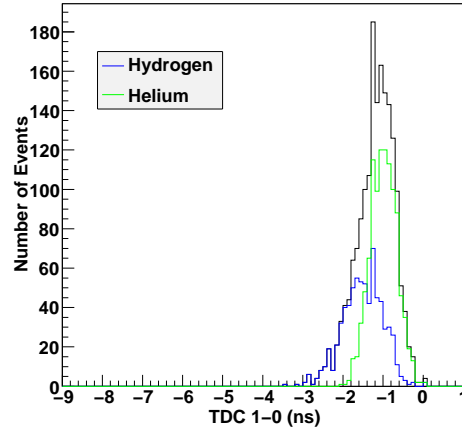
7.10 Reflective vs. Nonreflective Paddle-Wrapping Comparison

A version of the GEANT4 model was created with the surface properties of the aluminum wrapping changed from reflector to absorber. The motivation for this simulation is to assess the change on light levels arriving at each PMT and the effect (if any) on the performance of the TDC and ADC-based measurements.

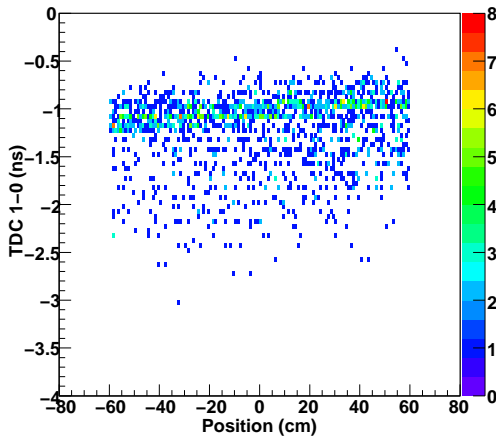
The argument for the presence of some sort of specular reflective wrapping around the paddle is to scatter photons back into the scintillator or light guides which manage to escape the optical components because they are incident at angles smaller than the critical angle of $\theta \simeq 39.3^\circ$ (measured from the vertical) for total internal reflection in the BC408 scintillator material (which has an index of refraction of 1.58 [58]). The specular reflectors will reflect the photons at random angles, thus some will re-enter the optical components at angles sufficient to be trapped by total internal reflection.



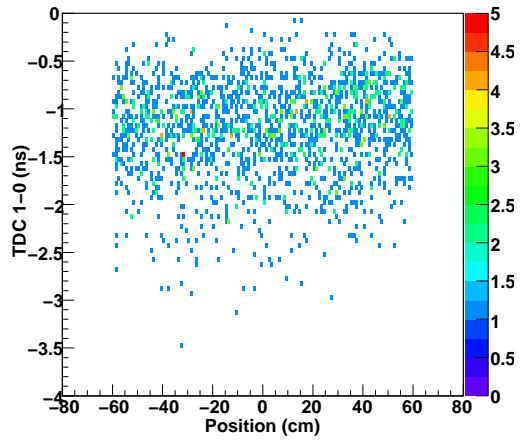
(a) TDC threshold 1-0 time differences (ns) for unconvolved values, for simulated hydrogen and helium primary nuclei. The solid black curve is the overall total population that would be observed experimentally.



(b) TDC threshold 1-0 time differences (ns) for convolved values, for simulated hydrogen and helium primary nuclei. The solid black curve is the overall total population that would be observed experimentally.



(c) TDC threshold 1-0 time differences (ns) for unconvolved values as a function of location of the hit along the paddle.



(d) TDC threshold 1-0 time (ns) for convolved values as a function of location of the hit along the paddle.

Fig. 7.7 Comparison of TDC threshold 1-0 time difference as a charge measurement technique. Simulated times with no electronics resolution convolved in are shown in (a) and (c), and in (b) and (d) the equivalent distributions are shown, broadened by additional electronics resolution folded in. These plots include 1000 simulated 10 GeV protons and 2000 simulated 10 GeV helium nuclei.

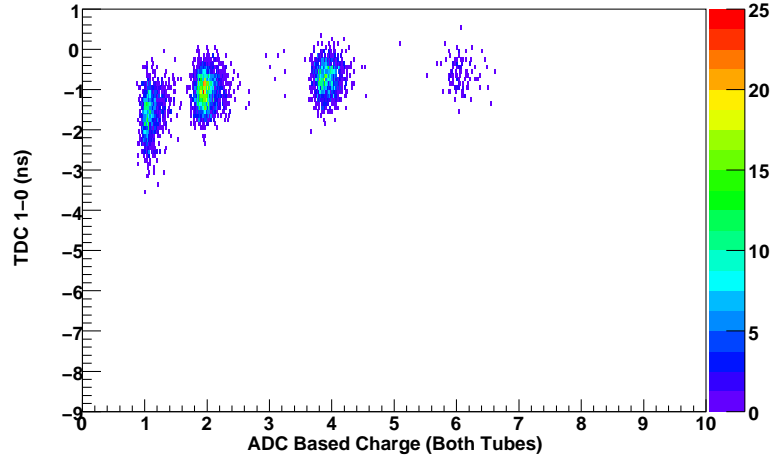


Fig. 7.8 TDC Threshold 1-0 (Tube 0) time difference as a function of the ADC-based charge measurement for simulated 10GeV hydrogen, helium, beryllium, and carbon (average of both tubes). The times shown on the Y-axis are negative here because TDC 0 will have a larger measured signal than TDC 1, since they both measure elapsed time since their respective thresholds have been crossed. This ordering of the subtraction was chosen so higher-charged species would be more positive in TDC timing difference.

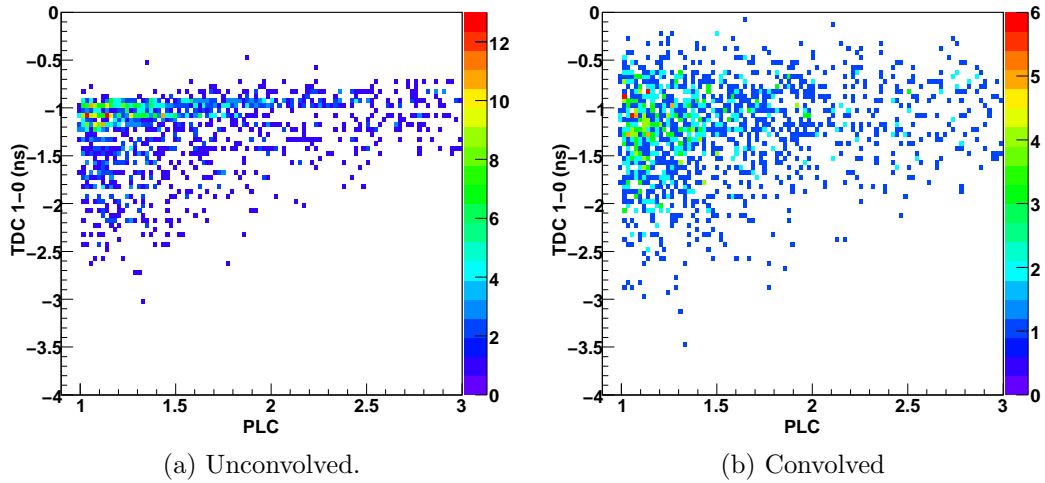


Fig. 7.9 Comparison of TDC threshold 1-0 time difference as a function of PLC. These plots include 1000 simulated 10 GeV protons and 2000 simulated 10 GeV helium nuclei. The color scale here is bin-counts in the 2-D histogram, and no color-coding of the individual species is present.

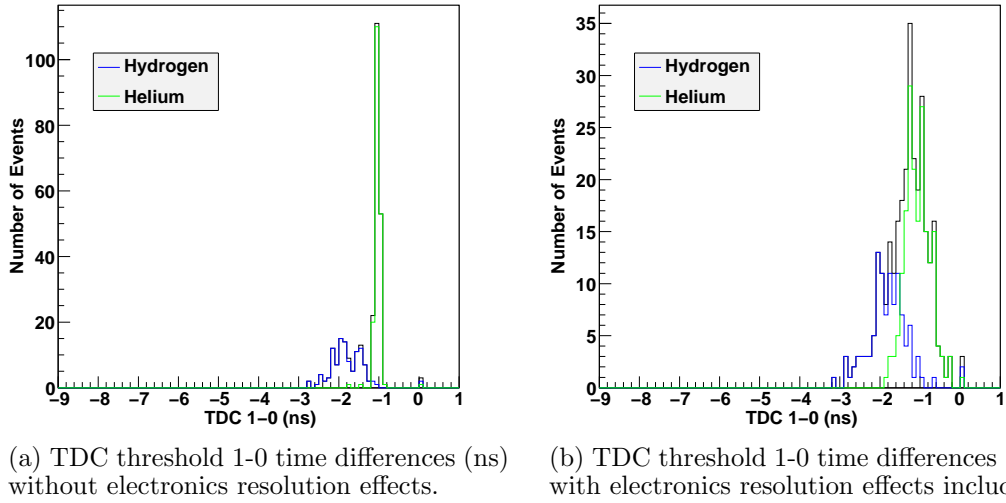
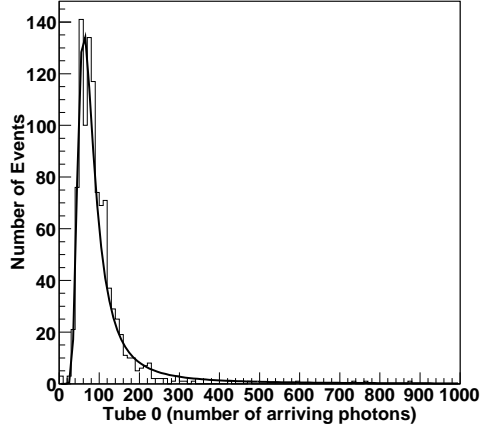


Fig. 7.10 Comparison of TDC threshold 1-0 time difference for charge measurement, with and without electronics resolution effects folded in. A position restriction of $x = \pm 20$ cm and $PLC < 1.5$ has been applied. These plots include 1000 simulated 10 GeV protons and 2000 simulated 10 GeV helium nuclei. In each case the top black line shows the total population.

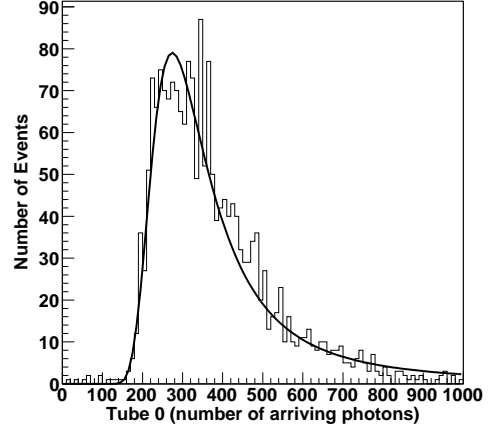
An argument against a diffusely reflective wrapping in the sort of prompt readout scheme done in CREAM is that all the photons you might recover from the wrapping will be highly inclined ones, and thus will diffuse much more slowly than the photons which were emitted traveling nearly parallel to the optical surfaces. If a charge-summing amplifier or other type of PMT pulse-integration technique were utilized, it is clear that a substantial reduction in signal size might occur. However, since both the TDC and ADC readouts are dependent only on the photons which arrive in the first few ns or so, it is reasonable to suspect that the reflective wrapping is unnecessary.

As can be seen from Figure 7.11 and Table 7.1 there is a substantial reduction in the number of photons arriving at each PMT photocathode if a non-reflective paddle wrapping is used. Light yields for the non-reflective wrapping configuration is $\sim 54.6 \pm 1.1\%$ for the simulated hydrogen events and $53.13 \pm 0.63\%$ for the helium compared with the reflective wrapping values. This is not unexpected as discussed above, however we still must investigate what effect this has on the TDC and ADC readouts, if any.

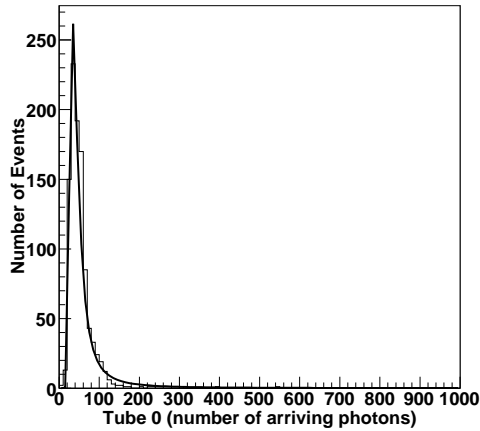
Figure 7.12 shows the path-length and square-root corrected (but with no attenuation correction) simulated ADC response for 1000 hydrogen and 2000 helium (all 10 GeV). For the ADC readout very little change is evident when comparing the non-reflective and reflective wrappings. The mean ADC response (Table 7.2) for the non-reflective wrapping configuration is still $\sim 88.21 \pm 0.81\%$ for the hydrogen and $\sim 88.09 \pm 0.55\%$ for the helium events shown relative to the response using a reflective wrapping. This is not very surprising given that the peak PMT signal is going to be made up of a superposition of photons arriving all in the first few ns.



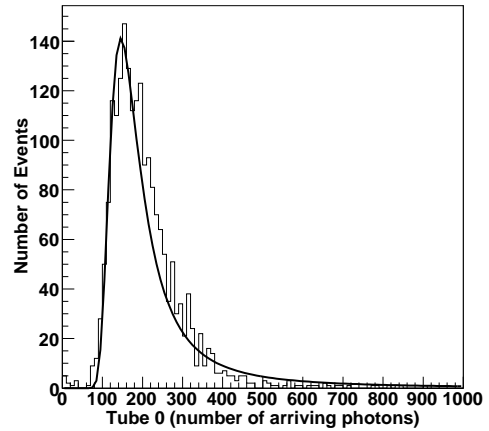
(a) Number of arriving photons at one PMT for simulated hydrogen events, with reflective wrapping.



(b) Number of arriving photons at one PMT for simulated helium events, with reflective wrapping.

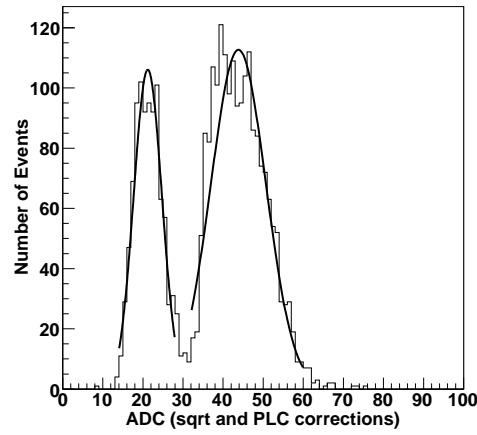


(c) Number of arriving photons at one PMT for simulated hydrogen events, with non-reflective wrapping.

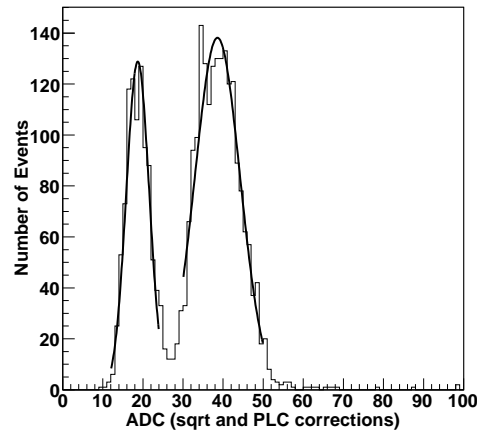


(d) Number of arriving photons at one PMT for simulated helium events, with non-reflective wrapping.

Fig. 7.11 Comparison of photon arrival numbers for H and He with both reflective and non-reflective paddle wrappings. These plots include 1000 simulated 10 GeV protons and 2000 simulated 10 GeV helium nuclei. Fit-parameters from the Landau-distribution fits shown are summarized in Table 7.1.



(a) Reflective Wrapping.



(b) Non-reflective Wrapping.

Fig. 7.12 Comparison of ADC response (one tube) for H and He with both reflective and non-reflective paddle wrappings. These plots include 1000 simulated 10 GeV protons and 2000 simulated 10 GeV helium nuclei. The distributions have been path-length and square-root corrected consistent with Equation 6.3, but no attenuation corrections have been applied. Results of the fits are summarized in Table 7.2.

<i>Paddle Photon Number Output</i>				
<i>Species</i>	<i>Reflective Wrapping</i>		<i>Non-Reflective Wrapping</i>	
	<i>MPV</i>	σ	<i>MPV</i>	σ
Hydrogen	64.10 ± 0.95	12.90 ± 0.47	34.91 ± 0.48	6.39 ± 0.26
Helium	284.4 ± 2.3	46.4 ± 1.2	151.1 ± 1.3	24.43 ± 0.65

Table 7.1 Most-probable-values and widths (σ) from Landau fits performed on the distributions in Figure 7.11. Results are in number of photons arriving at the single simulated PMT.

<i>Relative ADC Outputs</i>				
<i>Species</i>	<i>Reflective Wrapping</i>		<i>Non-Reflective Wrapping</i>	
	<i>Mean (Channels)</i>	σ (Channels)	<i>Mean (Channels)</i>	σ (Channels)
Hydrogen	21.21 ± 0.14	3.52 ± 0.12	18.71 ± 0.12	2.844 ± 0.092
Helium	43.82 ± 0.18	6.84 ± 0.16	38.60 ± 0.17	5.63 ± 0.17

Table 7.2 Mean ADC response and Gaussian distribution widths for the histograms in Figure 7.12.

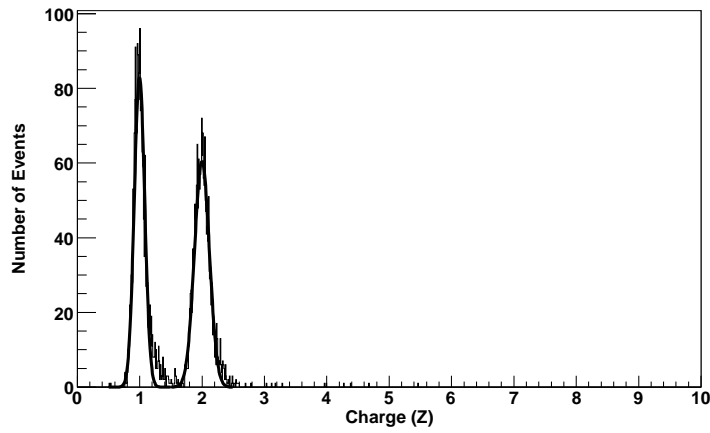
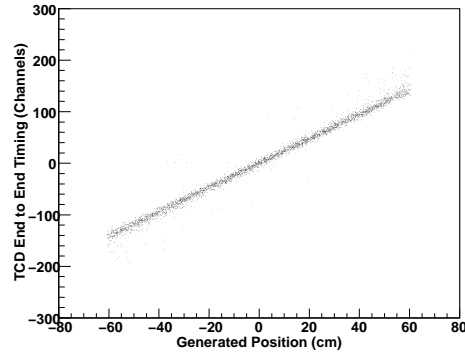
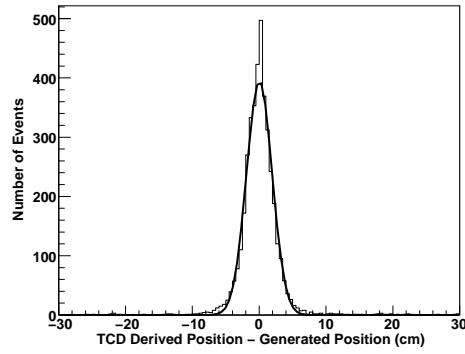


Fig. 7.13 ADC-based charge measurement for simulated 10 GeV H and He with a non-reflective paddle wrapping.

Applying the same correction regime used in Section 7.8, we see from Figure 7.13 that the non-reflective paddle has nearly identical ADC charge resolutions of $0.0834 \pm 0.0018e$ for hydrogen and $0.1192 \pm 0.0025e$ for helium. For TDC resolution we can compare Figure 7.14 to Figure 7.4 (a and b). We arrive at a resolution arising from photon propagation of 1.923 ± 0.029 cm, which is identical to the value found in Section 7.6 above (within uncertainty). So it seems that a non-reflective wrapping offers no great advantages or disadvantages for a detector utilizing readout similar to the CREAM TCD. If any sort of pulse integration technique were used however, the substantial loss of slower photons would impact signal readout.



(a) End-to-end paddle time difference as a function of paddle hit position for a non-reflective wrapping.



(b) Residual distribution of timing derived position compared to generated hit position, for a non-reflective wrapping.

Fig. 7.14 Position measurement accuracy from GEANT4 model with non-reflective paddle wrapping.

Chapter 8

CREAM II Spectra

To be able to generate cosmic-ray spectra, we require both a particle charge-measurement as found in the previous chapter, and an energy determination. For CREAM II the primary energy measurement detector is the calorimeter. A very thorough calibration and analysis of the CREAM calorimeters (for all flights to date) has been an ongoing task of the collaboration since well before the first flight. Numerous beam tests conducted at CERN (involving both heavy-ion fragment beams, pions and electrons), Monte-Carlo simulations and analysis of flight data have been conducted. A number of results have been published to date detailing both the calibration campaign, and preliminary spectral results for H and He, BCNO, and higher species ([1],[6],[55],[73]). The calorimeter energy-reconstruction presented here is not an official CREAM collaboration result, with many important details not included (though they will be briefly discussed). The ultimate accuracy of the resulting spectra presented here is therefore unknown unfortunately. However, this exercise in evaluating the performance of the TCD for charge measurement is quite useful.

8.1 Calorimeter Energy Reconstruction

A description of both the physical construction and readout of the calorimeter is presented in more detail in Section 2.2.5. The fiber-optic readout from each ~ 1 cm calorimeter ribbon is divided optically into a low-, mid-, and high-dynamic range, respectively. The 3 ranges are read out by individual pixels in HPD devices and digitized by ~ 11 bit ADCs.

Before any gain-stitching, total energy deposit or tracking is carried out with the calorimeter, subtraction of electronics-pedestals is conducted for all CAL ADCs. During the flight, pedestal runs were conducted every 5 min with the resulting pedestal measurements stored in an ASCII file with a file name encoding the date and time in a human-readable format (a similar scheme was used for all data files as well) with a *.spi3* extension appended on the end. In this analysis, the pedestal value measured closest in time to the event time is used. Coherent noise was also measured during the pedestal runs, and stored in separate files. Ribbons with noisy/bad readouts from the coherent-noise files are masked off as part of the pedestal-subtraction process as well.

The operating voltage of the HPDs and the preamplifier gain is adjusted such that the ADC readout (in Channels) is roughly calibrated to be numerically equal to the energy deposit in the CAL ribbon (in MeV) for the low-range (highest-gain) readout. Since the optical-division ratio for the *low/mid* readout is $37/5 = 7.4$ (Section 2.2.5), the mid-range ADC signals need to be multiplied by this factor to be on the same scale as the low ones. The high-range ADCs were not used in this analysis.

For each ribbon, the mid-range ADC is selected if it is on scale, otherwise the low-range is used. Whichever range is selected, it is required to be above a noise level of 7 ADC channels. A total energy deposit in the calorimeter is then calculated by summing all of the ribbons with signal present (shown in Figure 8.1). Also shown in Figure 8.1 is the total energy deposit for events for which tracking (as described in Section 8.2) produced a valid track. To estimate the original energy of the primary particle, a sampling fraction 0.148% is assumed for the calorimeter as a whole [6].

The estimated incident energy for all species (again requiring that tracking was successful) is shown in Figure 8.2. The events with energy measured to be above 1 TeV were considered for this analysis. The events were binned by energy consistent with Figure 8.2, using the bins defined in Table 8.1

<i>Energy Bin Number</i>	<i>Bin Minimum TeV</i>	<i>Bin Maximum TeV</i>	<i>Bin Minimum $\log_{10} \text{ GeV}$</i>	<i>Bin Maximum $\log_{10} \text{ GeV}$</i>
0	1.00	1.58	3.0	3.2
1	1.58	2.51	3.2	3.4
2	2.51	3.98	3.4	3.6
3	3.98	6.31	3.6	3.8
4	6.31	10.0	3.8	4.0
5	10.0	15.8	4.0	4.2
6	15.8	25.1	4.2	4.4
7	25.1	39.8	4.4	4.6
8	39.8	63.1	4.6	4.8
9	63.1	100	4.8	5.0
10	100.	158	5.0	5.2
11	158	251	5.2	5.4
12	251	398	5.4	5.6
13	398	631	5.6	5.8
14	631	1000	5.8	6.0

Table 8.1 Definitions of the energy bins used in the analysis presented in this chapter.

Again it should be noted that the energy reconstruction presented here does not contain relative or absolute gain corrections between all the different ADCs necessary for definitive energy measurements. These gain corrections (and a more proper gain-range stitching) have been conducted by other groups in the CREAM collaboration however. This is an ongoing effort involving the analysis of beam test data, Monte-Carlo simulations and flight data.

8.1.1 Bin Energy Value

The correct energy value to report for a given bin in energy is an important parameter. As pointed out by Lafferty & Wyatt [74], the bin center and the mean energy of the bin contents (barycentre) are both incorrect choices for the reported bin

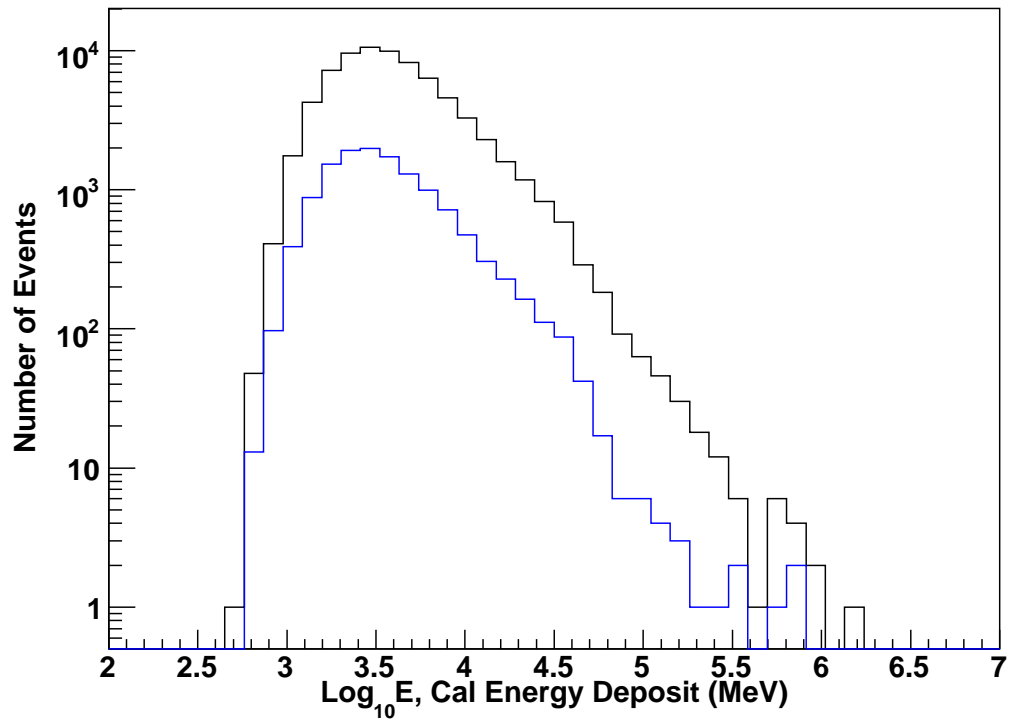


Fig. 8.1 The total energy deposit in the CREAM II calorimeter for all events with calorimeter signals present. The blue distribution represents events for which the tracking described in Section 8.2 was successful.

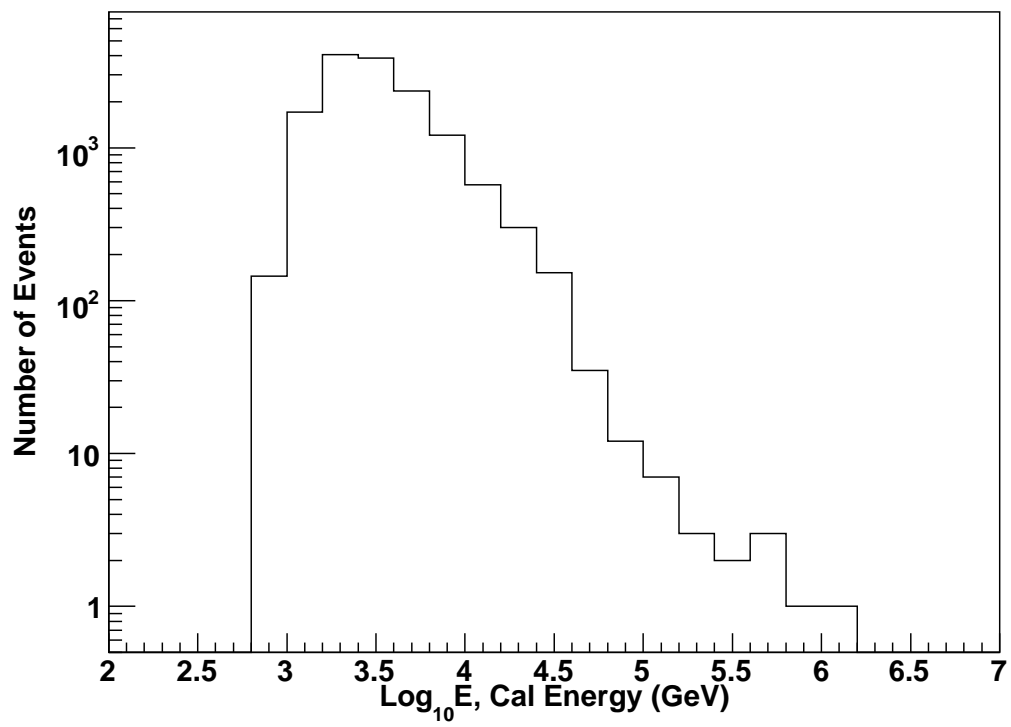


Fig. 8.2 Estimated incident energy for all CREAM II events as measured by the calorimeter (and requiring successful tracking).

energy, especially for bins covering a large energy range. The correct choice is a point which lies on the theoretical spectral function $g(E)$ (if known) and is given by:

$$g(E_B) = \frac{1}{E_{max} - E_{min}} \int_{E_{min}}^{E_{max}} g(E) dE. \quad (8.1)$$

For a falling power-law spectrum of the form $g(E) = dN/dE = AE^{-\gamma}$ which is well established for cosmic-ray spectra, the above equation yields a bin energy-position choice of:

$$E_B = \left(\frac{E_{max}^{1-\gamma} - E_{min}^{1-\gamma}}{(1-\gamma)(E_{max} - E_{min})} \right)^{\frac{-1}{\gamma}}. \quad (8.2)$$

This is of course dependent on γ , so a starting best-guess is required, followed by an iterative loop over the data until an arbitrary level convergence is achieved to the value of γ consistent with the data. This was the approach taken here, with convergence achieved in only a few iterations of the loop.

8.2 Tracking

In other analyses ([1],[73]) the Calorimeter has been used to produce tracking of accuracy ~ 1 cm when projected to the SCD. This has been used to successfully pick out the hit-location area in the SCD, to exclude most contamination from albedo particles. According to Monte Carlo simulations and beam tests [75], the expected contamination from albedo is reduced to $\sim 2 - 3\%$ when this tracking-based selection method is used.

Unfortunately, in the limited time available for this thesis' work, the author was unable to reproduce this tracking to the same degree of accuracy. Ribbon hits were weighted by the (pedestal-subtracted and gain-corrected/stitched) energy deposit values. Attempts were made using both Linear Regression and Singular Value Decomposition methods to generate straight-line fits in the XZ and YZ planes of the calorimeter. Both methods agreed with each other to a large degree, but did not demonstrate the ability to reliably generate tracking. Several attempts were made to apply multiple-pass fits to exclude outlying points and to apply χ^2 requirements on fit quality as well.

To check the calorimeter track-fitting effectiveness, the maximum-hit SCD pixels were selected (one for each layer). This was after pedestal-subtracting and masking of dead/noisy pixels. For hydrogen and helium events, this method is not reliable at picking out the true hit locations of the primary, at least not for events with much albedo present. However, for higher-charged species such as carbon and above, the problem of albedo contamination producing a false hit location was much diminished. The quality of calorimeter-based tracking schemes was then judged by comparing the projected track hit location in the SCD (as calculated from the CAL reconstruction) to the location of the maximum-hit pixels in the SCD. No acceptable schemes were found, especially none nearly as successful as those produced by others in the collaboration.

An alternate tracking scheme was implemented in this analysis to allow for an instrument-wide primary-particle track to be determined for events within the acceptance

of the TCD and calorimeter. This scheme is similar to that implemented in the charge-calibration of the TCD discussed in Chapter 6. However, in this procedure, the TCD was used to measure a hit location at the top of the instrument while the calorimeter hits were used to measure a hit location at the bottom.

As mentioned above, CAL-based tracking was not available for this analysis, however, a much simpler and robust quantity was available to calculate: a mean hit location. This was just the weighted mean of all ribbons in the X, Y, and Z coordinates. Thus a well-defined point in the calorimeter was reliably measured that had a very high likelihood of lying along the particle track.

The measurement of the hit location in the TCD is a bit more complicated since, for events producing a calorimeter shower, the most probable scenario involves all TCD paddles being hit (Figure 8.3). To select the pair of paddles which were the most probable to have been hit by the primary (if the primary is actually within the geometry of the TCD), the time-of-flight variables (Section 5.4) are compared and the X paddle and Y paddle with the most positive TOF are chosen as the candidate hit paddles.

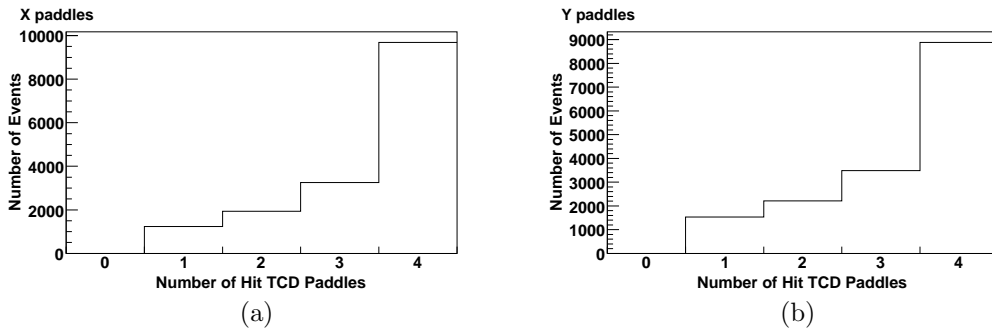


Fig. 8.3 The number of hit TCD paddles per event (TDC threshold 0 crossed for the PMTs at both ends) for the CREAM II flight for events with Calorimeter data present. It is clear that there is a large amount of albedo present for any events having a CAL signal. (a) is for the X-going paddles while (b) is for the Y-going.

At this point the tracking scheme is still going to generate false tracks reconstructed to have TCD hit locations for events outside of the TCD acceptance (events which entered the calorimeter or CAL targets at large angle and produced albedo particles which impacted the TCD). Two more steps can be taken to remove most of these types of events. The first is a cut to require that the measured hit positions in the two chosen TCD paddles actually agree with the physical region defined by the overlap of the two paddles (agreement to within 10 cm of the tile boundaries was used in this analysis). This cut will not remove any hits from primary particles (except for some outliers), but will remove some fraction of albedo hits, since these types of hits generally involve a number of simultaneous particles all across the TCD paddles.

The second cut which can be applied to finish requiring that tracks be within the TCD acceptance is to calculate the mean TOF variable for the two chosen paddles

and cut those which are clearly due to albedo (Figure 8.4). Events above -130 channels in the TOF are selected as having been downward-going (primaries), while those more negative than this are discarded as albedo.

In addition to selecting the TCD hit location, tracking described above was also used to pick out a hit location in the SCD, so a redundant charge measurement could be available. In the other various analyses mentioned above, the CAL-only tracking was used for this purpose as already noted. Also as discussed above, selection of the hit location in the SCD is necessary to correctly identify lower-charged species (hydrogen and helium). The stump CREAM II analysis code records hit locations and signals from the SCD (not depending on any tracking) under the condition that the maximum-hit pixels in the top and bottom layers agree on a hit location to within 5 cm in X and Y. These variables are stored in the *tscd* and *bscd* data branches, respectively, in the ROOT files output by the analysis code.

To produce more robust SCD-hit locations and exclude as much albedo as possible, the tracking was used to select a rectangular area $5 \times 5 \text{ cm}^2$ in each SCD layer and the maximum-pixel signals within each of those layers were recorded (in this case in the *ttq* branch). The exclusion of probable albedo hits can be seen in Figure 8.5.

The calibration of the SCD into charge units was previously discussed in Section 6.3. Previously the SCD hit locations were used for tracking purposes in the charge calibration of the TCD. Now however, we will use it for charge measurement only and rely on the tracking above. Figure 8.6 shows the improvement in identification for hydrogen and helium using the tracking to select the hit locations over a method of just selecting the maximum-hit pixel in each SCD layer. The SCD displays very good charge resolution, with fits to the peaks in Figure 8.6b yielding resolutions as quoted in Table 8.2.

8.3 TCD Charge Measurement With Both Layers

Once the two TCD paddles are selected by the time-of-flight measurement and the upward-going albedo events are excluded, the TCD ADC readouts can be used to generate a charge measurement, as described in Chapter 6. In fact two independent charge measurements are available from the TCD, one for each layer. Traditionally, when two charge-measurements are available (as done with the TCD and SCD in [28]), charge agreement between the two measurements is enforced either with a simple requirement that the two measure agree to within some arbitrary amount, or a bit more sophisticated cut is applied in the form of circular cuts around the integer charge numbers (in the 2-D parameter space of the two charge measurements). The width of these circular cuts is generally some fraction of the averaged charge resolution for each species, so no biases are introduced favoring the narrower distributions.

This sort of agreement requirement is desirable to both eliminate particles which undergo charge-changing interactions in the instrument after initial and final measurement, as well as to cut down on contamination caused by fluctuations to higher (or lower) energy deposit in the charge detectors. In the CREAM I TRD-based analysis (discussed in [28]), this approach was both possible and necessary because the number of events

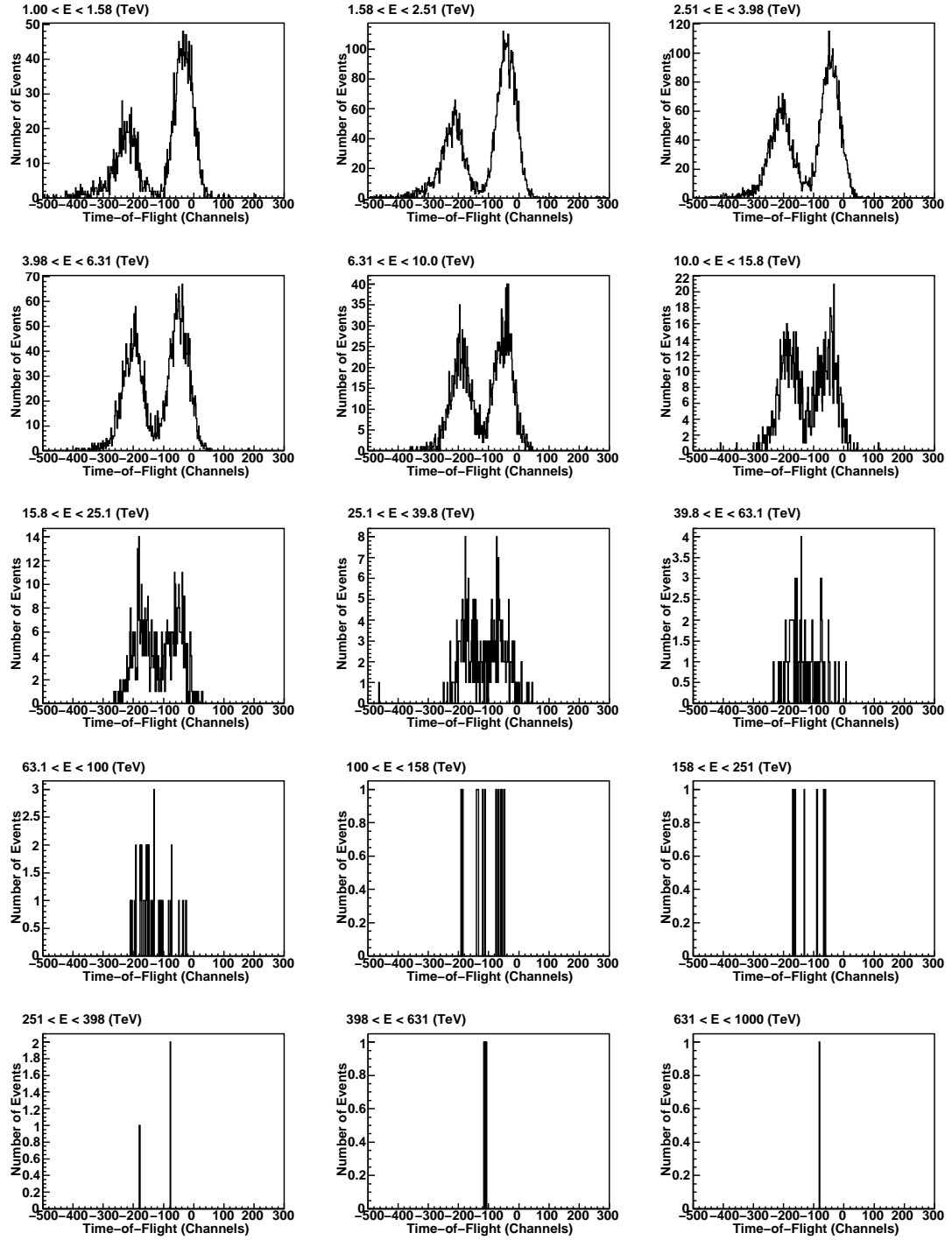


Fig. 8.4 Time-of-Flight measures for progressively higher energy bins (energy from Calorimeter) as measured from the TCD paddles to the S3 detector. The time is shown in TDC channels here with an arbitrary (but consistent between paddles) offset. The rightmost distributions are for downward-going events, while the leftmost are for albedo.

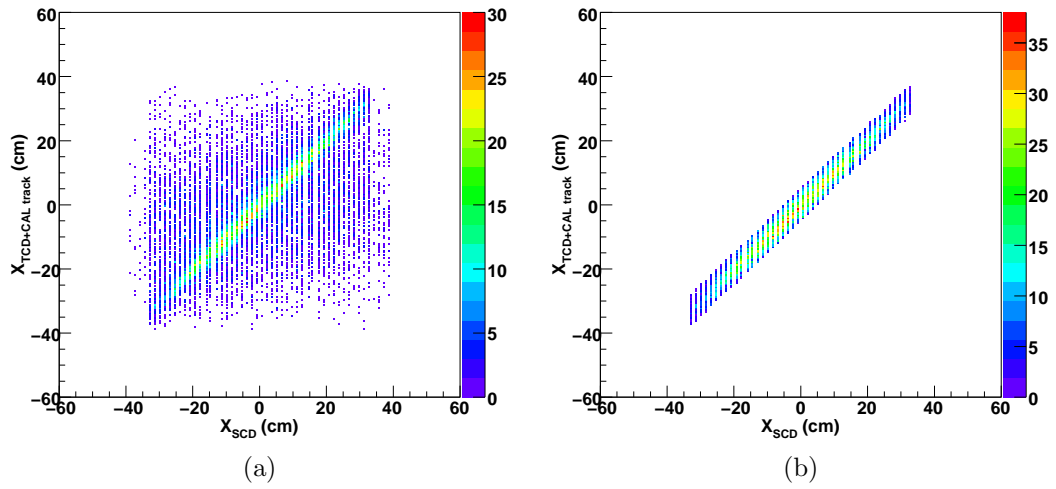


Fig. 8.5 (a) The predicted X hit locations in the CREAM II SCD (top layer only) from the TCD timing and CAL CM-based tracking shown on the Y axis as a function of the stored location of the maximum hit pixel in the SCD as recorded independently of tracking. There are a large number of hits which do agree with the tracking, but also significant outliers due to false hits caused by albedo particles (primarily for hydrogen and helium primary events). (b) The same plot but with the maximum-SCD pixel selected only from within 5 cm of the tracking. The Y direction and the bottom SCD layer display similar behavior as the X layer shown here.

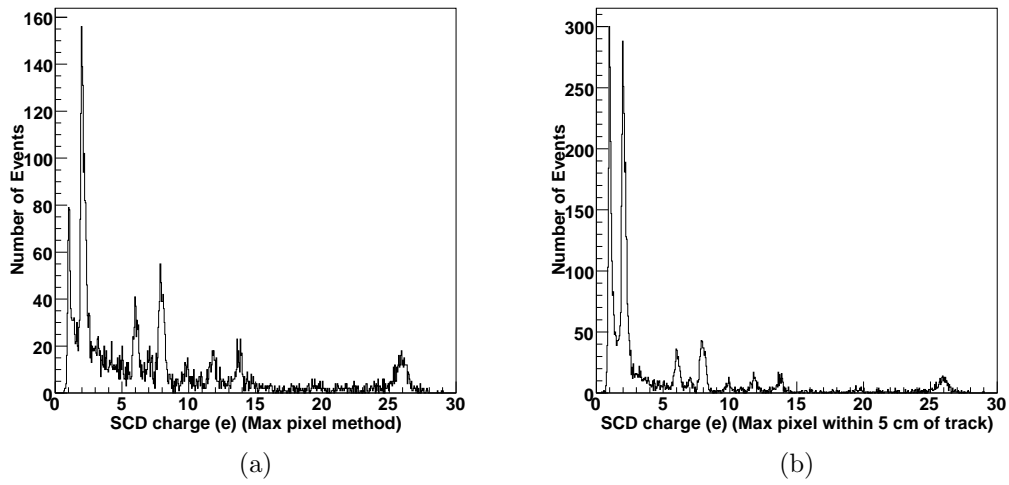


Fig. 8.6 (a) The charge measurement for the SCD using the maximum-pixel selection method for the entire SCD (no tracking used for hit-location selection). The charge is reconstructed as outlined in Section 6.3, and the tracking available is used for path-length correction ($\sec \theta$) correction. Both layers are averaged together here. (b) The reconstructed SCD charge using the maximum pixel within 5 cm of the tracking. Additionally, the charge measures from both layers are required to agree to within one charge unit. Even with this additional cut, far more hydrogen and helium hits are correctly identified.

was large enough and the secondary/primary ratios are very sensitive (at small values) to charge mis-identifications.

Internally in the CREAM TCD, for events of high energy (those producing calorimeter showers), we face a different set of circumstances. Here charge mis-identification is still undesirable, but less of an issue since all of the species under study are primary species, and the impact on their relative abundances is expected to be much less extreme. Additionally, the issue of very low statistics in the higher energy events favors an approach that is not as restrictive.

Finally there is an important issue specific to the TCD: albedo contamination of ADC signals. Recall that the TCD ADCs recorded the largest PMT level to come through in a several ms window of the initial trigger, thus, albedo contamination will be present at some level for some events. Figure 8.3 suggests that for events where a Calorimeter shower is present, we can expect the paddles hit by the primary particle to also often be hit by additional albedo particles within the time window of the ADCs (recall that the albedo only takes several ns to arrive). For higher charged species this is not an issue since the signal from the primary is so much larger, but for hydrogen and helium this will be important. Hydrogen events in the scintillator already have large Landau fluctuations producing an extended tail, and this added albedo signal will extend that and lead to some charge mis-identification (Figure 8.7). Additionally, we expect (and will show shortly) the problem to grow with particle energy (CAL shower size, more albedo).

A very simple approach was taken in this analysis to reduce (but not eliminate) these albedo-induced (and fluctuation-induced) charge mis-identifications: the two hit TCD paddles were examined, and the paddle with the *lowest* measured charge was taken as the correct one for the event. Additionally, a small multiplicative factor of 1.03 was applied to the measured TCD charge to shift the charge peaks to integer values. Recall that the charge calibration process in Chapter 6 used primarily events with no Calorimeter signal present, and thus were dominated by sub-TeV energy events. Thus, events below minimum-ionizing will produce larger light signals in the TCD, which can bias the TeV scale energy events to a slightly lower charge measurement. As can be seen by the small correction factor introduced however, the effect was small. Figure 8.8 shows all TCD charge measurements (after the tracking and timing cuts previously discussed) for events with a Calorimeter signal present. A total of 14423 events survive for the entire flight. Worth noting here is that the higher range ADCs have not been corrected to date, so species above oxygen can not yet be reliably measured by the CREAM II TCD. From the previous work on CREAM I analysis in [28] and [13], the TCD will be quite effective for species above oxygen to past iron once the two higher gain-range ADCs are corrected and included in the analysis.

To estimate individual species counts, fits are needed since (especially for hydrogen and helium) the distributions for each species do overlap. The fits used in this analysis are shown in Figure 8.8. The carbon and oxygen populations are fitted with simple Gaussian functions (over a limited range) included in the ROOT analysis package. The fitting procedure for hydrogen and helium is a bit more complicated. For hydrogen a convolved Gaussian and Landau function was used, which was adapted from the *langaus.C* example available on the ROOT collaboration web site. Since the helium distribution is embedded

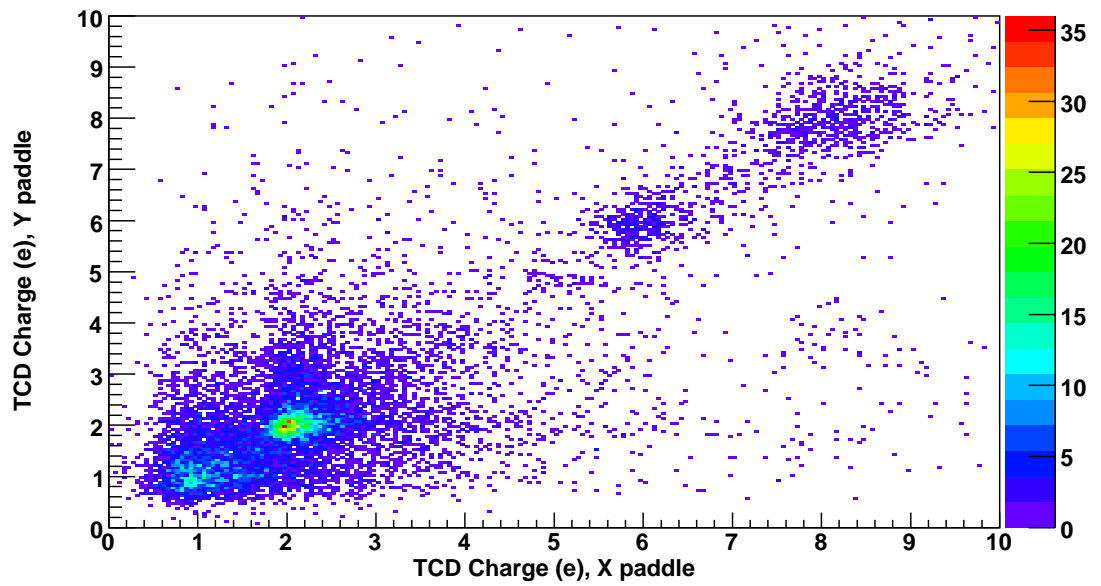


Fig. 8.7 TCD measured charge for events having a calorimeter signal (shower present), for the two TCD layers. The long tails from hydrogen and helium are clearly visible, arising both from energy-deposit fluctuations and from albedo contamination.

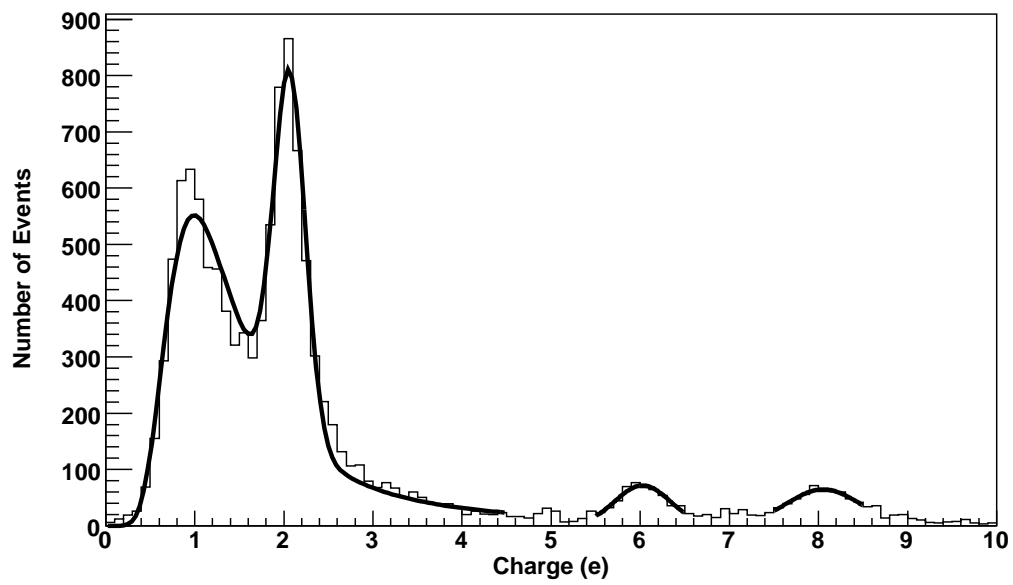


Fig. 8.8 TCD-measured charge for events having a calorimeter signal, using the minimum measured charge in the two layers. This procedure reduces the effect of the long tails from hydrogen and helium. A total of 14423 events are measured for the CREAM II flight in the TCD (after cuts).

in the hydrogen population, a combined fitting routine was created using the convolved Gaussian and Landau function and a second Gaussian function added in for the helium. In order for the combined fitting function to converge correctly to the present population, the parameters corresponding to the peak positions of the distributions had to be rather tightly constrained to a region very close to the histogram peaks. This procedure was repeated for each energy slice manually.

The charge resolution for the TCD observed using the above cuts and fits is summarized in Table 8.2. Recall that the observed resolution found for representative Paddle 1 in the previous chapter was $\sigma_{He} = 0.16888 \pm 0.00080e$ and $\sigma_C = 0.405 \pm 0.028e$. Not much change in the helium is introduced by the combination of the two layers, but some improvement in the carbon is introduced. Again, the SCD does still display superior charge resolution for all species. For comparison, the charge resolution found for the corrected TCD ADCs in CREAM I (using excellent TRD-derived tracking and corrected for CD-measured β), was $\sigma \simeq 0.2e$ for oxygen, but this was in a lower energy regime.

<i>Species</i>	<i>TCD Charge Resolution</i> (<i>e</i>)	<i>SCD Charge Resolution</i> (<i>e</i>)
Hydrogen	0.2769 ± 0.0052	0.0749 ± 0.0029
Helium	0.1780 ± 0.0056	0.1582 ± 0.0060
Carbon	0.311 ± 0.023	0.217 ± 0.013
Oxygen	0.415 ± 0.047	0.2055 ± 0.0083

Table 8.2 Charge resolutions of the TCD and SCD from this analysis for listed species. This is done here for all events with a calorimeter signal present and with the respective charge detector producing a proper charge reconstruction. The above resolutions were derived from fits performed on Figure 8.8 (for the TCD) and Figure 8.6b (for the SCD). Helium, carbon and oxygen quoted resolutions are the σ parameter from Gaussian fits, while the quoted quantity for hydrogen for the SCD is σ from a Landau distribution fit. The hydrogen in the TCD was fitted with a convolved Gaussian and Landau distribution function, and the quoted resolution here is the quadrature sum of the Gaussian and Landau σ parameters.

Also of interest is the rejection of events which undergo charge-changing interactions in the instrument. These will be visible as particles tagged as a higher-charged species in the TCD than in the SCD. Such interactions have been studied previously for the CREAM I instrument [76]. The number of charge-changing events seen in CREAM II (for events with a Calorimeter signal) is very small to non-existent (Figure 8.9).

Curiously there do appear to be some events tagged as carbon or oxygen in the SCD but as hydrogen or helium in the TCD. By selecting the event population in Figure 8.9 which the TCD measures as hydrogen or helium but the SCD measures as carbon or oxygen (the lower-right region of the figure), and comparing the number of entries to the population of events for which the detectors agree that the particles are carbon and

oxygen, we estimate the population with a smaller TCD charge to be about 18% of the size of the population with agreement.

Presumably some of these are out-of-geometry (for the TCD) events which entered the SCD and CAL, with albedo particles only hitting the TCD. Additionally, some could be highly-inclined primaries only hitting the CAL, with albedo producing non-meaningful signals in both the TCD and SCD. Yet another possible source of events with TCD-measured charges smaller than the SCD one are events where the primary particle edge-clipped one or more scintillator paddles, thus traversing a smaller path-length through the material. Such events were observed in CREAM I [28] and were excluded by a tracking-based cut removing events with tracks close to scintillator edges. Since the tracking in CREAM II is not sufficiently precise to produce such a cut without throwing out an excessive number of events, this type of tracking-based quality cut cannot be implemented. Unfortunately the minimum-signal method as implemented here for TCD charge-reconstruction is prone to pick out the edge-clipping events.

To estimate the approximate fraction of charge identifications affected by this edge-clipping effect, a simple Monte-Carlo model was constructed in C++. The model consisted of 4 geometric regions representing scintillator material in the CREAM TCD. Each scintillator volume had dimensions of $59.95 \times 29.95 \times 0.5 \text{ cm}^3$ and was placed with a 1 mm gap between paddles. Random tracks were generated by picking a random point directly above the paddles in an area $65 \times 65 \text{ cm}^2$ and also picking a random point in a region below the paddles having the approximate position and size of the SCD detector. The two points thus defined a track similar to those of the events in Figure 8.9. If the track was found to pass through both the top and bottom surfaces of the scintillator, the track was counted as a full track. If, however, it hit one but not the other, it was counted as an edge-clipping event. Events which hit within 1 cm of the ends of the paddles were also counted as edge-clippers since a lap-joint is present on the ends which reduces the thickness of scintillator material there to one-half the normal thickness. This Monte-Carlo code was then run for 10^6 tracks and the fraction of total tracks found to be edge-clipping was $\sim 3.2\%$.

Thus, the majority of the events for which the TCD and SCD disagree on charge identification (with the TCD choosing a smaller charge) are not due to edge-clippers but must be due to some other effect such as albedo contamination in the SCD or charge identifications resulting from albedo particles only. Without an alternate form of tracking such as from the CAL (so consistency can be required and out-of-geometry tracks rejected), the avenues available to refine the charge measurements of the events presented in this thesis are not clear (further work on this was also limited by the time available to complete this thesis). Because of the very low statistics available in this analysis at higher energy, no removal of these events (where the SCD and TCD disagree) was carried out. Only the TCD is used for charge identification in the remainder of this analysis.

8.4 TCD Charge With Energy

For the energy bins described in Table 8.1, charge histograms were created from the TCD. These are shown in Figure 8.10. One feature to note here is the greater

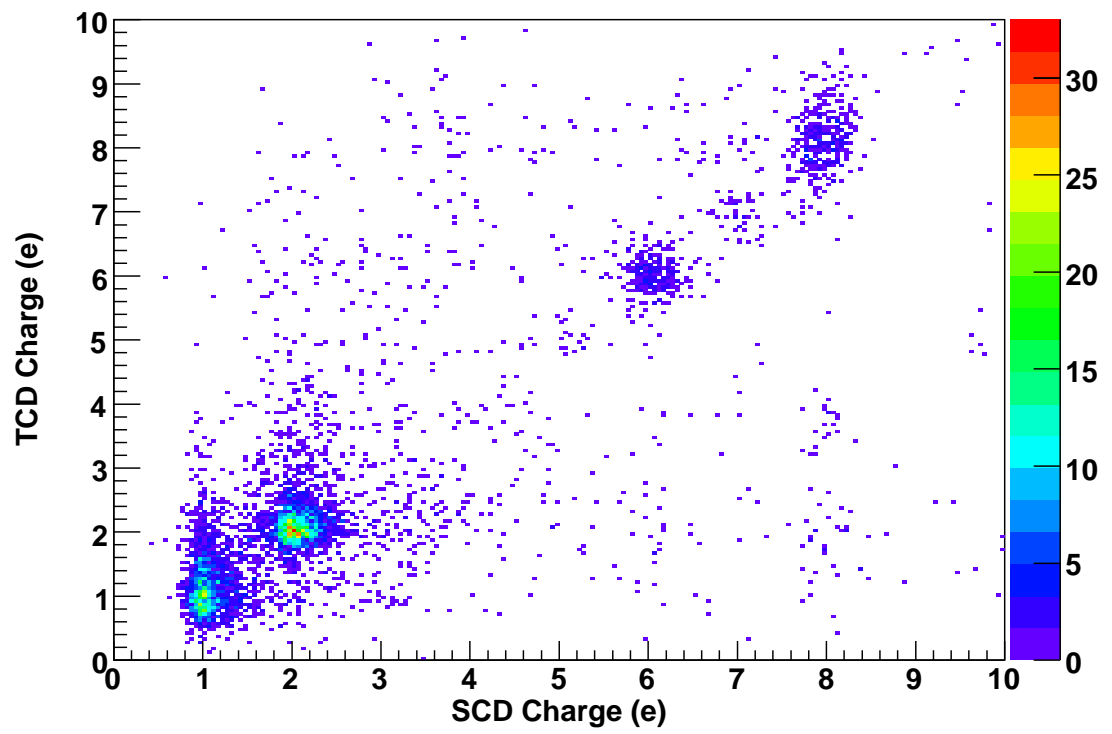


Fig. 8.9 TCD-measured charge as a function of the SCD-assigned charge, for events with both of these present (and with a calorimeter signal). Very few (perhaps no) charge-changing events appear to be present.

contamination of the hydrogen signal with higher energy, as more albedo particles are produced. Unfortunately this limits the usefulness of the ADC based TCD charge measurement to hydrogen events not much beyond ~ 10 TeV, or the first of the 3 decades in energy ultimately of interest to the CREAM project (for the calorimeter-based energy determination events).

To estimate the populations of species in each graph in Figure 8.10, the fitting routine as outlined in the last section was run for each histogram. The fitting routine for the hydrogen and helium populations required careful manual tuning to converge properly to reasonable fits. This consisted of manually estimating the hydrogen peak-positions and limiting the Landau+Gaussian distribution peak-position fit parameter to a narrow range about that point and also doing the same for the Gaussian intended to fit the helium peak.

To then estimate the number of each species present, the fit functions were numerically integrated using the parameters determined from the fitting. The results from these integrations are shown in Tables 8.3, 8.4, 8.5 and 8.6. For all species, the limits of integration were chosen to be $\pm 2\sigma$ as measured for that particular energy-bin. This is consistent with previous analyses conducted by other groups in the CREAM collaboration [1].

<i>Hydrogen Events</i>			
<i>Energy Bin Number</i>	<i>Energy (TeV)</i>	<i>Number of Events</i>	<i>Flux (AU)</i>
0	1.31	1028 ± 64	1758 ± 55
1	2.07	1988 ± 66	2145 ± 48
2	3.29	1544 ± 48	1051 ± 27
3	5.21	904 ± 33	388 ± 13
4	8.26	404 ± 21	109.6 ± 5.4
5	13.1	209 ± 15	35.7 ± 2.5
6	20.7	94.6 ± 9.8	10.2 ± 1.0

Table 8.3 The energy reported for each energy-bin, estimated number of hydrogen events and flux (in arbitrary units). The reported uncertainty on the number of events is the quadrature-sum of the Poisson uncertainty (\sqrt{N}) and the uncertainty of the numerical integral. The energy values are the result of looping Equation 8.2 with a starting guess of the spectral index of $\gamma = -2.5$ and requiring agreement to 0.0001 between loops. Values were found to be convergent after only the second execution of the loop. The fluxes quoted here are the number of events divided by the energy bin-width.

Some variation was observed in the helium distribution peak-positions and widths with energy (Figure 8.11a, Figure 8.12, Table 8.7 and Table 8.8), so the limits of integration were adjusted on a per-bin basis. Larger variations were observed in the hydrogen response, with the position of the charge-peak rising to ~ 1.4 e for the highest energy-bin and the width increasing as well. The widths of the hydrogen distributions quoted here are the quadrature-sums of the Landau and Gaussian distributions which were convolved

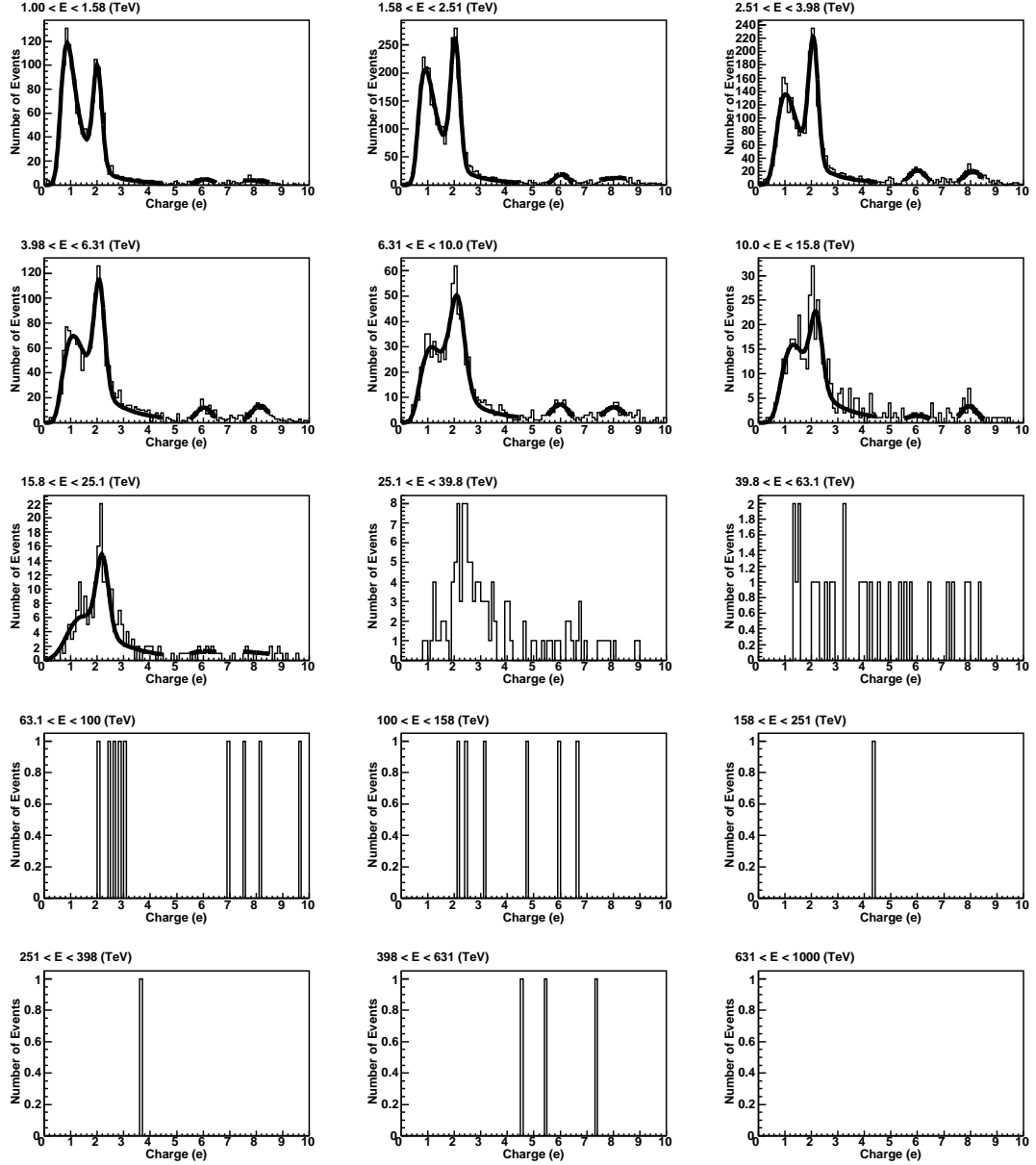


Fig. 8.10 TCD-measured charge for events having a calorimeter signal. Each histogram is for one energy bin in Table 8.1 and starts with 1 TeV. Fits were done for H, He, C and O, as described in the text. Several C and O fits fail for low-statistics histograms, and species populations are instead estimated by counting histogram contents as described in this section.

<i>Helium Events</i>			
<i>Energy Bin Number</i>	<i>Energy (TeV)</i>	<i>Number of Events</i>	<i>Flux (AU)</i>
0	1.31	342 ± 37	585 ± 32
1	2.07	931 ± 45	1004 ± 33
2	3.29	779 ± 34	530 ± 19
3	5.21	408 ± 22	175.1 ± 8.7
4	8.26	239 ± 16	64.8 ± 4.2
5	13.1	77.8 ± 8.9	13.3 ± 1.5
6	20.7	57.2 ± 7.6	6.17 ± 0.82

Table 8.4 Energy bin values, number of events and fluxes (in arbitrary units) for helium events. Same error estimation as in Table 8.3.

<i>Carbon Events</i>			
<i>Energy Bin Number</i>	<i>Energy (TeV)</i>	<i>Number of Events</i>	<i>Flux (AU)</i>
0	1.31	36 ± 12	61 ± 10
1	2.07	125 ± 16	134 ± 12
2	3.28	164 ± 16	111.9 ± 8.7
3	5.20	90 ± 10	38.6 ± 4.1
4	8.24	58.8 ± 7.9	15.9 ± 2.1
5	13.1	36.0 ± 6.1	6.2 ± 1.0
6	20.7	15.0 ± 3.9	1.62 ± 0.42

Table 8.5 Energy bin values, number of events and fluxes (in arbitrary units) for carbon events. Same error estimation as in Table 8.3.

<i>Oxygen Events</i>			
<i>Energy Bin Number</i>	<i>Energy (TeV)</i>	<i>Number of Events</i>	<i>Flux (AU)</i>
0	1.31	54 ± 15	92 ± 13
1	2.07	160 ± 19	173 ± 14
2	3.28	174 ± 16	118.6 ± 9.1
3	5.20	109 ± 11	46.8 ± 4.5
4	8.25	58.0 ± 7.9	15.7 ± 2.1
5	13.1	26.1 ± 5.2	4.47 ± 0.88
6	20.7	15.0 ± 3.9	1.62 ± 0.42

Table 8.6 Energy bin values, number of events and fluxes (in arbitrary units) for oxygen events. Same error estimation as in Table 8.3.

together from the fit to the hydrogen events. The limits of integration were chosen to be ± 2 width to be consistent with the limits used for helium. Beyond the first 7 bins, there is still a significant number of hydrogen and helium events present, but the ability of the TCD to discriminate between the species has been lost due to both the low statistics and to the increasing width and position of the hydrogen peak, eventually causing it to merge with the helium one.

For carbon and oxygen, contamination from nearby species is less of an issue, but the low statistics eventually limit the highest energy accessible. Gaussian fits were attempted for all the energy-bin graphs in Figure 8.10 to estimate the numbers of these species present. Where the fits were visually observed to fail (bins 5 and 6 for carbon, 0,1, and 6 for oxygen), all events within $\pm 2\sigma$ of $Z = 6$ and 8 were counted directly from the histogram. The σ values used here were those measured from Figure 8.8 which had all events (with a CAL signal) present. This is justified because as Figures 8.11b and 8.12 show, very little variation in the widths of these species distributions were observed with energy.

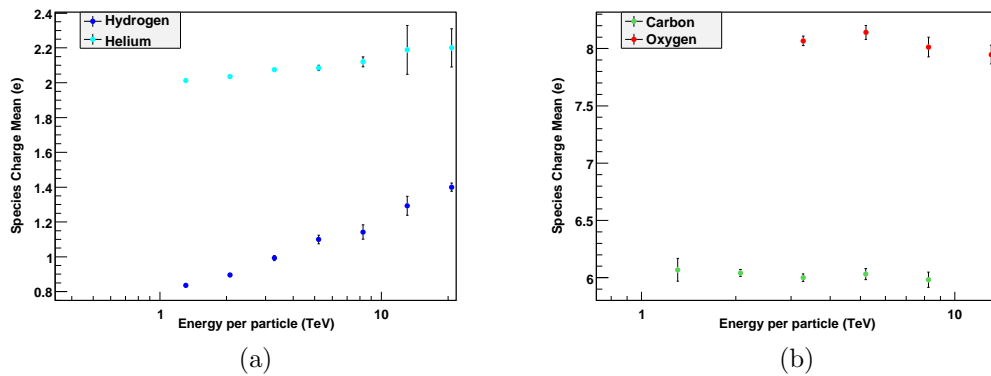


Fig. 8.11 (a) The peak-positions for the species fits performed on the first 7 energy-bin histograms shown in Figure 8.10. The hydrogen peak value is the peak of a convolved Gaussian and Landau distribution while the helium value is derived from another Gaussian which was convolved with the hydrogen function to deal with the mixing between the populations. (b) The peak-positions for carbon and oxygen also from Figure 8.10. The Gaussian fits were unsuccessful for bins 5 and 6 for carbon and 0, 1 and 6 for oxygen.

8.5 Measured Spectra

As mentioned above, the number of hydrogen, helium, carbon and oxygen events present in 7 energy bins (as measured by the CREAM II calorimeter) were estimated by fitting various functions to the charge-histograms (as measured by the Timing Charge Detector) generated for each energy bin. Some of the carbon and oxygen measurements were alternately estimated by counting entries in the histograms when fitting failed.

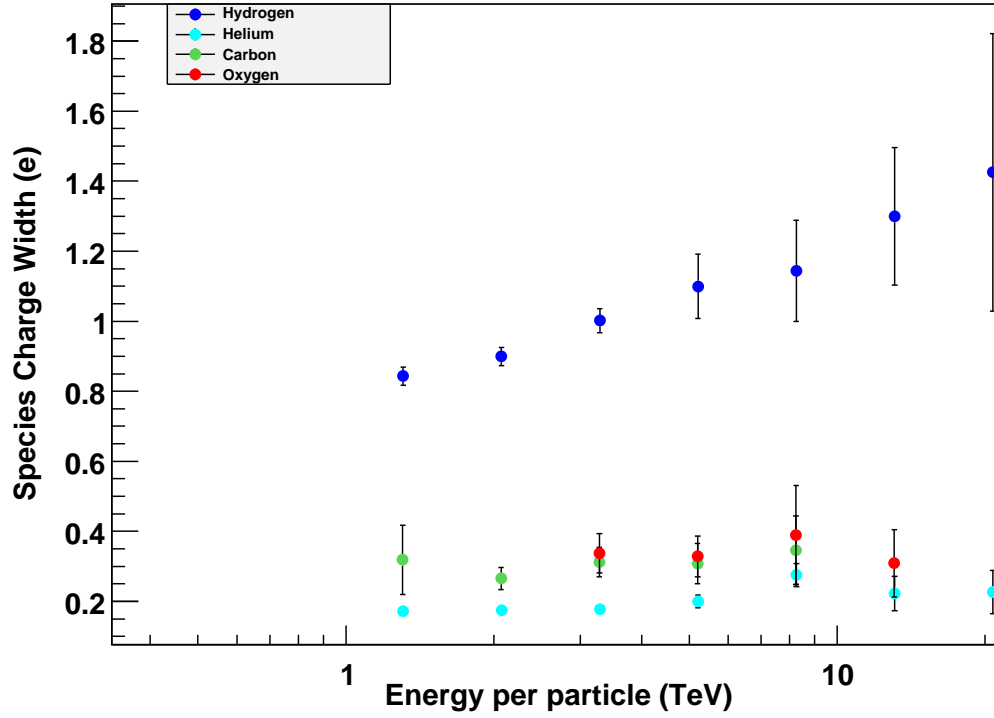


Fig. 8.12 The distribution-widths for the individual species fits shown in Figure 8.10. The hydrogen width is the quadrature-sum of the widths of the convolved Gaussian and Landau distributions used to fit this species. The other species widths are all the Gaussian σ parameters from the fits.

<i>Energy Bin Number</i>	<i>Hydrogen Peak (e)</i>	<i>Helium Peak (e)</i>	<i>Carbon Peak (e)</i>	<i>Oxygen Peak (e)</i>
0	0.836 ± 0.012	2.013 ± 0.013	6.069 ± 0.099	X
1	0.896 ± 0.010	2.0353 ± 0.0076	6.041 ± 0.030	X
2	0.993 ± 0.015	2.0746 ± 0.0088	6.001 ± 0.032	8.067 ± 0.042
3	1.099 ± 0.025	2.085 ± 0.015	6.031 ± 0.049	8.141 ± 0.061
4	1.142 ± 0.041	2.120 ± 0.029	5.982 ± 0.066	8.013 ± 0.086
5	1.293 ± 0.055	2.19 ± 0.14	X	7.947 ± 0.082
6	1.400 ± 0.023	2.20 ± 0.11	X	X

Table 8.7 The peak positions for the species-fits performed in Figure 8.10. These are also plotted in Figure 8.11. Measurements marked with an “X” represent fits that were unsuccessful.

<i>Energy Bin Number</i>	<i>Hydrogen Width (e)</i>	<i>Helium Width (e)</i>	<i>Carbon Width (e)</i>	<i>Oxygen Width (e)</i>
0	0.843 ± 0.026	0.171 ± 0.012	0.319 ± 0.099	X
1	0.899 ± 0.026	0.1749 ± 0.0088	0.265 ± 0.031	X
2	1.002 ± 0.034	0.1772 ± 0.0098	0.311 ± 0.042	0.337 ± 0.056
3	1.099 ± 0.092	0.199 ± 0.018	0.307 ± 0.057	0.328 ± 0.058
4	1.14 ± 0.14	0.275 ± 0.033	0.346 ± 0.098	0.39 ± 0.14
5	1.30 ± 0.20	0.223 ± 0.049	X	0.309 ± 0.096
6	1.43 ± 0.40	0.227 ± 0.061	X	X

Table 8.8 Widths of the species-fits performed in Figure 8.10. These are plotted in Figure 8.12. Measurements marked with an “X” represent fits that were unsuccessful.

The flux for each species and bin was then calculated (in arbitrary units) by dividing the estimated number of events by the bin width (in TeV). Both the number of events and the fluxes are tabulated in Tables 8.3, 8.4, 8.5 and 8.6. Here the uncertainties are estimated on the number of events by the quadrature sum of the uncertainty of the numerical integral and the Poisson statistics (\sqrt{N}).

The energy reported for each species and for each bin was chosen by taking Equation 8.2 with a first guess value for the spectral index of $\gamma = -2.5$ for all species, then measuring the spectral index (excluding the lowest-energy data points from the fitting) and re-evaluating the expression. It was found that after the second iteration of the loop the spectral index values for all four species had converged to within 0.0001 and no further executions of the loop were needed. The spectral indices were calculated both by fitting a power-law function ($f = f_0 E^\gamma$ with f the flux) to the values shown in the above tables (excluding the first two data points due to low calorimeter efficiency for this energy range) and by alternately fitting a first-degree polynomial to the logs of those values. No significant difference was observed between the results of these two methods (Table 8.9). The distribution of the fluxes as a function of the energy is shown in Figure 8.13. Also shown are the results of the power-law fits measuring the spectral indices for the four separate species.

The uncertainty of the energy-values measured here is reported as zero, though this is not realistic. The calorimeter has a reported energy-resolution of $\sim 50\%$ for individual events, however, this is not the energy one would report uncertainty of the bin contents for large statistics. An attempt was made to assume the bin-edges as the size of horizontal the error bars. This was abandoned however after the spectral-index fits failed to produce reasonable fits to the data points. It was also probably not a realistic estimate for the uncertainty. The energies reported here should probably be assumed to be only accurate to a factor of 2-4 regardless, because of the limited nature of the calorimeter energy reconstruction that was able to be implemented here.

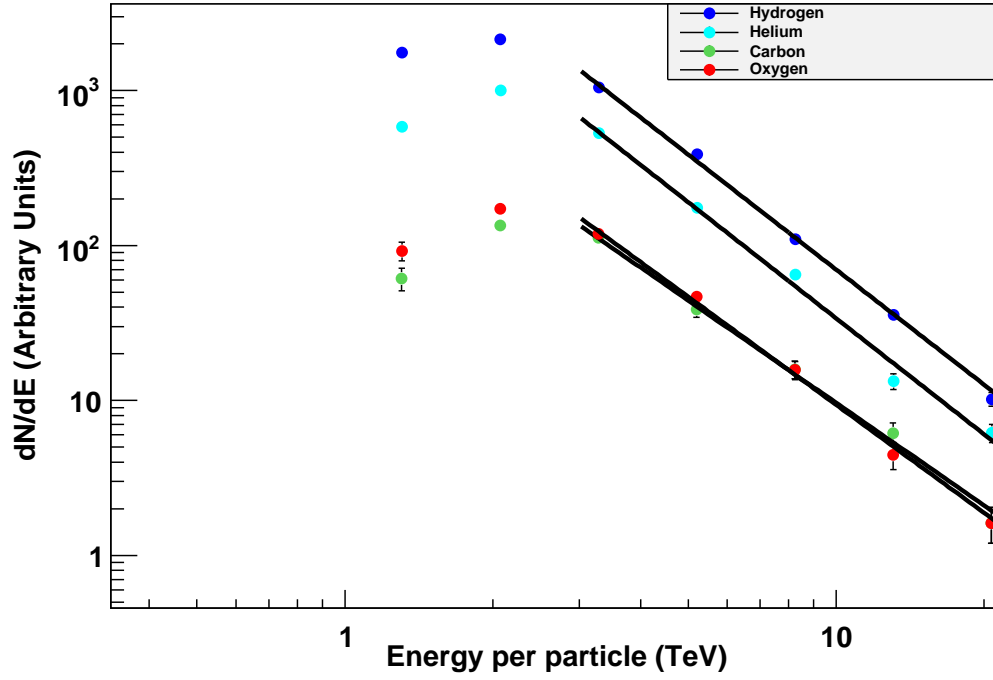


Fig. 8.13 The spectra for hydrogen, helium, carbon and oxygen with charges identified by the TCD and energies reported by the calorimeter. The individual data points are summarized in Tables 8.3, 8.4, 8.5 and 8.6. The measured spectral indices are reported in Table 8.9

<i>Species</i>	<i>Spectral Index (γ) (from power-law fit)</i>	<i>Spectral Index (γ) (from 1st order polynomial fit)</i>
Hydrogen	2.467 ± 0.034	2.465 ± 0.035
Helium	2.488 ± 0.049	2.448 ± 0.049
Carbon	2.195 ± 0.094	2.177 ± 0.090
Oxygen	2.315 ± 0.093	2.313 ± 0.093

Table 8.9 The spectral indices measured for the indicated species as shown in Figure 8.13. The fits were performed excluding the two lowest-energy data points for each species.

8.6 Note on Absolute Fluxes

As already mentioned, the author was unable to recreate the CAL-based tracking produced by other groups in the CREAM collaboration. Such tracking, if available would improve the overall tracking available, and could potentially be used in place of the TCD-based tracking used here. However, the tracking presented here might also prove complementary to the analysis undertaken by the collaboration since it does not cut events which have a poor calorimeter track reconstruction.

Not included in this analysis are several corrections necessary for an accurate determination of absolute fluxes. One is proper atmospheric corrections to the individual species fluxes arising from interactions above the instrument before detection. This is discussed elsewhere, such as in [13] for energies below those studied here, and in ongoing research for events of interest to the calorimeter conducted by other members of the collaboration. Also needed are the instrumental efficiencies arising from the physics of the detectors and from the geometrical acceptance of the overall instrument. These have been extensively investigated by several Monte Carlo models ([8], [73]). For these reasons, all the flux results presented above from this analysis are either in arbitrary units, fractions or scaled by arbitrary fractions to match previous measurements at lower energies.

8.7 Comparison with Previous Measurements

Figures 8.14 and 8.15 show the hydrogen and helium measurements reported in this thesis in comparison with the results from several other experiments. The first two data points reported above have been removed in Figure 8.15 because they are clearly suppressed in flux due to instrumental inefficiencies at the lower end of the energy scale. The fluxes here are multiplied by a factor of $E^{2.5}$ to flatten the spectra and make relative differences easier to see. An arbitrary scale factor of $10^{-8.6}$ has also been applied to the H and He data obtained here (which are in arbitrary units and not units of flux) to make hydrogen consistent with previous experimental results.

Most likely, the lowest-energy data point for H and He here is also suppressed in flux due to instrumental inefficiencies. The remaining 4 highest-energy points for hydrogen appear largely consistent with previous experimental results (with the appropriate normalization factor in flux) and appear quite flat in these energy-scaled flux units (though this is a very narrow energy range). The helium points also seem to display a very flat response (with the lowest-energy point excluded) but have a flux suppressed by almost an order of magnitude compared to the results of CREAM I, ATIC II, and JACEE. The fluxes are more consistent with those found by RUNJOB however. Possible reasons for this suppressed flux could be differing instrumental efficiencies in the calorimeter and instrument trigger which have not been taken into account, as well as some sort of systematic undercounting of helium relative to hydrogen due to the fitting method used to estimate the species counts from the histograms in Figure 8.10. The use of the common normalization factor for H and He is thus probably not justified in this circumstance, and little weight should be given to the suppressed relative flux obtained for helium here, because proper corrections for instrumental response are not included.

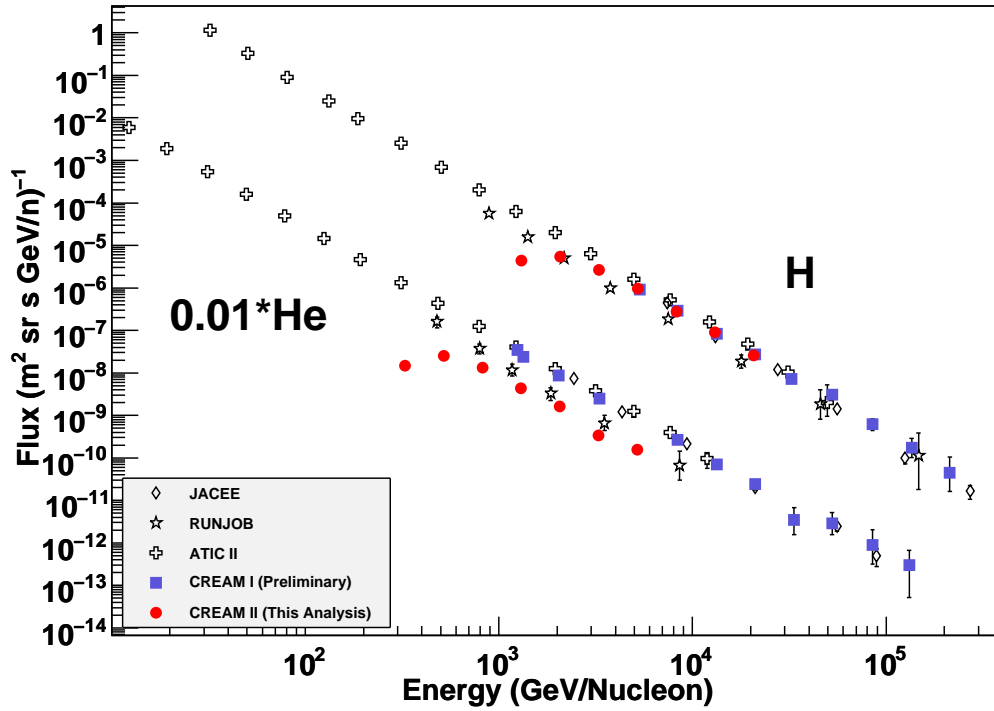


Fig. 8.14 The elemental abundances of cosmic-ray hydrogen (top) and helium (bottom) nuclei as found in the analysis presented in this thesis. Results from several recent experiments are also presented for comparison (RUNJOB [14], JACEE [15], ATIC II [16] and CREAM I preliminary results presented in [6]). The CREAM II results from this thesis have also been scaled by an arbitrary factor of $10^{-8.6}$ to make the arbitrary units compatible with previous measurements of the absolute flux for hydrogen. All the helium fluxes have further been scaled by additional factor of 0.01 to better separate the species.

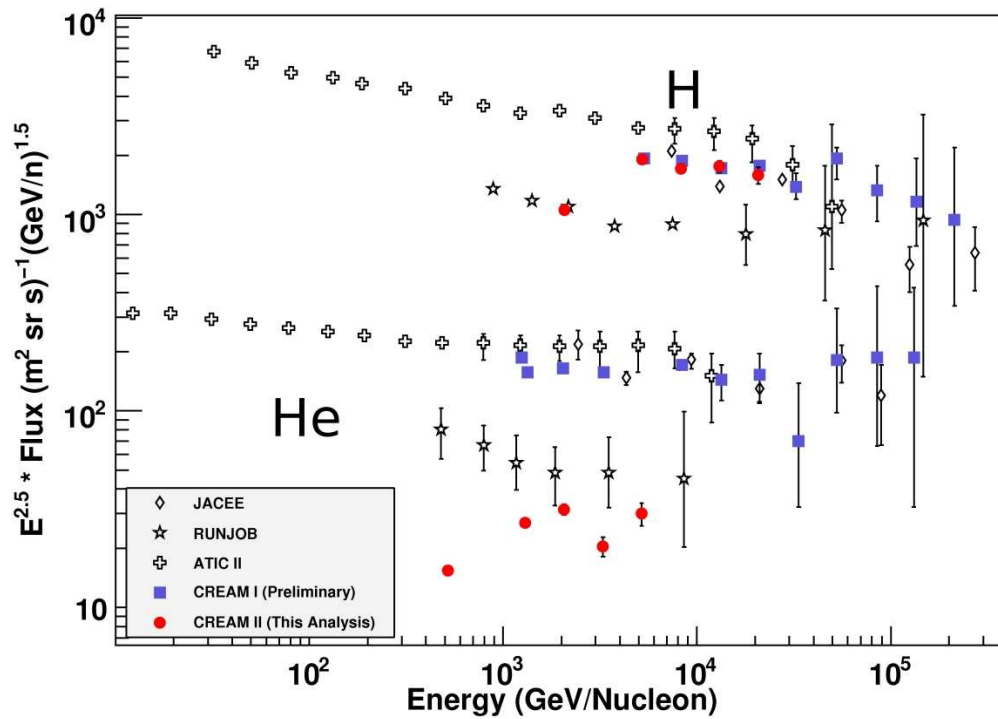
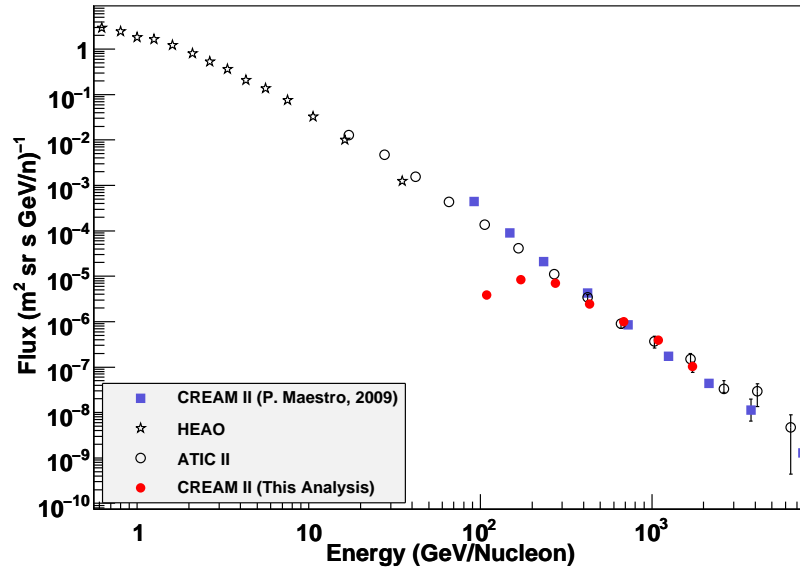


Fig. 8.15 The same results as presented in Figure 8.14, except that the fluxes are scaled by $E^{2.5}$ to flatten the spectra and make visual comparison of the spectral indices easier. Also, the two lowest-energy data points have been removed since their fluxes are clearly suppressed due to instrumental inefficiencies at the lower end of the energy scale. The helium fluxes have not been scaled by the additional factor of 0.01 that was applied in Figure 8.14.

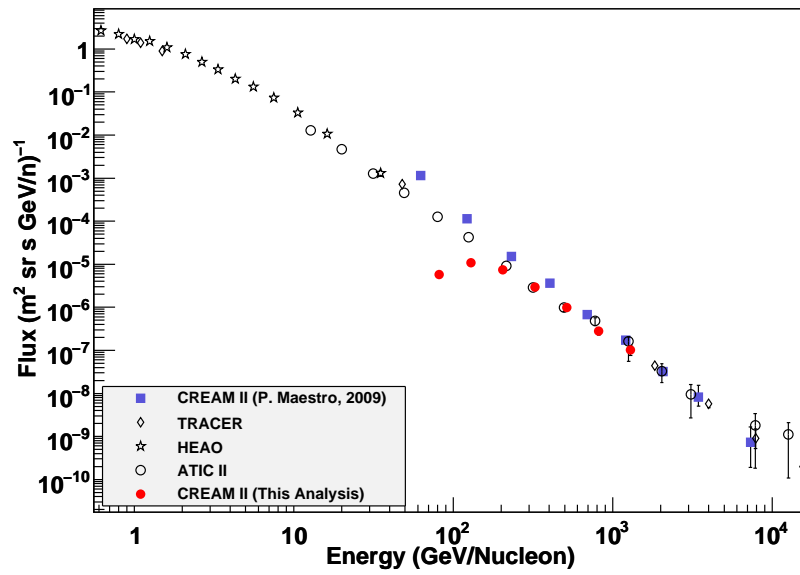
The results of CREAM I and ATIC II strongly suggest that the spectral indices of cosmic-ray hydrogen is steeper than for helium. This is not clear evidence for the behavior predicted for SNR shock acceleration in Section 1.3.3 where a hard break in the flux of each species would be expected (with the cutoff for each species scaling with Z). It is *suggestive* of some sort of rolling off of the efficiency of the Galactic accelerators of cosmic-ray hydrogen. As already discussed (Sections 1.5.3 and 1.6) the KASCADE air-shower array measurements suggest an enrichment of heavier species in the cosmic-ray flux at energies of order 1000 TeV and above. Whether a hard break in the hydrogen spectrum does exist remains an unresolved question however.

The carbon and oxygen spectra found here are shown in Figure 8.16, along with a separate recent analysis presented by P. Maestro [1] which used just the SCD for charge identification. Here the lower-energy inefficiencies in the flux estimations presented in this analysis are quite clear. Again, an arbitrary scale factor (of $10^{-7.2}$) have been applied to our fluxes (in arbitrary units) to make them coincident with the alternative CREAM analysis. The higher-energy points are more consistent with the other results, with the slope clearly approaching (but not quite reaching) the slope of the points from the alternative analysis. P. Maestro finds quite consistent spectral indices for the primary cosmic-ray species beyond helium (C, O, Ne, Mg, Si and Fe), with all found to be very close to 2.66. These results are very consistent with previous measurements at and below this energy range, as shown in Figure 8.16.

In light of the comparisons above with other data sets, the spectral indices were remeasured by now excluding the first three lowest-energy data points for all species (previously only the first two had been excluded). These new measurements are shown in Table 8.10. All species except carbon were found to have larger spectral indices than before, after excluding this extra data point. However, the values still do not agree with previous measurements, especially the carbon and oxygen values. The spectral indices of carbon and oxygen in this energy range and (directly below, as mentioned by [1]) have well-established values around 2.66. The values measured here are all less, though oxygen is closer (almost within quoted errors) of the accepted value. Though the hydrogen spectral index quoted here is steeper than that for the other species presented, we cannot make a definitive statement about whether it actually is steeper due to the lack of instrumental and atmospheric corrections, which were not available to be included here. The values are perhaps *suggestive* however, and could certainly be said to be consistent with a steeper hydrogen trend in the data.



(a) Carbon.



(b) Oxygen.

Fig. 8.16 Carbon and Oxygen spectra as measured by the CREAM II experiment. The results found in this thesis have been scaled in flux by an arbitrary factor of $10^{-7.2}$ to make them consistent with the absolute-flux corrected points from the analysis by P. Maestro [1]. Energy-dependent efficiencies in the calorimeter response are probably largely responsible for the suppressed flux at lower energy. Also shown are results from the space-based HEAO-3-C2 [17] experiment and the TRACER [18] and ATIC II [16] balloon-borne experiments.

<i>Species</i>	<i>Spectral Index (γ)</i>
Hydrogen	2.629 ± 0.061
Helium	2.567 ± 0.085
Carbon	2.18 ± 0.14
Oxygen	2.48 ± 0.16

Table 8.10 The spectral indices measured for the four studied species in this analysis, after excluding the first 3 lower-energy data points shown in Figure 8.13. Only the power-law fit values are quoted here since the linear-fit method discussed above was again found to be consistent. The quoted uncertainties are those from the power-law fit performed on the data-points. Since this analysis does not include important instrumental and atmospheric corrections, the quoted spectral indices are not within errors of an alternative CREAM analysis presented in [1].

Chapter 9

Conclusions

9.1 TCD Performance

The CREAM II Timing Charge Detector was observed to have individual charge resolution (derived from peak-detector type ADCs) for species from hydrogen to oxygen for events having energy greater than 1TeV in the analysis presented in this thesis. The resolutions for individual species as a function of energy are discussed in more detail in the previous chapter (Section 8.4). The detector's ability to discriminate between hydrogen and helium events was observed to degrade substantially however for higher energies, with the hydrogen resolution worsening from $0.843 \pm 0.026e$ to $1.43 \pm 0.40e$ as the energy ranged from approximately 1-20 TeV/particle. Over this same range the helium resolution worsened from $0.171 \pm 0.012e$ to $0.227 \pm 0.061e$. This is believed to be mainly due to greater contamination from albedo particles traveling up from the calorimeter module, after being generated in showers induced by the high-energy cosmic rays in the carbon targets. The resolutions for carbon and oxygen were much more consistent however, with both staying near the values measured for the all-energy charge distribution (Figure 8.8), namely $0.311 \pm 0.023e$ for carbon and $0.415 \pm 0.047e$ for oxygen.

The Time-to-Digital Converters were determined to have insufficient timing resolution to discriminate between hydrogen and helium (when used to try and determine the PMT pulse leading-edge slope); however, some discrimination between the light (hydrogen+helium) and the medium (carbon and oxygen) species was demonstrated (Section 6.7). Some charge discrimination using instead just the threshold crossings should also be possible but was not explored here.

9.2 Elemental Spectra

The proton and helium elemental spectra measured in this thesis were found to be consistent with the spectral indices measured by other groups in the energy range studied, as long as the lower 3 data points were excluded due to suspected instrumental inefficiencies and threshold effects which were not corrected for (due to a lack of time and information). However, the energy range was relatively small (approximately 1-20 TeV/particle), so the ability to draw any further conclusions from the observed spectral indices is limited.

The absolute fluxes of hydrogen and helium were not determined, but the observed fluxes (in arbitrary units) were scaled to be consistent with previous measurements (for hydrogen). The helium flux was found to be suppressed relative to the hydrogen, more consistent with RUNJOB results than more contemporary measurements made by ATIC

II and CREAM I. This is most likely due to necessary instrumental and atmospheric corrections which were not available to include in this analysis.

Carbon and oxygen events were also observed and their spectra measured. The measured spectral indices were lower than those typically accepted for these species (2.66 is a well-established value for both, but 2.18 ± 0.14 for carbon and 2.48 ± 0.16 for oxygen were observed).

Spectral indices for hydrogen (2.629 ± 0.061) and helium (2.567 ± 0.085) were also measured. While the hydrogen index is the largest one of the four species studied in this thesis, the indices for hydrogen and helium appear consistent with each other within the experimental uncertainty here. We cannot claim with certainty that a steeper hydrogen spectral index is present, as had been reported in a separate CREAM analysis [77], where a hydrogen spectral index of 2.66 ± 0.03 was found to be softer than the helium one at 2.57 ± 0.04 , though the results here certainly are consistent with that.

9.3 The Author's Contributions to the CREAM Project

I have participated in the CREAM collaboration in support of the Timing Charge Detector system from the early production phase until the present (four total flights so far). I was involved with the quality-checking of the scintillator materials used in the CREAM I payload (checking for uniform thickness). I participated heavily in the testing and debugging of the prototype TCD readout electronics and the PMT active-base electronics, and in the fabrication of the eventual flight hardware. I have also been heavily involved in the integration of the TCD into the total CREAM payload (mainly the first 3 flights) and in one beam-test campaign at CERN in 2003.

Before the first flight of CREAM, I (along with several others) worked to correct the TCD PMT power supply HV-breakdown issue discussed in Section 4.2 (with only a few weeks' time available before the ship date). I was one of the TCD representatives in Antarctica for the CREAM II flight which launched in December of 2005, and I provided the main TCD support for the instrument checkout and eventual certification of flight readiness. Following a shipping accident that damaged the CREAM III payload, I assisted in the repair of the TCD systems.

I also produced a GEANT4-based [72] simulation of one TCD scintillator paddle which included optical physics. This allowed us to deconvolve the electronics-based resolution of the TCD from the photon-propagation based resolution. This was helpful in understanding the slew-rate measurements from the Time-to-Digital Converter readouts in the TCD readout electronics. This optical model also found valuable use when modified for evaluating a novel design for a charged-particle veto paddle system for the CREST [41] project, and a proposed new charge detector design for the TRACER [18] payload. I have conducted an analysis of the CREAM II flight data with the goal of producing charge identifications for primary cosmic rays which were within the geometrical acceptance of the TCD detector.

9.4 The Way Forward for CREAM

The data set analyzed in this thesis, and the method used, are not sufficient to answer all the questions of interest to this experiment. One issue is the limited exposure available with just analyzing data from one flight (though it is still quite large compared to most other direct measurements, excluding the emulsion experiments such as JACEE and RUNJOB). This issue will be addressed by combining the data for all the flights, once sufficient work has been done (and much already has been by the collaboration) to correct the data sets sufficiently so that they can be combined, accounting for instrumental variation from one flight to the next.

The analysis technique presented here also suffered from several limitations. The first is that it inherently selects fewer events within its acceptance (defined by the TCD and CAL) than for events just requiring the SCD and CAL. Furthermore, accurate calorimeter tracking was not available for this analysis (though it has been implemented successfully by other groups in the project), and it might have provided a useful quality cut and consistency check for the TCD timing-derived tracking used here. The ability of the TCD timing-based tracking to produce instrument tracks when the CAL tracking routine fails, however, might be of interest to the collaboration to ‘rescue’ some events which otherwise are rejected due to no tracking being available. Hopefully the redundant (based on the TCD) charge measurement technique presented here will also prove useful to the CREAM enterprise as well, for the subset of events to which it applies.

Appendix A

Particle Interactions in Matter Relevant for Detection

A.1 The Bethe-Bloch Equation

The primary means of energy loss for charged particles (heavier than electrons and at least moderately relativistic) passing through matter are ionization-losses in the material. When the particle passes through the material, Coulomb interactions between the particle and electrons in the material will transfer particle kinetic energy to the electrons. The Bethe-Bloch equation below describes this energy loss quite well within a large energy range and for many materials [3], with the values and meaning of the variables shown in Table A.1.

$$-\frac{dE}{dx} = 4\pi N_A r_e^2 m_e c^2 z^2 \frac{Z}{A} \frac{1}{\beta^2} \left[\frac{1}{2} \ln \frac{2m_e c^2 \beta^2 \gamma^2 T_{max}}{I^2} - \beta - \frac{\delta(\beta\gamma)}{2} \right] \quad (\text{A.1})$$

Quantity	Definition	Value or Units
z	Charge of the incident particle	e (unit charges)
Z	Charge of the absorber species	e (unit charges)
A	Atomic mass of absorber	$g \text{ mol}^{-1}$
$m_e c^2$	Electron mass $\times c^2$	$0.510998918(44) \text{ MeV}$
T_{max}	Maximum energy transferable to absorber electrons	MeV
N_A	Avogadro's number	$6.0221415(10) \times 10^{23} \text{ mol}^{-1}$
r_e	Classical electron radius	$2.817940325(28) \text{ fm}$
$\delta(\beta\gamma)/2$	Density effect correction	
I	Mean excitation energy	eV

Table A.1 Quantities appearing in the Bethe-Bloch equation.

Here the first terms have the value $4\pi N_A r_e^2 m_e c^2 / A = 0.307 \text{ MeV } g^{-1} \text{ cm}^2$ for $A = 1 g \text{ mol}^{-1}$. The mean excitation energy (I) is theoretically the logarithmic-average of the atomic orbital frequencies ν with the oscillator strengths of the atomic levels as weights [59]. Generally, empirical values are necessary. The maximum energy transferable to an absorber electron can be found using relativistic kinematics, and for particles with $M \gg m_e$ has the value $T_{max} \simeq 2m_e c^2 (\beta\gamma)^2$ [59]. The Bethe-Bloch equation for several types of absorbers and incident particles is shown in Figure A.1.

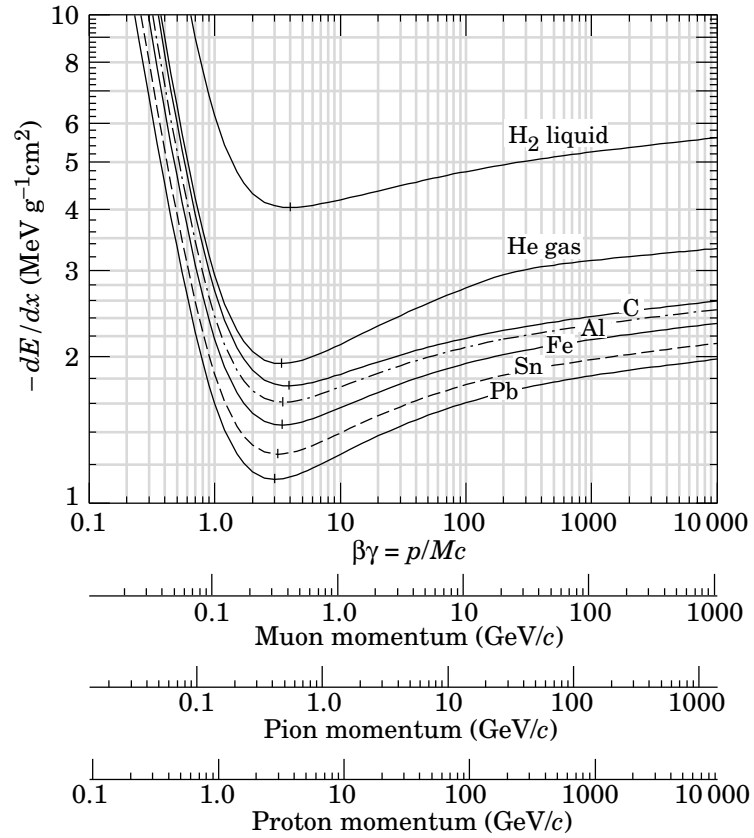


Fig. A.1 Results of the Bethe-Bloch equation for several types of typical absorber materials. Scales showing momentum for several different types of incident-particles are shown as well. This figure is from the Particle Data Group [3]

The density effect correction arises because the incident charged particle polarizes atoms in its path. Thus electrons far from the track will be partially shielded from the incident particle's electric field. This term is normally a semi-empirical function of $\beta\gamma$ and the density of the material, and becomes more important at higher energy.

A.2 Scintillators

Scintillator materials function by converting energy deposited by ionizing radiation into optical photons. The physical process that produces the light initially is the excitation of molecular electrons to higher-energy states and the subsequent *prompt* emission of photons. In plastic organic scintillators such as the ones used in CREAM, the electrons which produce the scintillation light are free valence electrons associated with specific molecules in the material, and not specific atoms [59].

The initial scintillation light is primarily in the UV, and is non-ideal for use since PMTs typically have poor response in the UV, and the plastic scintillation materials typically have shorter attenuation lengths in the UV. To side-step these issues, a wavelength-shifting fluorescent material is usually added, which will absorb the UV, and promptly re-emit some percentage as visible light (typically blue or green). The overall total efficiency of plastic scintillators is of order 1 photon per 100 eV of energy deposited in the material [3].

Some scintillation materials have much longer decay times than rise times. This is especially true for many non-organic crystals (some in the hundreds of ns) and for some organics such as the standard reference material anthracene (~ 30 ns). In these cases the rise time can generally be ignored and the response can be modeled by a decaying exponential function. In practice there are often two exponential terms, one with a fast decay time and one with a slow decay time, depending on the specific properties of the material.

Plastic scintillators and most other organics typically have fast decay times in their response (\sim a few ns). In this case the rise time cannot be ignored from the picture. A useful empirical equation to fit to specific scintillator response is a Gaussian function convolved with an exponential:

$$N(t) = N_0 f(\sigma, t) e^{\left(\frac{-t}{\tau}\right)} \quad (\text{A.2})$$

with $f(\sigma, t)$ a Gaussian distribution (Equation A.3) of width σ , and τ the decay time of the exponential factor. For BC-408, the scintillator used in the CREAM TCD, the parameters are $\sigma = 1.06$ ns and $\tau = 2.1$ ns [58].

$$f(\sigma, t) = \frac{1}{\sigma\sqrt{2\pi}} e^{\left(-\frac{t-t_0}{2\sigma^2}\right)} \quad (\text{A.3})$$

As a general practical approximation, the response of scintillators is linear with dE/dx , but this breaks down, especially for more highly-charged particles like fully-ionized atomic nuclei such as cosmic rays. A first-order empirical approximation of this

behavior is given on a species-by-species basis by *Birk's law* below.

$$\frac{dL}{dx} = \frac{A \frac{dE}{dx}}{1 + k_B \frac{dE}{dx}} \quad (\text{A.4})$$

Here A is an absolute efficiency of the scintillation process and k_B is a parameter experimentally relating density of ionization centers in the material to the energy deposit dE/dx . In practice, higher order corrections can also be necessary as well.

A.3 Silicon

A silicon p-n junction operated under reverse bias produces a detector sensitive to ionizing radiation. In this sort of detector, the particle ionizes electron-hole pairs which then produce a signal detectable by readout electronics directly. One advantage of this sort of detector is that the energy deposit required for ionization is typically a factor of 10 less than that of a gas detector [59]. Other advantages are the very thin sizes possible, generally good linearity and reasonably fast response times in the range of a few times 10 ns.

A.4 Cherenkov Radiation

Whenever a charged particle velocity exceeds the speed of light $\beta c = v = c/n$ in a dielectric material (with n the index of refraction for the material), an optical shock-wave will be present which emits photons [59]. This is already included in the energy losses described by the Bethe-Bloch equation above. The threshold for production of Cherenkov radiation is thus exceeded whenever $v > c/n$.

The photons will be emitted in a cone, with angle given by,

$$\cos \theta_C = \frac{1}{\beta n(\omega)} \quad (\text{A.5})$$

with ω the frequency of the emitted radiation. Leo [59] shows that the number of emitted photons per unit length per unit wavelength λ is:

$$\frac{d^2 N}{d\lambda dx} = \frac{2\pi z^2 \alpha}{\lambda^2} \left(1 - \frac{1}{\beta^2 n^2(\lambda)} \right) = \frac{2\pi z^2 \alpha}{\lambda^2} \sin^2 \theta_C \quad (\text{A.6})$$

with α the fine structure constant. This can be integrated over the wavelength range of interest (to which the photodetectors are sensitive) to yield the number of emitted photons per unit length. As can be seen, the rate of photon production scales as $1/\lambda^2$, which implies that the number of emitted photons diverges for small λ . For any real material however, as $\lambda \rightarrow 0$, $n(\lambda)$ becomes large. Eventually the condition $\beta > 1/n(\lambda)$ is no longer satisfied and a lower limit for λ (maximum photon energy) is found.

A.5 Transition Radiation

Transition radiation consists in photon emission which occurs when a charged particle transits from vacuum into a medium with plasma frequency ω_P . The total emission is given by [3]:

$$I = \frac{\alpha z^2 \gamma \hbar \omega_P}{3} \quad (\text{A.7})$$

with α the fine structure constant and z the charge of the incident particle. The typical emission angle for the photons is $\sim 1/\gamma$, so for large velocity particles the emitted photons are nearly co-moving with the particle track. For materials such as styrene, $\hbar \omega_P \simeq 20$ eV. For particles with $\gamma \simeq 10^3$ the photons emitted are chiefly soft X-rays. The number of photons emitted with $\hbar \omega \geq \hbar \omega_0$ is

$$N_\gamma(\hbar \omega \geq \hbar \omega_0) = \frac{\alpha z^2}{\pi} \left[\left(\ln \frac{\gamma \hbar \omega_P}{\hbar \omega_0} - 1 \right)^2 + \frac{\pi}{12} \right]. \quad (\text{A.8})$$

Bibliography

- [1] MAESTRO, P. and ET AL. (2009 (submitted)) “Elemental energy spectra of cosmic rays measured by CREAM-II,” *Proc. 31st Int. Cosmic Ray Conf.*
- [2] CRONIN, J., T. K. GAISSER, and S. P. SWORDY (1997) “Cosmic Rays at the Energy Frontier,” *Scientific American*, **276**(1), pp. 62–67.
- [3] AMSLER, C. and THE PARTICLE DATA GROUP (2008) “Review of Particle Physics,” *Physics Letters*, **B667**(1), pp. 254–260.
- [4] SIMPSON, J. A. (1983) “Elemental and Isotopic Composition of the Galactic Cosmic Rays,” *Ann. Rev. Nucl. Part. Sci.*, **33**, pp. 323–382.
- [5] APEL, W. D. and ET AL. (2009) “Energy Spectra of Elemental Groups of Cosmic Rays: Update on the KASCADE Unfolding Analysis,” *Astroparticle Physics*, **31**, pp. 86–91.
- [6] YOON, Y. S. and ET AL. (2007) “H and He spectra from the 2004/05 CREAM-I flight,” *Proc. 30th Int. Cosmic Ray Conf.*, **2**, pp. 55–58.
- [7] SEO, E. S. and ET AL. (2007) “Approaching the Knee with Direct Measurements,” *Nuclear Physics B - Proc. Suppl.*, **175-176C**, pp. 155–161.
- [8] AHN, H. S. and ET AL. (2007) “The Cosmic Ray Energetics and Mass (CREAM) Instrument,” *Nucl. Inst. & Meth. A*, **579**, pp. 1034–1053.
- [9] UNIVERSITY OF MARYLAND, “CREAM Flight 2004 (Web Site),” .
URL <http://cosmicray.umd.edu/cream/cream-flights/flight-2004.html>
- [10] AHN, H. S. and ET AL. (2009) “The Cosmic Ray Energetics and Mass (CREAM) timing charge detector,” *Nucl. Inst. & Meth. A*, **602**, pp. 525–536.
- [11] NASA AND THE UNIVERSITY OF MARYLAND COSMIC RAY PHYSICS LABORATORY, “Cosmic Ray Energetics and Mass (CREAM) (Web Site),” .
URL <http://cosmicray.umd.edu/cream/>
- [12] ARCTURUS NETWORKS (2002) *uCDimm ColdFire 5272 Hardware/Firmware Reference Guide*.
URL slac.stanford.edu/grp/lcls/controls/global/standards/hardware/UC5272UM.pdf
- [13] CONKLIN, N. B. (2009) *The Boron-to-Carbon Ratio From the First COSMIC RAY ENERGETICS AND MASS Balloon Campaign*, PhD in Physics, The Pennsylvania State University, University Park, Pennsylvania.
- [14] DERBINA, V. A. and ET AL. (2005) “Cosmic-Ray Spectra and Composition in the Energy Range of 101000 TeV per Particle Obtained by the RUNJOB Experiment,” *The Astrophysical Journal*, **628**, pp. L41–L44.

- [15] ASAKIMORI, K. and ET AL. (1998) “Cosmic-Ray Proton and Helium Spectra: Results from the JACEE Experiment,” *The Astrophysical Journal*, **502**, pp. 278–283.
- [16] WEFEL, J. P. and ET AL. (2007) “Revised Energy Spectra for Primary Elements (H–Si) above 50 GeV from the ATIC-2 Science Flight,” *Proc. 30th Int. Cosmic Ray Conf.*, **2**, pp. 31–34.
- [17] ENGELMANN, J. J., P. FERRANDO, A. SOUTOUL, P. GORET, and E. JULIUSSEN (1990) “Charge composition and energy spectra of cosmic-ray nuclei for elements from Be to Ni - Results from HEAO-3-C2,” *Astronomy and Astrophysics*, **233**, pp. 96–111.
- [18] AVE, M., P. J. BOYLE, F. GAHBAUER, C. HÖPPNER, J. R. HÖRANDEL, M. ICHIMURA, D. MÜLLER, and A. ROMERO-WOLF (2008) “Composition of Primary Cosmic-Ray Nuclei at High Energies,” *Astrophysical Journal*, **678**, pp. 262–273.
- [19] LONGAIR, M. S. (1992, 2nd edition) *High Energy Astrophysics*, vol. 2, Cambridge University Press.
- [20] ——— (1992, 2nd edition) *High Energy Astrophysics*, vol. 1, Cambridge University Press.
- [21] GREISEN, K. (1966) “End to the Cosmic-Ray Spectrum?” *Physical Review Letters*, **16**, pp. 748–750.
- [22] ZATSEPIN, G. T. and V. A. KUZ’MIN (1966) “Upper Limit of the Spectrum of Cosmic Rays,” *Journal of Experimental and Theoretical Physics Letters*, **4**, pp. 78–80.
- [23] ABBASI, R. U. and ET AL. (2008) “First Observation of the Greisen-Zatsepin-Kuzmin Suppression,” *Phys.Rev.Lett.*, **100**.
- [24] ATKINS, P. (1998, 6th edition) *Physical Chemistry*, W. H. Freeman and Company.
- [25] STRONG, A. W., I. V. MOSKALENKO, and V. S. PTUSKIN (2007) “Cosmic-Ray Propagation and Interactions in the Galaxy,” *Annual Review of Nuclear and Particle Science*, **57**, pp. 285–327.
- [26] GAISSER, T. K. (1990) *Cosmic Rays and Particle Physics*, Cambridge University Press.
- [27] CASTELLINA, A. and F. DONATO (2005) “Diffusion Coefficient and Acceleration Spectrum From Direct Measurements of Charged Cosmic Ray Nuclei,” *Astropart.Phys.*, **24**, pp. 146–159.
- [28] WAKELY, S. P. and ET AL. (2008) “Measurements of Cosmic-Ray Secondary Nuclei at High Energies With the First Flight of the CREAM balloon-Borne Experiment,” *Astropart. Phys.*, **30**, pp. 133–141.

- [29] FRENCH, A. P. (1968) *Special Relativity*, W. W. Norton & Company.
- [30] COUTU, S. and ET AL. (1999) “Cosmic-Ray Positrons: Are There Primary Sources?” *Astropart. Phys.*, **11**, pp. 429–435.
- [31] PICOZZA, P. and ET AL. (2007) “The Physics of Pamela Space Mission,” *Proc. 30th Int. Cosmic Ray Conf.*, **2**, pp. 19–22.
- [32] FUKU, H. and ET AL. (2008) “Current status and future plans for the general antiparticle spectrometer (GAPS),” *Advances in Space Research*, **41**, pp. 2056–2060.
- [33] NAKAMURA, R. and ET AL. (2009) “The Nature of a Cosmic-Ray Accelerator, CTB37 B, Observed with Suzaku and Chandra,” *Publ. Astron. Soc. Japan*, **61**, pp. S197–S207.
- [34] NASA-WALLOPS FLIGHT FACILITY, “Super Pressure Balloons - General Information (Web Site),” .
URL <http://sites.wff.nasa.gov/code820/gendescription.html>
- [35] TAKAHASHI, Y. and ET AL. (1998) “Elemental Abundance of High Energy Cosmic Rays,” *Nuclear Physics B (Proc. Suppl.)*, **60B**, pp. 83–92.
- [36] HAREYAMA, M. and ET AL. (2003) “Primary Proton and Helium Spectra Observed by RUNJOB Collaboration,” *Proc. 28th Int. Cosmic Ray Conf.*, **2**, pp. 1837–1840.
- [37] CHANG, J. and ET AL. (2008) “An excess of cosmic ray electrons at energies of 300–800 GeV,” *Nature*, **456**, pp. 362–365.
- [38] ADRIANI, O. and ET AL. (2009) “Observation of an anomalous positron abundance in the cosmic radiation,” *Nature*, **458**, pp. 607–609.
- [39] ABDO, A. A. and ET AL. (2009) “Measurement of the cosmic ray $e^+ + e^-$ spectrum from 20 GeV to 1 TeV with the Fermi Large Area Telescope,” *Phys. Rev. Lett.*, **102**.
- [40] WASHINGTON UNIVERSITY ST. LOUIS, “Trans Iron Galactic Element Recorder (Web Site),” .
URL <http://cosray.wustl.edu/tiger/index.html>
- [41] MUSSER, J., “Cosmic Ray Electron Synchrotron Telescope(CREST) (Web Site),” .
URL <http://physics.indiana.edu/~jmusser/CREST.html>
- [42] GORHAM, P. and ET AL. (2009) “New Limits on the Ultra-high Energy Cosmic Neutrino Flux from the ANITA Experiment,” *Phys. Rev. Lett.*, **103**.
- [43] JET PROPULSION LABORATORY, “Voyager (Web Site),” .
URL <http://voyager.jpl.nasa.gov/>
- [44] MARTIN, T., “Alpha Magnetic Spectrometer (Web Site),” .
URL <http://ams-02project.jsc.nasa.gov/>

- [45] THE AMS COLLABORATION (1999) “Search for antihelium in cosmic rays,” *Phys. Lett.*, **B461**, pp. 387–396.
- [46] INSTITUTE FOR COSMIC RAY RESEARCH, UNIVERSITY OF TOKYO, JAPAN, “AGASA (Akeno Giant Air Shower Array) (Web Site),” .
URL <http://www-akeno.icrr.u-tokyo.ac.jp/AGASA/>
- [47] THE PIERRE AUGER COLLABORATION (2008) “Observation of the suppression of the flux of cosmic rays above $4 \times 10^{19} \text{eV}$,” *Phys. Rev. Lett.*, **101**.
- [48] BIRD, D. J. and ET AL. (1993) “Coincident Observations of Air Showers by the Hires Prototype and CASA/MIA Experiments,” *Proc. 23rd Int. Cosmic Ray Conf.*, pp. 4283–4286.
- [49] WEEKES, T. C. and ET AL. (2002) “VERITAS: the Very Energetic Radiation Imaging Telescope Array System,” *Astropart. Phys.*, **17**, pp. 221–243.
- [50] HOFMANN, W. and ET AL. (2003) “Status of the H.E.S.S. project,” *Proc. 28th Int. Cosmic Ray Conf.*, pp. 2811–2814.
- [51] AHARONIAN, F. and ET AL. (2008) “The energy spectrum of cosmic-ray electrons at TeV energies,” *Phys. Rev. Lett.*, **101**.
- [52] AMENOMORI, M. and ET AL. (2006) “Are protons still dominant at the knee of the cosmic-ray energy spectrum?” *Phys. Lett.*, **B632**, pp. 58–64.
- [53] KAMIOKA OBSERVATORY, ICRR, UNIV. OF TOKYO, JAPAN, “Super-Kamiokande (Web Site),” .
URL <http://www-sk.icrr.u-tokyo.ac.jp/sk/index-e.html>
- [54] THE ICECUBE COLLABORATION, “IceCube Neutrino Observatory (Web Site),” .
URL <http://icecube.wisc.edu/>
- [55] SEO, E. S. and ET AL. (2007) “The Cosmic Ray Energetics and Mass (CREAM) Overview,” *Proc. 30th Int. Cosmic Ray Conf.*, **2**, pp. 47–50.
- [56] BUÉNERD, M. and ET AL. (2007) “CHERCAM: the Cherenkov imager of the CREAM experiment, results in Z=1 test beams.” *Proc. 30th Int. Cosmic Ray Conf.*, **2**, pp. 453–456.
- [57] Teledyne Reynolds, Inc. (1999) *High Voltage Coaxial Shielded Cable*.
URL <http://www.teledynereynolds.com/product/0wireandcable/pdf/purple.pdf>
- [58] SAINT-GOBAIN INDUSTRIAL CERAMICS (2002) *BC-400/BC-404/BC-408/BC-412/BC-416 Premium Plastic Scintillators (Data Sheet)*.
URL <http://www.detectors.saint-gobain.com/media/documents/bc400416.pdf>
- [59] LEO, W. R. (1994, Revised 2nd edition) *Techniques for Nuclear and Particle Physics Experiments*, Springer-Verlag.

- [60] SAINT-GOBAIN INDUSTRIAL CERAMICS (2005) *BC-802 Premium UVA Acrylic Plastic (Data Sheet)*.
URL <http://www.detectors.saint-gobain.com/media/documents/pdsbc802.pdf>
- [61] Emerson & Cuming (2007) *STYCAST 4640 Lightweight, RTV Silicone Encapsulant (Data Sheet)*.
URL <http://207.250.200.229:8080/1/doc?id=50638>
- [62] Ultravolt (1998) *“A” Series High Voltage Power Supply*.
URL <http://www.ultravolt.com/products.htm>
- [63] NASA/CSBF, “Columbia Scientific Balloon Facility (Web Site),” .
URL <http://www.nsbfnasa.gov/>
- [64] NASA, “Goddard Space Flight Center (Web Site),” .
URL <http://www.nasa.gov/centers/goddard/home/index.html>
- [65] Vicor Corporation (2009) *VI-J00, VE-J00 Half Brick DC-DC Converters 25 to 100 Watts (Data Sheet)*.
URL http://cdn.vicorpower.com/documents/datasheets/ds_vi-j00.pdf
- [66] High Voltage Corporation (2006) *Miniature, Regulated High Voltage Power Supplies, C-Series*.
URL <http://www.emcohighvoltage.com/ourprods.htm>
- [67] Photonis Imaging Sensors (1998) *Photomultiplier Tubes Product Specification, XP2020*.
URL <http://irfu.cea.fr/Sphn/Tp/xp2020.pdf>
- [68] BEATTY, J. J. and ET AL. (2003) “The Cosmic Ray Energetics and Mass (CREAM) Experiment Timing Charge Detector,” *Proceedings of International Society for Optical Engineering*, **4858**, pp. 248–254.
- [69] BRUN, R. and F. RADEMAKERS (1997) “ROOT - An Object Oriented Data Analysis Framework,” *Nucl. Inst. & Meth. A*, **389**, pp. 81–86.
- [70] CERN, “class TTree (Web Site),” .
URL <http://root.cern.ch/root/html/TTree.html>
- [71] MARROCCHESI, P. S. and ET AL. (2008) “Preliminary results from the second flight of CREAM,” *Advances in Space Research*, **41**, pp. 2002–2009.
- [72] AGOSTINELLI, S. and ET AL. (2003) “GEANT4-A Simulation Toolkit,” *Nucl. Inst. & Meth. A*, **506**, pp. 250–303.
- [73] AHN, H. S. and ET AL. (2007) “Elemental Spectra from the CREAM-I Flight,” *Proc. 30th Int. Cosmic Ray Conf.*, **2**, pp. 63–66.
- [74] LAFFERTY, G. and T. WYATT (1995) “Where to stick your data points: The treatment of measurements within wide bins,” *Nucl. Inst. & Meth. A*, **355**, pp. 541–547.

- [75] PARK, N. H. and ET AL. (2007) “Effect of albedo particles on charge measurement,” *Proc. 30th Int. Cosmic Ray Conf.*, **2**, pp. 381–384.
- [76] BRANDT, T. J. and ET AL. (2007) “Charge Identification in the CREAM Experiment,” *Proc. 30th Int. Cosmic Ray Conf.*, **2**, pp. 377–380.
- [77] AHN, H. S. and ET AL. (2009) “Deviations of cosmic ray elemental spectra from a single power law,” *Submitted to Nature*.

Vita

Samuel Adam Isaac Mognet

Education

The Pennsylvania State University State College, Pennsylvania 1999–Present
Ph.D. in Physics, December 2009
Area of Specialization: Experimental Particle Astrophysics
University of Southern Maine Portland/Gorham, Maine 1994–1999
B.A. in Physics, *magna cum laude* with a minor in Mathematics

Awards and Honors

NASA Group Achievement Award to CREAM Science and Mission Support Team 2006
University of Southern Maine Physics Department Physics Achievement Award 1999

Research Experience

Doctoral Research The Pennsylvania State University 2000–Present
Thesis Adviser: Prof. Stephane Coutu (James Beatty 2000-2004)
My research has been concerned with primary cosmic ray spectra measured with the CREAM series of balloon-borne cosmic ray detector experiments. I have been involved with detector development, construction, data analysis, simulation and operation.

Teaching Experience

Teaching Assistant The Pennsylvania State University 1999–present
I taught labs and recitation sections for introductory calculus-based physics (PHYS 211) for several semesters. I also served as the assistant for an advanced undergraduate lab course for one semester (PHYS 457).
Physics department tutor for undergraduate physics classes University of Southern Maine, Portland/Gorham, Maine 1997–1999